ABSTRACT

STOCHASTIC MODELING OF FLOWS IN MEMBRANE PORE NETWORKS

by
Binan Gu

Membrane filters provide immediate solutions to many urgent problems such as water purification, and effective remedies to pressing environmental concerns such as waste and air treatment. The ubiquity of applications gives rise to a significant amount of research in membrane material selection and structural design to optimize filter efficiency. As physical experiments tend to be costly, numerical simulation and analysis of fluid flow, foulant transport and geometric evolution due to foulant deposition in complex geometries become particularly relevant. In this dissertation, several mathematical modeling and analytical aspects of the industrial membrane filtration process are investigated. A first-principles mathematical model for fluid flow and contaminant advection/deposition through a network of cylindrical pores, and time evolution of membrane pore geometry, is proposed, formulated as a system of ordinary and partial differential equations. Membrane filter performance metrics, including total throughput (total volume of filtered fluid) and foulant concentration at membrane pore outlets, among others, are thoroughly studied against membrane geometric features such as porosity and tortuosity (average normalized distance traveled by fluid through pores between membrane top and bottom surfaces). The influence of the underlying, often complex, pore geometries on the performance of the membrane filters is explored in the following setups: (1) layered planar membrane structures with intra-layer pore connections; (2) general pore networks generated by a random graph generation protocol; (3) pore size variations in a pore network and (4) pore size gradient in a banded membrane network. Future work should include

studying pore size variations on porosity graded networks and stochastic modeling of large-particle sieving in pore networks.

In Chapter 1, an overview of the experimental, computational and theoretical literature on membrane filtration is given to motivate the following Chapters. In Chapter 2, a mathematical model is proposed for multilayered membrane filters with interconnected pores in the junction between layers. A side-by-side comparison is carried out between three simple geometries that have various degrees of pore connectivity and the same initial pore radius in each layer. Pore size heterogeneities, modeled as a random perturbation on initial pore size, are also studied in detail. Via variations in the strength of the pore-size perturbation, the statistical and physical influence on key properties of membrane filters, such as initial resistance, total throughput and foulant concentration at pore outlets, are analyzed and discussed. This work appeared in Journal of Fluid Mechanics.

In Chapters 3 and 4, a random graph generation protocol is devised to generate pore networks that generalize the structures considered in Chapter 2. A membrane filter is modeled as a graph with vertices and edges representing pore junctions and pore throats respectively. Local fluid and foulant transport equations are posed on each edge, coupled with conservation laws to produce global equations that capture the connectivity of the network. When a uniform initial pore radius is assumed (Chapter 3), initial membrane porosity is found to be a strong predictor for total throughput via a power law; and accumulated foulant concentration at membrane pore outlets satisfies a negative exponential relationship to membrane tortuosity. When pore size variations are imposed as pore-wise noise perturbation, however (Chapter 4), it is observed that network variations induced from the random graph generation have a stronger influence on membrane performance, unless noise strength is large. Membrane initial porosity is again found to be a crucial geometric feature.

The work of these Chapters appeared in SIAM Journal on Applied Mathematics and Journal of Membrane Science, respectively.

In Chapter 5, a variant of the protocol described in Chapter 3 is developed to generate banded pore networks in which the pore radius decreases from one band to the next, creating a pore-size gradient. Under specific assumptions, an optimal radius gradient in the depth of the banded membrane that maximizes either total throughput of filtrate or the particle retention capability of the membrane, is found. Finally, in Chapter 6, conclusions from the previous chapters are discussed, along with two open questions for future work.

STOCHASTIC MODELING OF FLOWS IN MEMBRANE PORE NETWORKS

by
Binan Gu

A Dissertation
Submitted to the Faculty of
New Jersey Institute of Technology and
Rutgers, The State University of New Jersey – Newark
in Partial Fulfillment of the Requirements for the Degree of
Doctor of Philosophy in Mathematical Sciences

Department of Mathematical Sciences
Department of Mathematics and Computer Science

August 2022

APPROVAL PAGE

STOCHASTIC MODELING OF FLOWS IN MEMBRANE PORE NETWORKS

Binan Gu

Linda J. Cummings, Dissertation Co-Advisor — Date
Professor of Mathematical Sciences, NJIT

Lou Kondic, Dissertation Co-Advisor — Date
Distinguished Professor of Mathematical Sciences, NJIT

James N. MacLaurin, Committee Member — Date
Assistant Professor of Mathematical Sciences, NJIT

Anand U. Oza, Committee Member — Date
Assistant Professor of Mathematical Sciences, NJIT

Ian M. Griffiths, Committee Member — Date
Professor of Industrial Mathematics and Royal Society University Research Fellow, University of Oxford, Oxford, United Kingdom

BIOGRAPHICAL SKETCH

Author: Binan Gu

Degree: Doctor of Philosophy

Date: August 2022

Undergraduate and Graduate Education:

- Doctor of Philosophy in Mathematical Sciences,
  New Jersey Institute of Technology, Newark, NJ, USA (2022)
- Master of Science in Mathematics,
  New York University, New York, NY, USA (2016)
- Bachelor of Science in Mathematics,
  University of Southern California, Los Angeles, CA, USA (2013)
- Bachelor of Arts in Economics,
  University of Southern California, Los Angeles, CA, USA (2013)

Major: Mathematical Sciences

Presentations and Publications:

B. Gu, L. Kondic, and L. J. Cummings. "On Pore-size Gradient in Membrane Networks". *In preparation.*

B. Gu, L. Kondic, and L. J. Cummings. "Network-based Membrane Filters: Influence of Network and Pore Size Variability on Filtration Performance". *Journal of Membrane Science*, 657, 5 (2022).

B. Gu, L. Kondic, and L. J. Cummings. "A Graphical Representation of Membrane Filtration". *SIAM Journal on Applied Mathematics*, 82, 3 (2022).

B. Gu, D. L. Renaud, P. Sanaei, L. Kondic and L. J. Cummings. "On the Influence of Pore Connectivity on Performance of Membrane Filters". *Journal of Fluid Mechanics*, 902, A5 (2020).

B. Gu, L. Kondic and L. J. Cummings, "A Graphical Representation of Membrane Filtration," *16th Northeast Complex Fluids and Soft Matter Workshop (NCS16)*, Princeton University, Princeton, New Jersey, Jan 2022.

B. Gu, L. Kondic and L. J. Cummings, "A Graphical Representation of Membrane Filtration," *74th American Physical Society Division of Fluid Dynamics*, Phoenix, Arizona, Nov 2021.

B. Gu, L. Kondic and L. J. Cummings, "A Graphical Representation of Membrane Filtration," *InterPore 13th International Conference on Porous Media & Annual Meeting (virtual)*, May 2021.

B. Gu, P. Sanaei, L. Kondic and L. J. Cummings, "Stochastic Modelling of Adsorption and Sieving in a Pore Network," *InterPore 12th International Conference on Porous Media & Annual Meeting (virtual)*, Aug 2020.

B. Gu, P. Sanaei, L. Kondic and L. J. Cummings, "Stochastic Modelling of Sieving in Membrane Filters with Complex Pore Morphology," *72nd American Physical Society Division of Fluid Dynamics*, Seattle, Washington, Nov 2019.

B. Gu, P. Sanaei, L. Kondic and L. J. Cummings, "Stochastic Modelling of Sieving," *Fluid Mechanics of Cleaning and Decontamination, Special Interest Group*, Oxford University, Oxford, United Kingdom, Jul 2019.

B. Gu, D. L. Renaud, P. Sanaei, L. Kondic and L. J. Cummings, "Modeling Connectivity and Asymmetry in Membrane Filters," *Transport in Disordered Systems*, Princeton University, Princeton, New Jersey, Jan 2019.

B. Gu, D. L. Renaud, P. Sanaei, L. Kondic and L. J. Cummings, "Modeling Connectivity and Asymmetry in Membrane Filters," *10th Northeast Complex Fluids and Soft Matter Workshop (NCS10)*, Rutgers University, New Brunswick, New Jersey, Jan 2019.

B. Gu, D. L. Renaud, P. Sanaei, L. Kondic and L. J. Cummings, "Modeling Connectivity and Asymmetry in Membrane Filters," *71st American Physical Society Division of Fluid Dynamics*, Atlanta, Georgia, Nov 2018.

B. Gu, D. L. Renaud, P. Sanaei, L. Kondic and L. J. Cummings, "Modeling Asymmetry of Membrane Filters with Complex Morphology," *9th Northeast Complex Fluids and Soft Matter Workshop (NCS9)*, University of Pennsylvania, Philadelphia, Pennsylvania, May 2018.

先做人，其次做艺术家，再次做音乐家，最后做钢琴家。
You must first of all be a man, then an artist, then a musician and lastly a pianist.

傅雷
Fu Lei

Dedicated to my loving parents Yinrui Yang, Hongren Gu, and endearing partner Vivi.

ACKNOWLEDGMENT

I give my deepest thanks to my advisors, Prof. Linda Cummings and Prof. Lou Kondic. They have not only taught me the ways of scientific research and methods of effective writing, but also, more importantly, given me the freedom to pursue my own ideas in the various inquiries on which we have embarked. Their open guidance has led to the breadth of fields in applied mathematics endowed in this dissertation.

I would like to thank Prof. Pejman Sanaei. He was my student mentor who happened to see that my research interest and his crossed when I just arrived at NJIT. It was he who introduced to me the various mathematical aspects of the problem in membrane filtration. He pointed to the road I have been paving for the past six years.

I also thank my committee members, Prof. James Maclaurin, Prof. Anand Oza, and Prof. Ian Griffiths for their insightful comments on my work. I also thank Prof. Griffiths for hosting my visit in the summer of 2019 at Oxford University.

Several professors have taught courses that left marks on my (ongoing) learning process, including Prof. Cyrill Muratov, Prof. Brittany Froese Hamfeldt and Prof. David Shirokoff among many others. I give them my sincerest thanks.

I thank the NSF for supporting my research (grant No. DMS-1615719 and DMS-2133255). I am grateful for NJIT and the Department of Mathematical Sciences for accommodating my learning and research experience with the most helpful and gracious staff and ample facilities.

Immense gratitude is given to my friends and colleagues, Axel, Erli and Jimmie, among many others, for the endless discussions and selfless support through the years of studies, and for being trustworthy buddies. Jim, we gotta finish that Hele-Shaw project.

I thank my parents, Yinrui Yang and Hongren Gu, for not only bringing me up, suggesting the major of mathematics, but also giving me the maximum possible

amount of freedom and space to pursue what I love. The sacrifice they have made for this Ph.D. to come through, though not tangible to observers, secretly shows up everywhere.

Last but not least, I thank my partner, Vivi Liu for spending most of my Ph.D. years by my side, supporting the quality of my life while also putting up with my clumsy mental health management. Without her, my mind would have slipped far away and this journey would have been much more uphill.

TABLE OF CONTENTS

Chapter **Page**

1 INTRODUCTION 1

- 1.1 Motivation for Membrane Filtration 1
- 1.2 Structure of This Dissertation 5

2 ON THE INFLUENCE OF PORE CONNECTIVITY ON PERFORMANCE OF MEMBRANE FILTERS 8

- 2.1 Overview 8
- 2.2 Introduction 8
- 2.3 Mathematical Modeling 11
  - 2.3.1 Homogeneous Model 12
  - 2.3.2 Heterogeneous Model 18
  - 2.3.3 Measures of Performance 21
- 2.4 Scaling and Nondimensionalization 22
  - 2.4.1 Homogeneous Model 22
  - 2.4.2 Heterogeneous Model 24
- 2.5 Results 24
  - 2.5.1 Results for Homogeneous Membranes 26
  - 2.5.2 Results for Heterogeneous Membranes 38
- 2.6 Ending Remarks 50

3 A GRAPHICAL REPRESENTATION OF MEMBRANE FILTRATION . 53

- 3.1 Overview 53
- 3.2 Introduction 53
- 3.3 Modeling 57
  - 3.3.1 Graph Theoretical Setup 57
  - 3.3.2 Graph Generation for a Membrane Network 59
  - 3.3.3 Flow in an Edge 61

TABLE OF CONTENTS
(Continued)

Chapter **Page**

3.3.4 Operators and Function Spaces on Graphs 62

3.3.5 Flow on a Graph 64

3.3.6 Foulant Advection and Adsorptive Fouling 65

3.3.7 Measures of Performance 69

3.4 Nondimensionalization 70

3.5 Algorithm 71

3.6 Results 72

3.6.1 Geometric Network Parameters 73

3.6.2 Initial Void Volume and Average Number of Neighbors 74

3.6.3 Tortuosity 79

3.7 Ending Remarks 83

4 NETWORK-BASED MEMBRANE FILTERS: INFLUENCE OF NETWORK AND PORE SIZE VARIABILITY ON FILTRATION PERFORMANCE 86

4.1 Overview 86

4.2 Introduction 86

4.3 Setup: General Pore Networks 89

4.3.1 Network Generation 91

4.3.2 Fluid Flow 91

4.3.3 Advection and Adsorptive Fouling 92

4.3.4 Network Notations 94

4.3.5 Scales 95

4.3.6 Performance Metrics 96

4.4 Investigation Methods 97

4.5 Results and Discussions 100

4.5.1 Detailed Example: Low Porosity Network in Low Noise Regime 101

4.5.2 Results for Varied Noise Amplitude and Porosity 105

TABLE OF CONTENTS
(Continued)

Chapter **Page**

4.6 Ending Remarks 113

5 ON PORE-SIZE GRADED MEMBRANE NETWORKS 115

5.1 Overview 115

5.2 Introduction 115

5.3 Mathematical Modeling 119

5.3.1 Pore Size-Graded Networks 120

5.3.2 Governing Equations 126

5.4 Performance Metrics 128

5.5 Scales 130

5.6 Results and Discussions 131

5.6.1 Total Porosity Evolution 136

5.6.2 Band Porosity Evolution 138

5.6.3 Performance Metrics with Flux Threshold 142

5.7 Ending Remarks 145

6 CONCLUSIONS AND FUTURE WORK 149

6.1 Conclusions 149

6.2 Future Work 153

6.2.1 Non-constant Band Radius for Pore-size Graded Networks . . . 153

6.2.2 Sieving 155

APPENDIX A SUPPLEMENTARY MATERIAL FOR CHAPTER 2 160

A.1 Norms for Accuracy and Sufficient Penetration 160

A.2 Calculations and Proofs 162

APPENDIX B SUPPLEMENTARY MATERIAL FOR CHAPTER 3 166

B.1 Justification for the Pore Radius Evolution Model 166

B.2 Tortuosity 167

B.3 Worked Example 173

TABLE OF CONTENTS
(Continued)

Chapter **Page**

APPENDIX C SUPPLEMENTARY MATERIAL FOR CHAPTER 4 176

C.1 Network Generation 176

C.2 The Graph Laplacian 176

C.3 Performance Metrics 178

C.4 Tortuosity 180

C.5 Porosity Correction 180

APPENDIX D SUPPLEMENTARY MATERIAL FOR CHAPTER 5 182

D.1 Junctions and Pores in a Band 182

D.2 Number of Random Points in Each Band 184

D.3 Analytical Results on Pore Closure Time 185

REFERENCES 191

LIST OF TABLES

Table **Page**

2.1 Key Nomenclature 12

3.1 Key Nomenclature 57

4.1 Key Dimensional Quantities 95

4.2 Key Dimensionless Parameters 96

4.3 Key Output Quantities 101

5.1 Key Nondimensional Parameters 132

5.2 Key Nondimensional Quantities 132

5.3 Optimal Radius Gradient Value for Each Performance Metric 146

LIST OF FIGURES

Figure **Page**

1.1 Schematic of three membrane filtration methods: (a) tangential; (b) dead-end and (c) direct-flow. Figure courtesy of [54]. 4

2.1 Magnified membrane images showing (a) gradation of pores sizes through membrane depth, and in-plane inhomogeneity of pore sizes [76]; (b) connectivity and junction layer [141] and (c) pore size distributions [119]. 9

2.2 Illustration of a connected, branched-pore membrane and volumetric flow rate balance at pore junctions. (a) An $m = 3$ layer pore-network with unit cell area $(2W)^2$. (b) Schematic bifurcation of a single pore (left) and two pores merging into one (right), homogeneous in both cases. In the former case $Q_1 = 2Q_2$, and in the latter $2Q_1 = Q_2$, by mass conservation. 13

2.3 Schematic of a connected branching pore membrane with $m = 2$ layers, pressure drop P_0 and upstream particle concentration C_0. Flow is assumed to be entirely in the X-direction. 20

2.4 The three distinct pore architectures compared: (a) single-inlet non-connected branch membrane; (b) single-inlet connected membrane; (c) two-inlet connected membrane. The ordered color coding (black, blue and red) is used throughout Section 2.5. 25

2.5 Homogeneous models: pore radius evolution for each layer. (a) Non-connected branch membrane (b) single-inlet connected (c) two-inlet connected membrane. For all calculations, $\phi_{\text{top}} = 0.539$ (maximum comparable porosity), $\lambda = 30$, $m = 5$ and the initial resistance $r_0 = 1$. 27

2.6 Homogeneous models: volumetric flow rate evolution for non-connected branch membrane (black), single-inlet connected (blue) and two-inlet connected membrane (red). The solid black curve lies under the solid blue curve. For all calculations, $\phi_{\text{top}} = 0.539$ (maximum comparable porosity), $\lambda = 30$, $m = 5$ and the initial resistance $r_0 = 1$. 27

LIST OF FIGURES
(Continued)

Figure **Page**

2.7 Homogeneous models: volumetric flow rate versus throughput for non-connected (black), single-inlet connected (blue), and two-inlet connected (red) membrane structures. Curves with the same line style represent equivalent values of ϕ_{top} for each model. The solid black curve lies under the solid blue curve. For all simulations, $\lambda = 30$, $m = 5$ and initial resistance $r_0 = 1$. 29

2.8 Homogeneous models: (a) total throughput versus ϕ_{top} for non-connected (black), single-inlet connected (blue), and two-inlet connected (red) membrane structures. (b) Volumetric flow rate versus throughput for connected membranes with ν_1-inlet pores and $\phi_{\text{top}} = 0.539$. For all simulations, $\lambda = 30$, $m = 5$ and initial resistance $r_0 = 1$. 29

2.9 Homogeneous models: (a) initial particle concentration at outlet of first layer, $c_1(0)$, versus deposition coefficient λ for single-inlet structures. Note that the results are identical for both connected and non-connected single-inlet models because they have the same initial top pore radius a_{10}. (b) Initial particle concentration at i-th layer pore outlets, $c_i(0)$, versus λ for single-inlet non-connected (black) and connected (blue) models with $\phi_{\text{top}} = 0.709$. The vertical range is extended below zero for clarity only; $c_i(0) > 0$ always. For all simulations, $m = 6$ and $r_0 = 1$. 31

2.10 Homogeneous models: total throughput versus λ for single-inlet non-connected (black) and connected (blue) membrane structures. Each set of curves represents equivalent initial top layer porosity. Each black dot is an equivalence point between the two models such that the same total throughput is achieved with the same λ. For all simulations, $m = 6$ and $r_0 = 1$. 32

2.11 Homogeneous models: (a)-(c) concentration at pore outlet versus throughput for (a) non-connected, (b) single-inlet connected, and (c) two-inlet connected membrane structures. (d) Two-inlet connected model: the concentration of particles leaving the first layer downstream surface (c_1, solid red curve) and cross-sectionally averaged first layer pore velocity ($\overline{u}_{\text{p},1}$, dashed red curve) are shown. For all calculations, $\lambda = 30$, $m = 5$, $\kappa = 0.6$ and $r_0 = 1$. 34

2.12 $c_{\text{diff}}\,(\lambda; m)$ defined in Equation (2.45) versus λ for (a) single-inlet non-connected (b) single-inlet connected and (c) two-inlet connected membrane structures. (d) Zero level set of the function g defined in Theorem 1 for single-inlet model (blue), two-inlet model (red) and the branch model (black). The colored data points are the pairs of x-intercepts with their respective m values from panels (a), (b) and (c), respectively. For all simulations, $\phi_{\text{top}} = 0.4$ and $r_0 = 2$. 37

LIST OF FIGURES
(Continued)

Figure **Page**

2.13 Heterogeneous models: average volumetric flow rate Equation (2.53) versus throughput Equation (2.54) of single-inlet (blue) and two-inlet (red) connected models for varying noise amplitude, b. (a),(c) $\kappa = 0.95$ and (b),(d) $\kappa = 0.6$. All results are averaged over $\mathbf{10^4}$ simulations, with common parameters $\lambda = 30$ and $m = 5$. 42

2.14 Heterogeneous models: average volumetric flow rate versus throughput of non-connected branch model (black); and connected branch model with $\nu_i = 2^{i-1}$ (magenta), (a),(c) $\kappa = 0.95$ (b),(d) $\kappa = 0.6$. All results are averaged over $\mathbf{10^4}$ simulations, with common parameters $\lambda = 30$ and $m = 5$. 43

2.15 Heterogeneous models: results for the single-inlet connected model. (a) Initial average volumetric flow rate $\overline{u}_b(0)$ (blue) and reciprocal of initial average resistance $1/\overline{r}_b(0)$ (black) vs. noise amplitude, b. (b) a large sample approximation of the Jensen gap $\mathcal{J}$ (given in Equation (2.57)), vs. noise amplitude, b. All results are averaged over $\mathbf{10^4}$ simulations, with common parameters $\lambda = 30$ and $m = 5$. 43

2.16 Heterogeneous models: average initial resistance for (a) single-inlet connected model and (b) two-inlet connected model. All results are averaged over $\mathbf{10^4}$ simulations, with common parameters $m = 5$ and $\lambda = 30$. 47

2.17 Heterogeneous models: partial derivative of expected initial resistance with respect to noise amplitude b for (a) single-inlet connected model and (b) two-inlet connected model. For all simulations, $m = 5$ and $\lambda = 30$. 48

2.18 Initial average membrane outlet concentration versus geometric coefficient, κ, for the single-inlet connected model. For all simulations, $m = 5$ and $\lambda = 30$. 48

3.1 Schematic: (a) an experimental image with lateral view of a filter cross-section [6]; (b) a corresponding (partial) graph representation with inlets on the top surface (blue) and interior pore junctions and throats (red). 54

LIST OF FIGURES
(Continued)

Figure **Page**

3.2 (a) 2D schematic of the 3D graph generation; (b) 3D realization with the periodic metric. Labels for (a) and (b): red filled circles form V_{int}, blue filled circles form induced inlets V_{top}, and black filled circles form induced outlets V_{bot}. In (a), blue dotted lines are cutting lines (planes in 3D), and magenta circles are discarded points. The blue and orange dotted circles form the search annulus enforced by D and D_{min}. In (b), periodicity is enforced only through the four interior walls per Equation (3.2). 60

3.3 Total throughput h_{final} vs initial void volume Vol_0 (loglog scales). (a) Isolated network setup; (b) periodic setup. Line of best fit for $d = 0.45$ is in black, with gradient m given in legend (with $R^2 = 0.99989$ and 0.99993, respectively). Distribution of error for each data point is given in the histograms in the supplement. 75

3.4 Total throughput h_{final} vs average number of neighbors N (loglog scales). (a) Isolated network setup; (b) periodic setup. Line of best fit for $d = 0.45$ is in black, with gradient m given in legend. Distribution of error for each data point is given in the histograms in the supplement. Same setup for (c) and (d) with $h_{\text{final}}/\text{Vol}_0$ as vertical axis (loglog scales). 76

3.5 Final accumulated foulant concentration $c_{\text{acm}}(t_{\text{final}})$ vs initial void volume Vol_0 (loglog scales). (a) Isolated network setup; (b) periodic setup. Distribution of error for each data point is given in the histograms in the supplement. 78

3.6 Final accumulated foulant concentration $c_{\text{acm}}(t_{\text{final}})$ vs tortuosity τ (semilog plot). (a) Isolated network setup; (b) periodic setup. The line of best fit is in black in each plot, with gradient m given in the legend (with $R^2 = 0.99838$ and 0.9961, respectively). The blue and red boxes at top left are shown as zooms in (c) and (d), respectively, for small tortuosity values (same data as (a) and (b), respectively). Distribution of error for each data point is given in the histograms in the supplement. 80

3.7 Total throughput h_{final} vs tortuosity τ (semilog plot). (a) Isolated setup; (b) periodic setup. Error distribution for each data point is provided in the supplement. Same scale for h_{final} as in Figure 3.3. 81

3.8 Initial void volume vs tortuosity (semilog plot). (a) Isolated setup; (b) periodic setup. Error distribution for each data point is provided in the supplement. 82

LIST OF FIGURES
(Continued)

Figure **Page**

4.1 2D schematic of the 3D network generation with periodic boundary conditions showing: interior junctions $\mathcal{V}_{\text{int}}$ (red filled circles); pore inlets $\mathcal{V}_{\text{in}}$ (blue filled circles) and outlets $\mathcal{V}_{\text{out}}$ (black circles) induced by the cutting process; the cutting planes blue dashed lines; discarded points (magenta filled circles). Solid lines represent pores, while dash-dotted lines are pores that arise from the periodic boundary condition (red are interior to the membrane). $l_{\max}W$ and δW are prescribed maximum and minimum pore lengths, respectively. 90

4.2 Schematic of a 3D network with $l_{\max} = 0.15$ and $N_{\text{total}} = 2000$. Solid red lines are interior pores; dashed red lines are pores created by the periodic boundary conditions. Blue dots are inlets. Black dots are outlets. 92

4.3 Scatter plot of throughput versus porosity, under (a) noise realizations, (b) network realizations (with each network perturbed once). The black rectangle in (b) shows the horizontal and vertical range of (a). For both plots, $\beta = 0.06$. 103

4.4 Histogram of throughput score, under (a) noise realizations, (b) network realizations (with each network perturbed once). Same parameters as in Figure 4.3. 103

4.5 Scatter plot of concentration versus tortuosity. Same description and parameters as in Figure 4.3. 104

4.6 Histogram of tortuosity under (a) noise realizations (b) network realizations. Same parameters as in Figure 4.3; same data as Figure 4.5. . 105

4.7 Histogram of concentration and tortuosity scores, respectively under (a,c) noise realizations and (b,d) network realizations. Same parameters as in Figure 4.3. 106

4.8 Mean throughput $\overline{h}_{\text{noise}}$, $\overline{h}_{\text{net}}$ (a,b) and mean throughput scores $\overline{\widehat{h}}_{\text{noise}}$, $\overline{\widehat{h}}_{\text{net}}$ (c,d) versus noise amplitude β under noise and network realizations. Low porosity $\phi \approx 0.25$ (a,c) and high porosity $\phi \approx 0.6$ (b,d) cases are shown. Vertical error bars are standard deviations for each mean value. Note that the scores (c,d) show relative change, so that, *e.g.*, an increase from 0 to 0.6 on the vertical axes means a 60% increase. 107

4.9 Ratio of standard deviations of raw throughput (black squares) and throughput scores (black diamonds) for (a) Low porosity (corresp. Figures 4.8a and 4.8c) and (b) high porosity (corresp. Figures 4.8b and 4.8d). 108

LIST OF FIGURES
(Continued)

Figure **Page**

4.10 Mean concentration and concentration score. Same setup as in Figure 4.8. 109

4.11 Same setup as Figure 4.9 for raw concentration and concentration scores. (a) Low porosity (corresp. Figures 4.10a and 4.10c) and (b) high porosity (corresp. Figures 4.10b and 4.10d). 110

4.12 Mean tortuosity and tortuosity score. Same setup as in Figure 4.8. . . . 111

5.1 Schematic of a 3D banded network represented in 2D. Colored junctions and pores correspond to each band as follows: red 1st band; green 2nd band; light blue 3rd band and indigo 4th band. Blue dots are inlets. White dots are outlets. Dashed lines are pores created by the periodic boundary conditions (see Equation (D.3) in Appendix D.1). 121

5.2 Performance metrics against radius gradient. (a) Total throughput; (b) initial flux; (c) accumulated foulant concentration; and (d) filter mass capacity. 133

5.3 Total porosity evolution. (a) $a_{\max} = 0.1$; (b) $a_{\max} = 0.15$; (c) $a_{\max} = 0.2$. In (d), for each $a_{\max}$, membrane porosity usage (Equation (5.23b)) is plotted against radius gradient s. $\Phi(0) = 0.6$ is the initial porosity. . . 137

5.4 Band porosity evolution with $a_{\max} = 0.1$. (a) 1st band; (b) 2nd band; (c) 3rd band (d) 4th band. Each inset subfigure plots band porosity usage (the total change in band porosity over the filter lifetime) as a function of radius gradient s. 139

5.5 Same setup as Figure 5.4. $a_{\max} = 0.15$. 141

5.6 Same setup as Figure 5.4. $a_{\max} = 0.2$. 142

5.7 (a) Total throughput; (b) ACO; (c) filter mass capacity; and (d) porosity usage. Flux Threshold is 2×10^{-6}. 143

A.1 Single-inlet model: region of parameters that are δ_1-accurate and allow sufficient δ_2 penetration. Parameter choice: $\delta_1 = 0.05$, $\delta_2 = 0.3$, $\beta = \frac{1}{3}$, $r_0 = 1$, $\phi_{\text{top}} = 0.4$. 161

A.2 Heterogeneous models: initial resistance for single-inlet model (a) Average $\bar{u}_b(0)$ over 10^5 simulations; (b) exact large number limit $\mathbb{E}[r_b(0)]$. . . . 165

LIST OF FIGURES
(Continued)

Figure **Page**

B.1 Tortuosity limit: (a) Isolated setup (unit cube); (b) periodic setup (unit cube and a square of side length 2 containing the bottom surface of the unit cube). X (blue) and Y (red) are uniformly sampled from the top and bottom membrane surface, respectively. K (black) in both figures is the projection of X onto the bottom surface; XK in both figures has length 1. 173

B.2 2D schematic of a reflected-Y network with labelled physical quantities presented in Section 3.4. 175

D.1 Schematic of a simplified setup for Theorem 2. Colored junctions and pores correspond to each band as follows: red upstream pores and indigo downstream pores. Blue dots are inlets. The red dot is an interior junction. White dots are outlets. Here $n_{\mathrm{up}} = 4$ and $n_{\mathrm{down}} = 5$. 186

CHAPTER 1

INTRODUCTION

1.1 Motivation for Membrane Filtration

The practice of filtration dates back to primitive water filters made with rushes and plants. Ancient Egyptians used porous clay pots as ceramic filters to remove sediments from boiled water. The Greek physician Hippocrates invented the "Hippocrates Sleeve", a cloth bag that serves a similar purpose with better control over the undesired content. *Sushruta Samhita*, an ancient Sanskrit text on medicine, suggested using sand and gravel to purify water, a water treatment technique still used in the modern world [9]. However, these water purification methods were still insufficient to prevent water-borne illnesses caused by microbes and bacteria. Richard Adolf Zsigmondy invented the first membrane filters at the turn of the 20th century that saw commercial production and uses in microbiology and assessment of potable water [146]. Through the long history of filtration, the porous gaps within filter materials have been getting smaller and smaller, from slivers between leaves and stems, to sand grains, and finally polymer fibers only microns apart. This trend primarily owes to advances in other areas such as imaging and chemical analysis, which inform our knowledge about the size of some of the unwanted substance particles in the process fluid, from visible rocks and soil sediments to previously undetectable microorganisms and heavy metal ions [136].

Nowadays, the use of membrane filters spans a wide range of modern applications. Implementations of membrane filters are ubiquitous in industrial plants serving a variety of functions such as waste water treatment [59], radioactive sludge removal [25, 2] and nuclear waste treatment [33]. Commercial membrane filters also aid in manufacturing processes such as water purification [88], beer clarification [133, 78], semiconductor and microelectronics processing [59] and membrane bioreactors [88, 35]. Furthermore, daily household cleaning efforts, such as air conditioning [80, 36, 3, 134], kitchen grease filtration [137] and counter-top water purification systems [11], also benefit from utilizing membrane filters.

There are two general types of membrane materials used in commercial filters: polymeric and ceramic [65, 42], with further sub-categorizations depending on the specific chemical compositions. Most polymeric membranes are made with low-cost organic materials and thus are popular in industrial applications. However, they are often not suited for applications involving large thermal fluctuations and aggressive chemical treatment. Ceramic membrane filters can fill this role, and offer additional benefits such as high hydrophilicity to produce a larger fluid filtrate flux [79]. Though ceramic filters tend to yield better filtration results, their specific design using metallic oxides tends to increase the cost significantly. Finding the proper design with existing materials to balance production costs has become a central relevant topic in membrane filtration research.

Membrane filters also admit a variety of underlying pore microstructures that are either formed naturally or manufactured to satisfy specific needs in applications. Common configurations include node-fibril [105], flat-sheet [114] and multitube [84]. Four distinct filtration processes may be distinguished, dictated by the scale of the pore size: microfiltration for removing micron-sized particles such as colloids and smoke molecules, ultrafiltration for filtering bacteria and viruses, nanofiltration for removing monovalent ions, and reverse osmosis for removing even smaller multivalent ions and particles (making it popular in obtaining pure water) [131]. At each associated pore scale in any filtration process, there are also three main fouling mechanisms: 1) adsorption, where particles far smaller than the pore size adhere to the pore walls due to chemical attraction between the particle and the membrane material; 2) sieving, where particles with size at the order of the pore size partially cover or completely clog pore channels; and 3) cake formation, which happens at a later stage of filtration when the previous two fouling modes have saturated – particles of various sizes accumulate on the membrane's upstream surface to form a new layer of porous media. These fouling modes have been studied via experiments and numerical simulations, both in isolation and with multiple modes operating simultaneously, by many researchers with a goal of developing predictive modeling; see for example the works of [99] and [16] on adsorption, [60, 13] on blocking, [32, 97] on caking, and [8, 17, 56, 110, 112, 113] for multiple simultaneous modes.

Depending on the application and the selected membrane materials, industrialists practice three typical membrane filtration methods – tangential [24], dead-end [116] and direct flow [54, 28]. In dead-end filtration (Figure 1.1a), a contaminated fluid is driven in a direction perpendicular to the membrane surface via an applied transmembrane pressure. In tangential flow (also known as cross-flow, see Figure 1.1b), a process fluid is driven by an applied pressure parallel to the membrane surface. Particles smaller than the pore size or gaps on the membrane surface will pass through, while larger particles are circulated by the tangential flow back to the feed solution, thus delaying filter clogging. Tangential filtration prolongs filter lifetime but suffers from low rate of filtrate (also known as permeate) production. Unlike filters under dead-end filtration, those under tangential flow give lower *rate* of filtrate production, but have longer filter lifetimes due to decreased fouling (the interested reader is referred to [33] for a more detailed discussion on the relative merits of these two processes). In direct flow filtration (Figure 1.1c), the flow pattern is similar to that in tangential flow on the membrane surface. But instead of circulating the flow, a cap is placed at the end of the filter, perpendicular to flow. This mode is midway between the two previous methods, utilizing a fair balance of fluid flux maintenance and filter lifetime. Each of these methods may be implemented under conditions of constant flux or constant pressure: in the former, the applied pressure

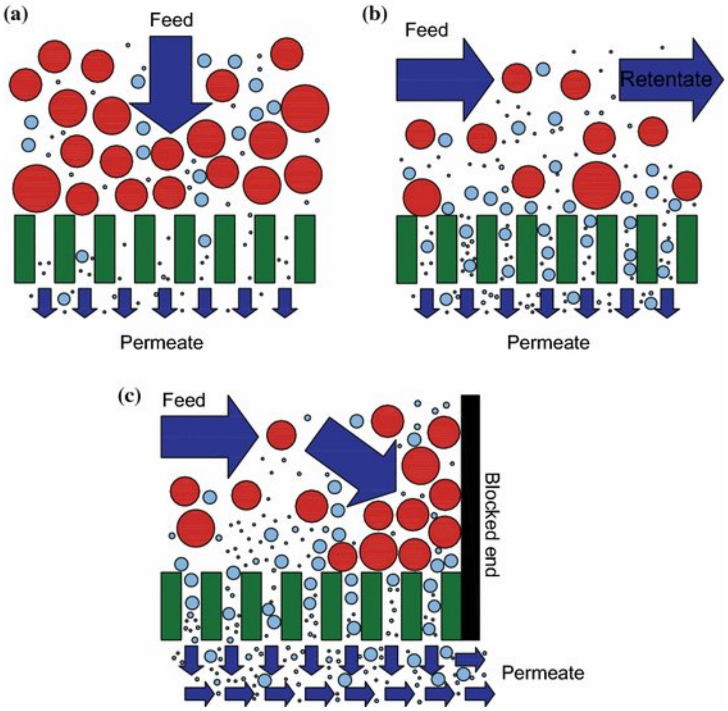

Figure 1.1 Schematic of three membrane filtration methods: (a) tangential; (b) dead-end and (c) direct-flow.
Figure courtesy of [54].

increases as the membrane fouls, resulting in increasing costs of operation but a guaranteed amount of filtrate, whereas in the latter, fluid flux decreases over time but energy is saved.

The membrane filtration process has garnered interest from a wide range of scientific research disciplines, including chemical and mechanical engineering, image processing, and now applied mathematics. Research efforts initially focused on experiments of membrane fouling and performance metrics such as fouling rates (how quickly the membrane clogs) and selectivity (the ratio of the amount of undesired particles in the product and in the feed; the lower the ratio, the higher the selectivity) [55, 40, 104, 77, 109]. Since the turn of the 21st century, a variety of experimental studies have investigated how membrane performance depends on the interior structure of the membrane filter (see, for example, Beuscher *et al.* [94, 82] among many others; also see [61, 17, 16] for extensive reviews on fouling and membrane design). Multilayered membrane filter designs have shown promise in manufacturing and much improved performance guarantees [21, 3, 93]. Several theoretical groups have also contributed greatly to the modeling, simulation and analysis of the membrane filtration process, at the single pore level with multiple fouling mechanisms [110, 44, 97], for pleated filters [113, 122], on repeated cells of planar membrane [74], reactive filters [68, 83, 69] and on multilayered membrane structures [46, 39, 112], among many others. In particular, network representations of multilayered membrane filters have been proposed by various authors, including works on modeling and simulations [139, 8, 45, 47, 13], multiple-scale analysis and homogenization techniques [102, 83, 7, 69], filter design and material optimization [97, 72, 71, 122], image analysis [14] and porosity visualization [123], which are particularly relevant for this dissertation.

The goal of this dissertation is two-fold: 1) to address open questions on membrane filters, such as the influence of pore interconnectivity, pore size heterogeneity under various structural settings and porosity gradient in the direction of fluid flow; and 2) to provide a sound mathematical background for computations and simulations on network representations of membrane filters, including multilayered filters.

1.2 Structure of This Dissertation

This dissertation consists of several completed published manuscripts, which may contain overlapping introductory descriptions. We introduce the essence of each chapter as follows.

In Chapter 2, we introduce simple branching pore models to describe the microstructure of a membrane filter, and use these models to discuss whether having connected layers of pores is a design favorable for optimizing filter performance (as measured by metrics such as filtrate production and contaminant control). We consider several simple “layered” pore network models with varying degrees of connectivity and compare their performance. We also investigate how pore size variations in each layer affect initial membrane performance characteristics. The content presented in Chapter 2 was published in the Journal of Fluid Mechanics [50].

In reality, membrane filters have more complicated microstructures than the models considered in Chapter 2. To examine this feature, we generalize the simple hierarchical pore structures considered there to a random network of pores in Chapter 3, continuing our analysis on models of membrane filters. We investigate how membrane performance correlates with network geometric characteristics, such as maximal allowed pore length, initial membrane porosity, and tortuosity of the pore network. In this chapter, we also derive equations for fluid flow and contaminant transport on a general network, laying the mathematical groundwork for the following Chapters. The content presented in Chapter 3 was published in the SIAM Journal on Applied Mathematics [48].

Furthermore, the manufacturing of membrane filters is not always perfect. Even if a manufacturer strives to manufacture a membrane with homogeneous pores, initial pore sizes throughout the membrane will differ, leading to *pore size variations*. To address the impact of this phenomenon and harness the potential insights it may offer on filter design, we investigate in Chapter 4 the influence of these imperfections on the performance of pores networks considered in Chapter 3. The content presented in Chapter 4 was published in the Journal of Membrane Science [49].

One versatile feature of a multilayered membrane filter design is to have a specific pore size assigned to each layer to distinguish layer functions. Larger pores upstream allow fluid to pass through more efficiently, while smaller pores downstream capture contaminants more effectively. This distribution of pore sizes leads to a pore-size gradient. In Chapter 5, we explore this setup via a pore-size graded network model. We focus on several key filtration performance metrics and investigate how they correlate with the pore-size gradient, with a particular interest in identifying optimal gradient values. The content presented in Chapter 5 is undergoing final revisions before submission for publication in a scientific journal.

In Chapter 6, we conclude our findings presented in this dissertation and discuss preliminary ideas concerning two open questions.

CHAPTER 2

ON THE INFLUENCE OF PORE CONNECTIVITY ON PERFORMANCE OF MEMBRANE FILTERS

2.1 Overview

In this chapter, we study the influence of a membrane filter's internal pore structure on its flow and adsorptive fouling behaviour. Membrane performance is measured via 1) comparison between volumetric flow rate and throughput during filtration; and 2) control of concentration of foulants at membrane pore outlets. Taking both measures into account, we address the merits and drawbacks of selected membrane pore structures. We first model layered planar membrane structures with intra-layer pore connections, and present comparisons between non-connected and connected structures. Our model predicts that membrane filters with connected pore structures lead to higher total volumetric throughput than those with non-connected structures, over the filter lifetime. We also provide a sufficient criterion for the concentration of particles escaping the filter to achieve a maximum in time (indicative of a membrane filter whose particle retention capability can deteriorate). Additionally, we find that the influence of intra-layer heterogeneity in pore-size distribution on filter performance, depends on the connectivity properties of the pores.

2.2 Introduction

Increasing interest in studying filter design and filtering efficiency has resulted in many comprehensive review articles, such as that by Bowen & Jenner [19], who provide a thorough overview of membrane separation technology, by Iritani [61], who surveys the various fouling mechanisms that operate during a membrane filtration process, and more recently by Chew *et al.* [24], who compiled experimental and modeling results on interfacial interactions and membrane fouling in tangential

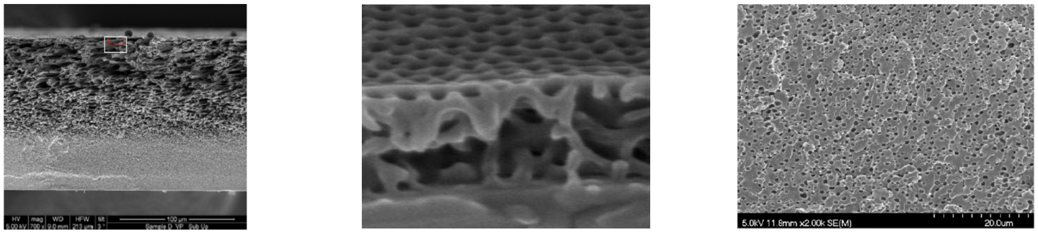

(a) **(b)** **(c)**

Figure 2.1 Magnified membrane images showing (a) gradation of pores sizes through membrane depth, and in-plane inhomogeneity of pore sizes [76]; (b) connectivity and junction layer [141] and (c) pore size distributions [119].

filtration. Other reviews survey different aspects of membrane filtration, such as filtration materials [143], filtration techniques [38] and applications to chemical waste treatment [33].

There is considerable industrial interest in designing and manufacturing layered filters that allow for fine control of particle removal while maintaining a reasonable filter lifetime. Such filters typically have pore size that decreases from one layer to the next (in the direction of flow, see Figure 2.1a). In this way, pore closure occurs more uniformly throughout the filter, since fouling begins at the upstream side of the membrane, and thus the fouling rate is a decreasing function of depth through the membrane (as is the concentration of particles in the feed). Such layered structures may incorporate varying degrees of *connectivity* between pores in different layers, seen in Figure 2.1b.

The literature on the influence of membrane morphology (pore structure and connectivity) on filtration efficiency is too large to provide a comprehensive review (but see, for example, [31], [45, 46], [55], [67] and [147]). Here we briefly outline the most relevant work that provides the primary motivation for our paper. The starting point for our modeling is the work of Sanaei and Cummings [111], who introduced a simple bifurcating-pore model to capture some of the layering features described above. In that paper, adsorption is the sole fouling mechanism: small particles are transported through a network of initially circularly-cylindrical pores, and deposited on the pore walls. The particle concentration in the flow decreases as the pore network is traversed, with the goal that it reaches a sufficiently low level by the time the flow exits the filter. While the bifurcations model inter-layer pore connectivity, there is no additional *intra-layer* connectivity (see Figure 2.1b) to allow interactions between pores in the same layer. Griffiths *et al.* [46] accounted for such a feature by means of an *ad hoc* connectivity parameter, which can be tuned to adjust the degree of communication (allowed flux) between pores that occupy the same layer. An important new feature of our present work is the incorporation of inter-layer junctions with concentration and pressure equalizing capabilities that influence membrane performance metrics (detailed in Section 2.3.3). Furthermore, neither [111] nor [46] consider pore-size variation within individual layers. Such pore size variation (which we term intra-layer heterogeneity or *heterogeneity*, in short), is another novel feature of the present work: it is inevitable due to imperfect manufacturing and, as we shall see, it may have non-intuitive implications for membrane performance.

In this work, we introduce simple models of membrane pore networks that incorporate both intra-layer connectivity and heterogeneity. Our goal is to study and explain the effects of membrane connectivity and investigate the influence of pore size variations introduced by manufacturing defects. We consider dead-end filtration as the primary type of filtration and adsorption as the dominant fouling mechanism. This approach facilitates a simpler system than would be obtained by considering all fouling modes, allowing us to focus on gaining insight into the effects of pore connectivity. We defer the study of multiple fouling modes in a pore-network model to a future work. The chapter is arranged as follows: in Section 2.3, we describe a mathematical model for the flow inside a membrane with homogeneous intra-layer structure and its heterogeneous analogue; in Section 2.4, we give appropriate scalings and nondimensionalizations for these models; and in Section 2.5, we present results and discuss their implications and limitations. Lastly in Section 2.6 we present our conclusions and discuss several ideas for future extensions of this work.

2.3 Mathematical Modeling

In this work, we consider a planar membrane filter whose top (upstream) surface resides in the Y-Z plane, as shown in Figure 2.2a. The flow is (at least initially) assumed to be entirely unidirectional, in the positive X direction. Furthermore, the membrane pore structure is assumed homogeneous in the Y-Z plane, but is allowed to vary internally along the X-axis, thereby imparting depth-dependent permeability. Throughout this work, uppercase symbols denote dimensional quantities, while lowercase symbols are dimensionless (see Section 2.4 below).

We assume a membrane consists of units that repeat periodically in the Y-Z plane of the membrane in a square lattice pattern, with period $2W$. Globally, we assume incompressible unidirectional Darcy flow [103] across the porous medium, in which the superficial Darcy velocity, $\mathbf{U} = (U(X,T), 0, 0)$, is directly proportional to the pressure gradient,

$$U = -\frac{K(X,T)}{\mu}\frac{\partial P}{\partial X}, \quad \frac{\partial U}{\partial X} = 0, \quad 0 \leq X \leq D, \tag{2.1}$$

where $K\left(X,T\right)$ is the permeability at depth X and D is the thickness of the entire membrane. A pressure difference across the membrane acts as the driving force for fluid flow; hence, the following boundary conditions are imposed

$$P(0,T) = P_0, \quad P(D,T) = 0. \tag{2.2}$$

Locally, the membrane's pore network is modelled as a composition of cylindrical tubes, of circular cross-section. The Hagen-Poiseuille model, which provides the local permeability $K(X,T)$ in terms of the local pore radii, is a suitable framework for this structure.

Table 2.1 Key Nomenclature

$U = U_i$	Superficial Darcy velocity in the i-th layer	$\overline{U}_{\mathrm{p},i}$	Cross-sectionally averaged velocity in the i-th layer
P_i	Pressure in the i-th layer	P_0	Pressure drop across the membrane
Q	Global volumetric flow rate	Q_i	Local volumetric flow rate through each pore of the i-th layer
C_i	Concentration in the i-th layer	C_0	Particle concentration at membrane inlet
A_i	Pore radius in i-th layer	D_i	Thickness of i-th layer
R_i	Pore resistance in i-th layer	D	Membrane thickness
R	Total membrane resistance	m	Number of layers
Λ	Deposition coefficient	ϵ_{ij}	Noise amplitude (see 4)

Uppercase fonts denote dimensional quantities; lowercase are dimensionless.

2.3.1 Homogeneous Model

We now present our connected pore model, first in the simplest homogeneous case in which all pores within a given layer are identical. To incorporate intra-layer connectivity, here referred to simply as connectivity, we require that at least two pores in the i-th layer connect in the $(i+1)$-th layer; see Figure 2.2a for an example of a two-inlet connected membrane. In this example, the basic period-unit has a top layer that consists of two inlet pores (identical tubes of length D_1 and radius A_1) on the upstream membrane surface. Flow from these two pores enters the first inter-layer region, where mixing occurs. The flow then enters the second layer of the membrane, consisting of three identical tubular pores of length D_2 and radius A_2, which exit into the second inter-layer region, where mixing again occurs. This structure repeats, so that the i-th layer contains $i+1$ pores, with mixing in each inter-layer region.

More generally, for a membrane with m layers and ν_i pores in layer i, we assume that the inter-layer junction regions are short enough to have negligible resistance so that the pressure drop between the exit of pores in layer i, and the entrance of pores in layer $i+1$, is negligible (also see [22] and [111]). Because all pores in the i-th layer have the same initial radius and length, they consequently experience the same local volumetric flow rate, Q_i. Incompressibility (mass conservation) conditions for

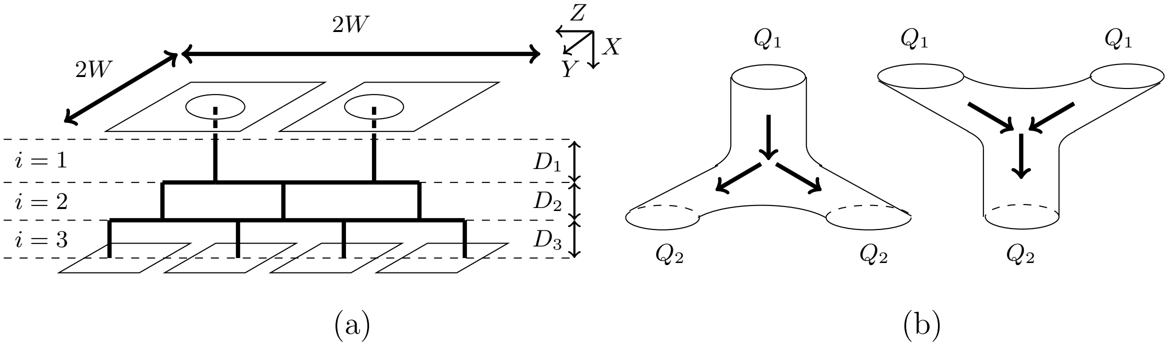

Figure 2.2 Illustration of a connected, branched-pore membrane and volumetric flow rate balance at pore junctions. (a) An $m = 3$ layer pore-network with unit cell area $(2W)^2$. (b) Schematic bifurcation of a single pore (left) and two pores merging into one (right), homogeneous in both cases. In the former case $Q_1 = 2Q_2$, and in the latter $2Q_1 = Q_2$, by mass conservation.

the fluid yield

$$\frac{\partial Q_i}{\partial X} = 0, \quad 1 \le i \le m, \tag{2.3}$$

where Q_i through any pore in the i-th layer can be related to the corresponding cross-sectionally averaged pore velocity $\overline{U}_{\mathrm{p},i}$,

$$Q_i = \pi A_i^2 \overline{U}_{\mathrm{p},i}, \quad X_{i-1} \le X \le X_i, \quad X_i = \sum_{j=0}^{i} D_j, \quad D_0 = 0, \quad 1 \le i \le m, \tag{2.4}$$

with $A_i = A_i(X, T)$ and D_i the radius and the length of each pore in the i-th layer, respectively. The chosen cylindrical pore geometry allows us to calculate Q_i using the Hagen-Poiseuille equation,

$$Q_i = -\frac{(P_i - P_{i-1})}{\mu R_i}, \quad R_i = \frac{8}{\pi}\int_{X_{i-1}}^{X_i} \frac{dX}{A_i^4\,(X,T)}, \tag{2.5}$$

where P_i is the pressure at the exit and R_i the total resistance, for each pore in the i-th layer. By continuity, we have

$$Q \equiv (2W)^2 U = \nu_i Q_i, \quad 1 \le i \le m, \tag{2.6}$$

where Q is the global volumetric flow rate across the membrane, U the global superficial Darcy velocity and ν_i the number of pores in the i-th layer, which will vary depending on the exact pore architecture chosen (in the example of Figure 2.2a, $\nu_i = i + 1$). Volumetric flow rate through the i-th layer in the membrane, $\nu_i Q_i$, can then be related to the local pore velocity, $\overline{U}_{\mathrm{p},i}$, under the assumption that the pressure gradient is uniform across each layer (an assumption implicit in Equation (2.5)). For the case that the imposed pressure is the same at each inlet, this condition becomes equivalent to stating that at each junction the flow rate "splits" evenly — *i.e.*, the fluid mass is divided at each junction according to the number of pores.

Note that Equations (2.5) and (2.6) together yield m equations for the global superficial Darcy velocity, U, and the inter-layer pressures, P_i. Solving successively for P_i gives

$$(2W)^2 U = \frac{P_0}{\mu R}, \quad R = \sum_{i=1}^{m} \frac{R_i}{\nu_i}. \tag{2.7}$$

The above equation for R describes the net resistance of the membrane.

To compare and contrast with the single-inlet non-connected bifurcating pore model presented by [111] (where $\nu_i = 2^{i-1}$), we will consider single-inlet and two-inlet connected pore models, with linear growth in the number of pores through each layer. In these two cases, $\nu_i = i$ and $i + 1$, respectively in Equation (2.6).

Particle transport and fouling

The model described above constitutes Darcy flow through the membrane with the specified pore architecture, and we now develop the model for the transport and deposition of foulants. In this work, we consider membrane fouling due to adsorption (also known as standard blocking) only, as we intend to study the effect of different pore architectures rather than the complexities of multiple fouling mechanisms. Adsorptive fouling is the process of small particles adhering to the walls of the pores, thereby shrinking the pore radius, and is dominant in many applications. To model this, within each pore we follow [110], where an asymptotic analysis of the advection-diffusion equation governing particle transport down pores is carried out, revealing that (in a certain distinguished Péclet number limit) diffusion dominates in the radial direction, leading to particle concentration that is approximately uniform across the pore cross-section, while variation in concentration along the length of the pore is governed by an advection equation,

$$\overline{U}_{\mathrm{p},i}\frac{\partial C}{\partial X} = -\Lambda\frac{C}{A_i}, \quad X_{i-1} \leq X \leq X_i, \quad 1 \leq i \leq m. \tag{2.8}$$

Here, $A_i\,(X,T)$ is the pore radius, $C(X,T)$ is the local concentration of adsorption foulants carried by the flow in the membrane, $\overline{U}_{\mathrm{p},i}$ is the cross-sectionally averaged pore velocity (see Equation (2.4)), and Λ is a parameter (with dimensions of velocity) that captures the physical attraction between particles and pore walls. This equation is solved subject to a specified particle concentration at the upstream surface,

$$C(0,T) = C_0. \tag{2.9}$$

In real filters, it is desirable to have membrane outlet concentration $C\,(D,T)$ significantly smaller than C_0 and therefore C must vary spatially in X. In fact, according to Equation (2.8), C changes continuously through the depth of the filter since the concentration at the downstream surface of a given layer must match with that at the upstream surface of the next. At the same time, since the pore radius A_i jumps in value between layers (by design), we must in general expect $\partial C/\partial X$ to be discontinuous at layer junctions. In the next subsection we will justify and carry out a coarse-grained discretization of Equation (2.8), which leads us to a simple approximate model for the particle concentration within each layer.

The rate of pore radius shrinkage in each layer is proposed to be proportional to the local concentration of particles. The assumption underlying our deposition law, similar to that in [111], is that (at a given location X in the pore) in a time increment

δT the change in pore area, $2\pi A_i \delta A_i$, is proportional to the void fraction of particles locally (αC, where α is an effective particle volume), the deposition coefficient Λ, and the pore circumference available for particles to stick to:

$$\frac{\partial \left(\pi A_i^2\right)}{\partial T} = 2\pi A_i \frac{\partial A_i}{\partial T} = -\Lambda \alpha C \left(2\pi A_i\right) \iff \frac{\partial A_i}{\partial T} = -\Lambda \alpha C, \tag{2.10a}$$

$$X_{i-1} \leq X \leq X_i, \quad A_i\left(0\right) = A_{i0}, \quad 1 \leq i \leq m. \tag{2.10b}$$

Spatial discretization (Coarse-grained model)

The system of PDEs described by Equations (2.8)–(2.10) must be solved numerically. [111] did not consider pore-size variation within layers and were able to solve the full system of PDEs as presented above to obtain results. In our case, our later simulations for heterogeneous membranes require simulations where the radii of pores in the same layer are randomly assigned, and a large number of simulations is needed to obtain reliable statistics representative of an entire membrane, which is numerically expensive. Therefore, we propose instead a coarse-grained discretization of the model Equations (2.8)–(2.10) in which we solve for quantities A_i, C_i that represent approximations to pore radius and particle concentration within layer i, respectively.

If one assumes that the layers are sufficiently numerous that the particle concentration does not change appreciably across a single layer (corresponding to an assumption that $32\Lambda\mu D^2/(\pi m P_0 W^3) \ll 1$, see Equation (2.8)), then such a coarse-grained approximation should be reasonable. The particle concentration can then be approximated by a piecewise (spatially) constant function, $C_i(T)$, changing in value from one layer to the next. We note that if $C_i(T)$ is assumed independent of X across a given layer i, then consistency requires that the pore radii must also be independent of X in layer i, $A_i(T)$, and therefore shrink uniformly within a given layer over time. The particle concentration within the first layer is taken to be C_0, the concentration in the feed, making a jump to the value C_1 at the boundary between first and second layers. More generally, the concentrations within each layer are taken to satisfy

$$\overline{U}_{\mathrm{p},i}\frac{C_i - C_{i-1}}{D_i} = -\Lambda\frac{C_i}{A_i}, \quad 1 \leq i \leq m, \tag{2.11}$$

(replacing Equation (2.8)) with C_0 specified as in Equation (2.9). This equation allows the particle concentration C_i in each pore in layer i to be expressed in terms of the concentration in the previous layer as

$$C_i = \frac{\overline{U}_{\mathrm{p},i}C_{i-1}}{\overline{U}_{\mathrm{p},i} + \Lambda D_i/A_i}, \quad 1 \leq i \leq m. \tag{2.12}$$

For the pore radius we propose

$$\frac{\partial A_i}{\partial T} = -\Lambda\alpha C_{i-1}, \quad 1 \leq i \leq m, \tag{2.13}$$

as the coarse-grained discretization of Equation (2.10). Note the shift of index on the right-hand side: since particle deposition occurs first at the upstream side of pores, it is the concentration at pore inlets that dominates the fouling and pore closure, hence (we have confirmed) using the upstream value C_{i-1} gives more accurate results than using either the downstream value C_i or an average $(C_i + C_{i-1})/2$. At the same time local resistance R_i, previously defined in Equation (2.5), reduces to

$$R_i = \frac{8D_i}{\pi A_i^4}, \tag{2.14}$$

since each pore in the i-th layer has length D_i.

To check the accuracy of our coarse-grained model, we carried out simulations and compared with solutions to the full PDE model over a range of geometric and material parameters. In all simulations presented in this work we use parameter values such that the coarse-grained model gives less than 5% error when compared with fully-converged solutions to the PDE model (see Appendix A.1 for more details of how this determination of accuracy was made).

2.3.2 Heterogeneous Model

Until now, we have focused on a homogeneous model in which all pores within a given layer of the membrane are identical. Now, we turn our attention to heterogeneous connected pore membranes in which the initial pore sizes within a given layer may vary. Consequently, pores in the i-th layer do not necessarily experience identical volumetric flow rates. Similar to Equation (2.4), the net volumetric flow rate through pores is given by

$$Q_{ij} = \pi A_{ij}^2 \overline{U}_{\mathrm{p},ij}, \quad 1 \leq i \leq m, \quad 1 \leq j \leq \nu_i, \tag{2.15}$$

where A_{ij} and $\overline{U}_{\mathrm{p},ij}$ are the radius of the j-th pore in the i-th layer and the cross-sectionally averaged pore velocity, respectively. By balancing the flow rates through a mass-conservation argument (cf. Figure 2.2b), we allow for non-uniform splitting of the flow at each junction. A general representation of this model in terms of the global superficial Darcy velocity (and global volumetric flow rate Q) is given by

$$Q = (2W)^2 U = \sum_{j=1}^{\nu_i} Q_{ij}, \quad 1 \leq i \leq m. \tag{2.16}$$

Again, the junction regions are assumed to be sufficiently low-resistance that pressure is spatially uniform within them, with perfect mixing of the flow in these regions so that the concentration C of suspended particles is spatially uniform. Similarly to Equation (2.5), Q_{ij} through and resistance R_{ij} of the j-th pore in layer i becomes

$$Q_{ij} = -\frac{(P_i - P_{i-1})}{\mu R_{ij}}, \quad R_{ij} = \frac{8}{\pi} \int_{X_{i-1}}^{X_i} \frac{dX}{A_{ij}^4(X,T)}, \quad 1 \leq i \leq m, \quad 1 \leq j \leq \nu_i. \tag{2.17}$$

By continuity, Q and $\sum_{j=1}^{\nu_i} Q_{ij}$ must be equal. In view of this, Equations (2.16) and (2.17) lead to m equations which, when solved successively for P_i, yield

$$Q = (2W)^2 U = \frac{P_0}{\mu R}, \tag{2.18}$$

(cf. Equation (2.7)), where R is the total resistance of the membrane, now given by

$$R = \sum_{i=1}^{m} \left(\sum_{j=1}^{\nu_i} \frac{1}{R_{ij}} \right)^{-1}. \tag{2.19}$$

Comparing this expression with resistors in an electrical circuit, one can see the ν_i pores in the i-th layer are analogous to resistors in a parallel circuit, while the total resistance of each layer is summed as for resistors in series. Using Equations (2.16) and (2.18) to isolate $P_i - P_{i-1}$ in Equation (2.17), we arrive at an explicit expression for Q_{ij}

$$Q_{ij} = \pi A_{ij}^2 \overline{U}_{\mathrm{p},ij} = \frac{P_0}{\mu R \big(R_{ij} \sum_{j=1}^{\nu_i} \frac{1}{R_{ij}} \big)}, \quad 1 \le i \le m, \quad 1 \le j \le \nu_i. \tag{2.20}$$

Particle transport and fouling

Fouling and foulant transport for the heterogeneous scenario are governed similarly to the homogeneous case, but here particle concentrations at the outlets of pores in a given layer are not the same because the pores have differing initial radii, which leads to different fouling behaviour. Continuity of concentration is therefore not automatic in the inter-layer regions and we need to invoke our perfect mixing assumption in order to close the model. The transport equations now read

$$\overline{U}_{\mathrm{p},ij} \frac{\partial C_{ij}}{\partial X} = -\Lambda \frac{C_{ij}}{A_{ij}}, \quad X_{i-1} \le X \le X_i, \quad 1 \le i \le m, \quad 1 \le j \le \nu_i, \tag{2.21}$$

where C_{ij} is the cross-sectionally averaged concentration of foulants in the j-th pore of layer i. The initial condition is

$$C_{01}(T) = C_0. \tag{2.22}$$

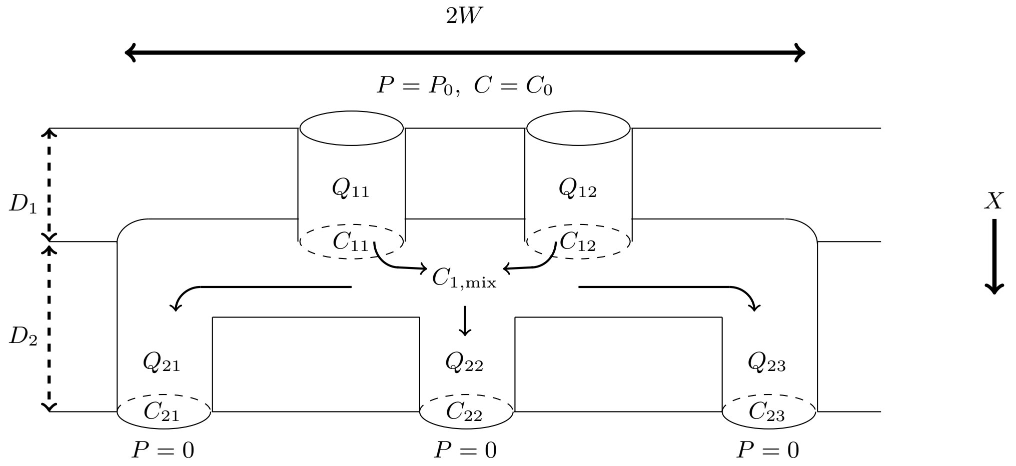

Figure 2.3 Schematic of a connected branching pore membrane with $m = 2$ layers, pressure drop P_0 and upstream particle concentration C_0. Flow is assumed to be entirely in the X-direction.

With our perfect mixing assumption the uniform particle concentration, $C_{i,\text{mix}}$, in the junction region below the i-th layer satisfies

$$C_{i,\text{mix}} := \frac{\sum_{j=1}^{\nu_i} Q_{ij} C_{ij}}{\sum_{j=1}^{\nu_i} Q_{ij}}, \quad 1 \le i \le m. \tag{2.23}$$

With C_{ij} calculated from Equation (2.21), $C_{i,\text{mix}}$ then provides the boundary (upstream) condition to calculate $C_{i+1,j}$.

The rate of change in pore radius is again determined as in Equation (2.10). The only modification is the introduction of double indices, so that the rate of change of radius of the j-th pore in layer i is given by

$$\frac{\partial A_{ij}}{\partial T} = -\Lambda \alpha C_{i-1,j}, \quad 1 \le i \le m, \quad 1 \le j \le \nu_i, \tag{2.24}$$

with the initial pore radii specified: $A_{ij}(0) = A_{ij0}$. Note that this general heterogeneous model reduces to the homogeneous model when all pores in a given layer are identical.

Spatial discretization (Coarse-grained model)

We modify Equation (2.11) according to the concentration rebalance introduced in

Equation (2.23), replacing C_{i-1} by the appropriate upstream value $C_{i-1,\mathrm{mix}}$. The heterogeneous analogue of Equation (2.12) then becomes:

$$C_{ij} = \frac{\overline{U}_{\mathrm{p},ij} C_{i-1,\mathrm{mix}}}{\overline{U}_{\mathrm{p},ij} + \Lambda D_i / A_{ij}}, \quad C_{0,\mathrm{mix}} = C_0, \quad 1 \leq i \leq m, \quad 1 \leq j \leq \nu_i, \tag{2.25}$$

and the radius of pore j in the i-th layer evolves at the following rate

$$\frac{\partial A_{ij}}{\partial T} = -\Lambda \alpha C_{i-1,\mathrm{mix}}, \quad 1 \leq i \leq m, \quad 1 \leq j \leq \nu_i. \tag{2.26}$$

Similar to Equation (2.14), R_{ij}, total resistance of the j-th pore in the i-th layer, defined in Equation (2.17), now reduces to

$$R_{ij} = \frac{8 D_i}{\pi A_{ij}^4}. \tag{2.27}$$

2.3.3 Measures of Performance

There are several primary measures of membrane performance used in applications. First, volumetric throughput (referred to simply as throughput henceforth), which represents the total cumulative volume of filtered fluid (filtrate) collected at the outlet of the filter by time T, is defined as the time integral of the global volumetric flow rate Q, *i.e.*,

$$V(T) = \int_0^T Q(T')\, dT'. \tag{2.28}$$

Q is often plotted against throughput V to illustrate the relative efficiency of the filter. A desirable performance would be represented by a relatively uniform Q during most of the filtration, during which significant throughput is achieved, followed by a sharp drop in Q towards the end of the filter's lifetime when fouling is severe.

Another important performance metric is the concentration of foulants at the outlet of the membrane, $C_m(T) \equiv C_{m,\mathrm{mix}}(T)$ (see Equation (2.23)). Calculating these performance measures using our model, our simulations will allow us to study the dynamics of filtration, infer dependence on material and geometric parameters, and ultimately infer the most efficient filtration scenarios.

2.4 Scaling and Nondimensionalization

2.4.1 Homogeneous Model

The model presented in Section 2.3.1 is nondimensionalized using the following scalings

$$\begin{gathered} P_i = P_0 p_i, \qquad (X, D_i) = D\,(x, d_i)\,, \qquad C_i = C_0 c_i, \qquad A_i = W a_i, \\ \left(U, \overline{U}_{\mathrm{p},i}\right) = \frac{\pi W^2 P_0}{32 \mu D \hat{r}_0}\left(u, \overline{u}_{\mathrm{p},i}\right), \qquad T = \frac{W}{\Lambda \alpha C_0} t, \end{gathered} \tag{2.29}$$

where the physical scaling quantities are defined in Table 2.1 (with the exception of $\hat{r}_0$, a representative value of the membrane resistance, which is defined below). After applying the boundary conditions for pressure,

$$p_0\,(t) = 1, \quad p_m\,(0) = 0, \tag{2.30}$$

the resulting dimensionless model for $u\,(t)$, $\overline{u}_{\mathrm{p},i}(t)$, $r\,(t)$, $a_i(t)$, and $c_i(t)$ (global Darcy velocity, cross-sectionally averaged pore velocity, total membrane resistance, radius of pores in the i-th layer, and particle concentration in the i-th pore, respectively) is

$$r = \frac{1}{\hat{r}_0}\sum_{i=1}^{m}\frac{d_i}{\nu_i a_i^4}, \tag{2.31}$$

$$u = \frac{1}{r}, \quad u = \frac{\nu_i}{4}\pi a_i^2 \overline{u}_{\mathrm{p},i}, \tag{2.32}$$

$$c_i = \frac{\overline{u}_{\mathrm{p},i}\, c_{i-1}}{\overline{u}_{\mathrm{p},i} + \lambda d_i / a_i}, \qquad \lambda = \frac{32 \mu D^2 \hat{r}_0}{\pi P_0 W^3}\Lambda, \quad \frac{\partial a_i}{\partial t} = -c_{i-1}, \quad 1 \le i \le m. \tag{2.33}$$

Here $\hat{r}_0$ is chosen from a typical value[1] of

$$\hat{r}\,(0) = \sum_{i=1}^{m}\frac{d_i}{\nu_i a_i^4\,(0)}, \tag{2.34}$$

---

[1] $\hat{r}_0 = 15000$ in most of the cases we analyze. See Section 2.5 for more details.

to ensure r and u take order-one values (at least initially), and λ is a dimensionless deposition parameter that describes the competition between the affinity of the foulant particles for the membrane material, and the downstream flow (which depends on physical quantities such as viscosity μ, transmembrane pressure P_0, etc.). Note that this choice of scaling (rather than simply scaling on the membrane's initial resistance in all cases) enables us to make direct comparisons of membranes with different initial resistances.

We also define dimensionless volumetric flow rate $u\left(t\right)$ and throughput $v\left(t\right)$:

$$Q = \frac{\pi W^4 P_0}{8\mu D \hat{r}_0} u, \qquad V = \frac{\left(2W\right)^2 D}{\alpha C_0} v, \qquad v\left(t\right) = \frac{1}{\lambda} \int_0^t u\left(t'\right) dt'; \tag{2.35}$$

see the definitions of dimensional global volumetric flow rate Q and throughput V Equations (2.18) and (2.28). These quantities are often compared when studying membrane performance. We make comparisons between real membranes with variations only in Λ while all other physical parameters ($e.g.$, μ, D, P_0, W) are held fixed. The resulting variations in λ are directly reflected in the time scale in Equation (2.29), but no other scalings are affected. The factor of $1/\lambda$ in v then emerges naturally after using the scales of Q, V and T in the definition of throughput Equation (2.28).

Nondimensionalized boundary and initial conditions are given by

$$c_0(t) = 1, \qquad a_i(0) = a_{i0}, \tag{2.36}$$

with a_{i0} specified for $1 \leq i \leq m$. This closes the system described by Equation (2.31)–Equation (2.33).

2.4.2 Heterogeneous Model

The heterogeneous model is also nondimensionalized using the scalings of Equation (2.29). The relevant nondimensional equations are then

$$r = \frac{1}{\hat{r}_0} \sum_{i=1}^{m} d_i \left(\sum_{j=1}^{\nu_i} a_{ij}^4 \right)^{-1}, \tag{2.37}$$

$$u = \frac{1}{r}, \quad \overline{u}_{\mathrm{p},ij} = \frac{4}{\pi} a_{ij}^2 \frac{1}{r(\sum_{j=1}^{\nu_i} a_{ij}^4)^{-1}}, \tag{2.38}$$

$$c_{ij} = \frac{\overline{u}_{\mathrm{p},ij}\, c_{i-1,\mathrm{mix}}}{\overline{u}_{\mathrm{p},ij} + \lambda d_i / a_{ij}}, \qquad c_{i,\mathrm{mix}} = \frac{\sum_{j=1}^{\nu_i} a_{ij}^2 \overline{u}_{\mathrm{p},ij}\, c_{ij}}{\sum_{j=1}^{\nu_i} a_{ij}^2 \overline{u}_{\mathrm{p},ij}}, \qquad \lambda = \frac{32 \Lambda \mu D^2}{\pi P_0 W^3} \hat{r}_0, \tag{2.39}$$

$$\frac{\partial a_{ij}}{\partial t} = -c_{i-1,\mathrm{mix}}, \quad 2 \le i \le m, \quad c_{0,\mathrm{mix}} = c_{0j}, \tag{2.40}$$

where $1 \le j \le \nu_i$ and $1 \le i \le m$. The following nondimensional boundary and initial conditions also apply,

$$\begin{cases} c_{0j}(t) = 1, & 1 \le j \le \nu_1, \forall t \ge 0, \\ c_{ij}(0) = 0, & 1 \le i \le m,\ 1 \le j \le \nu_i, \\ a_{ij}(0) = a_{ij0}, & 1 \le i \le m,\ 1 \le j \le \nu_i, \end{cases} \tag{2.41}$$

with a_{ij0} specified for $1 \le i \le m$ and $1 \le j \le \nu_i$. This closes the system given by equations Equations (2.37)–(2.41).

2.5 Results

We now present results of the models summarized in Sections 2.4.1 and 2.4.2 above. Our focus is on comparing membranes with different internal pore structures, with particular emphasis on how the intra-layer pore connectivity affects filtration performance. We mainly consider the three basic pore architectures sketched in Figure 2.4. Results for homogeneous membranes (all pores in a given layer identical)

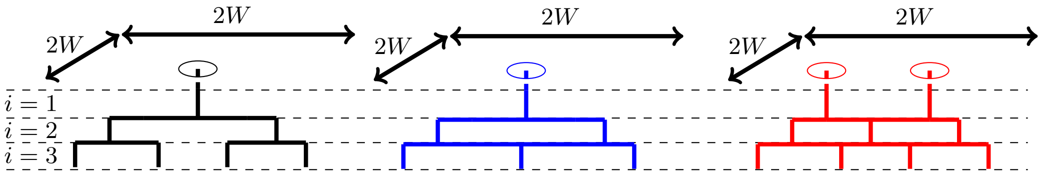

(a) (b) (c)

Figure 2.4 The three distinct pore architectures compared: (a) single-inlet non-connected branch membrane; (b) single-inlet connected membrane; (c) two-inlet connected membrane. The ordered color coding (black, blue and red) is used throughout Section 2.5.

are obtained using the system Equations (2.31)–(2.36), while results for heterogeneous membranes are obtained from Equations (2.37)–(2.41). The stopping criterion for a simulation is when the radius of the top pore $a_1(t)$ reaches 0, at a time we label t_{final}, defined more precisely as,

$$t_{\text{final}} = \left\{ t > 0 : \lim_{t' \to t} a_1(t') = 0 \right\}. \tag{2.42}$$

The reason why the first layer pore always closes first in practical situations will be discussed later.

In Section 2.5.1, we highlight differences in flow and fouling behaviour between the three membrane types and consider how various performance metrics are influenced by membrane structure. Then, in Section 2.5.2, we address the influence of membrane inhomogeneity by examining simulations of the heterogeneous model.

In order to make the most representative comparison between the three membrane pore structures, we simulate fouling of structures that have equivalent initial total membrane resistance $r(0) = r_0$. Thus, in the absence of fouling, compared membranes should behave identically under the same imposed pressure drop.

2.5.1 Results for Homogeneous Membranes

For all homogeneous models, the total dimensionless membrane resistance is given by

$$r\left(t\right)=\frac{1}{\hat{r}_0}\sum_{i=1}^{m}\frac{d_i}{\nu_i a_i^4(t)}, \tag{2.43}$$

where $\hat{r}_0$ is the typical membrane resistance given in Equation (2.29) (see also Equation (2.34)) and in layer i, ν_i is the number of pores and $a_i(t)$ is the radius of each pore. Per Figure 2.4, for the non-connected membranes $\nu_i = 2^{i-1}$, while $\nu_i = i$ and $i+1$ for the single-inlet connected and the two-inlet connected membrane, respectively. We specify the initial value of the resistance, $r(0) = r_0$. Additionally, in all simulations layers are of equal thickness. Thus $d_i = 1/m$, where m is the total number of layers.

The initial radii of pores within each layer are taken to decrease geometrically with layer depth. This geometry is selected in order to retain tractability of the models in terms of the number of parameters, but other scenarios can be easily implemented. Thus,

$$a_i(0) = a_1\left(0\right)\kappa^{i-1}, \tag{2.44}$$

with $0 < \kappa \leq 1$ the geometric ratio, which characterizes the extent of the membrane heterogeneity across layers. There are two parameters in Equation (2.44): $a_1\left(0\right)$ and κ. We impose the value of one of these parameters; the other is then determined by using Equation (2.43), subject to the constraint that $r(0) = r_0$. In physical membranes, surface porosity, $\phi_{\text{top}} = \nu_1 \pi a_1\left(0\right)^2/4$, is a fairly controllable and readily measurable membrane property. For this reason, we typically specify ϕ_{top} in our simulations. Nonetheless, in order to quantify more fully the differences between

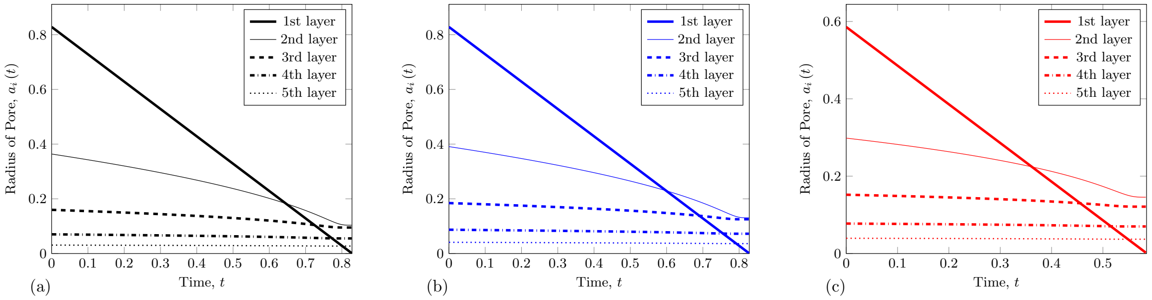

Figure 2.5 Homogeneous models: pore radius evolution for each layer. (a) Non-connected branch membrane (b) single-inlet connected (c) two-inlet connected membrane. For all calculations, $\phi_{\text{top}} = 0.539$ (maximum comparable porosity), $\lambda = 30$, $m = 5$ and the initial resistance $r_0 = 1$.

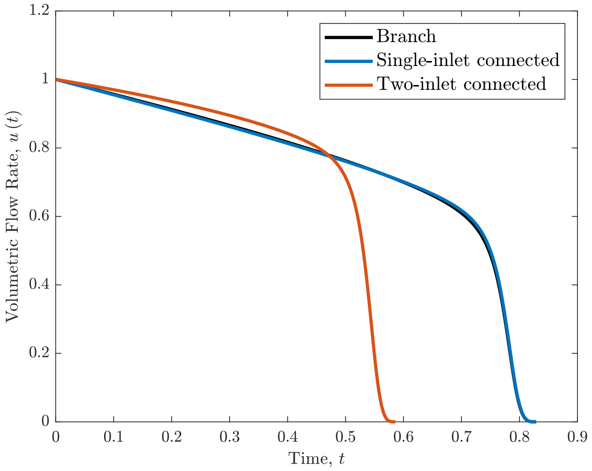

Figure 2.6 Homogeneous models: volumetric flow rate evolution for non-connected branch membrane (black), single-inlet connected (blue) and two-inlet connected membrane (red). The solid black curve lies under the solid blue curve. For all calculations, $\phi_{\text{top}} = 0.539$ (maximum comparable porosity), $\lambda = 30$, $m = 5$ and the initial resistance $r_0 = 1$.

the three membrane types, we also briefly compare membranes with equal geometric coefficients, κ. [2]

In most simulations, we compare membranes with $m = 5$ layers, initial dimensionless resistance $r_0 = 1$, and with the dimensionless deposition coefficient set to $\lambda_{\text{typical}} = 30$, chosen so that the membrane particle removal efficiency is in qualitative agreement with typical requirements in applications.

---

[2] Note that Equation (2.44) in general leads to porosity gradients within the filter, with (initial) porosity ratio between adjacent layers readily calculated from Equation (2.44) if desired, as $\phi_i(0)/\phi_{i-1}(0) = \kappa^2\nu_i/\nu_{i-1}$.

Figure 2.5 shows simulations for the pore radius evolution in each layer for all three membranes with identical top-layer porosity $\phi_{\text{top}} = 0.539$. Note that this is the largest possible surface porosity for a two-inlet membrane of the type in Figure 2.4a. Both single-inlet models display notably longer membrane lifetimes than the two-inlet model — the value of t_{final}, determined by when the radii of pores in the top layer go to zero, is larger. This is because for a fixed value of ϕ_{top}, $a_1(0)$ must decrease as the number of pores in the first layer increases.

We also observe that the radius evolution of the second layer pores presents interesting curvature changes towards the end of the simulation. We attribute this change in curvature to the top layer pore radius becoming smaller than the radii of downstream pores. When the top pore is largest among all pores, it provides the dominant contribution to particle removal. However, when it becomes smaller than the second layer pores, it incurs a higher local pore velocity due to conservation of mass (analyzed in a later discussion involving Figure 2.11d) increasing the advective flux of foulants further into the membrane to the second layer, which now takes on the majority of particle removal. The second layer radius will then decrease more rapidly due to this higher inflow of particles. A similar reasoning can be used for layers further downstream at later times, though the effect is less visible than for the second layer, until the filtration ends with the top pore closing to zero. This hypothesis is further supported by Figure 2.6, which shows the evolution of $u\,(t)$ (volumetric flow rate) for each model. For each plot, we can associate the onset of rapid decrease in u with the time at which the top pore becomes appreciably smaller than the second and third layer pores, shown in Figure 2.5.

In order to quantify the relative performance of our membranes, we investigate their dimensionless volumetric flow rate $u(t)$ versus throughput $v(t)$ characteristics (see Equation (2.35)). Figure 2.7 plots $u(t)$ versus $v(t)$ for the (equal initial resistance) single-inlet non-connected, single-inlet connected and two-inlet connected

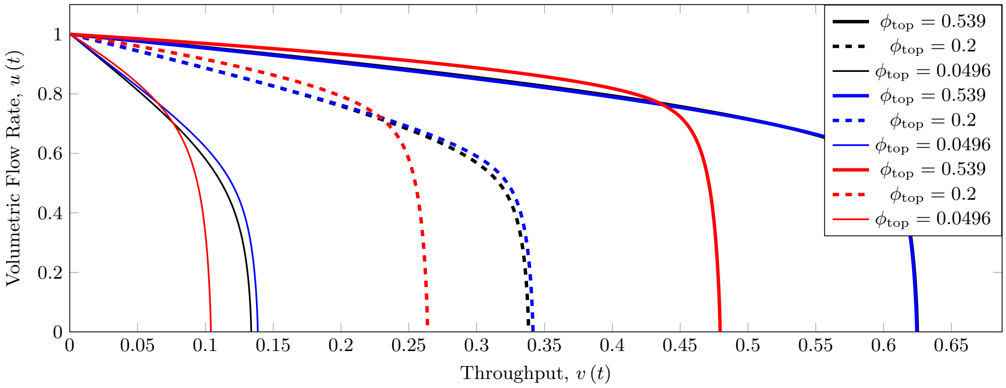

Figure 2.7 Homogeneous models: volumetric flow rate versus throughput for non-connected (black), single-inlet connected (blue), and two-inlet connected (red) membrane structures. Curves with the same line style represent equivalent values of ϕ_{top} for each model. The solid black curve lies under the solid blue curve. For all simulations, $\lambda = 30$, $m = 5$ and initial resistance $r_0 = 1$.

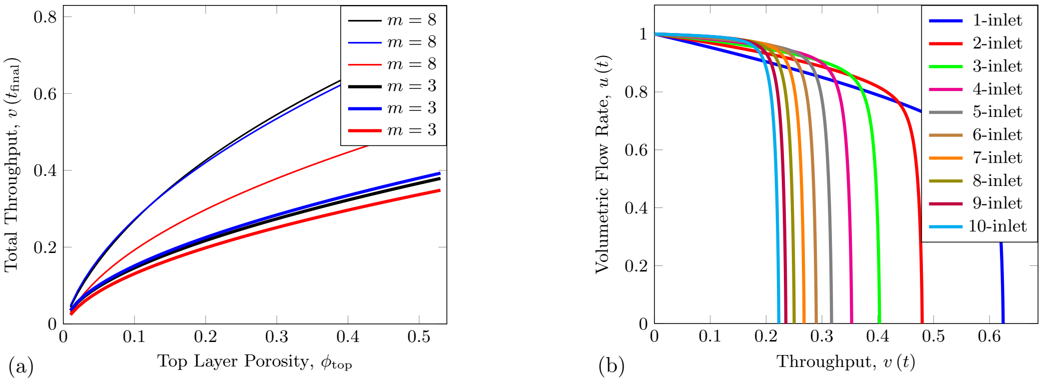

Figure 2.8 Homogeneous models: (a) total throughput versus ϕ_{top} for non-connected (black), single-inlet connected (blue), and two-inlet connected (red) membrane structures. (b) Volumetric flow rate versus throughput for connected membranes with ν_1-inlet pores and $\phi_{\text{top}} = 0.539$. For all simulations, $\lambda = 30$, $m = 5$ and initial resistance $r_0 = 1$.

membranes depicted in Figure 2.4, for three different values of the top-layer porosity ϕ_{top}. Figure 2.8a shows total throughput versus porosity results for the different pore architecture membranes as the number of layers m varies, while Figure 2.8b illustrates $u\left(t\right)$ versus $v\left(t\right)$ performance as the number of inlet pores ν_1 varies (of these architectures, only $\nu_1 = 1$ and $\nu_1 = 2$ are sketched, in Figures 2.4a and 2.4b, respectively). Together, Figures 2.7 and 2.8a show that for each system, the best throughput performance is realized when ϕ_{top} is maximized, or equivalently, the initial pore radius is the widest possible at the upstream side. As ϕ_{top} increases (for fixed initial resistance), membranes process more filtrate and sustain larger volumetric flow rates that decay sharply — an advantageous attribute indicating that the system performs at a high level before failure. We also find that (for the chosen model parameters) the single-inlet models outperform their two (or more) inlet counterparts. When comparing systems with equivalent ϕ_{top}, we find that the two-inlet model exhibits notably shorter membrane lifetimes, consistent with the results shown previously for pore radii evolution in Figure 2.5. Consequently, the total throughput of such systems is diminished. We remark that the results of Figures 2.7 and 2.8a reveal the two single-inlet models to exhibit strikingly similar performance. In these simulations the two models share the same top layer radius while the geometric ratio κ differs slightly (relative κ difference is $\sim 6\%$). This indicates that for the chosen parameters, the morphology in lower layers, including intra-layer connections, does not play a prominent role in membrane performance as measured by total throughput. Moreover, Figure 2.8a shows that for each selected membrane structure, with fixed top layer porosity and the same deposition coefficient λ, membranes with more layers yield larger total throughput. This is because under the equal initial resistance constraint (in addition to fixed top layer porosity), a membrane with more layers has a larger κ-value and therefore larger pores in upper layers, which take longer to close than the smaller pores of a membrane with fewer

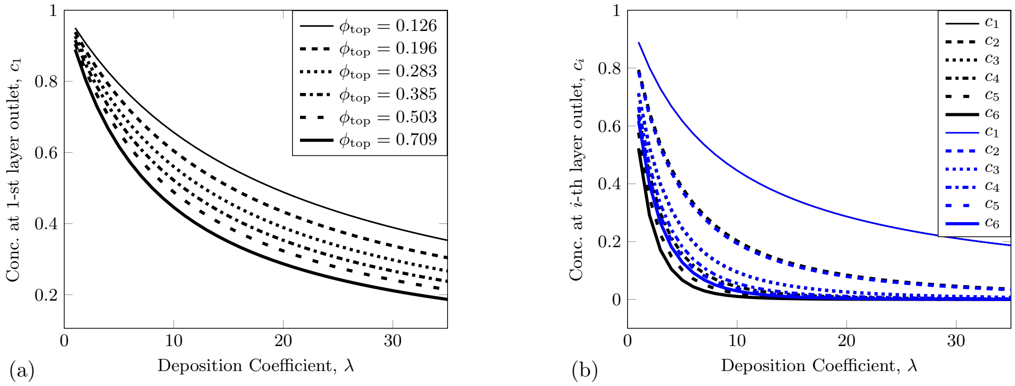

Figure 2.9 Homogeneous models: (a) initial particle concentration at outlet of first layer, $c_1(0)$, versus deposition coefficient λ for single-inlet structures. Note that the results are identical for both connected and non-connected single-inlet models because they have the same initial top pore radius a_{10}. (b) Initial particle concentration at i-th layer pore outlets, $c_i(0)$, versus λ for single-inlet non-connected (black) and connected (blue) models with $\phi_{\text{top}} = 0.709$. The vertical range is extended below zero for clarity only; $c_i(0) > 0$ always. For all simulations, $m = 6$ and $r_0 = 1$.

layers. Motivated further by the observations of Figure 2.8a, we probe the effect of having more than two inlets on the upstream surface (again while fixing the top-layer porosity ϕ_{top}) in Figure 2.8b. We find that, as the number of inlet pores is increased, total throughput decreases. This is because the more pores a membrane has in its top layer (with pore size constrained by circle packing in the designated square), the smaller the initial pore sizes are in the top layer. These pores shrink to zero faster than those in a membrane with fewer inlets (see the third equation in Equation (2.33)) and lead to less total throughput.

We also observe a common feature from Figures 2.7 and 2.8b that volumetric flow rate $u(t)$ decreases very sharply towards the end of the filtration. This is due to the radii of top pore(s) becoming smaller than those of the downstream ones. The radius of the top pore contributes more dramatically to total resistance (per Equation (2.43)) when it is very small (smaller than pore radii in downstream layers), thus increasing the rate at which $u(t)$ decreases via Equation (2.32).

We next investigate the effect of variations of λ, as induced by changes in the dimensional coefficient Λ, corresponding to changes in specific material properties of

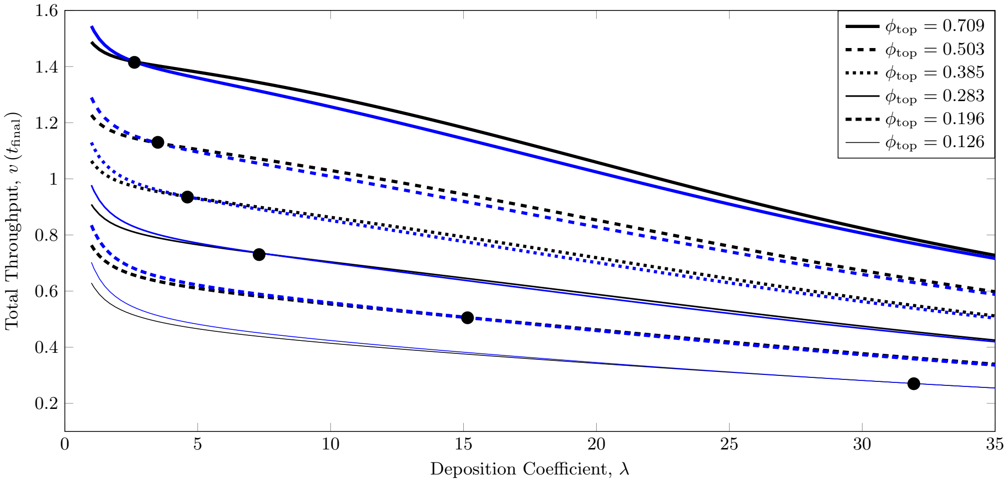

Figure 2.10 Homogeneous models: total throughput versus λ for single-inlet non-connected (black) and connected (blue) membrane structures. Each set of curves represents equivalent initial top layer porosity. Each black dot is an equivalence point between the two models such that the same total throughput is achieved with the same λ. For all simulations, $m = 6$ and $r_0 = 1$.

the filter or the particles in the feed. This coefficient captures the overall attraction strength or "stickiness" of the pore wall, per Equation (2.33): in general, a larger value means that particles carried by the feed solution will adhere to the walls of a pore more easily. This in turn causes faster pore shrinkage and a shorter membrane lifetime. Conversely, smaller values of λ lead to reduced adsorption and more particles escaping capture by the membrane. As Λ appears in the chosen time scale (see Equation (2.29)), such variations in λ effectively change the time scale. This effect is manifested in Equation (2.35), where total throughput $v(t)$ is inversely proportional to λ.

In Figures 2.9 and 2.10 we show results as λ varies for $m = 6$ layer single-inlet membranes with initial dimensionless resistance $r_0 = 1$ and several values of the top layer porosity. Figure 2.9a illustrates the (initial) particle capture within the first layer of the membrane. The results show that, as λ increases, the percentage of particles captured by the first layer pore rapidly increases, exceeding 50% in all cases by the time $\lambda = 20$. In Figure 2.9b, we plot the (initial) particle capture within all layers of the membrane. We note that as λ decreases, differences in performance between the two models become more apparent. For smaller λ-values membrane internal structure begins to play a more prominent role, as a greater percentage of particles reach the lower layers. This is shown, for $\lambda \leq 5$, by the widening gaps in the graphs of c_i as i increases, between the connected and non-connected models in Figure 2.9b. The non-connected branch model (black curves) achieves lower particle concentration at the outlet of each layer, because its more numerous downstream pores are able to contribute more to overall retention capability when upstream pores capture fewer particles (the small-λ effect).

For both connected and non-connected single-inlet models, over the range of λ considered the membrane total throughput increases as λ decreases, as Figure 2.10 demonstrates. Furthermore, when λ becomes large, the total throughputs of the single-inlet models converge towards one another, suggesting that, for large λ, filtration performance is dominated by the top-layer pore (which is identical in these two models). This conclusion is further supported by Figure 2.9a. Finally, we draw attention to the existence of total throughput equivalence points in Figure 2.10. For certain values of λ, the total throughput of the two models is the same (see black solid dots). To determine if either morphology is preferential at equivalence points, we consider the concentration of particles remaining in the filtrate as it exits the membrane, $c_m(t)$, which measures the retention capability of the membrane. Additional simulations (not shown here) indicate that the non-connected model does a marginally better job (lower particle concentration at outlet) at equivalence points, consistent with our remarks on Figure 2.9b above.

In Figure 2.11, we further analyze the influence of membrane morphology on particle removal efficiency for our three models. In Figures 2.11a–2.11c, particle concentration in the filtrate is plotted as a function of instantaneous throughput for all three membrane structures, and for three different κ-values. From the y-intercepts of those figures, we see that a smaller κ value (and consequently smaller downstream

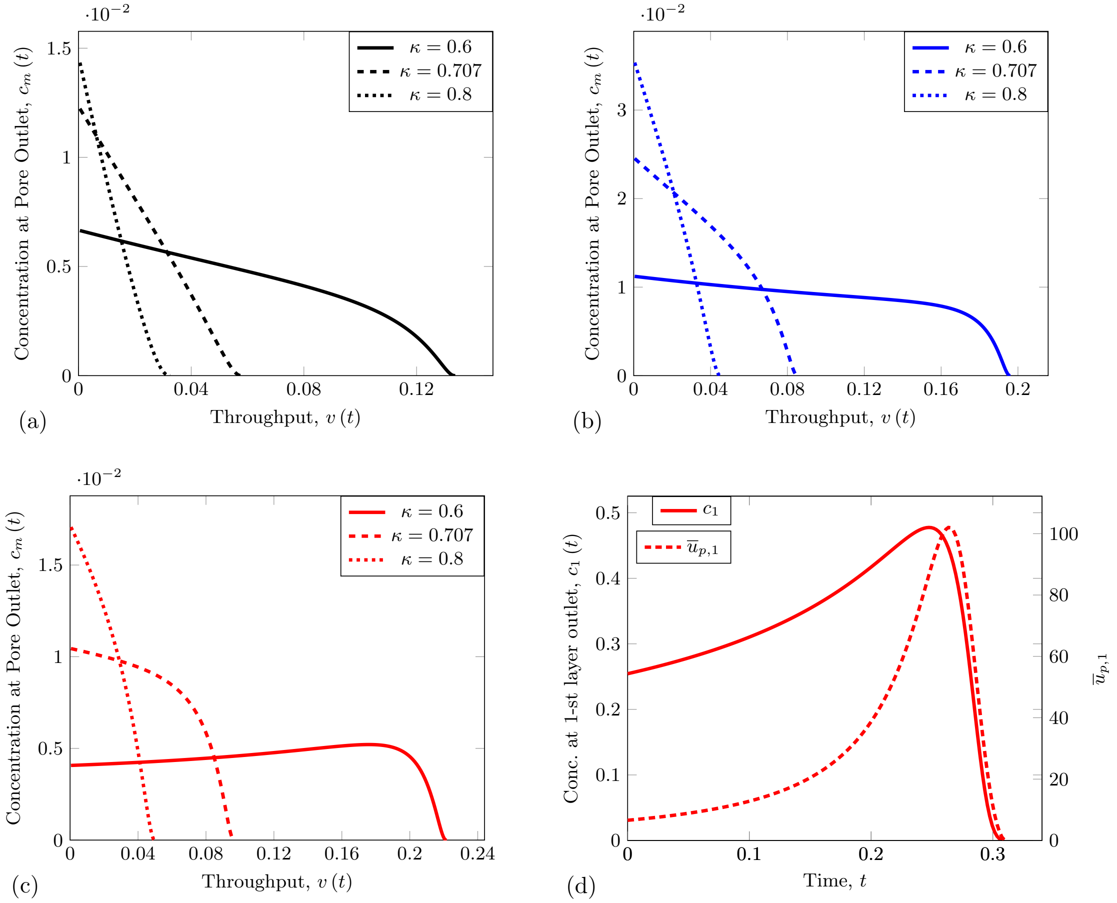

Figure 2.11 Homogeneous models: (a)-(c) concentration at pore outlet versus throughput for (a) non-connected, (b) single-inlet connected, and (c) two-inlet connected membrane structures. (d) Two-inlet connected model: the concentration of particles leaving the first layer downstream surface (c_1, solid red curve) and cross-sectionally averaged first layer pore velocity ($\overline{u}_{\mathrm{p},1}$, dashed red curve) are shown. For all calculations, $\lambda = 30$, $m = 5$, $\kappa = 0.6$ and $r_0 = 1$.

pores) contributes to lower initial particle concentration in the filtrate, indicating that a steeper porosity gradient in the filter medium leads to greater initial foulant retention. Interestingly, however, for the selected parameters we observe that the outlet particle concentrations $c_m(t)$ do not necessarily decrease monotonically in time for all choices of geometric coefficients examined. For example, in Figure 2.11c for $\kappa = 0.6$, the value of $c_m(t)$ for the two-inlet model increases over a considerable portion of the membrane lifetime before finally decreasing and dropping to zero due to complete fouling of the first layer. This phenomenon, which we investigate more thoroughly below, is especially important because in many applications it is necessary for membranes to maintain a guaranteed particle removal efficacy throughout their operational lifetimes. We hypothesize that this non-monotonic behaviour is linked to the corresponding increase in cross-sectionally averaged pore velocity, $\overline{u}_{\mathrm{p},i}$, as shown in Figure 2.11d. As $\overline{u}_{\mathrm{p},i}$ increases due to the reduction of pore size through adsorptive fouling, particles in the feed solution are advected through pores faster. The upshot is that more particles are advected through the membrane before they have the opportunity to adhere to the pore walls, in contrast to the low pore velocity situation.

In order to understand better which parameter regimes lead to the observed increase in filtrate particle concentration, we plot the normalized difference between the initial and maximum filtrate particle concentrations,

$$c_{\mathrm{diff}}\left(\lambda; m\right) = \frac{\max\limits_{0 \le t \le t_{\mathrm{final}}} c_m\left(t\right) - c_m(0)}{c_m(0)}, \tag{2.45}$$

as a function of λ. If, for a given value of λ, the outlet concentration monotonically decreases for the entire membrane lifetime, then $\max_{0 \le t \le t_{\mathrm{final}}} c_m\left(t\right) = c_m(0)$ and c_{diff} vanishes. Conversely, a positive value of c_{diff} is indicative of a deteriorating particle retention capability over at least some of the filter lifetime. Figures 2.12a–2.12c show c_{diff} plotted against the dimensionless deposition parameter λ for the single-inlet non-connected model, and the single and two-inlet connected models respectively, for a range of layer numbers m. Here we choose initial (dimensionless) resistance $r_0 = 2$ in order to include a large range of m-values (for a given κ-value, large m leads to very small pores in lower layers, particularly for the non-connected model, hence a larger net resistance).

It is, in fact, possible to find a sufficient condition that characterizes parameter choices guaranteeing the existence of a maximum in the function $c_m(t)$. Our sufficient condition takes the form of an inequality, depending entirely on initial conditions of the problem and model parameters, and is summarized by the following Theorem (proved in Appendix A.2):

Theorem 1. *Let*

$$f_j(\lambda, m) = \frac{1}{1 + \frac{\gamma\lambda}{m}\nu_j\kappa^{j-1}}, \quad 1 \le j \le m, \quad f_0 = 1, \quad \gamma = \frac{\pi a_1(0) r_0}{4},$$

and define

$$g\left(\lambda, m; \gamma, \{\nu_j\}_{j=1}^{j=m}\right) := \left(\sum_{j=1}^{m} \nu_j \prod_{i=0}^{j} f_i(\lambda, m)\right)\left(\sum_{j=1}^{m} \frac{1}{\nu_j \kappa^{4(j-1)}}\right) \tag{2.46}$$

$$-4\left(\sum_{j=1}^{m} \nu_j \kappa^{j-1} f_j(\lambda, m)\right)\left(\sum_{j=1}^{m} \frac{\prod_{i=0}^{j-1} f_i(\lambda, m)}{\nu_j \kappa^{5(j-1)}}\right). \tag{2.47}$$

If $g > 0$, then there exists $s_{\lambda,m} > 0$ such that $\frac{dc_m}{dt}(s_{\lambda,m}) = 0$ and $c_m(s_{\lambda,m})$ is maximal.

We first provide some intuition for the terms in the theorem. The f_j are closely related to the first equation in Equation (2.33). In fact, each f_j is the ratio of the initial particle concentrations in the j-th and $(j-1)$-th layers (see Appendix A.2 for the derivation of this relation). The function g arises from the expression of $c_m'(0)$, the initial slope of the particle concentration function $c_m(t)$, in terms of the f_j and the model parameters. Note that the sufficient condition depends only on λ, m and

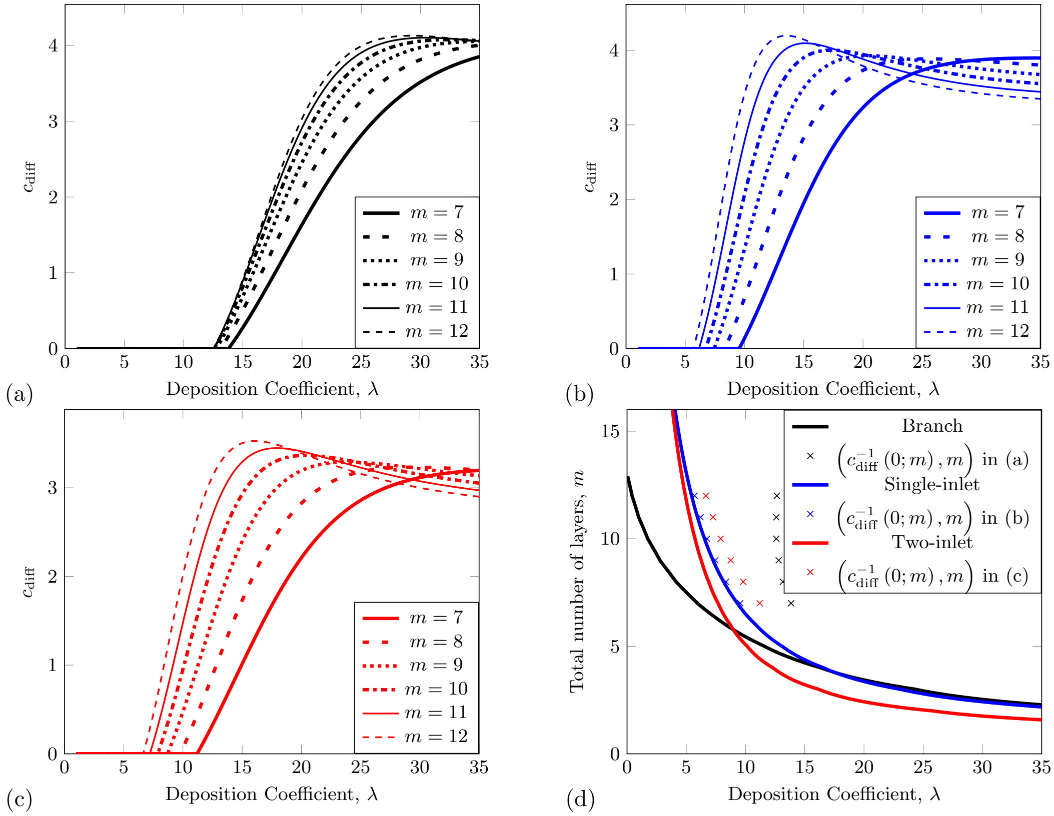

Figure 2.12 $c_{\text{diff}}(\lambda; m)$ defined in Equation (2.45) versus λ for (a) single-inlet non-connected (b) single-inlet connected and (c) two-inlet connected membrane structures. (d) Zero level set of the function g defined in Theorem 1 for single-inlet model (blue), two-inlet model (red) and the branch model (black). The colored data points are the pairs of x-intercepts with their respective m values from panels (a), (b) and (c), respectively. For all simulations, $\phi_{\text{top}} = 0.4$ and $r_0 = 2$.

the membrane geometry, which is parametrised by γ (defined in the theorem) and the number of pores per layer, ν_i. Even though κ appears in the inequality, it is uniquely determined via Equation (2.43) once $a_1(0)$ (or ϕ_{top}) and r_0 are specified.

We can illustrate the region of parameters that satisfy the inequality given in Theorem 1, with specified initial resistance r_0 and top layer porosity ϕ_{top}. In Figure 2.12d, we present the level curves $\{(\lambda, m) : g = 0\}$ for each model membrane with γ and ν_j specified. Two observations may be made about these contour curves. First, for large λ, the two single-inlet models nearly coincide. This is because membrane fouling occurs primarily in the first layer when the material has a high affinity for the passing particles. However, in relatively small λ regimes ($\lambda \approx 5$ and lower), the single-inlet and two-inlet connected models exhibit very similar behaviour. This is because for small λ, more particles are able to penetrate to the lower layers, where the single and two-inlet models share more or less the same structure (differing by just one pore per layer). For applications, in order to assure particle retention performance that does not deteriorate in time, the region to the right of the level curves in Figure 2.12d should be avoided. This region represents the set of parameters that satisfy the inequality, namely, the region of sufficiency for deteriorating particle retention given by $\{(\lambda, m) : g > 0\}$. To check the tightness of the bound provided by the theorem, we extract the x-intercepts (roots of $c_{\text{diff}} = 0$) in Figures 2.12a–2.12c, and pair them with their respective m values as the second component. Together, these ordered pairs (λ, m) make up the data points (the $\times$'s) presented in Figure 2.12d. Indeed, as expected, the data points, representing the onset of local maxima in $c_m(t)$ with various parameter choices, all lie in the region of sufficiency of the theorem. The bound is particularly tight for the single-inlet connected model (in blue), and reasonably so for the two-inlet connected model (red). However, it is rather poor for the single-inlet non-connected model (black), and becomes worse as m increases. This is because in this case, the number of pores per layer $\nu_j = 2^{j-1}$ $(1 \leq j \leq m)$ grows much faster with layer number than in the other cases ($\nu_j = j, j+1$), making the difference between the two terms in $g(\lambda, m)$ larger as m increases.

2.5.2 Results for Heterogeneous Membranes

In general, the complex membranes found in real-world systems do not possess homogeneous geometries of the kind modelled in Section 2.3.1 and studied so far. For this reason, we also consider membranes with varying degrees of heterogeneity in the pore structure. Further motivation is provided by considering industrial fabrication processes. Due to manufacturing precision limitations, even if it were desirable to make a membrane with perfect in-plane pore homogeneity, it would not be possible.

It is therefore worthwhile to consider how in-plane variation in pore sizes, and manufacturing tolerance limitations, may influence membrane performance. Based on the assumption that membrane manufacturers attempt to specify the pore size to control permeability, we address this issue by introducing variations to the radius of each pore within our layered structure. The same basic pore structure is considered, but pores are no longer described by a single layer-dependent radius a_i. For each model, individual pore radii are specified by introducing a random perturbation on top of the analogous homogeneous pore radius. More precisely, we suppose that the initial radius of the j-th pore in the i-th layer is now given by

$$a_{ij}(0) = a_i(0)(1 + \epsilon_{ij}), \tag{2.48}$$

where $a_i(0) = a_1\,(0)\,\kappa^{i-1}$ as in the homogeneous case, and ϵ_{ij} is a continuous random variable drawn independently for each (i, j) pair from a uniform distribution centered about zero and with half-width – or *noise amplitude* – b, *i.e.*,

$$\epsilon_{ij} \sim \mathrm{unif}(-b, b), \quad 0 \leq b \leq 1. \tag{2.49}$$

For each realisation, ϵ_{ij} may result in a larger *or* smaller initial pore size than if unperturbed (corresponding to $b = 0$). In this way, by carrying out a suitably large number N of such simulations and studying quantities such as volumetric flow rate, throughput and membrane resistance averaged over all simulations, we are able to gain qualitative insight into the influence of heterogeneity, and the specific effects of varying the noise amplitude.

The admissible range of b is chosen so as to ensure that the perturbed pore radii satisfy a physical constraint: loosely speaking, that the maximally-perturbed pores will fit within the box of containment (a square of side length 2 in our dimensionless units). The perturbation applied to the initial pore sizes will lead to changes in the initial membrane resistance, the volumetric flow rate through the membrane, and ultimately the total throughput of filtrate. We address the influence of the perturbations by first fixing κ, m (geometric ratio of pore sizes between layers, total number of layers), and r_0 (initial membrane resistance) for the underlying homogeneous model, calculating the corresponding layer-dependent initial pore radii $a_i\,(0)$, then perturbing these radii using Equation (2.48), before observing the performance of the resulting heterogeneous membrane. Before so doing, we first provide several definitions that we will need for this heterogeneous model.

In view of Equations (2.37)–(2.40) where nondimensional formulas for global resistance r, and Darcy velocity u are given, we can analogously define the dimensionless heterogeneous initial resistance and Darcy velocity as

$$r_b\,(t=0) = \frac{1}{\hat{r}_0}\sum_{i=1}^{m} d_i \left(\sum_{j=1}^{\nu_i} a_{ij}^4(0)\right)^{-1}, \quad u_b\,(t=0) = \frac{1}{r_b\,(t=0)}. \tag{2.50}$$

Note that this formula is only valid for the connected models, for which the pore-inlet pressure is the same for each pore in a given layer, whereas in the non-connected heterogeneous model, the pressures at different junctions in the same layer are not necessarily the same. For the non-connected branch model, we utilize the self-similar structure – the left and right branch at each connecting junction – and calculate the total resistance iteratively through each layer as follows: for an m-layer membrane with non-connected branch structure,

$$r_{b,ij}\,(t) = \frac{d_i}{a_{ij}^4\,(t)} + \left(\frac{1}{r_{b,i+1,2j-1}\,(t)} + \frac{1}{r_{b,i+1,2j}\,(t)}\right)^{-1}, \quad 1 \le i \le m-1, \quad 1 \le j \le 2^{i-1}, \tag{2.51}$$

$$r_{b,m,j} = \frac{d_m}{a_{m,j}^4\,(t)}, \quad 1 \le j \le 2^{m-1}, \tag{2.52}$$

where $r_{b,ij}\,(t)$ represents, for a fixed perturbation strength b, the aggregate resistance in the branch originating from the j-th pore in the i-th layer. We initialize the iteration on i with $i = m-1$ using Equation (2.51) and the resistance from each pore in the m-th layer via Equation (2.52). More generally, for each i, we find $r_{b,ij}$ for each j and then proceed to $i-1$ and so on, until we reach $r_{b,11}(t) =: r_b(t)$, the total resistance of the membrane with a non-connected branch structure.

As indicated previously, for a given value of the noise amplitude b, we average over a large number of simulations N to obtain sample averages for membrane performance measures. Thus, average volumetric flow rate through the membrane is defined more precisely by

$$\overline{u}_b(t) = \frac{1}{N}\sum_{i=1}^{N} u_{b,i}(t), \tag{2.53}$$

where $u_{b,i}(t)$ is the volumetric flow rate obtained for the i-th simulation of the ensemble. Lastly, the average throughput is defined (analogously to Equation (2.35)) by

$$\overline{v}_b(t) = \frac{1}{\lambda}\int_0^t \overline{u}_b(t')dt'. \tag{2.54}$$

After some numerical experimentation the value $N = 10^4$ was chosen as a sufficiently large number of simulations to obtain reliable averaged results. We did generate selected results using $N = 10^6$ simulations, but found only minor qualitative changes when compared to $N = 10^4$. In light of the significantly larger computational cost of 10^6 simulations, we use $N = 10^4$ to obtain all results in the following section.

Before presenting the detailed results of the evolution of heterogeneous membranes, we briefly remind the reader of the principal structural difference between the connected and non-connected models under this heterogeneous regime. In Figure 2.4c, the non-connected branch model, each pore leads to two downstream pores, with different initial radii, and pores in the same layer are connected only to their direct sibling from the same upstream pore, and not to any other pores in that layer. Hence, pores within the same layer can experience different upstream (and downstream) pressures, and different particle concentrations at their inlets. However,

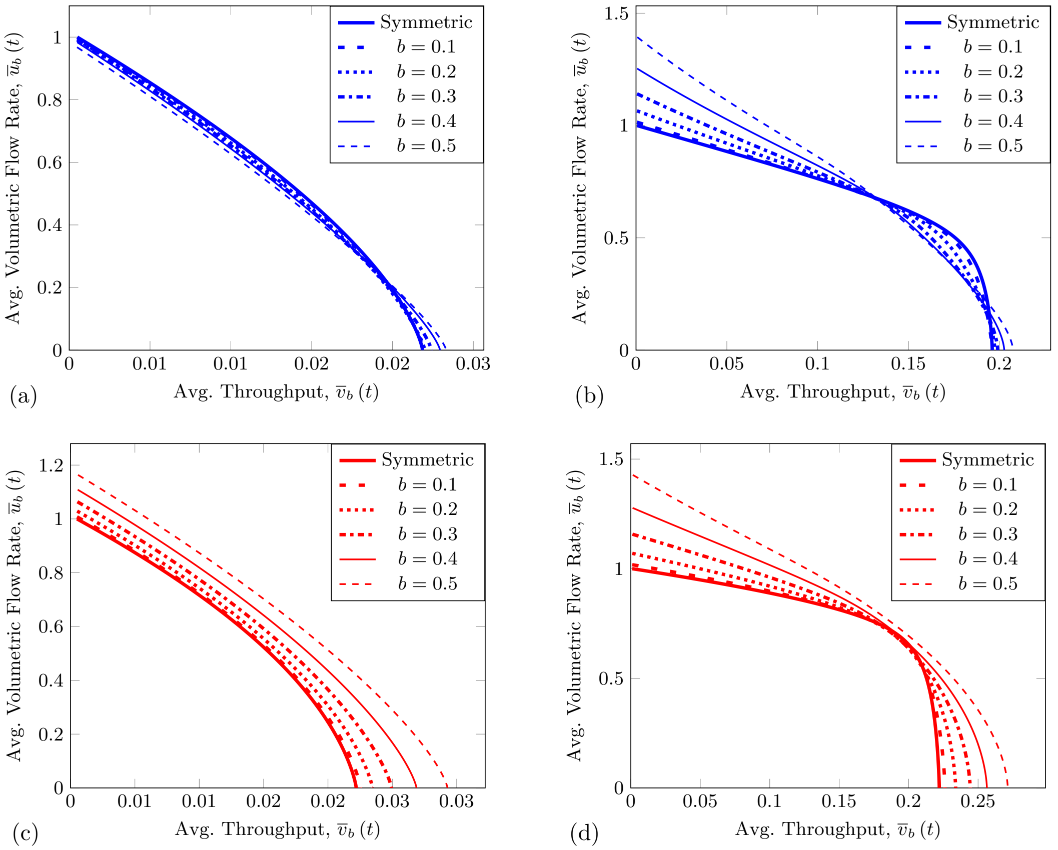

Figure 2.13 Heterogeneous models: average volumetric flow rate Equation (2.53) versus throughput Equation (2.54) of single-inlet (blue) and two-inlet (red) connected models for varying noise amplitude, b. (a),(c) $\kappa = 0.95$ and (b),(d) $\kappa = 0.6$. All results are averaged over $\mathbf{10^4}$ simulations, with common parameters $\lambda = 30$ and $m = 5$.

in the connected geometries of Figures 2.4b and 2.4c, pores within the same layer are connected via a junction layer, where our mixing assumption Equation (2.39) and the assumption of equalized pressure (see the beginning of Section 2.3.1) play important roles in distinguishing the qualitative differences between connected and non-connected models.

Expected volumetric flow rate vs. throughput

We first investigate the effects of noise on membrane performance by observing the average (expected) volumetric flow rate $\overline{u}_b(t)$ versus throughput $\overline{v}_b(t)$ for the heterogeneous models, with reference to the results for homogeneous membranes obtained earlier. We are also interested in how connected and non-connected pore

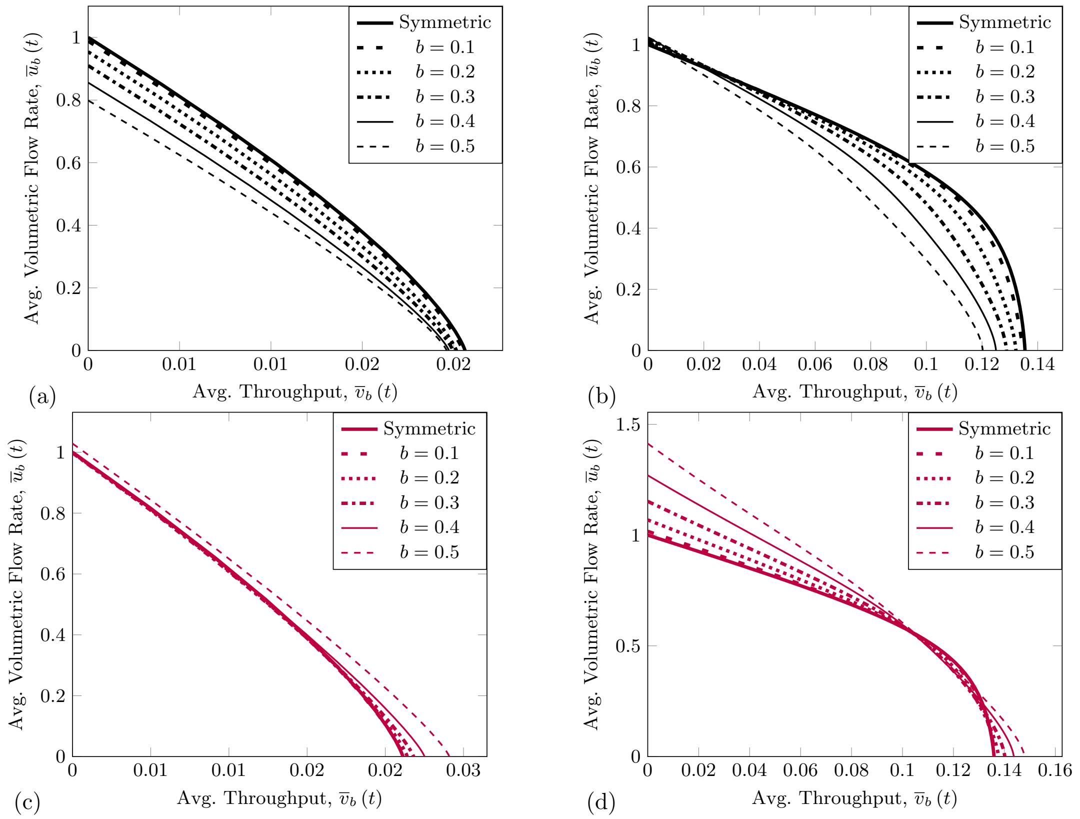

Figure 2.14 Heterogeneous models: average volumetric flow rate versus throughput of non-connected branch model (black); and connected branch model with $\nu_i = 2^{i-1}$ (magenta), (a),(c) $\kappa = 0.95$ (b),(d) $\kappa = 0.6$. All results are averaged over $\mathbf{10^4}$ simulations, with common parameters $\lambda = 30$ and $m = 5$.

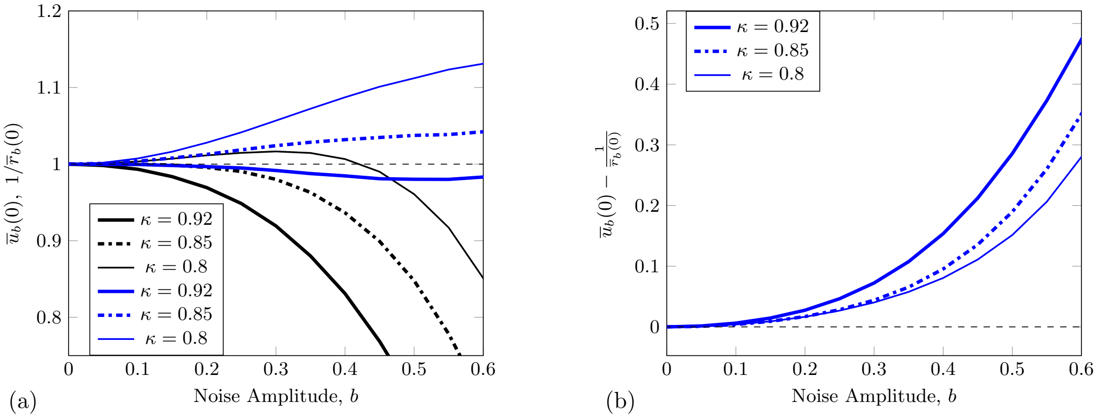

Figure 2.15 Heterogeneous models: results for the single-inlet connected model. (a) Initial average volumetric flow rate $\overline{u}_b(0)$ (blue) and reciprocal of initial average resistance $1/\overline{r}_b(0)$ (black) vs. noise amplitude, b. (b) a large sample approximation of the Jensen gap $\mathcal{J}$ (given in Equation (2.57)), vs. noise amplitude, b. All results are averaged over $\mathbf{10^4}$ simulations, with common parameters $\lambda = 30$ and $m = 5$.

structures compare. In Figure 2.13, we present the $\overline{u}_b(t)$ vs $\overline{v}_b(t)$ results, for 5-layer single-inlet connected and two-inlet connected membranes, with two choices of κ (0.95 and 0.6). We note the following two phenomena: firstly, we immediately observe from the horizontal intercepts of each graph that the greater the noise amplitude, the larger the average total throughput in both of these connected models (see blue and red curves in Figure 2.13a-d); and secondly, that the average initial volumetric flow rate $\overline{u}_b(0)$ generally increases with b, shown by the vertical intercepts in the same figures (with the exception of Figure 2.13a, an anomaly that we defer to a later discussion).

The corresponding $\overline{u}_b(t)$ vs $\overline{v}_b(t)$ results for the non-connected pore model, in Figure 2.14a and b, reveal that the greater the noise amplitude b, the smaller the average total throughput – exactly the opposite trend noted for the connected cases in Figure 2.13. There are two possible factors that might explain or at least contribute to these contrasting findings: 1) the much larger number of downstream pores in the non-connected branch model; and 2) the absence of the pressure/concentration-equalizing junction layer for the non-connected model. To investigate the first hypothesis, we consider a connected model with exactly the same number of pores per layer (*i.e.*, $\nu_i = 2^{i-1}$) as the non-connected branch model. Results are shown in Figure 2.14c and d, again for the two κ-values used in Figure 2.13 and the same b-values: it is clear from the horizontal intercepts in these plots that average total throughput again increases as b increases, much as for the original connected model results of Figure 2.13. This rules out the first possibility.

Continuing to the second hypothesis, we first note that by having a concentration- and pressure-equalizing junction layer, in particular in the heterogeneous regime, the connected branch model is able to split upstream volumetric flow rates into downstream pores depending on their sizes. This feature would lead to different average volumetric flow rate evolution for the two considered models (non-connected vs. connected) in Figure 2.14 under different signs of the pore-size perturbation. We claim that the equalizing junctions in the connected model contribute to the larger throughput observed when compared to the non-connected case. Since the two models only begin to differ at the outlets of the second layer and onward, we focus on the effects of initial pore-size perturbation on the pores in the second layer as an example. If both pores are under perturbations that yield larger initial radii, they will both experience larger initial volumetric flow rates $\overline{u}_b(0)$ than if unperturbed; such an effect on both connected and non-connected models is roughly the same. However, if either pore is under a perturbation that *reduces* initial pore radius and thus $\overline{u}_b(0)$, the equalizing junction in the connected model will help alleviate the volumetric flow rate-reducing effect via the mixing assumption, whereas the junctions in the same layer in the non-connected model behave independently from each other and are thus incapable of compensating in this way.

Now we return to the anomaly of Figure 2.13a, which showed that a small random perturbation to the pore sizes may cause $\overline{u}_b(0)$ to *decrease* in the single-inlet connected case, in contrast to the results from two-inlet models provided in Figure 2.13c and Figure 2.13d, where $\overline{u}_b(0)$ was seen to increase monotonically with respect to b. This is shown more clearly in Figure 2.15a, where we plot $\overline{u}_b(0)$ with respect to noise amplitude b, for various choices of κ for the single-inlet connected model. We find that $\overline{u}_b(0)$ may exhibit a minimum with respect to b, for certain κ values (*e.g.*, when $\kappa = 0.92$ in Figure 2.15a), illustrating the potential for non-monotonicity of $\overline{u}_b(0)$ as a function of b. Figure 2.15b is discussed in Section 2.5.2 below.

It is not immediately clear why average initial flow rate $\overline{u}_b(0)$ through the membrane should depend on perturbation amplitude (with our chosen parameters). The intriguing behaviour indicated by these sample numerical simulations motivates an analytical approach to calculate explicitly the expected values of key quantities such as this.

Expected initial volumetric flow rate and membrane resistance

Motivated by the observations in the previous subsection, we now present further analysis to explain why, in certain parameter regimes, average initial resistance and volumetric flow rate behave non-monotonically with respect to variations in noise amplitude b. For each choice of b, we carry out simulations of the model described in Equations (2.37)–(2.41)) and calculate average initial volumetric flow rate $\overline{u}_b(0)$ via the sample mean definitions in Equation (2.53).

First, we proceed with basic sampling theorems to derive key quantities of interest. By the strong law of large numbers [64], the sample average converges to the true mean. More specifically, for a fixed choice of b,

$$\overline{u}_b\left(0\right) \overset{N\to\infty}{\to} \mathbb{E}\left[u_b\left(0\right)\right], \textit{almost surely}, \tag{2.55}$$

where N is the number of simulations and $\mathbb{E}\left[\cdot\right]$ is the expectation under the joint probability density of $\epsilon_{ij}, 1 \leq j \leq \nu_i, 1 \leq i \leq m$.

As $\overline{u}_b(0)$ is inversely proportional to initial membrane resistance for each realization of the random perturbation to the pore sizes, ϵ_{ij}, it is also of interest to study the effect of perturbations on the expected initial resistance. The relationship between expected initial volumetric flow rate and resistance is characterized by Jensen's inequality [64]

$$\mathbb{E}\left[u_b\left(0\right)\right] = \mathbb{E}\left[\frac{1}{r_b\left(0\right)}\right] > \frac{1}{\mathbb{E}\left[r_b\left(0\right)\right]}, \tag{2.56}$$

by which the reciprocal of expected initial resistance provides a lower bound for expected initial volumetric flow rate. The inequality is strict because the convex function, here $1/x$, is non-affine, while $r_b\left(0\right)$ is a non-constant random variable, almost surely.

As a result, we cannot claim a similar governing law $u = 1/r$ as in the homogeneous case. To visualize Jensen's inequality, we refer to Figure 2.15a and

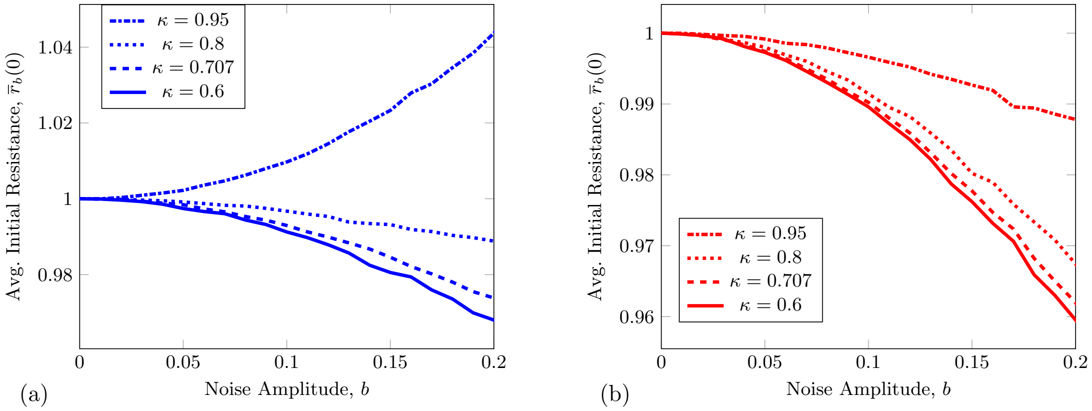

Figure 2.16 Heterogeneous models: average initial resistance for (a) single-inlet connected model and (b) two-inlet connected model. All results are averaged over $\mathbf{10^4}$ simulations, with common parameters $m = 5$ and $\lambda = 30$.

Figure 2.15b, which together illustrate the terms on both sides of Jensen inequality, and the Jensen gap, defined as

$$\mathcal{J}\left(1/x, \mathcal{P}\right) = \mathbb{E}\left[\frac{1}{r_b\left(0\right)}\right] - \frac{1}{\mathbb{E}\left[r_b\left(0\right)\right]}, \tag{2.57}$$

where $1/x$ and $\mathcal{P}$ are the convex function and the probability distribution of $r_b\left(0\right)$, respectively.

Now, upon rearrangement of Equation (2.56), we have

$$\mathbb{E}\left[r_b\left(0\right)\right]\mathbb{E}\left[u_b\left(0\right)\right] > 1. \tag{2.58}$$

From this inequality, we can immediately conclude that if $\mathbb{E}\left[u_b\left(0\right)\right] < 1$ for some b, then the corresponding expected initial resistance for the same b must necessarily satisfy $\mathbb{E}\left[r_b\left(0\right)\right] > 1$. This provides a necessary condition for the phenomenon observed in Figure 2.13a, where $\overline{u}_b(0)$ does not monotonically increase with respect to b.

To elicit further information regarding the emergence of the non-monotone dependence of average initial resistance $\overline{r}_b\left(0\right)$ on noise amplitude b, we study the quantity $\mathbb{E}\left[r_b\left(0\right)\right]$, the large number limit of $\overline{r}_b\left(0\right)$. More precisely, we seek mathematical reasons that could yield physical insight into the non-monotonic

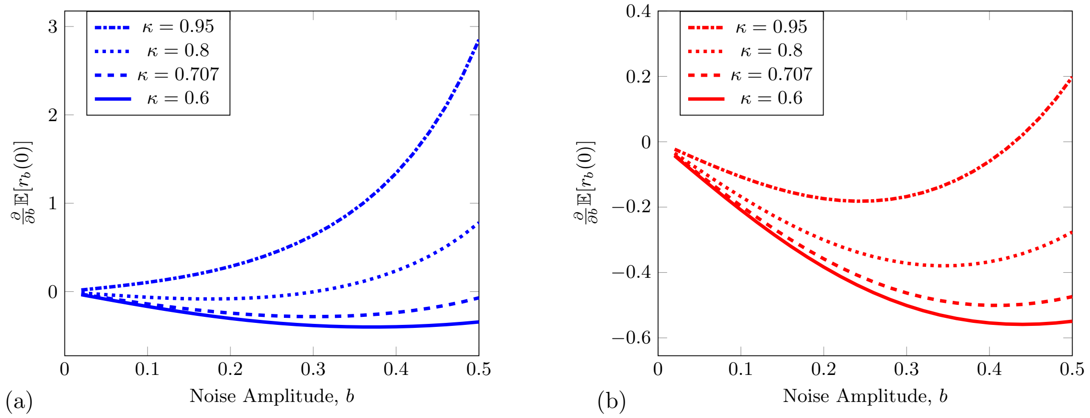

Figure 2.17 Heterogeneous models: partial derivative of expected initial resistance with respect to noise amplitude b for (a) single-inlet connected model and (b) two-inlet connected model. For all simulations, $m = 5$ and $\lambda = 30$.

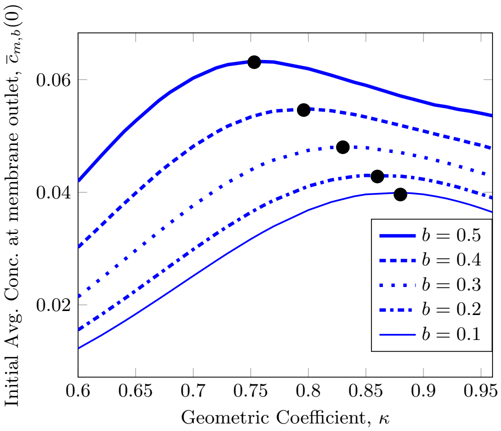

Figure 2.18 Initial average membrane outlet concentration versus geometric coefficient, κ, for the single-inlet connected model. For all simulations, $m = 5$ and $\lambda = 30$.

behaviour. In Figure 2.16a and Figure 2.16b, several plots of average initial resistance $\overline{r}_b(0)$ (averaged over 10^4 simulations) with different geometric coefficients are given, for the single- and two-inlet models, respectively. In the single-inlet case, the behaviour of $\overline{r}_b(0)$ with b undergoes a qualitative change as κ varies. For κ close to 1, $\overline{r}_b(0)$ increases monotonically with increasing b. For κ smaller than some threshold value between 0.8 and 0.95, $\overline{r}_b(0)$ always decreases with increasing b. This complex behaviour does not, however, persist in the two inlet case, as shown in Figure 2.16b, where $\overline{r}_b(0)$ is monotonically decreasing for all selected values of κ.

To attempt to explain these observations, we study the sensitivity of $\overline{r}_b(0)$ to b as the geometric coefficient κ is varied. With the aid of an explicit formula for $\mathbb{E}[r_b(0)]$ (Equation (A.10), derived in Appendix A.2), we plot in Figure 2.17 the initial slope of $\mathbb{E}[r_b(t)]$ as b varies, the partial derivative $\frac{\partial}{\partial b}\mathbb{E}[r_b(0)]$. Evidently, for the considered values of κ, with the exception of $\kappa = 0.95$ in the single-inlet connected model, $\frac{\partial}{\partial b}\mathbb{E}[r_b(0)]$ is negative, and only turns positive for very large noise amplitude b. Another interesting observation is that in the single-inlet connected model, there is a range of κ values that guarantees monotonic growth of $\mathbb{E}[r_b(0)]$ with b, yet for the two-inlet case, even for large geometric coefficients ($\kappa = 0.95$) the expected initial resistance is initially decreasing as b increases. Moreover, we observe the difference in the order of magnitude of the partial derivatives for the two models, manifested by the range of the vertical axis in both graphs. This indicates that the level of sensitivity to manufacturing error varies with the internal pore structure of the membrane. Qualitatively, this observation has real implications for the design of filters. For single-inlet membrane filters, a suitable level of manufacturing imprecision in the initial pore size distribution could, in fact, lead to improved initial performance due to the decreased average initial resistance, provided there is no serious negative impact on particle retention by the membrane.

Figure 2.18 shows the effect of varying both the geometric coefficient and noise amplitude on the average particle concentration at membrane outlet for the single-inlet connected model. In all cases, a local maximum is observed (worst particle retention scenario): our work makes explicit the dependence of this maximum on the noise amplitude. In particular, we observe that as the noise amplitude increases, the local maximum shifts towards smaller values of κ. This implies that when fabricating filters with known dimensional pore-size tolerances, the appropriate geometric coefficient should be chosen in order to optimize particulate removal. For the results shown in Figure 2.18, regardless of the fabrication precision (large or small b), filters with smaller κ should be selected.

2.6 Ending Remarks

In this chapter, we have modelled connected-pore membrane filters by studying fluid flow and particle transport and fouling in layered pore networks, focusing on selected specific membrane pore structures characterized by a geometric relationship (with ratio κ) between pore radii in adjacent layers. We first considered in-plane-homogeneous membrane filters (the homogeneous models) composed of cylindrical pores with flow governed by the Hagen–Poiseuille law. The local fluid volumetric flow rate in each pore is then related to the superficial Darcy velocity in order to measure the global flow behaviour via conservation of mass. To incorporate fouling, we modelled the adsorption of feed solution particles onto the pore wall. We obtained flow and fouling results for connected membranes and compared these results to those for non-connected membranes with equal initial resistance. In addition to the study of connectivity in homogeneous membranes, we also probe the influence of manufacturing imprecision, manifested as random in-plane perturbations to the initial pore sizes, on overall performance of the filter in terms of total throughput and particle retention capability.

For homogeneous models, our results reveal that the relative performance of non-connected and connected membranes does not strongly depend on either intra-layer connections or surface porosity. Rather, for our assumed periodically-repeating pore structure in which the membrane is assumed to consist of a square lattice of identical pore networks (see Figure 2.4) the differentiating factor is the number of inlet pores in each unit of the lattice. Because adsorption occurs predominantly in the first layer, the performance of membranes with equivalent top-layer porosity is governed by the dimensions of the first layer pore(s). Judging from radii evolution Figure 2.5 and volumetric flow rate-throughput Figure 2.7 results, we observe that within the scope of our study, single-inlet membranes yield the best overall performance. We have also shown that connected and non-connected single-inlet models can exhibit nearly identical performance depending on the choice of λ, the dimensionless deposition coefficient. Finally, we have demonstrated that for certain morphology parameter choices, the concentration of particles leaving the membrane can increase over time. We attribute this phenomenon to the particle advection rate, which increases as pores shrink and may (in some cases) outweigh the increased particle adsorption that occurs in shrinking pores. To characterize and quantify this behaviour, we have derived a sufficient condition with a general set of initial conditions and parameters for the appearance of a maximum in concentration at the membrane outlet. To avoid decreasing particle retention capability during filtration, one should not design membrane filters with geometric parameters that satisfy our sufficient condition.

In addition to our findings for homogeneous model membranes, we have found that the effects of membrane pore connectivity are more prominent in the heterogeneous case (modelled by a random perturbation of the initial pore sizes), where the mixing in inter-layer junction regions Equation (2.23) distinguishes connected models from the non-connected case. Regarding the average influence of noise perturbation to pore sizes on membrane performance as characterized by total throughput, we have shown that the filtrate collection efficiency of non-connected membranes is highly susceptible to noise, whereas the connected models are more robust, remaining relatively unchanged (see Figures 2.13 and 2.14). This contrast shows that from this perspective, connected membrane filters are superior filtrate processors because of their enhanced capability to alleviate negative effects of (inevitable) heterogeneity, facilitated by the inter-layer junction regions where mixing occurs and pressure is equilibrated.

We also observe that average initial resistance does not always depend monotonically on the strength of noise perturbation, exemplified by Jensen's inequality. This further implies that statistically averaged Darcy's law does not hold with equality, but rather, a strict inequality, as specified in Equation (2.58). In order to characterize the effect of noise more generally, we provide a full formula for the expression of average initial resistance of the connected models in Equation (A.10), which we use to show that the two-inlet model responds to increasing noise strength with a favourable decreasing trend.

The study on the internal pore structures of the membranes presented in this work is by no means a universal characterization of real membranes. Nonetheless, arising from physical observations and industrial motivation, the assumptions and results of our work are novel extensions to earlier efforts (*e.g.*, [111] and [46]), producing complex behaviour in both flow and foulant control under deterministic and random regimes. Furthermore, additional fouling mechanisms and their interaction with membrane connectivity will certainly lead to more complex problems, which may require more advanced mathematical and physical tools to tackle. We defer a more comprehensive study of multiple fouling modes acting on complex membrane structures to a future work.

CHAPTER 3

A GRAPHICAL REPRESENTATION OF MEMBRANE FILTRATION

3.1 Overview

In this chapter, we analyze the performance of membrane filters represented by pore networks using two criteria: 1) total volumetric throughput of filtrate over the filter lifetime and 2) accumulated foulant concentration in the filtrate. We first formulate the governing equations of fluid flow on a general network, and we model transport and adsorption of particles (foulants) within the network by imposing an advection equation with a sink term on each pore (edge) as well as conservation of fluid and foulant volumetric flow rates at each pore junction (network vertex). Such a setup yields a system of partial differential equations on the network. We study the influence of three geometric network parameters on filter performance: 1) average number of neighbors of each vertex; 2) initial total void volume of the pore network; and 3) tortuosity of the network. We find that total volumetric throughput depends more strongly on the initial void volume than on average number of neighbors. Tortuosity, however, turns out to be a universal parameter, leading to almost perfect collapse of all results for a variety of different network architectures. In particular, the accumulated foulant concentration in the filtrate shows an exponential decay as tortuosity increases.

3.2 Introduction

In many real membrane filters, cavities in the membrane material (pore junctions) are connected by capillaries or channels (pore throats) of length significantly larger than their radius (see Figure 3.1). Such slender geometry allows for simplifications of the equations governing filtration. At the same time, the membrane pore structure can be viewed as a complex network with vertices and edges, which represent the pore junctions and pore throats, respectively [66, 123]. A fluid feed with foulants is then driven across the membrane through these channels by the transmembrane pressure, while foulant is deposited on the pore walls.

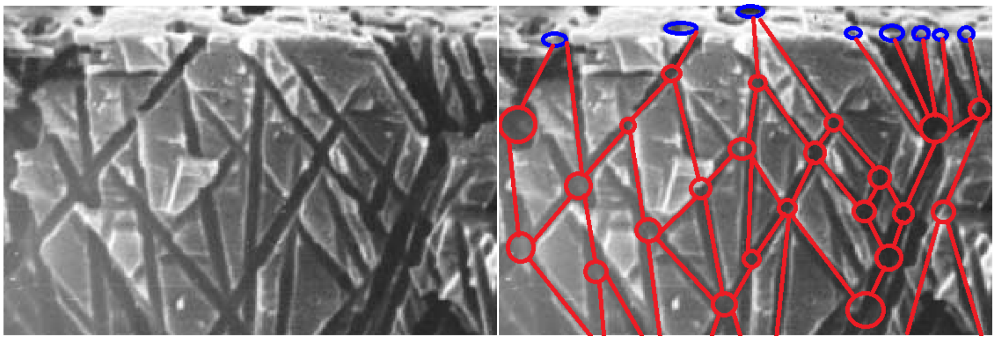

(a) Experimental Image **(b)** Inlets and Interior Junctions

Figure 3.1 Schematic: (a) an experimental image with lateral view of a filter cross-section [6]; (b) a corresponding (partial) graph representation with inlets on the top surface (blue) and interior pore junctions and throats (red).

There is a broad range of studies involving dynamics on networks, such as models of the cardiovascular network [22], chemical reaction networks [132] and optimal control in networks of pipes and canals [29], among many others. Accordingly, there are various graph models that may be used to represent complex networks, including pore networks in porous media. One such setup is the random geometric graph (RGG) model that has garnered significant attention from theoreticians [96, 30], as well as from applied scientists working on applications such as sensor networks [37], social science [138, 53, 145, 18], neuroscience [91] and, most relevant to our work, filtration modeling [128, 47]. The RGG setup involves generating a specified number of random points, uniformly distributed within a specified domain, and then connecting any pair of points that are closer than some search radius (according to the chosen metric).

Within the specific RGG setup used by Griffiths *et al.* [47] for filtration modeling, the chosen domain is a unit cube (normalized on the membrane thickness and representing a portion of the filter membrane); the metric is the usual 3D Euclidean distance; and to model top inlets and bottom outlets (see Figure 3.1a) random points are uniformly distributed on the top and the bottom surfaces of the cube. This setup requires four parameters: the number of interior points; the search radius; the number of top inlets; and the number of bottom outlets. Furthermore, the fluid flow is modelled by the Hagen-Poiseuille equations, whose validity relies on the physical assumption that the edges have a small aspect ratio (radius vs. length), prompting an additional constraint on the network generation.

Another important aspect of modeling the dynamics of filtration on the membrane network is fouling. Membrane fouling occurs when contaminants transported by the fluid feed within the pore network become trapped within it. There are three primary fouling mechanisms in membrane filtration: 1) adsorption; 2) sieving and 3) cake layer formation. Adsorption occurs when small particulate foulants are deposited on the pore walls due to physical or chemical interactions with membrane material (or with existing particle deposits). Sieving involves fouling particles of size comparable to the pore size that may partially cover or completely block upstream pore entries or internal junctions. Cake formation occurs during the later stages of filtration, where fouling particles are packed against each other inside the pore throats or on top of the membrane surface, further restricting fluid flow.

In this work, we consider adsorptive fouling only, modeling two main features. First, the fouling particles (referred to simply as particles, henceforth) deposit on pore walls as they are advected by fluid flow, thereby reducing foulant concentration in the feed as it traverses the network. Second, pore radius decreases due to the particle deposition on the pore wall. Within a continuum model for the particle concentration, the first effect can be captured by an appropriate sink term in the advection equation for the particle concentration, while the second may be modeled by an evolution equation for the pore radius.

Classical models of particle advective transport on graphs were developed and studied by Chapman & Mesbahi [23], but these authors did not incorporate a sink term to capture external effects such as fouling. Meanwhile, Gu *et al.* [50] considered a coarse discretization of a transport equation with deposition on regular layered pore structures with interconnections, which can be generalised to more complex networks (represented by graphs). In this work, we combine these two approaches and formulate a transport equation on the network using the graph theoretical framework.

Our principal contributions are to develop and solve a fluid flow and fouling problem on a graph representing the pore network within a membrane filter, by constructing the associated operators based on the underlying graph; and to use our model to identify important correlations between measurable network properties and key filtration performance metrics. The novel random graph generation technique we use achieves two primary goals: the constructed network is such that physical assumptions for the Hagen-Poiseuille fluid flow model remain valid; and the overall number of model parameters is minimized. Our model is described in detail in Section 3.3: in Section 3.3.1, we introduce the aspects of graph theory relevant to the present problem; in Section 3.3.2 we present a specific graph construction that represents a membrane network; in Section 3.3.3, we describe the fluid flow in an arbitrary pore (edge of the graph), before defining the necessary graph operators and associated function spaces on graphs in Section 3.3.4. With these building-blocks we are then able to set up the governing equations for fluid flow and foulant transport on a graph in Sections 3.3.5 and 3.3.6, respectively. In Section 3.3.7, we define the metrics that will be used to characterize filter performance. In Section 3.4 we introduce appropriate scalings to nondimensionalize the model and in Section 3.5 we outline the algorithm we use to solve it. Section 3.6 contains our results, presented in the context of the performance metrics defined in Section 3.3.7. In Section 3.7 we discuss our findings and summarize conclusions.

Table 3.1 Key Nomenclature

v_i	i-th vertex	e_{ij}	An edge connecting vertices v_i and v_j
V	Set of all vertices	E	Set of all edges
V_{top}	Set of vertices on the top membrane surface	V_{bot}	Set of vertices at the bottom membrane surface
$\mathbf{L_W}$	(Weighted) Graph Laplacian of G	$\mathbf{W}$	Weighted adjacency matrix of G
$\mathbf{M}$	Incidence matrix of G	$\mathbf{M}^{\mathrm{T}}$	Incidence matrix transpose
$\boldsymbol{P}(v_i)$	Pressure at the vertex v_i	$\boldsymbol{C}_i$	Concentration in vertex v_i (unit of number per volume)
P_0	Pressure at membrane top surface	C_0	Foulant concentration in the feed solution
$\mathbf{K}_{ij}$	Conductance of edge e_{ij}	$\mathbf{Q}_{ij}$	Flux through edge e_{ij}
R_{ij}	Radius of edge e_{ij}	A_{ij}	Length of edge e_{ij}
W	Side length of the square cross-section	$\chi(\cdot,\cdot)$	Metric on V
D	Search radius	N_{total}	Total number of vertices
D_{min}	Minimal edge length	τ	Tortuosity
μ	Fluid viscosity	α	Parameter related to particle volume
Λ	Affinity between the foulant and the pore wall (unit of velocity)	N	Average number of neighbors for a graph G
H	Throughput	C_{acm}	Accumulated foulant concentration at membrane outlet

3.3 Modeling

In this section, we describe and construct a graph that models a membrane filter pore network, and set up the governing equations of fluid flow and foulant transport through the network. We then introduce the performance measures associated with our membrane filter, which we will use to characterize filtration effectiveness. We refer the reader to Table 3.1 for all notation used in this work.

3.3.1 Graph Theoretical Setup

We consider a membrane filter as a slab of porous material that consists of an upstream (top) surface containing pore inlets, a downstream (bottom) surface containing pore outlets, and a porous interior comprising membrane material as the solid region and pore junctions and throats as the void region. We restrict attention to a cubic sub-region of the membrane slab in which the top and bottom surfaces are squares with side length W separated by distance W (the membrane depth). The pore throats in the interior of this sub-region are assumed to be circular cylinders connected at pore junctions, forming a network. We model this interior network of pores by a graph G consisting of a set of vertices V (the pore junctions) and edges E (the pore throats; see Figure 3.1), more compactly written as $G = (V, E)$. The set of vertices V consists of pore inlets on the membrane top (upstream) surface, pore junctions in the interior of the membrane material where edges (pores) meet, and pore outlets at the downstream surface of the filter. Each edge $e \in E$ represents a pore throat that connects two vertices. From a fluid dynamics perspective the graph forms a flow network, with fluid flowing along the edges and through the vertices. Each edge of the graph is associated with a weight to be specified depending on the context; in our model the weights are associated with the fluid flux through the edge. In constructing G we begin with an undirected graph, with directionality to be imparted by the direction of fluid flow (once defined).

Each vertex $v \in V$ is associated with a Euclidean position vector $\boldsymbol{X}(v) = (X_1(v), X_2(v), X_3(v)) \in \mathbb{R}^3$, where coordinates X_1, X_2 lie in the plane of the membrane, while X_3 is measured perpendicular to the membrane in the direction of flow.

Definition 1. *(Vertex set) Let $X_3(v)$ be the depth of the vertex v, measured by the shortest distance from the vertex to the membrane inlet surface. Let $V_{\text{top}}, V_{\text{bot}} \subset V$ be the set of vertices that lie in the top and bottom membrane surfaces, respectively,*

$$V_{\text{top}} = \{v \in V : X_3(v) = 0\}, \quad V_{\text{bot}} = \{v \in V : X_3(v) = W\}$$

where W is the depth of the membrane. The set of vertices in the interior of the membrane is given by $V_{\text{int}} = V \setminus (V_{\text{top}} \cup V_{\text{bot}})$.

We further assume that the graph is simple, *i.e.*, no vertex is connected to itself, equivalent to the assumption that fluid always flows out of a pore junction.

Definition 2. *An edge $e_{ij} \in E \subseteq V \times V$ is a pair (v_i, v_j), with $i \neq j$ whose existence is governed by a connection law (to be described). We do not distinguish between the order of the pair, namely, $e_{ij} = e_{ji}$.*

3.3.2 Graph Generation for a Membrane Network

Here we describe a random graph model in the specific context of membrane filtration by clarifying the constituents of V_{top}, V_{bot}, V_{int} and E, using a variant of the random geometric graph.

In the interior of a rectangular box Ω with square cross-sections of side length W and height $2W$, $\Omega := [0, W] \times [0, W] \times \left[-\frac{W}{2}, \frac{3W}{2}\right]$, we generate independent uniformly distributed random points in each cartesian coordinate, from which our set of vertices will be taken. To set up a connection rule for vertices in order to define edges, we first introduce a physically-motivated assumption. Earlier work such as that of Iritani [61] and Siddiqui *et al.* [115] suggests that pore throats in certain types of membrane filters are approximately cylindrical and slender, with $R_{ij}/A_{ij} \ll 1$, where R_{ij} and A_{ij} are the radius and length respectively of the edge (pore throat) e_{ij} connecting vertices (pore junctions) v_i and v_j. We assume our model membrane filter to be of this type, justifying the use of the Hagen-Poiseuille framework [103] to model steady laminar flow of fluid, assumed to be Newtonian with viscosity μ, within each edge (details of the flow model are in Section 3.3.5 later). In all simulations, we present, the initial edge radii are the same for all i, j (though they will shrink at different rates under subsequent fouling depending on local particle concentration), thus validity of the Hagen-Poiseuille model requires that the length of each edge must exceed a certain threshold, D_{min}. Meanwhile, to tune vertex connectivity, we prescribe a parameter D as the maximum possible edge length. More precisely, we define the edge set,

$$E = \{(v, w) \in V \times V : D_{\text{min}} < \chi(v, w) < D\}, \tag{3.1}$$

where $\chi(\cdot, \cdot)$ is the metric on our graph. In this work, we investigate and compare two distinct metrics: 1) Ω is treated as an isolated domain, with no pores entering or leaving through the four sides parallel to the X_3-direction, representing an isolated sub-unit of the whole membrane (*isolated* case) and 2) Ω is treated as a periodic domain such that any pore exiting through one of these four sides re-enters on the opposite side (*periodic* case). In each of these two cases the metric is defined by

$$\chi\left(v,w\right)=\begin{cases}\left\|\boldsymbol{X}\left(v\right)-\boldsymbol{X}\left(w\right)\right\|_2, & \text{isolated}\\ \min_{\boldsymbol{z}}\left\|\boldsymbol{X}\left(v\right)-\boldsymbol{X}\left(w\right)-\left(\boldsymbol{z},0\right)\mid \boldsymbol{z}=\left\{-W,0,W\right\}^2\right\|_2,\ D\leq\frac{W}{2}, & \text{periodic}\end{cases}\tag{3.2}$$

where we note that the periodic metric wraps points around the boundaries in the X_1 and X_2 directions. This metric effectively determines the pore lengths $A_{ij}=\chi\left(v_i,v_j\right)$. All scenarios considered in this work have search radius $D\leq\frac{W}{2}$, so we avoid the complication of having pores connect to each other twice (in the periodic case).

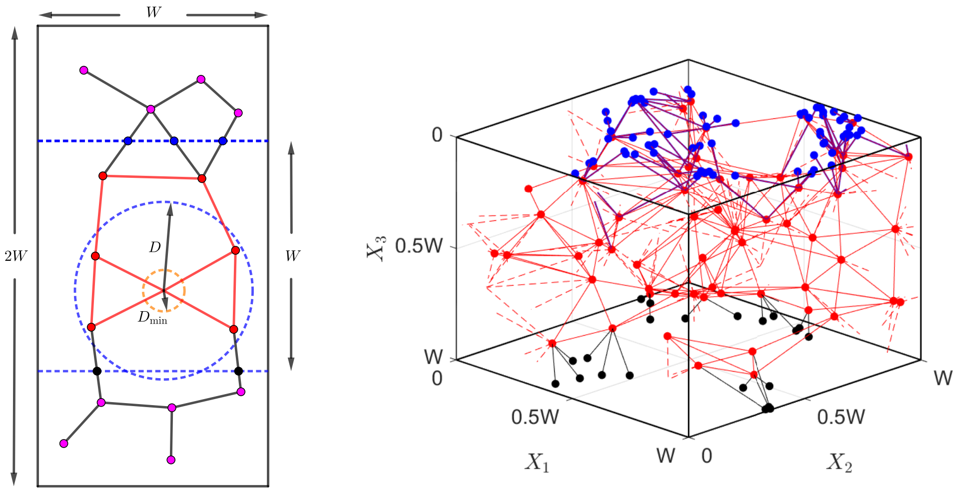

(a) **(b)**

Figure 3.2 (a) 2D schematic of the 3D graph generation; (b) 3D realization with the periodic metric. Labels for (a) and (b): red filled circles form V_{int}, blue filled circles form induced inlets V_{top}, and black filled circles form induced outlets V_{bot}. In (a), blue dotted lines are cutting lines (planes in 3D), and magenta circles are discarded points. The blue and orange dotted circles form the search annulus enforced by D and $D_{\min}$. In (b), periodicity is enforced only through the four interior walls per Equation (3.2).

To generate the set of upstream (top) inlets V_{top} and downstream (bottom) outlets V_{bot}, we cut Ω with two horizontal planes, $X_3=0$ (upstream cutting plane) and $X_3=W$ (downstream cutting plane). The points of intersection of these planes and the edges defined by Equation (3.1) form the set of pore inlets V_{top} and outlets

V_{bot}, respectively (see Figure 3.2). All points between the planes $X_3 = 0, W$ form the set of interior vertices V_{int}. This cutting procedure effectively eliminates two parameters (number of inlets and outlets) from the RGG setup proposed by Griffiths *et al.* [47]. We also impose two geometric constraints: 1) total volume of the edges generated by the above scheme cannot exceed that of the box and 2) total cross-sectional area of all inlets (resp. outlets) cannot exceed the area of the top (resp. bottom) membrane surface.

Our setup ensures that vertices in the top and bottom membrane surfaces are not connected by any edges that lie in the same surface. Another nice feature of our graph generation is that top inlets and bottom outlets are always connected to interior points, a feature that the classical RGG setup does not guarantee (some inlets or outlets may be isolated with positive probability and must be regenerated).

3.3.3 Flow in an Edge

We now briefly describe how Newtonian fluid of viscosity μ flows through a single edge (pore), before introducing the definitions of the relevant graph operators and associated function spaces (in Section 3.3.4), necessary to describe flow through the whole network. Two key physical quantities specify the flow: pressure $\boldsymbol{P}(v_i)$ at each vertex $v_i \in V$ and flux $\mathbf{Q}_{ij}$ through each edge $(v_i, v_j) \in E$. For each such edge, with length A_{ij} and radius R_{ij} (assumed to depend only on i, j and time T in the following, but see the more detailed discussion in Section 3.3.6 below), we use the Hagen-Poiseuille equation to describe fluid flow through it. This law gives fluid flux $\mathbf{Q}_{ij}$ in (v_i, v_j) as

$$\mathbf{Q}_{ij} = \mathbf{K}_{ij}\left(\boldsymbol{P}(v_i) - \boldsymbol{P}(v_j)\right), \quad (v_i, v_j) \in E, \tag{3.3}$$

where $\mathbf{K}_{ij}$ are the entries of a weight matrix $\mathbf{K}$ listing the *conductance* of each edge,

$$\mathbf{K}_{ij} = \begin{cases} \frac{\pi R_{ij}^4}{8\mu A_{ij}}, & (v_i, v_j) \in E, \\ 0, & \text{otherwise.} \end{cases} \tag{3.4}$$

Note that $\mathbf{Q}_{ij}$ is spatially uniform within the edge under the Hagen-Poiseuille framework. Moreover, to ensure the Hagen-Poiseuille approximation remains valid we require that the aspect ratio of each edge, R_{ij}/A_{ij}, is small, enforced by choosing $D_{\min}$ (introduced in Equation (3.1)) sufficiently large that

$$\frac{R_{ij}}{A_{ij}} \leq \frac{\max\limits_{(v_i,v_j)\in E} R_{ij}}{D_{\min}} \ll 1.$$

To solve Equation (3.3) on a graph with many edges, we must utilize the graph structure to express, for example, the pressure difference $\boldsymbol{P}(v_i) - \boldsymbol{P}(v_j)$ in Equation (3.3), while maintaining flux conservation at each vertex. We introduce the necessary operators below.

3.3.4 Operators and Function Spaces on Graphs

We now introduce the function spaces and operators required to solve for the above-defined flow on our graph. First, define the set of *vertex functions*

$$\mathcal{V} = \left\{ \boldsymbol{u} : V \to \mathbb{R} : \sum_{x\in V} \boldsymbol{u}(x)^2 < \infty \right\}, \tag{3.5}$$

endowed with inner product $(\boldsymbol{u} \cdot \boldsymbol{v})_{\mathcal{V}} = \sum_{x\in V} \boldsymbol{u}(x)\, \boldsymbol{v}(x)$, and the set of *edge functions*

$$\mathcal{E} = \left\{ \boldsymbol{F} : E \to \mathbb{R} : \frac{1}{2} \sum_{x,y\in V} w_{xy} \boldsymbol{F}(x,y)^2 < \infty \right\}, \tag{3.6}$$

where $\boldsymbol{F}$ is a skew-symmetric function that satisfies

$$\boldsymbol{F}(x,y) = -\boldsymbol{F}(y,x), \tag{3.7}$$

also known as the *flow condition*, and w_{xy} are specified weights. This space is endowed with weighted inner product

$$(\boldsymbol{F}_1 \cdot \boldsymbol{F}_2)_{\mathcal{E}} = \frac{1}{2} \sum_{x,y \in V} w_{xy} \boldsymbol{F}_1 (x,y) \boldsymbol{F}_2 (x,y) .$$

An example of a vertex function in the context of our problem is the pressure at each pore junction, while flux is an edge function when a well-defined weight is specified.

We next introduce the incidence matrix (and its transpose), a matrix operator that encodes the most fundamental information of a network represented by a graph — an array specifying the vertices that each edge connects. Its operation on edge functions provides a finite difference of quantities prescribed at connected vertices.

Definition 3. *(Incidence matrix and transpose) Let $G = (V, E)$ be a graph. The incidence matrix* $\mathbf{M}$ *is a linear operator* $\mathbf{M} : \mathcal{V} \to \mathcal{E}$ *such that for* $\boldsymbol{u} \in \mathcal{V}$*,*

$$(\mathbf{M}\boldsymbol{u})(v_i, v_j) = \boldsymbol{u}(v_i) - \boldsymbol{u}(v_j), \quad v_i, v_j \in V. \tag{3.8}$$

The transpose $\mathbf{M}^{\mathrm{T}} : \mathcal{E} \to \mathcal{V}$ *is also a linear operator that satisfies*

$$(\mathbf{M}\boldsymbol{u} \cdot \boldsymbol{F})_{\mathcal{E}} = \left(\boldsymbol{u} \cdot \mathbf{M}^{\mathrm{T}}\boldsymbol{F}\right)_{\mathcal{V}}, \quad \boldsymbol{u} \in \mathcal{V}, \quad \boldsymbol{F} \in \mathcal{E}. \tag{3.9}$$

A direct calculation of Equation (3.9) using the above definitions yields the following identity

$$\left(\mathbf{M}^{\mathrm{T}}\boldsymbol{F}\right)(x) = \sum_{y:(x,y) \in E} w_{xy} \boldsymbol{F}(x,y), \tag{3.10}$$

which computes a weighted sum of the edge functions whose edges connect to x.

Moreover, each graph G can be associated with a graph Laplacian $\mathbf{L}$, an item central to graph analysis.

Definition 4. *(Graph Laplacian) The* $\mathbf{W}$*-weighted graph Laplacian is given by*

$$\mathbf{L}_{\mathbf{W}} := \mathbf{D} - \mathbf{W}, \tag{3.11}$$

where $\mathbf{D}$ *is the (diagonal)* $\mathbf{W}$*-weighted degree matrix for* G*, with entries*

$$\mathbf{D}_{ij} = \begin{cases} \sum_{k=1}^{|V|} \mathbf{W}_{ik}, & j = i, \\ 0, & \textit{otherwise}, \end{cases} \tag{3.12}$$

and $\mathbf{W}$ *is a weighted adjacency matrix, with nonnegative entries* $\mathbf{W}_{ij}$ *when* $(v_i, v_j) \in E$*, to be specified according to context. We also say that* e_{ij} *is an edge connecting* v_i *and* v_j *iff* $\mathbf{W}_{ij} > 0$ *(or simply,* v_i *and* v_j *are connected or adjacent).*

$\mathbf{L_W}$ is symmetric since $\mathbf{W}$ is, and the nonzero entries in the diagonal matrix $\mathbf{D}$ represent the respective row sums of $\mathbf{W}$. An unweighted version of $\mathbf{L_W}$ corresponds to the case where $\mathbf{W}_{ij} = 1$ for every $e_{ij} \in E$, and thus each entry of the adjacency matrix is an indicator that identifies an edge between a pair of vertices. In this case, each diagonal element of $\mathbf{D}$ is the number of edges connected to each vertex.

Combining Equations (3.8), (3.10) and (3.11), we obtain the classical result connecting the incidence matrix and the graph Laplacian.

Proposition 1. *For* $\boldsymbol{u} \in \mathcal{V}$*,* $\mathbf{M}^{\mathrm{T}}\mathbf{M}\boldsymbol{u} = \mathbf{L_W}\boldsymbol{u}$*.*

This result (a proof of which is given by Grady [43]) provides the basis for theoretical understanding of the structure of $\mathbf{M}$, and in turn, $\mathbf{L_W}$. The continuum analog of this result is the equivalence between the divergence of a gradient and the Laplacian.

In many applications, the choice of weights $\mathbf{W}$ depends on the physical problem of interest. In the context of membrane filtration, it is natural to consider weights such as conductance and flux, which we describe in Section 3.3.5 in more detail. We will apply Proposition 1 to set up the flow problem on our graph G.

3.3.5 Flow on a Graph

In this section, we outline a general approach to describe fluid flow on a graph using the definitions given in Section 3.3.4 above. We set up the system of governing equations using the structural information of G, *i.e.*, the graph Laplacian $\mathbf{L_W}$ with a properly chosen weight matrix $\mathbf{W}$.

First, we rewrite Equation (3.3) using the incidence operator Equation (3.8),

$$\mathbf{Q}_{ij} = \mathbf{K}_{ij}\left(\boldsymbol{P}\left(v_i\right) - \boldsymbol{P}\left(v_j\right)\right) = \mathbf{K}_{ij}\left(\mathbf{M}\boldsymbol{P}\right)\left(v_i, v_j\right), \quad \left(v_i, v_j\right) \in E, \tag{3.13}$$

where $\mathbf{K}_{ij}$ is given by Equation (3.4). The values of the pressure at the vertices, $\boldsymbol{P}\left(v_i\right)$ for each $v_i \in V$, form a vector of length $|V|$ (a *vertex function*, $\boldsymbol{P} \in \mathcal{V}$). The flux values $\mathbf{Q}_{ij}$ naturally form a matrix. Note that $\mathbf{Q}$ is an *edge function*, $\mathbf{Q} \in \mathcal{E}$, since it satisfies the flow condition Equation (3.7). Next, we impose conservation of flux at each junction,

$$\sum_{v_j:(v_i,v_j)\in E} \mathbf{Q}_{ij} = 0, \quad v_i \in V_{\text{int}}. \tag{3.14}$$

Using Equation (3.10) with $\boldsymbol{F} = \mathbf{M}\boldsymbol{P}$, Equation (3.13) and noting that $\mathbf{Q} \in \mathcal{E}$, we obtain for $v_i \in V_{\text{int}}$,

$$0 = \sum_{v_j:(v_i,v_j)\in E} \mathbf{Q}_{ij} = \sum_{v_j:(v_i,v_j)\in E} \mathbf{K}_{ij}\left(\mathbf{M}\boldsymbol{P}\right)\left(v_i, v_j\right) = \left(\mathbf{M}^{\mathrm{T}}\mathbf{M}\boldsymbol{P}\right)\left(v_i\right) = \left(\mathbf{L_K}\boldsymbol{P}\right)\left(v_i\right), \tag{3.15}$$

to which we append the boundary conditions

$$\boldsymbol{P}\left(v\right) = P_0, \quad v \in V_{\text{top}}; \quad \boldsymbol{P}\left(v\right) = 0, \quad v \in V_{\text{bot}}, \tag{3.16}$$

modeling the transmembrane pressure difference that drives fluid flow.

Once we solve the linear system Equations (3.15) and (3.16) for pressure $\boldsymbol{P}$, we use Equation (3.13) to compute the entries of the flux matrix $\mathbf{Q}$.

3.3.6 Foulant Advection and Adsorptive Fouling

The previous section was concerned solely with the flow of Newtonian fluid through the graph. Here we address the fact that in filtration the fluid is a feed solution carrying particles, which are removed by the filter, leading to fouling. Fouling can occur via a number of distinct modes; we consider only adsorptive fouling by particles much smaller than pores, which are transported through the network by the flow and deposit on pore walls.

We use a continuum model for the particle (foulant) concentration within the feed. To characterize particle transport on a network, we must describe the transport on each edge, accomplished via an advection equation with an adsorptive sink [111, 50], then impose conservation of particle flux at each vertex. For each edge $e_{ij} = (v_i, v_j)$ of length A_{ij}, with Y a local coordinate measuring distance along the edge from v_i (positive in the direction of flux $\mathbf{Q}_{ij}$), let $C_{ij}(Y, T)$ be the particle concentration at any point of the edge at time T, then

$$\mathbf{Q}_{ij} \frac{\partial C_{ij}}{\partial Y} = -\Lambda R_{ij} C_{ij}, \quad 0 \leq Y \leq A_{ij}, \tag{3.17a}$$

$$C_{ij}(0, T) = \boldsymbol{C}_i(T), \quad (v_i, v_j) \in E, \tag{3.17b}$$

where Λ is a parameter (with dimensions of velocity) that captures the affinity between the foulant and the pore wall. In practice this could change depending on whether the pore wall is clean, or already fouled by particle deposits; in this work we assume Λ is constant throughout the filtration. We denote by $\boldsymbol{C}_i(T)$ the foulant concentration at the vertex v_i, which acts as a boundary condition for the foulant concentration C_{ij} flowing to downstream edges. The array of $\boldsymbol{C}_i(T)$ values forms a vertex function $\boldsymbol{C}$. For $v_i \in V_{\text{top}}$, $\boldsymbol{C}_i(T)$ is prescribed by imposing a constant boundary condition (the concentration C_0 in the feed solution), and conservation of particle flux is imposed to determine the $\boldsymbol{C}_i(T)$ for $v_i \in V \backslash V_{\text{top}}$.

The system of Equations (3.17a) and (3.17b) is simple, but once coupled to an evolution equation for pore radii $R_{ij}(Y, T)$ and solved on many different (large) graph realizations to obtain reliable statistics, is time-consuming to solve numerically. We therefore adopt a convenient approximation (discussed further below), assuming that pore radius does not change appreciably along individual pores, and may thus be considered approximately independent of the coordinate Y. With this assumption, we observe that the system of Equations (3.17a) and (3.17b) has analytical solution

$$C_{ij}\left(Y,T\right) = \boldsymbol{C}_i\left(T\right)\exp\left(-\frac{\Lambda R_{ij}\left(T\right)}{\mathbf{Q}_{ij}}Y\right), \quad 0 \le Y \le A_{ij}. \tag{3.18}$$

We write $\tilde{C}_{ij}\left(T\right) := C_{ij}\left(A_{ij},T\right)$ to represent the foulant concentration flowing from v_i into an adjacent vertex v_j. Define

$$\mathbf{B}_{ij}\left(T\right) := \exp\left(-\frac{\Lambda R_{ij}\left(T\right)A_{ij}}{\mathbf{Q}_{ij}}\right), \tag{3.19}$$

as the multiplicative factor by which foulant concentration changes over the length A_{ij} of the edge. By conservation of particle flux at each vertex v_i (suppressing the temporal and spatial dependence for simplicity of notation),

$$\begin{aligned} 0 &= -\overbrace{\sum_{v_k:(v_i,v_k)\in E}\mathbf{Q}_{ik}\boldsymbol{C}_i}^{\text{outgoing}} + \overbrace{\sum_{v_k:(v_i,v_k)\in E}\mathbf{Q}_{ki}\tilde{C}_{ki}}^{\text{incoming}}, \quad v_i \in V\backslash V_{\text{top}}, && (3.20)\\ &= -\boldsymbol{C}_i\sum_{v_k:(v_i,v_k)\in E}\mathbf{Q}_{ik} + \sum_{v_k:(v_i,v_k)\in E}\mathbf{Q}_{ki}\tilde{C}_{ki}, \\ &= -\boldsymbol{C}_i\sum_{v_k:(v_i,v_k)\in E}\mathbf{Q}_{ki} + \sum_{v_k:(v_i,v_k)\in E}\mathbf{Q}_{ki}\mathbf{B}_{ki}\boldsymbol{C}_k, && (3.21)\\ \boldsymbol{C}_i\left(T\right) &= C_0, \quad v_i \in V_{\text{top}}, \quad \forall T \ge 0, && (3.22)\end{aligned}$$

where C_0 is the constant foulant concentration in the feed solution. Note the conservation of flux used here to derive Equation (3.21) follows a revised definition of the flux matrix $\mathbf{Q}$ (see Equation (B.6) in Appendix B.2). The first term in Equation (3.20) accounts for all outgoing particle flux from vertex v_i, the second for all incoming flux. Conservation of flux at each $v_i \in V\backslash V_{\text{top}}$ and the definition of $\tilde{C}_{ij}$ are applied in Equation (3.21), which can be written more compactly using $\mathbf{Q}$ as a weight matrix and the in-degree weighted graph Laplacian $\mathbf{L}_{\mathbf{Q}}^{\text{in}} : l^2\left(V\backslash V_{\text{top}}\right) \to l^2\left(V\backslash V_{\text{top}}\right)$,

$$\mathbf{L}_{\mathbf{Q}}^{\text{in}} := \mathbf{D}_{\mathbf{Q}^{\text{T}}} - \left(\mathbf{Q}\circ\mathbf{B}\right)^{\text{T}}, \tag{3.23}$$

where $\circ$ is the Hadamard product (element-wise matrix product). This operator is similar to Equation (3.11) but with a notion of directionality imparted by $\mathbf{Q}$ (also discussed by Chapman & Mesbahi [23]). The term $\mathbf{D}_{\mathbf{Q}^{\mathrm{T}}}$ is a $\mathbf{Q}^{\mathrm{T}}$-weighted degree matrix (per Equation (3.12)) that accounts for total incoming (upstream) flux of v_i (thereby "in-degree"). The last term, which contributes to the off-diagonal entries of $\mathbf{L}_{\mathbf{Q}}^{\mathrm{in}}$, displays the incoming flux reduced (multiplicatively) by the foulant deposition effect reflected in $\mathbf{B}$. Altogether, the transport equation for foulant concentration can be concisely written as

$$\mathbf{L}_{\mathbf{Q}}^{\mathrm{in}}\boldsymbol{C} = \left(\mathbf{Q}\circ\mathbf{B}\right)^{\mathrm{T}}\boldsymbol{C}_0, \quad \boldsymbol{C}\in l^2\left(V\backslash V_{\mathrm{top}}\right), \quad \forall T\geq 0, \tag{3.24}$$

$$\boldsymbol{C}_0\left(T\right) = \left(C_0,\ldots,C_0,0,\ldots,0\right)^{\mathrm{T}}, \tag{3.25}$$

with boundary condition C_0 specified for each $v\in V_{\mathrm{top}}$ (the number of nonzero entries C_0 in $\boldsymbol{C}_0$ is equal to $|V_{\mathrm{top}}|$, per Equation (3.22)). By solving this linear system, we obtain the particle concentration $\boldsymbol{C}_i$ at each vertex $v_i\in V\backslash V_{\mathrm{top}}$.

We assume that the pore radius shrinkage due to adsorption follows a simple model (used by Sanaei & Cummings [111], among others) such that its rate of change is proportional to local particle concentration. With the approximation introduced above, that pore radius R_{ij} varies only modestly with distance Y along the pore, we assume that its rate of shrinkage is determined by the foulant concentration at the upstream[1] vertex v_i,

$$\frac{dR_{ij}}{dT} = -\Lambda\alpha\boldsymbol{C}_i, \quad R_{ij}\left(0\right) = R_{ij,0}, \quad \left(v_i,v_j\right)\in E, \tag{3.26}$$

where α relates to foulant particle volume, see Appendix B.1. We also assume that all radii initially take the same value, *i.e.*, $R_{ij,0}=R_0$. This final equation Equation (3.26) closes the membrane filtration model with adsorption.

---

[1] This concentration is chosen because it will dictate, in practice, the fastest shrinkage rate at the upstream end of the pore, and pore resistance is dominated by the narrowest pore radius.

Our assumption that pore radius is spatially uniform is motivated by significant computational cost savings; we have verified that the simulations reported later in the manuscript are more than 100 times faster compared to those where this simplification is not used. The price to pay for this saving is a slight overestimate of the membrane resistance, and therefore underestimate of the total throughput. To confirm that the approximation introduced by the model has only a minor influence, we have directly compared a subset of results obtained using this model with results obtained using the full model that allows $R_{ij}(Y, T)$, finding that the difference in throughput is on average around 10% at maximum (and much smaller than 10% where the maximum pore radius D is small compared to the membrane thickness W). The differences in computed values of the particle concentration are smaller still. We consider that this is reasonable, in particular since the approximation allows us to perform efficiently a large number of simulations and explore the influence of variability of results with respect to the model parameters of interest.

In simulating filtration through a network, we impose a *stopping criterion* that membrane filtration ends when there exist no flow paths between any vertices in V_{top} and V_{bot}, due to pore closures (individually characterized by $R_{ij} = 0$). The criterion is checked by a pathfinding algorithm. We terminate the filtration at the earliest time T_{final} that the criterion is satisfied. Note that in physical membranes, even when adsorptive foulants have accumulated to the extent that the pore is essentially closed, leakage through the pore may still take place; we have not included such effects in the present model.

3.3.7 Measures of Performance

Volumetric throughput of a membrane filter over its operational lifetime is a commonly-used measure of overall efficiency.

Definition 5. *The volumetric throughput* $V(T)$ *through the filter is defined by*

$$H\left(T\right)=\int_{0}^{T}Q_{\text{out}}\left(T'\right)dT',\quad Q_{\text{out}}\left(T\right)=\sum_{v_j\in V_{\text{bot}}}\sum_{v_i:(v_i,v_j)\in E}\mathbf{Q}_{ij}\left(T\right)$$

where $Q_{\text{out}}\left(T\right)$ *is the total flux exiting the filter.*

In particular, we are interested in $H_{\text{final}}:=H\left(T_{\text{final}}\right)$, the total volume of filtrate processed by the filter over its lifetime.

Another performance measure is the accumulated foulant concentration in the filtrate, which captures the aggregate particle capture efficiency of the filter.

Definition 6. *The accumulated foulant concentration is defined by*

$$C_{\text{acm}}\left(T\right)=\frac{\int_0^T C_{\text{out}}\left(T'\right)Q_{\text{out}}\left(T'\right)dT'}{\int_0^T Q_{\text{out}}\left(T'\right)dT'},$$

where

$$C_{\text{out}}\left(T\right)=\frac{\displaystyle\sum_{v_j\in V_{\text{bot}}}\sum_{v_i:(v_i,v_j)\in E}\boldsymbol{C}_j\left(T\right)\mathbf{Q}_{ij}\left(T\right)}{Q_{\text{out}}\left(T\right)}.$$

Of particular interest is $C_{\text{acm}}\left(T_{\text{final}}\right)$, which provides a measure of the aggregate particle capture efficiency of the filter over its lifetime.

3.4 Nondimensionalization

We nondimensionalise the model presented in Section 3.3 with the following scales,

$$\begin{gathered}\boldsymbol{P}=P_0\boldsymbol{p},\qquad \boldsymbol{X}=W\boldsymbol{x},\qquad A_{ij}=Wa_{ij},\\ \left(D,D_{\min}\right)=W\left(d,d_{\min}\right),\qquad R_{ij}=Wr_{ij},\qquad R_0=Wr_0,\\ \mathbf{Q}_{ij}=\frac{\pi W^3P_0}{8\mu}\mathbf{q}_{ij},\qquad \mathbf{K}_{ij}=\frac{\pi W^3}{8\mu}\mathbf{k}_{ij},\qquad \mathbf{k}_{ij}=\frac{r_{ij}^4}{a_{ij}},\\ \boldsymbol{C}=C_0\boldsymbol{c},\qquad Y=Wy,\qquad \Lambda=\frac{\pi WP_0}{8\mu}\lambda,\qquad T=\frac{W}{\Lambda\alpha C_0}t,\qquad V=\frac{W^3}{\alpha C_0}v.\end{gathered}\tag{3.27}$$

Under these scalings we derive dimensionless equations for pressure $\boldsymbol{p}$ and flux $\mathbf{q}$,

$$\mathbf{L}_{\mathbf{k}}\boldsymbol{p}=0,\tag{3.28a}$$

$$\boldsymbol{p}(v) = 1, \quad \forall v \in V_{\text{top}}; \quad \boldsymbol{p}(v) = 0, \quad \forall v \in V_{\text{bot}}, \tag{3.28b}$$

$$\mathbf{q}_{ij} = \mathbf{k}_{ij}\left(\boldsymbol{p}(v_i) - \boldsymbol{p}(v_j)\right), \quad \forall (v_i, v_j) \in E, \tag{3.28c}$$

where $\mathbf{L}_{\mathbf{k}}$ is defined in Equation (3.11); for foulant concentration $\boldsymbol{c}$,

$$\mathbf{L}_{\mathbf{q}}^{\text{in}}\boldsymbol{c} = (\mathbf{q} \circ \mathbf{b})^{\mathrm{T}} \boldsymbol{c}_0, \quad \mathbf{L}_{\mathbf{q}}^{\text{in}} = \mathbf{D}_{\mathbf{q}^{\mathrm{T}}} - (\mathbf{q} \circ \mathbf{b})^{\mathrm{T}}, \quad \boldsymbol{c} \in l^2\left(V \backslash V_{\text{top}}\right), \tag{3.29a}$$

$$\boldsymbol{c}_0 = (1, \ldots, 1, 0, \ldots, 0)^{\mathrm{T}}, \quad \mathbf{b}_{ij} = \exp\left(\frac{-\lambda r_{ij} a_{ij}}{\mathbf{q}_{ij}}\right), \tag{3.29b}$$

where $\mathbf{L}_{\mathbf{q}}^{\text{in}}$ is given by Equation (3.23); and for pore radius r_{ij} (for the pore $e_{ij} = (v_i, v_j)$),

$$\frac{dr_{ij}}{dt} = -\boldsymbol{c}_i, \quad r_{ij}(0) = r_0, \quad \forall (v_i, v_j) \in E. \tag{3.30}$$

The dimensionless throughput is given by

$$h(t) = \frac{1}{\lambda} \int_0^t q_{\text{out}}(t')\, dt', \quad q_{\text{out}}(t) = \sum_{v_j \in V_{\text{bot}}} \sum_{v_i : (v_i, v_j) \in E} \mathbf{q}_{ij}(t), \tag{3.31}$$

and $h_{\text{final}} := h(t_{\text{final}})$. Dimensionless accumulated foulant concentration is written as

$$c_{\text{acm}}(t) = \frac{\int_0^t c_{\text{out}}(t')\, q_{\text{out}}(t')\, dt'}{\int_0^t q_{\text{out}}(t')\, dt'}, \tag{3.32}$$

where

$$c_{\text{out}}(t) = \frac{\displaystyle\sum_{v_j \in V_{\text{bot}}} \sum_{v_i : (v_i, v_j) \in E} \boldsymbol{c}_j(t)\, \mathbf{q}_{ij}(t)}{q_{\text{out}}(t)}.$$

3.5 Algorithm

We summarize the network generation protocol and solution technique for the proposed model equations in Algorithm 3.1. We refer the reader to a worked example in Appendix B.3 for a better visualisation of how the governing equations evolve on a very simple network and how our chosen performance metrics depend on the model parameters.

Algorithm 3.1 Filtration with adsorption.

```
1. Initialization
    (a) Generate uniformly $N_{\text{total}}$ random points in box $[0,1]^2 \times [-0.5, 1.5]$.
    (b) Connect all points separated by a distance smaller than $d$ but larger than $d_{\text{min}}$ using the metric $\chi$ (periodic or isolated). Discard isolated points.
    (c) Truncate the box with cutting planes at $x_3 = 0$ and $x_3 = 1$; record points with $0 < x_3 < 1$ as the set of interior points $V_{\text{int}}$; label intersections between cutting planes and edges as inlets $V_{\text{int}}$ for intersections at $x_3 = 0$ and outlets $V_{\text{out}}$ for those at $x_3 = 1$. Set $V = V_{\text{int}} \cup V_{\text{top}} \cup V_{\text{bot}}$.
    (d) Initialise radii $r_{ij,0}$ for $(r_{ij})_{(v_i,v_j)\in E}$.
2. Fluid Flow
    (a) Find pressures $\boldsymbol{p}$ and fluxes $\mathbf{q}$ by solving Equations (3.28a)–(3.28c).
3. Foulant Concentration
    (a) Initialise concentrations $\boldsymbol{c}_0$ (per Equation (3.29b)) for $v_i \in V_{\text{top}}$.
    (b) Find foulant concentration $\boldsymbol{c}$ by solving Equations (3.29a) and (3.29b).
4. Adsorption
    (a) Evolve each pore radius $r_{ij}$ via Equation (3.30) until it decreases to 0 and stays at 0 for the rest of the filtration.
5. Check stopping criterion. Stop if satisfied.
6. Compute throughput using Equation (3.31).
7. Update conductance $\mathbf{k}$ and weighted graph Laplacian $\mathbf{L_k}$.
8. Increment time $t \to t + dt$ and return to (2).
```

3.6 Results

In this section, we present numerical results on how filter performance metrics, such as total throughput and accumulative foulant concentration (introduced in Section 3.3.7), depend on filter geometry, characterized by three main geometric network parameters detailed below. For each metric/parameter pair considered, we first describe the observed trends and compare the results between the isolated and periodic network configurations. Then, we discuss how the findings are related, with a focus on identifying universal parameters that describe filter performance.

3.6.1 Geometric Network Parameters

To investigate different network architectures, we introduce three geometric parameters. The first is the average number of neighbors for interior vertices/junctions,

$$N := \frac{|E|}{|V_{\text{int}}|}.$$

This parameter provides one way to characterize the connectivity strength of a network. We compute N only over interior vertices, as any inlet or outlet has exactly one neighbor due to our network generation protocol. Second, the initial void volume,

$$\text{Vol}_0 = \frac{\pi}{2} \sum_{(v_i, v_j) \in E} a_{ij} r_{ij}^2 \, (t = 0) = \frac{\pi r_0^2}{2} \sum_{(v_i, v_j) \in E} a_{ij}, \tag{3.33}$$

provides an estimate of how much fluid the filter can process initially, and how much surface area is available for foulant adsorption (since the initial pore radius is the same for all pores, the initial total pore surface area is given by $2\text{Vol}_0/r_0$). Since the representative membrane volume we consider is a unit cube in our dimensionless framework, Vol_0 is exactly the initial membrane *porosity.* Lastly, we consider tortuosity τ, defined by the *average length of paths* (defined with respect to flow paths) that connect the top and bottom membrane surface through the network, normalized by the membrane thickness (the shortest possible path). A rigorous definition of τ is given in the appendix (Definition 9 and Equation (B.9)).

Our input parameters (d, N_{total}) (see Algorithm 3.1) are chosen so that the volume and area constraints (initial total pore volume should not exceed that of the representative unit membrane cube, and total pore cross-sectional area on membrane top and bottom surfaces should not exceed the area of the unit square, see Section 2.2) are not violated, and so that the generated graphs are nontrivially connected from top to bottom surfaces. The ranges of d and N_{total} are $[0.1, 0.45]$ and $[100, 5000]$, respectively. In all simulations, we fix $r_0 = 0.01$, $d_{\text{min}} = 0.06$, $\lambda = 5 \times 10^{-7}$ and produce data curves for each chosen d-value (represented by the same marker) by varying N_{total}.

Due to the random nature of our network generation, we compute the average of quantities of interest over a number of realizations. For simplicity, we do not use additional notation to indicate such averaged quantities. For all results below, each data point is obtained by averaging over 500 simulations, *i.e.*, 500 realizations of a random graph with parameter pair (d, N_{total}). We histogram these 500 realizations in the supplement for each pair (d, N_{total}), to demonstrate that their variance is influenced only by geometric parameters, justifying the sufficiency of this number of realizations. All results are shown for the two cases in which the underlying random graphs are generated with isolated and periodic boundary conditions, with results (data points in blue and red, respectively) compared side-by-side.

3.6.2 Initial Void Volume and Average Number of Neighbors

In this section, we present results showing the dependence of performance metrics on two geometric parameters: initial void volume Vol_0 and average number of neighbors N.

Figure 3.3 shows total throughput h_{final} against initial void volume Vol_0 on a log-log scale, for various d-values. Both quantities are increasing functions of the initially-specified number of random points, N_{total}, for each d. In both isolated and periodic cases we see a power law relationship emerge for sufficiently large Vol_0, with good collapse of the data for $\text{Vol}_0 \gtrsim 0.2$, $d \gtrsim 0.2$ onto a single line, hinting at a universal law. The fact that h_{final} is an increasing function of Vol_0 makes sense because the larger the initial pore volume, the more filtrate can be processed. In both setups, the data curves for smaller d-values begin to deviate from the universal power law for $\text{Vol}_0 \lesssim 0.3$, which enables us to observe some hierarchy. For similar Vol_0-values, corresponding to similar total length of edges per Equation (3.33), we see that larger

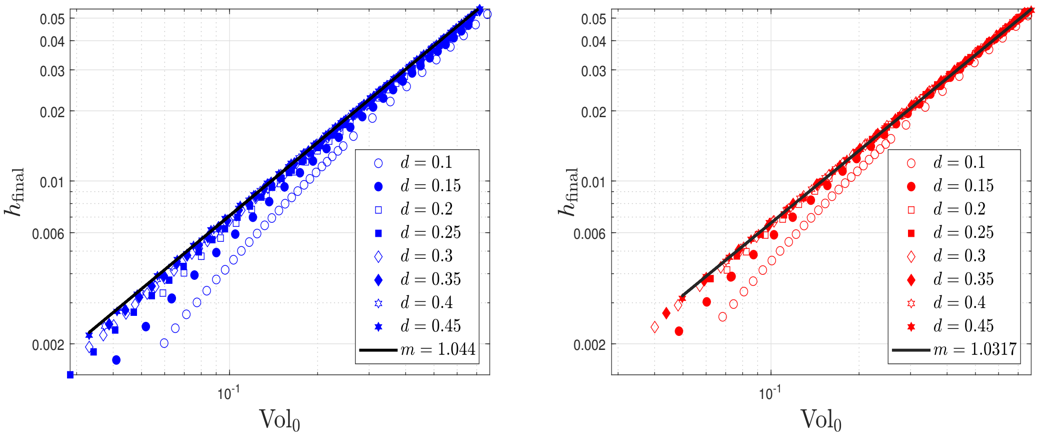

(a) **(b)**

Figure 3.3 Total throughput h_{final} vs initial void volume Vol_0 (loglog scales). (a) Isolated network setup; (b) periodic setup. Line of best fit for $d = 0.45$ is in black, with gradient m given in legend (with $R^2 = 0.99989$ and 0.99993, respectively). Distribution of error for each data point is given in the histograms in the supplement.

d-values lead to larger total throughput h_{final}. We attribute this to the fact that networks with larger d-values induce more inlets on the upstream (and downstream) membrane surfaces, allowing more filtrate to pass through. The differences between the isolated and periodic setups in Figure 3.3 are minor.

In Figures 3.4a and 3.4b, we plot total throughput h_{final} against average number of neighbors N (the average number of pores entering or leaving each vertex) for various values of the search radius d, using a log scale for both axes. Each data point shown corresponds to a different choice of N_{total}; and, as discussed above, represents results averaged over 500 individual random graph realizations. Several features are common to both plots: first, h_{final} is an increasing function of N for each d value and in particular, obeys a power law for sufficiently large N. For fixed N, the smaller the search radius d, the larger the average throughput h_{final}. This suggests that the number of pore junctions plays an important role in controlling and predicting total throughput. Second, the slopes for each d-value at large N are very similar for both isolated and periodic setups, suggesting a common power law relating h_{final}

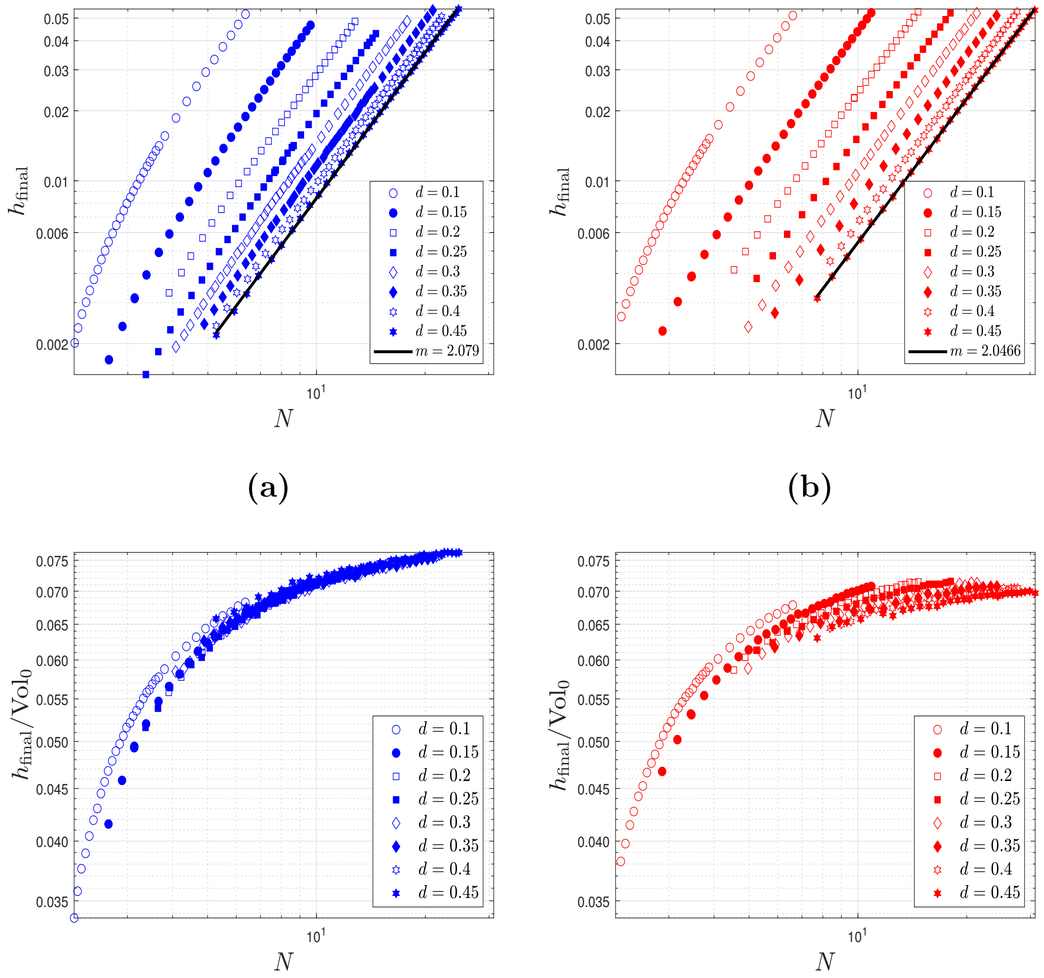

(a) **(b)**

(c) **(d)**

Figure 3.4 Total throughput h_{final} vs average number of neighbors N (loglog scales). (a) Isolated network setup; (b) periodic setup. Line of best fit for $d = 0.45$ is in black, with gradient m given in legend. Distribution of error for each data point is given in the histograms in the supplement. Same setup for (c) and (d) with $h_{\text{final}}/\text{Vol}_0$ as vertical axis (loglog scales).

and N for each d (see $d = 0.45$ in Figures 3.4a and 3.4b with slope ≈ 2 in both cases). Moreover, as d increases the curves in Figures 3.4a and 3.4b become more closely-spaced in both setups, demonstrating that filters with sufficiently large search radius perform similarly in terms of total throughput. In both cases the quantities N and h_{final} are increasing functions of N_{total} for each d.

We also highlight the differences between the two compared network connection metrics in Figures 3.4a and 3.4b. First, for small d (e.g. $d = 0.1, 0.15$), the isolated and periodic networks give similar throughputs since random graph generations under the two metrics do not differ greatly; however, as d increases, the periodic metric generates more edges than the isolated one (for the same value of N_{total}), hence the periodic setup yields higher throughput. By the same reasoning, for fixed h_{final}, N is much larger in the periodic setup than in the isolated one for each $d \gtrsim 0.3$ (the data curves in the isolated setup are seen to be more closely-spaced than those in the periodic setup as d increases). In other words, though N is an increasing function of d in each setup, it increases at a higher rate under the periodic metric.

Motivated by the strong relationship between total throughput and volume found in Figure 3.3, we also plot volume-scaled total throughput, $h_{\text{final}}/\text{Vol}_0$, against average number of neighbors N for both connection metrics in Figures 3.4c and 3.4d. This volume-scaled total throughput can be understood as a measure of efficiency of the membrane filter in terms of filtrate production capability. In Figure 3.4c, we observe a good collapse of data in the non-periodic setup, which suggests that the average number of neighbors is a good predictor for total throughput scaled by volume. We see a similar trend in Figure 3.4d for the periodic setup, though the collapse is less strong. We further note that in both non-periodic and periodic setups, data for $d = 0.1$ are slightly separated from the rest. This is consistent with the deviation of data for $d = 0.1$ in Figure 3.3 from the universal power law relating total throughput and volume.

Figure 3.5 shows final accumulated foulant concentration in the filtrate, $c_{\text{acm}}(t_{\text{final}})$, vs initial void volume, Vol_0, on a log-log scale, as d is varied. Both quantities are increasing functions of N_{total} for each d. The plots for both isolated and periodic network metrics show that $c_{\text{acm}}(t_{\text{final}})$ increases as search radius d increases for fixed Vol_0. This is because with similar initial pore volume and thus similar

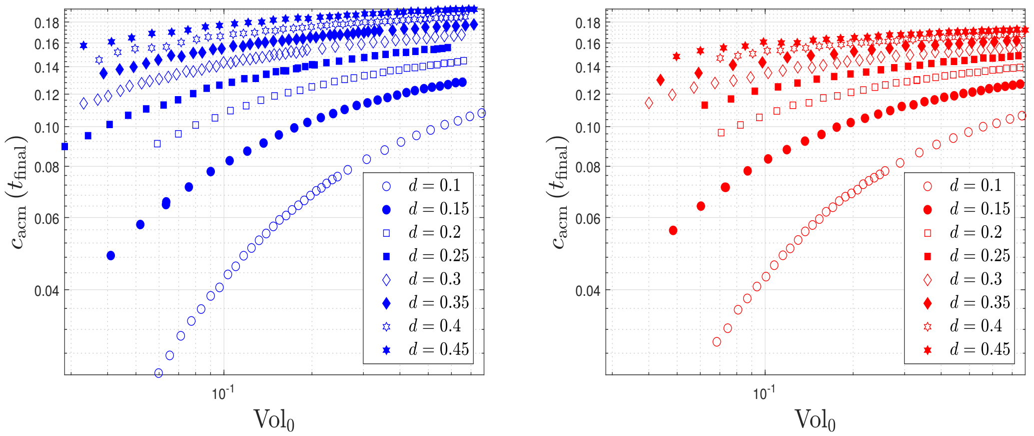

(a) **(b)**

Figure 3.5 Final accumulated foulant concentration $c_{\mathrm{acm}}(t_{\mathrm{final}})$ vs initial void volume Vol_0 (loglog scales). (a) Isolated network setup; (b) periodic setup. Distribution of error for each data point is given in the histograms in the supplement.

initial total edge length, networks with larger d have fewer edges to which foulants can adhere. Combining this finding with the result in Figure 3.3 for a fixed volume further confirms the intuition that networks producing larger throughput (larger d) also have worse foulant control. A second trait shared by both network setups is that for larger d (for example $d = 0.4, 0.45$), $c_{\mathrm{acm}}\,(t_{\mathrm{final}})$ is relatively insensitive to changes in Vol_0, while for smaller d (say $d = 0.1, 0.15$), the change in $c_{\mathrm{acm}}\,(t_{\mathrm{final}})$ with Vol_0 is much more dramatic. This says that in membrane networks with longer pores, final accumulated foulant concentration depends less on initial void volume than in networks with shorter pores. We further observe that for a given Vol_0, for small d, the values of $c_{\mathrm{acm}}\,(t_{\mathrm{final}})$ are similar for both isolated and periodic configurations. However, as d increases, the isolated case incurs larger $c_{\mathrm{acm}}\,(t_{\mathrm{final}})$ and thereby exhibits worse foulant control than the periodic case. We defer further discussion of this observation to Section 3.6.3 below. Lastly, we find that in practice, when a tolerance level of contaminant concentration in the filtrate is specified in Figure 3.5, networks with smaller d values have larger initial pore volume, which corresponds to larger total throughput via the strong relationship observed in Figure 3.3 (e.g. if a threshold of

$c_{\text{acm}}(t_{\text{final}}) = 0.06$ is set, filters with $d = 0.1$ are preferable as they have larger initial pore volume and thus larger total throughput).

3.6.3 Tortuosity

We now examine the dependence of our performance metrics on initial network tortuosity τ, the average distance travelled by a fluid particle from the top membrane surface to the bottom, before any fouling has occurred. A full characterization of τ is given by Definition 9 and Equation (B.9) in the appendix.

Our main result is that tortuosity is an important universal parameter that predicts accumulated foulant concentration independently of input parameters (d, N_{total}). Figures 3.6a and 3.6b plot accumulated foulant concentration in the filtrate, $c_{\text{acm}}(t_{\text{final}})$, vs tortuosity, τ, for various values of the search radius d. We readily observe the similar collapse of data points in both cases, particularly strongly in the isolated case. We find that $c_{\text{acm}}(t_{\text{final}})$ decays exponentially with τ, with a negative exponent, which implies that networks with more winding flow-paths make much better filters in terms of foulant control. This is because the extent of deposition (per Equation (3.18)) increases as distance travelled by the fluid increases. We also observe two further details: within the regime where the fit (solid black line) is strongest in the plots, the data for the isolated setup (Figure 3.6a) has a larger (negative) slope than that in the periodic setup (Figure 3.6b); and, for fixed τ, filters in the periodic setup have slightly higher accumulated foulant concentration.

Figures 3.6c and 3.6d show zoomed plots of the data from Figures 3.6a and 3.6b respectively, to probe the details of the low tortuosity regime, where accumulated foulant concentration is highest. To facilitate the discussion below, note that for each d, a larger value of N_{total} corresponds to a smaller tortuosity τ (*i.e.*, adding more vertices to the network decreases average path length). Figure 3.6d shows that for the periodic pore network we see an emergent nonlinear trend, breaking the exponential

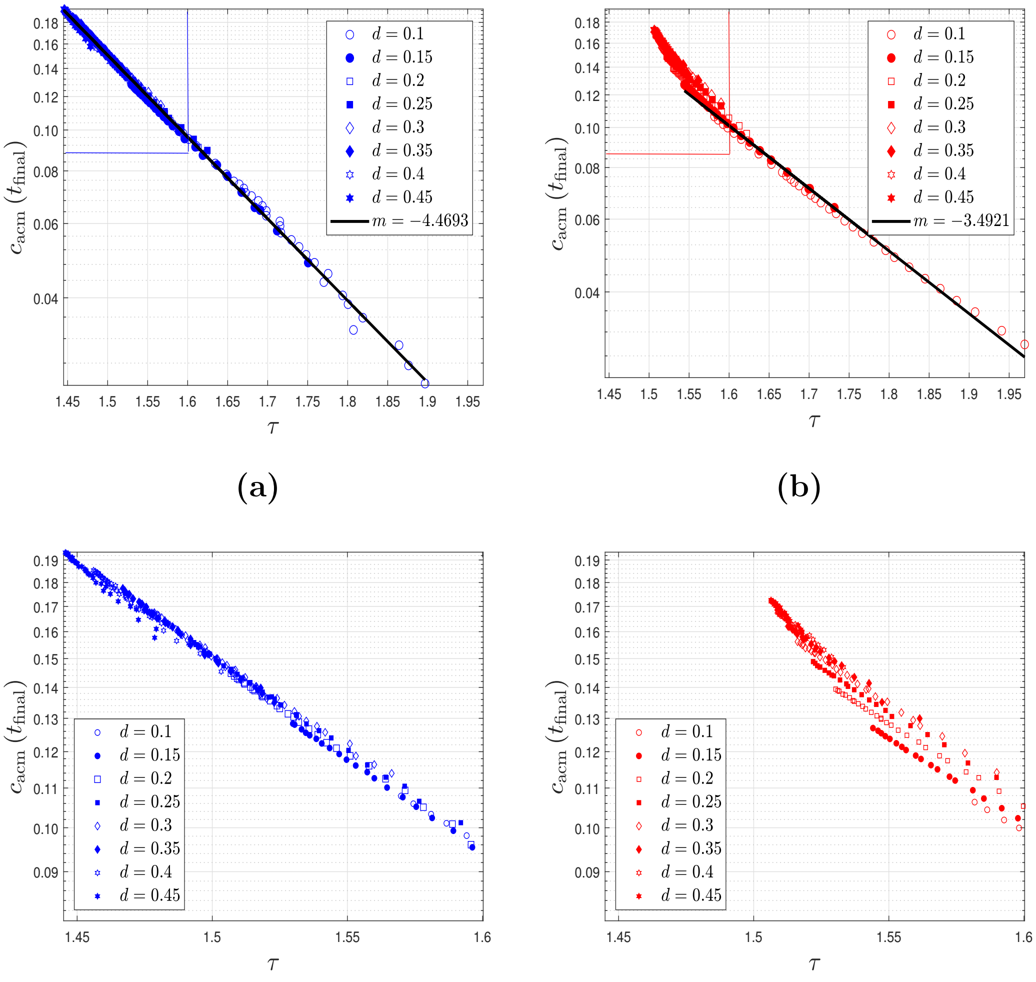

(a) **(b)**

(c) **(d)**

Figure 3.6 Final accumulated foulant concentration $c_{\text{acm}}(t_{\text{final}})$ vs tortuosity τ (semilog plot). (a) Isolated network setup; (b) periodic setup. The line of best fit is in black in each plot, with gradient m given in the legend (with $R^2 = 0.99838$ and 0.9961, respectively). The blue and red boxes at top left are shown as zooms in (c) and (d), respectively, for small tortuosity values (same data as (a) and (b), respectively). Distribution of error for each data point is given in the histograms in the supplement.

relation between $c_{\text{acm}}(t_{\text{final}})$ and τ as N_{total} is increased. Although the isolated setup in Figure 3.6c appears to persist in its linear (exponential relationship) trend, we note that for yet larger values of N_{total} this trend must break down due to the existence of a lower bound, τ_{min}, on tortuosity. While there is a trivial lower bound, $\tau_{\text{min}} \geq 1$ for each setup, in Appendix B.2 we show that bounds can be tightened to approximately

1.128 for the isolated setup and 1.304 for the periodic one. The bound is larger for the periodic case because, for a fixed set of vertices, the additional paths obtained from the periodic setup are on average longer, as they can penetrate through the boundaries; see Appendix B.2. Our simulations cannot access the breakdown in the power-law for the isolated case because, for the large values of N_{total} required to access this regime, we increasingly often violate the volume constraint for individual realizations of the random network.

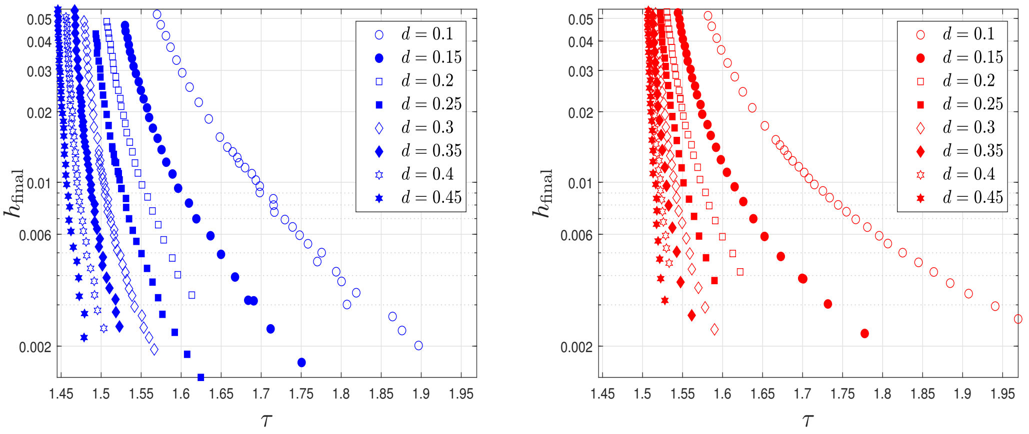

(a) **(b)**

Figure 3.7 Total throughput h_{final} vs tortuosity τ (semilog plot). (a) Isolated setup; (b) periodic setup. Error distribution for each data point is provided in the supplement. Same scale for h_{final} as in Figure 3.3.

Figure 3.7 shows total throughput h_{final} vs tortuosity τ for various d values, on a semilog scale. We note that h_{final} decreases as τ increases for each d because, if feed solution traverses longer paths (on average) through the filter, then it deposits more foulant and thus pores close faster. Second, for fixed h_{final}, larger d corresponds to smaller τ. Combining this finding with the results in Figure 3.6, we reach the following conclusion: between two membrane networks that produce the same total throughput, the one with shorter characteristic pore length (smaller d) is favoured since it also has larger tortuosity and thus better foulant control. Lastly, in both Figure 3.7a and Figure 3.7b, we see again the clear evidence of a limiting tortuosity

$\tau_{\min} > 1$: in the data curves for each $d \geq 0.35$, τ does not vary greatly as we vary N_{total}.

Now, we highlight the differences in Figure 3.7: first, for a fixed tortuosity τ (at a given d value), h_{final} in the isolated setup (Figure 3.7a) is lower than in the periodic one (Figure 3.7b), because the periodic boundary conditions give rise to more edges and hence a larger initial void volume Vol_0. We confirm this reasoning by plotting Vol_0 against τ in Figure 3.8. There, when we fix τ for each value of d, we observe a higher initial volume for the periodic case than the isolated one. This observation also explains why accumulated foulant concentration is higher in the periodic case for a fixed τ (per Figure 3.6) because networks with periodic boundary conditions, by having larger initial volume, process more filtrate (larger throughput) which leads to a greater quantity of foulant escaping the filter. This reasoning also explains the difference between $c_{\text{acm}}(t_{\text{final}})$ in Figures 3.5a and 3.5b by fixing Vol_0 for each d.

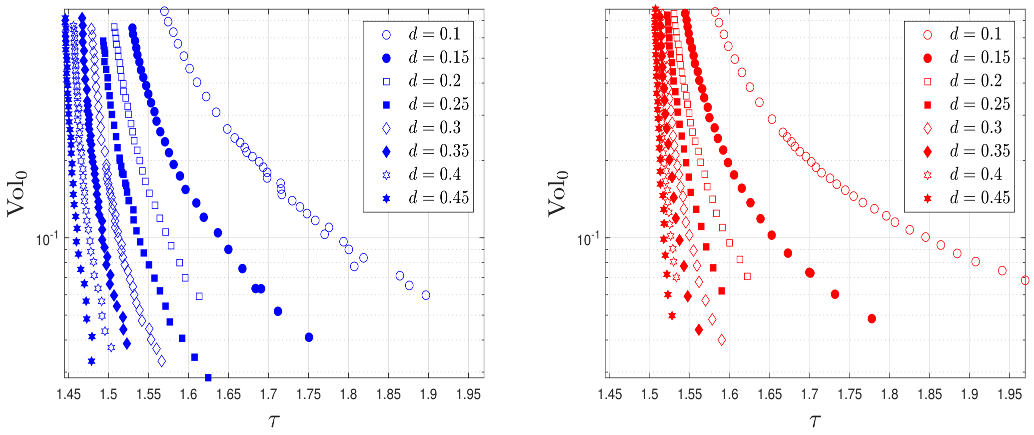

(a) **(b)**

Figure 3.8 Initial void volume vs tortuosity (semilog plot). (a) Isolated setup; (b) periodic setup. Error distribution for each data point is provided in the supplement.

3.7 Ending Remarks

We here summarize our findings on the connections between performance metrics of the network/filter and each characteristic geometric network parameter, and highlight areas for future work. We first collect our main findings:

1. Initial void volume Vol_0 is a good predictor of total throughput h_{final}, particularly when $\mathrm{Vol}_0 > 0.5$, when there appears to be a power-law relation between the two quantities (per Figure 3.3). Average number of neighbors N is also correlated with h_{final}, but is a weaker predictor in this respect than Vol_0 (per Figure 3.4).

2. Tortuosity τ fully characterizes final accumulated foulant concentration $c_{\mathrm{acm}}\left(t_{\mathrm{final}}\right)$ in the filtrate by a negative exponential relationship. See Figure 3.6.

3. When a minimum concentration requirement is imposed, membrane filters with small characteristic pore length should be considered since they have larger void volume and thus process more filtrate. See Figure 3.5.

4. When two membrane networks produce the same final throughput h_{final}, the one with shorter characteristic pore length should be favored, since it will have higher tortuosity and thus better foulant control. See Figure 3.8.

Griffiths *et al.* [47] showed that the particle removal efficiency, corresponding equivalently to $1 - c_{\mathrm{acm}}\left(t_{\mathrm{final}}\right)$ in our setup, increases as tortuosity increases, a trend consistent with our conclusion here regarding the negative exponential relationship between accumulated foulant concentration and tortuosity, though the exact relationship in both approaches is different (negative sub-exponential in that work [47]). Such differences may originate from the different graph generation protocols used in the two works.

We also find that the choice of network connection metric (isolated versus periodic) may significantly affect how the network functions as a filter. With identical input parameters N_{total} (representing the number of initial random points generated) and d (the search radius, or maximum edge length), the periodic setup yields larger average number of neighbors and thus higher connectivity. This is important, since the periodic setup provides a more realistic representation of a (large) membrane.

In recent years, many modern imaging techniques to study material properties have been developed which, in turn, provide fertile ground for graphical modeling approaches to membrane filtration and analysis of membrane performance. For example, Martinez *et al.* [66] have outlined a topological algorithm (Figure 1 in their paper) that translates a two-dimensional image of a membrane cross-section into a pore network. The idea is to take an original binary image where black and white represent membrane void and materials (respectively), and then construct a distance-to-nearest-object function (the DNO function) that computes the distance between a pixel to its nearest object (membrane material). Then, the location of pore junctions is determined by the local maxima of the DNO function, while the width of the edges connecting the junctions have widths determined by the minimal distance normal to the edge. For other techniques, see Sun *et al.* [121] and Sundaramoorthi *et al.* [123].

In future work, as well as utilizing some of the image analysis methods outlined above to generate more realistic networks, we plan to consider network models of membrane filters that include pore size variations, providing a more accurate representation of real membrane filters, due to inevitable manufacturing defects/inhomogeneities. We plan also to incorporate other fouling modes, such as blocking or sieving by large particles that may occlude pores, unaccounted for in this work. Including such large-particle blocking will add new dimensions of stochastic complexity to our modeling. In particular, a model that includes both extensions listed above may exhibit internal blockage at an earlier stage than the closure of top inlets (as always observed in our work here) when pore-size variations are sufficiently large, leading to much more complex flow and fouling behaviour. Our graphical description of the problem will allow us to investigate problems of this type in a systematic and computationally-efficient manner.

CHAPTER 4

NETWORK-BASED MEMBRANE FILTERS: INFLUENCE OF NETWORK AND PORE SIZE VARIABILITY ON FILTRATION PERFORMANCE

4.1 Overview

In this chapter, we model porous membrane filters as networks of connected cylindrical pores via a random network generation protocol, and their initial pore radii via a uniform distribution of widths that vary about some mean value. We investigate the influence of network and pore size (radius) variations on the performance of membrane filters that undergo adsorptive fouling. We find that membrane porosity variations, independently of whether induced by variations of the pore radii or of the random pore network, are an important factor determining membrane filter performance. Network and pore size variations still play a role, in particular if pore radii variations are significant. To quantify the influence of these variations, we compare the performance metrics of networks built from pores of variable radii to their (equal porosity) counterparts built from pores of uniform radius. We show that the effect of pore radii variations is to increase throughput, but also to reduce foulant control.

4.2 Introduction

Membrane filtration is an important separation process used in many industrial and commercial applications such as treatment of radioactive sludge, water purification, beer clarification [78], semiconductor and microelectronics processing [59], air filtration [80] and membrane bioreactors [35]. Membrane filters used in these applications have a wide range of architectures, ranging from single layer thin porous films to multilayered porous membranes [21, 93] to large scale continuous sheets of layered fibrous material [95, 1, 10].

Many models to describe the underlying membrane pore structure and/or geometry have been proposed and studied in recent years. For example, there are simple theoretical models to analyze the performance of membranes composed of multiple layers of different porous materials [39, 93], or membranes with simple branched structures that can incorporate porosity gradients ([111, 99], among many others). As recent advances in imaging techniques have greatly contributed to the ability to compare such structural models to experiments ([66, 121, 15, 123]; also see [14] for detailed images), more sophisticated models of membrane architecture have also been formulated, with a recent focus on accurate modeling of membrane filters with a network-type structure, for example, membranes where the solid component is comprised of fibres (so-called node-fibril type membranes) or those that transport feed through networks of capillaries [74, 47, 48] (also used in the context of condensate banking [106]).

The present work focuses on the latter type of pore network model that captures the sponge-like structure of the membrane selective layer [125, 126, 140]. Our analysis of pore size variations builds on a model introduced previously in [48]. Briefly, a network model involves vertices and edges that represent pore junctions and throats, respectively (referred to simply as *junctions* and *pores* from hereon, respectively). Each pore is assumed to be a circular cylinder of fixed radius, with Hagen-Poiseuille flow, and conservation of fluid flux is imposed at each junction. Foulant is advected through pores by fluid and deposits on pore walls via adsorptive fouling. Membrane filter performance is analyzed by recording total throughput (volume of filtrate collected during the lifetime of the filter) and accumulated foulant concentration at the membrane outlet.

The primary findings of [48] that motivate the present work are the following relationships. Firstly, the initial porosity (pore void volume divided by total domain volume) of the network is demonstrated to be an important material feature that predicts total throughput by a power law, which holds particularly well when initial porosity > 0.5. Secondly, it was found that the accumulated foulant concentration at the membrane outlet decays exponentially with the initial tortuosity of the network (defined as the average distance travelled by a fluid particle from membrane inlet to outlet, see Appendix C.4 for a detailed definition).

In addition to the features discussed above, pore size (radius) variation is another important aspect of membrane filter design, which has been investigated by a number of authors, in particular regarding how it affects membrane selectivity and particle retention in a variety of applications [89, 109, 67, 81, 127]. It has not, however, been extensively studied in the context of network models for membrane filters: though such models allow for cylindrical pores with a distribution of lengths [47, 48], random variations of the pore radii have not, to our knowledge, been considered. Accordingly, in this work, we focus on membrane filters whose pores may be considered as a network of interconnected capillaries of different initial radii. Henceforth in this work, the phrase "pore size variations" refers to variations in the initial pore radii, unless otherwise specified.

We present a novel characterisation of the membrane pore network and model pore size variations via a set of random initial conditions for the radii of pores. Our assumption on the pore size distribution, in contrast to the log-normal distribution usually assumed in applications [148], has the advantage of avoiding extreme values and offering easier control over the variance, while still providing a reasonable description of effects such as inhomogeneities during the manufacturing process. Other pore size distributions (including the log-normal) tend to have input parameters that affect both the mean and variance simultaneously; furthermore, distributions that can potentially yield very large pore radius values would require more complicated fluid flow models than considered in this work.

We use our network representation to investigate the effect of pore size variations on the performance of membrane pore networks, as characterized by foulant concentration and total throughput of filtrate over the filter lifetime. We expect our results to improve our understanding of particle retention inside membrane pore networks and of how the rate of membrane fouling depends on input parameters. We note that other authors have taken complementary approaches to such issues; for example, see [139] for numerical comparisons of a number of pore size distributions, [108] for a study of the influence of pore size distribution on rheology in two-phase porous media flow, [77] for experimental discussions, and [26] for a discussion of related considerations in tissue engineering.

The paper is structured as follows: in Section 4.3, we describe the network model setup and introduce the key performance metrics. In Section 4.4, we set out our investigation strategy for pore size variation in an algorithm and declare the main nomenclature used in the analysis. In Section 4.5, we present and discuss our main results and in Section 4.6, we conclude our findings.

4.3 Setup: General Pore Networks

In this section we construct our model of a membrane filter represented by a random network of connected cylindrical pores. In Section 4.3.1, we describe how we generate a network that represents the internal pore structure of a membrane filter; in Sections 4.3.2 and 4.3.3, we outline the governing equations for the Hagen-Poiseuille fluid flow, for the advection of foulant particles carried by the flow, and for the pore evolution in time; in Section 4.3.4 we specify our notation; in Section 4.3.5, we provide the relevant physical scales; and in Section 4.3.6, we introduce two metrics to characterize the performance of a membrane filter with a specified pore network.

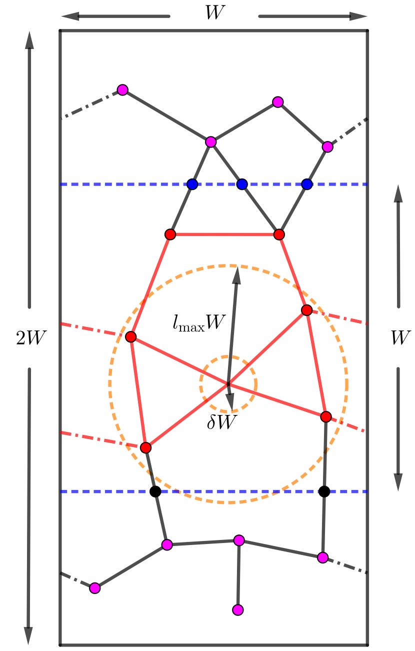

Figure 4.1 2D schematic of the 3D network generation with periodic boundary conditions showing: interior junctions $\mathcal{V}_{\text{int}}$ (red filled circles); pore inlets $\mathcal{V}_{\text{in}}$ (blue filled circles) and outlets $\mathcal{V}_{\text{out}}$ (black circles) induced by the cutting process; the cutting planes blue dashed lines; discarded points (magenta filled circles). Solid lines represent pores, while dash-dotted lines are pores that arise from the periodic boundary condition (red are interior to the membrane). $l_{\max}W$ and δW are prescribed maximum and minimum pore lengths, respectively.

4.3.1 Network Generation

We first demonstrate the 3D random network generation protocol employed in this work (following [48]). In Figure 4.1, for illustration purposes, we show a 2D schematic of this protocol: the domain is a rectangular cell (square prism in 3D) of lateral height two times its horizontal width W, assumed to repeat periodically at the lateral boundaries (more details in Appendix C.1). We generate a pore network by first uniformly distributing N_{total} (a large integer to be prescribed) points as the *junctions* (nodes of the network) inside the domain. We construct *pores* (the *edges* of the network) by connecting all pairs of points that lie within a prescribed maximal distance $l_{\max}W$, but at least some minimal distance δW apart. We then cut the prism horizontally at two locations (see blue dotted lines in Figure 4.1), and discard the end pieces to produce a square (or cube in 3D), which will represent an element of a membrane filter. The intersections of the two cutting planes and the pores (edges) naturally form membrane inlets and outlets, respectively (see Figure 4.2 for a 3D realization, with lengths scaled by W).

4.3.2 Fluid Flow

We next characterize fluid flow in the membrane network. The flow through the pores (which, within the current model, are cylinders of circular cross section) is assumed to obey the Hagen-Poiseuille model, valid provided the pores have sufficiently small aspect ratio (ensured in practice by choice of δ). The Hagen-Poiseuille equation states that fluid flux Q is proportional to pressure difference ΔP along each pore,

$$Q = K\Delta P, \quad K = \frac{\pi R^4}{8\mu L}, \tag{4.1}$$

where the conductance K depends on R and L, the radius and length respectively of the pore, and μ is fluid viscosity. To drive the flow, we prescribe the transmembrane pressure by setting the values on the top (P_0) and bottom (0) membrane surfaces,

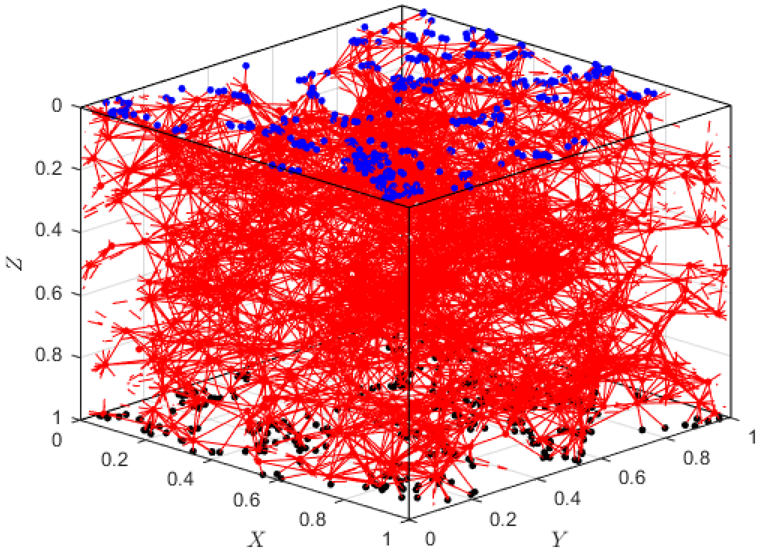

Figure 4.2 Schematic of a 3D network with $l_{\max} = 0.15$ and $N_{\text{total}} = 2000$. Solid red lines are interior pores; dashed red lines are pores created by the periodic boundary conditions. Blue dots are inlets. Black dots are outlets.

while the pressures at interior junctions are unknown. At each junction, we impose conservation of fluid flux, which leads to a system of equations (a discrete Laplace equation for these junction pressures, see Appendix C.2 for details). Once the pressures are found, flux through each throat is determined by Equation (4.1).

4.3.3 Advection and Adsorptive Fouling

Feed solution enters the membrane top surface with a fixed foulant concentration (simply referred to as *concentration* from hereon), which serves as a boundary condition. Foulant particles are advected by the fluid while depositing on the pore walls, causing pores to shrink and eventually close up, a process known as adsorptive fouling. For each pore, let $C(Y, T)$ be the particle concentration at any point Y of the pore at time T, where Y is a local coordinate measuring distance along a pore in the direction of fluid flow. The concentration is assumed to satisfy the steady state advection equation (see [48] and references therein)

$$Q\frac{\partial C}{\partial Y} = -\Lambda RC, \quad 0 \leq Y \leq L, \tag{4.2}$$

$$C\left(0,T\right) := C_{\text{up}}\left(T\right). \tag{4.3}$$

Here, the right hand side of Equation (4.2) is a sink of concentration that models foulant particles depositing on pore walls as they traverse the edge, with Λ (units of velocity) a parameter that captures the affinity between foulant particles and the membrane material. In reality Λ could change during filtration due to different affinities between the particles and the clean membrane, and the particles and the fouled membrane, the latter being more akin to particle-particle interactions; for simplicity, however, we assume Λ is a constant. In Equation (4.3) $C_{\text{up}}\left(T\right)$ is the concentration at the upstream entrance of a pore. For pores connected to the membrane top surface (at inlets), we prescribe a constant concentration $C_{\text{up}}\left(T\right) = C_{\text{top}}$ as the upstream boundary condition, representing the concentration in the feed solution. The foulant concentrations at interior junctions are solved for using conservation of foulant particle flux QC; that is, the total combined incoming particle flux from upstream pores must be equal to that entering downstream pores. Similar to the fluid flux conservation, this law can be expressed by a system of equations that accounts for the network connectivity (see Appendix C.2 and [48]).

Lastly, as foulant particles deposit on the pore wall, pore radius decreases at a rate depending on local upstream concentration $C_{\text{up}}\left(T\right)$,

$$\frac{dR}{dT} = -\Lambda\alpha C_{\text{up}}\left(T\right), \quad R\left(0\right) = R_0, \tag{4.4}$$

where α is a parameter related to particle volume (see the appendix of [48] for details). The filter lifetime T_{final} is reached when the outgoing flux at the membrane's downstream surface falls to zero.

Equation (4.4) implicitly assumes that the radius of each pore is a function only of time T and is independent of the local coordinate Y during its evolution, which is determined only by the upstream particle concentration. A more accurate model would be $\partial R(Y,T)/\partial T = -\Lambda\alpha C(Y,T)$; however, the simplification represented by Equation (4.4) yields only minor differences in model outcome, while providing significant computational benefit since it permits analytical solution of Equation (4.2), leading to immense computational speed-up (more than 100 times faster than the alternative). See [48] for further discussion, including a sufficient condition for this simplification to be reasonably valid. In particular, we have verified that the more accurate model leads to only a modest increase (at most 10%) in total throughput. The difference in accumulated foulant concentration is smaller still, and differences in the models' predictions of both performance measures are particularly insignificant when $l_{\max}$ (the ratio of the maximum pore length to the membrane thickness) is small. The computational savings afforded by this simplification facilitate the large number of simulations carried out in Section 4.4, needed to obtain reliable statistics.

4.3.4 Network Notations

In Sections 4.3.2 and 4.3.3, we introduced fluid flow and adsorptive fouling in each individual pore and described the conservation laws that govern the physical quantities of interest in a pore network. Since describing the dynamics of such quantities requires coupling of all junctions and pores, we introduce the following indexing scheme. We use a single index $(\cdot)_i$ to indicate junction dependence only, *e.g.*, pressure P_i at junction i. We use a double index $(\cdot)_{ij}$ to indicate dependence on the pore connecting junctions i and j. We do not distinguish between ij and ji for scalar quantities such as conductance K_{ij}; however, we do for quantities with a notion of direction, *e.g.*, Q_{ij} as fluid flux from pore i to pore j. We summarize all physical quantities in Table 4.1.

Table 4.1 Key Dimensional Quantities

Dimensional Quantity at time T	Symbol
Length of pore ij	L_{ij}
Radius of pore ij	$R_{ij}(T)$
Membrane unit length	W
Maximum pore length	$l_{\max}W$
Minimum pore length	δW
Pressure at junction i	$P_i(T)$
Concentration at junction i	$C_i(T)$
Flux in pore ij	$Q_{ij}(T)$
Deposition Coefficient	Λ

4.3.5 Scales

We nondimensionalize the fluid flow and foulant transport model described in the previous sections as follows:

$$\begin{gathered} L_{ij} = W l_{ij}, \quad \left(R_{ij}, R_{ij,0}\right) = W\left(r_{ij}, r_{ij,0}\right), \\ P_i = P_0 p_i, \quad \left(C_i, C_{ij}\right) = C_{\text{top}}\left(c_i, c_{ij}\right), \\ \Lambda = \frac{\pi W P_0}{8\mu}\lambda, \quad T = \frac{W}{\Lambda \alpha C_{\text{top}}} t, \end{gathered} \tag{4.5}$$

where the upper case symbols are dimensional quantities (listed in Table 4.1). Parameter values are listed in Table 4.2. We comment briefly regarding the parameter λ: its main influence is in determining the time scale on which fouling occurs in the problem, and how deep within the pore network fouling particles penetrate. The numerical value of λ is expected to be small; such values promote more efficient use of the filter by allowing particles to permeate deeper into the membrane interior (larger λ values lead to a majority of fouling occurring very close to the membrane

Table 4.2 Key Dimensionless Parameters

Parameter	Symbol	Values
Initial number of junctions	N_{total}	$500, 775$
Maximum pore length	$l_{\max}$	0.3
Minimum pore length	δ	0.06
Unperturbed pore radius	r_0	0.01
Noise Amplitude	β	$0.06, 0.25, 0.5, 0.7$
Number of networks	N_{net}	1000
Number of noise realizations	N_{noise}	500
Deposition coefficient	λ	5×10^{-7}

top surface). Our choice of the specific value, while somewhat arbitrary, satisfies this requirement. Further work, beyond the scope of this paper, would be needed to explore how the exact value assigned to this quantity influences the statistics of membrane performance metrics. We have confirmed numerically that moderate variations in λ do not change the trends that we describe in this work.

4.3.6 Performance Metrics

We evaluate the performance of a membrane network using the following two metrics: 1) total throughput (h) and 2) accumulated foulant concentration at membrane outlet (c). Total throughput is the total volume of filtrate collected at the membrane outlet over the lifetime of the membrane network filter (at time t_{final}, when the flux through the membrane falls to zero). Accumulated foulant concentration measures the aggregate concentration of foulant particles in the collected filtrate when the filter is exhausted. Precise definitions of these quantities are given in Appendix C.3.

4.4 Investigation Methods

We study pore size variations by prescribing a random initial condition for each pore radius, $r_{ij,0}$. More precisely, we consider perturbations to uniform pores by imposing a multiplicative noise,

$$r_{ij,0} = r_0 \left(1 + \epsilon_{ij}\right), \tag{4.6}$$

where $\epsilon_{ij} \sim \mathrm{Unif}\left(-\beta, \beta\right)$ is a uniform random variable with noise amplitude $0 < \beta < 1$, independent for each pore. For the rest of this work, when we use the terms *perturbation* or *noise*, we are referring to Equation (4.6). This assumption on the distribution of pore size variations has the advantage that we can directly control the width of the distribution via the input parameter β, making the analysis and interpretation of the results simpler.

We will study selected simulation outputs, f, as model parameters vary, with a primary focus on the influence of noise amplitude, β. Specifically, in this work f will be one of the following:

- h, total throughput (throughput),
- c, accumulated foulant concentration at membrane outlet (concentration),
- ϕ, initial network porosity (porosity),
- τ, initial tortuosity (tortuosity),

where the abridged terms in parentheses are used freely henceforth (see detailed definitions of h, c and τ in Appendix C.3 and Appendix C.4). We note also that since the nondimensional model operates in the domain of a unit cube, initial void volume and membrane porosity are equal in value. We refer to *porosity* only hereon.

A principal aim of this work is to compare the influence of two independent sources of randomness, namely, the random network generation process (*network variability* henceforth), and the random initial condition for the pore radius that yields pore radius variations (*noise variability* henceforth), on statistics of membrane filter performance metrics. In other words, network variability stems from variations in node and edge locations in membrane networks, while noise variability is due to pore size variations. Here we describe the methodology of our study, before summarizing the approach as an algorithm with enumerated steps below.

First, we generate a large number, N_{net}, of random membrane networks (per Section 4.3.1), each with the same initial pore radius r_0. We perturb the pore networks via Equation (4.6) in the following two distinct ways: To probe noise variability, we fix one particular "typical" (to be made precise in what follows) network from the N_{net} that were generated, perturb it independently N_{noise} times (for N_{noise} sufficiently large), solve the governing Equations (4.1), (4.2) and (4.4) (coupled over the entire network using continuity as described) and collect statistics of performance metrics from these N_{noise} realizations of noise. To probe network variability, we perturb each of the N_{net} networks independently just once, and collect performance statistics from the perturbed networks.

Perturbing the pore radii inevitably changes the porosity of the network. This is important, since initial network porosity was shown to influence strongly both of our membrane performance metrics in the unperturbed case [48]. To investigate the importance of such induced porosity changes, we devise the following strategy. First, note that the initial porosity of a network is given by

$$\phi = \frac{\pi}{2} \sum_{ij} r_{ij,0}^2 l_{ij} \overset{\textit{Equation (4.6)}}{=} \frac{\pi}{2} r_0^2 \sum_{ij} \left(1 + 2\epsilon_{ij} + \epsilon_{ij}^2\right) l_{ij}, \tag{4.7}$$

where the last expression implies that perturbed networks have larger porosities on average, since ϵ_{ij}^2 is nonnegative (the factor of 1/2 is needed because the double sum counts every pore twice). Note that this increase of porosity for perturbed network is influenced by the choice (uniform) of pore size perturbation distribution; other distributions (not considered in this work) that have nonzero mean may influence the porosity differently. For each perturbed network, we obtain its porosity via Equation (4.7). We then impose this porosity on the underlying *unperturbed* network by determining a new initial pore radius such that the unperturbed and perturbed networks have the same porosity. This new unperturbed network is referred to as a *porosity-corrected* network, from which we also collect performance statistics. With these preparations, we define a ‘score’ as the difference between the outputs of the perturbed and porosity-corrected networks, normalized by the outputs of the porosity-corrected ones.

Each of the N_{net} membrane networks has a fixed maximum pore length $l_{\max} = 0.3$, minimum pore length $\delta = 0.06$ and initial unperturbed pore radius $r_0 = 0.01$. We vary two parameters: 1) noise amplitude β; and 2) total number of junctions N_{total}. The ensuing study first fixes an *average* porosity by fixing N_{total}, while varying β. All geometric parameters used in the algorithm are listed in Table 4.2, with their values.

We summarize the above procedures in the following algorithm:

1. (*Random network generation*) Choose N_{total}. Generate N_{net} unperturbed networks. Compute the initial porosity ϕ_0 for each network.

2. (*Noise perturbation*) Choose noise amplitude β.

   (a) (*noise variability*) Fix a typical network and perturb it N_{noise} times independently. Compute the outputs of the perturbed networks, f_{noise}, referred to as *output under noise realizations.* The typical network is chosen such that its porosity is the closest to the average porosity of the ensemble, a posteriori.

   (b) (*network variability*) Perturb each unperturbed network once independently via Equation (4.6). Compute the associated outputs f_{net}, referred to as *output under network realizations.*

3. (*Porosity correction*) For each perturbed network, consider its underlying *unperturbed* equal-porosity network (created by prescribing the appropriate uniform pore radius for its pores; see Appendix C.5 for a short derivation). This new network is called a *porosity-corrected* network, with output labeled f_{pc}.

4. (*Scores*) We construct two scores that characterize the noise and network variability when comparing networks of equal porosity. The two scores are constructed independently from each other, so there is no confusion between notations.

    (a) (*Noise score*) We compute the following score,

    $$\widehat{f}_{\text{noise}} = \frac{f_{\text{noise}} - f_{\text{pc}}}{f_{\text{pc}}}, \tag{4.8}$$

    where f_{noise} and f_{pc} are computed via Items 2a and 3, respectively. All quantities in Equation (4.8) are vectors of length N_{noise}. The subtraction and division are element-wise.

    (b) (*Network score*) Perform Item 2b to obtain the outputs under network realizations f_{net}. Compute the following score,

    $$\widehat{f}_{\text{net}} = \frac{f_{\text{net}} - f_{\text{pc}}}{f_{\text{pc}}}, \tag{4.9}$$

    where f_{pc} are computed via Item 3. All quantities in Equation (4.9) are vectors of length N_{net}. The subtraction and division are element-wise.

    In the following discussions, we refer to the quantities defined by Equation (4.8) or Equation (4.9) as *porosity-corrected* scores.

5. Obtain the means and standard deviations of model outputs, $\overline{f_{\text{noise}}}$ and $\overline{f_{\text{net}}}$, and scores, $\overline{\widehat{f}_{\text{noise}}}$ and $\overline{\widehat{f}_{\text{net}}}$. The means under noise and network realizations are computed by averaging over the number of noise (N_{noise}) and network (N_{net}) realizations, respectively.

6. Go back to Item 2 with a different β.

7. Go back to Item 1 with a different N_{total} (to vary initial porosity).

All outputs computed in this algorithm are summarized in Table 4.3.

4.5 Results and Discussions

In Section 4.5.1, we study the performance metrics under a specific choice of model parameters as an example. First, we compare the noise and network variability of the raw metrics (throughput and concentration) and geometric quantities (porosity

Table 4.3 Key Output Quantities

Output	Symbol
Porosity-corrected	f_{pc}
Noise realizations	f_{noise} $(\overline{f_{\text{noise}}}, \sigma_{f_{\text{noise}}})$
Network realizations	f_{net} $(\overline{f_{\text{net}}}, \sigma_{f_{\text{net}}})$
Noise score	$\widehat{f}_{\text{noise}}$ $(\overline{\widehat{f}_{\text{noise}}}, \sigma_{\widehat{f}_{\text{noise}}})$
Network score	$\widehat{f}_{\text{net}}$ $(\overline{\widehat{f}_{\text{net}}}, \sigma_{\widehat{f}_{\text{net}}})$

The quantities in parentheses are the mean and standard deviation of the corresponding output.

and tortuosity). Then, we compare the porosity-corrected scores under noise (per Equation (4.8)) and network (per Equation (4.9)) realizations (steps 4a and 4b in the algorithm, respectively). In Section 4.5.2, we reinforce the example by a thorough sweep of the parameter space and present our main results.

4.5.1 Detailed Example: Low Porosity Network in Low Noise Regime

In this section, we present a set of results for membrane pore networks in the regime of low noise amplitude perturbations to the pore radii and low initial porosity. We choose this parameter regime as a detailed example because the results at higher porosities are qualitatively similar but more time-consuming to compute. We generate N_{net} networks with an initial number of points N_{total}, which yield an *ensemble average* initial porosity $\phi \approx 0.25$ (averaged over N_{net} unperturbed networks). The noise ϵ_{ij} is realized N_{noise} times for each network, with fixed noise amplitude $\beta = 0.06$ here. We give values of $N_{\text{net}}, N_{\text{noise}}$ and N_{total} in Table 4.2 and have found that these numbers are sufficient to account for the random nature of the network and noise generation protocol; larger numbers produce similar results.

When we study noise variability (per Item 2a in the algorithm), we fix a typical network with initial porosity very close to the ensemble average, 0.25. We first compare the statistics of performance metrics (per Items 4a and 4b in the algorithm) and then discuss the similarities and differences in the network and noise scores calculated for the initial porosity and tortuosity of the networks, similarly averaged over many network and noise realizations. In particular, we focus on the two relationships found in [48] as example results: throughput vs. porosity, and concentration vs. tortuosity.

Throughput and Porosity

Figure 4.3 shows throughput versus porosity under (a) noise and (b) network realizations, respectively. Both figures show that, as expected, throughput is an increasing function of porosity because more porous filters process more filtrate. However, we note the different scales in the two figures: in Figure 4.3b we also plot a black rectangle that represents the total range of Figure 4.3a showing that, before we correct for induced porosity changes, network variations incur much more variation in total throughput than pore size variations in this noise/porosity regime. In other words, the variability induced by noise is significantly smaller than that induced by network variability.

As noted in Section 4.4 (per Equations (4.6) and (4.7)), and as evident from Figure 4.3, each pore size perturbation leads to a porosity variation. Since initial porosity is known to be a key parameter determining filter performance [48], we proceed by considering the *noise* and *network scores* that correct for induced porosity changes, formulated in Equations (4.8) and (4.9) in Item 4 of the algorithm in Section 4.4. Figure 4.4 presents histograms of throughput scores under noise and network realizations. We see that the two histograms are very similar. Comparing Figures 4.3 and 4.4, we deduce that the porosity change is the crucial factor (at least

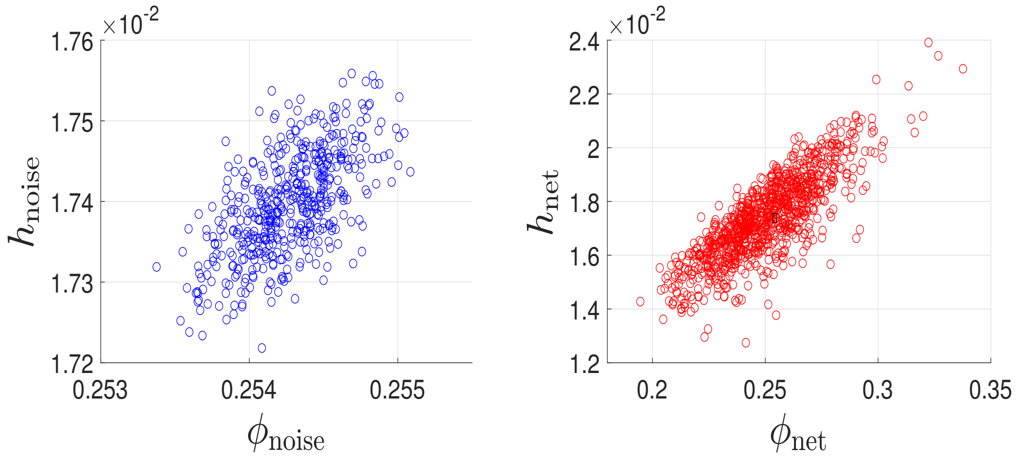

(a) **(b)**

Figure 4.3 Scatter plot of throughput versus porosity, under (a) noise realizations, (b) network realizations (with each network perturbed once). The black rectangle in (b) shows the horizontal and vertical range of (a). For both plots, $\beta = 0.06$.

for the present (ϕ, β) values) since Figure 4.4, in marked contrast to Figure 4.3, shows that variations of network and noise as measured by the scores have a very similar effect.

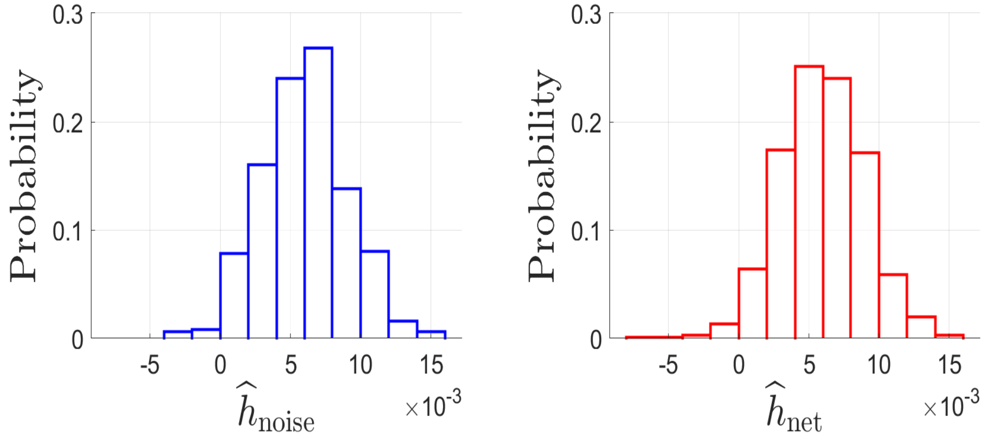

(a) **(b)**

Figure 4.4 Histogram of throughput score, under (a) noise realizations, (b) network realizations (with each network perturbed once).
Same parameters as in Figure 4.3.

Concentration and Tortuosity

We next investigate the influence of noise perturbation on the accumulated concentration of particle impurities in the filtrate (concentration) and the tortuosity of the pore network (see Appendix C.4 for a detailed definition), quantities that are strongly related in unperturbed pore networks [48].

Figure 4.5 shows concentration versus tortuosity under (a) noise and (b) network realizations. First, both figures show that concentration is a decreasing function of tortuosity. This makes sense because the longer foulant particles travel in the network, the more likely they are to adsorb to the pore walls, leading to lower concentration at the membrane outlet. Second, we point out that the black rectangle in Figure 4.5b covers the total range of Figure 4.5a, showing, once again, that before induced porosity changes are accounted for, network variability dominates over noise, for the present choice of parameters.

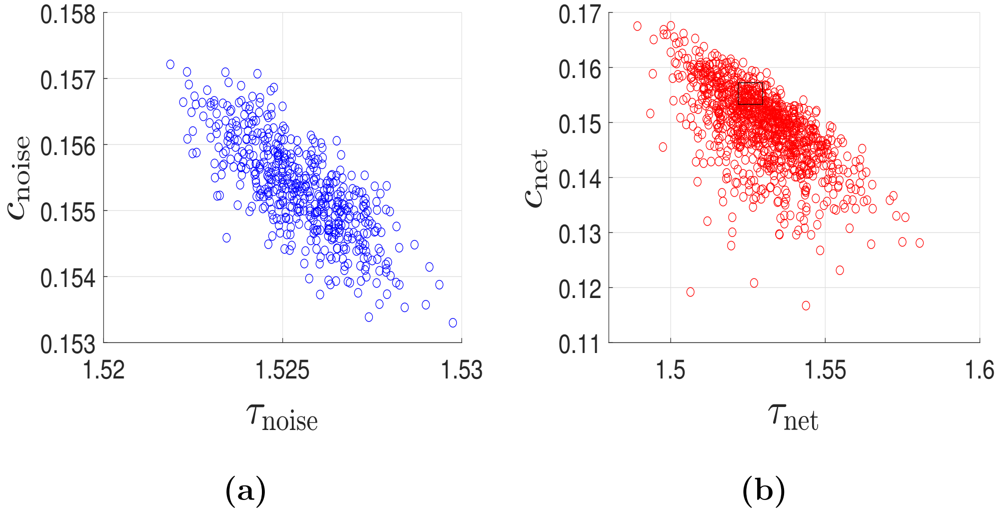

(a) **(b)**

Figure 4.5 Scatter plot of concentration versus tortuosity.
Same description and parameters as in Figure 4.3.

Figures 4.6a and 4.6b plot the data of Figure 4.5 as a histogram of tortuosity under noise and network realizations (respectively). Note the different horizontal ranges on the two plots (cf. Figure 4.5). Also, in Figure 4.6b, we see that the distribution of tortuosity shifts slightly to the right relative to the unperturbed case, possibly due to some subtle geometric influence from the random network generation, not yet understood.

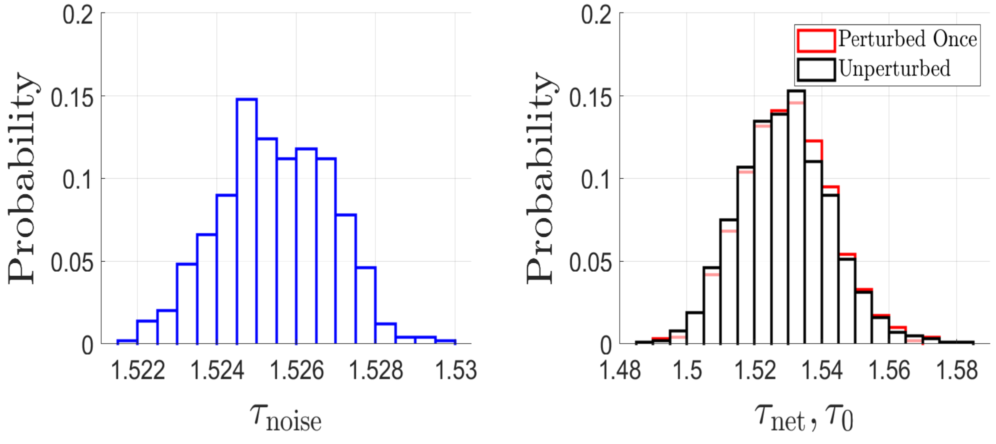

(a) (b)

Figure 4.6 Histogram of tortuosity under (a) noise realizations (b) network realizations.
Same parameters as in Figure 4.3; same data as Figure 4.5.

Section 4.5.1 shows histograms for the porosity-corrected concentration and tortuosity scores under noise (Figures 4.7a and 4.7c, generated using Equation (4.8)) and network (Figures 4.7b and 4.7d, generated using Equation (4.9)) realizations. The histograms of concentration scores in Figures 4.7a and 4.7b are very similar in shape and width, suggesting that, after we correct for porosity differences, perturbing one network many times is equivalent to perturbing many networks once.

4.5.2 Results for Varied Noise Amplitude and Porosity

We now explore the influence of noise amplitude, β, and of initial network porosity, ϕ. For brevity, we condense results for different initial porosity regimes in terms of the *average* outputs (see Item 5 of the algorithm) and their standard deviations (shown via error bars; see Table 4.3 for their notations) plotted as functions of β.

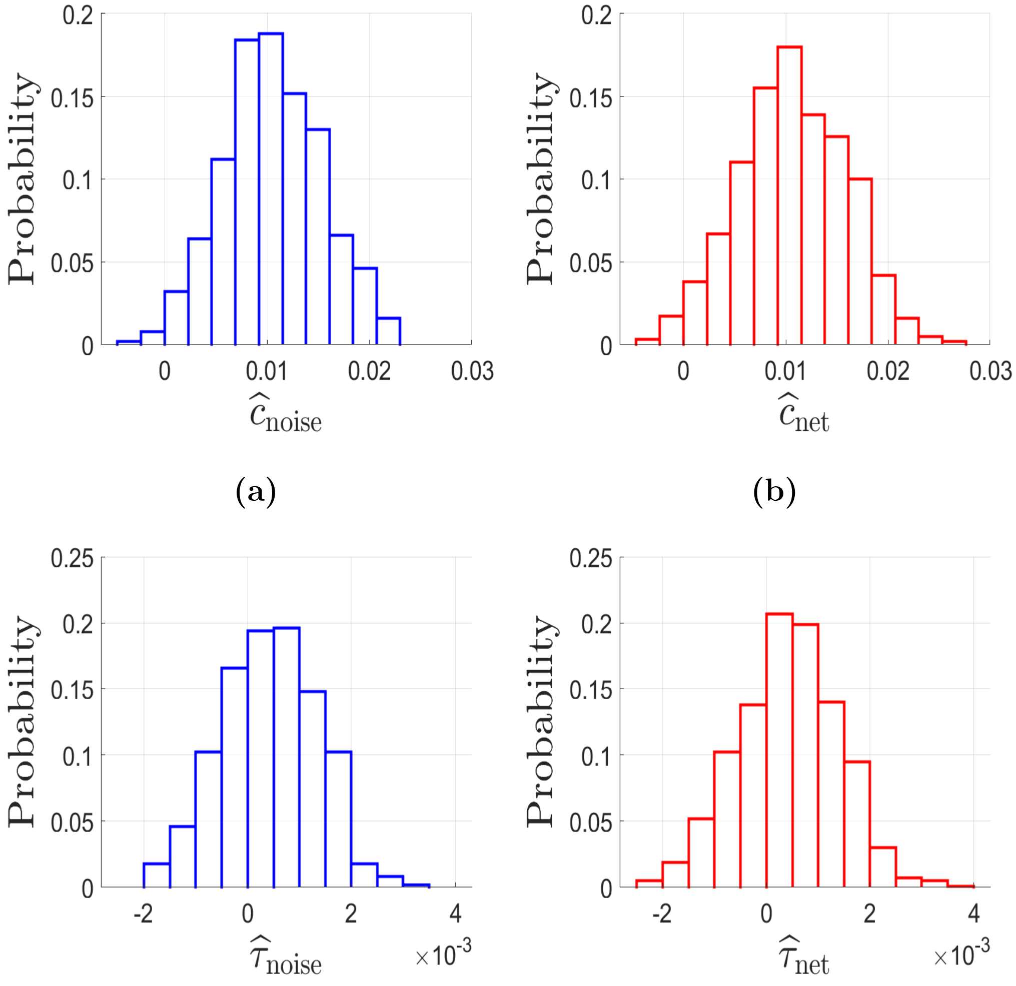

(a) **(b)**

(c) **(d)**

Figure 4.7 Histogram of concentration and tortuosity scores, respectively under (a,c) noise realizations and (b,d) network realizations.
Same parameters as in Figure 4.3.

Figures 4.8a and 4.8b plot the raw mean throughputs $\overline{h_{\text{noise}}}$ and $\overline{h_{\text{net}}}$ against noise amplitude β for low and high network porosity regimes, respectively. These raw mean throughputs are increasing functions of β, an observation that we attribute largely to the fact that an increase of β on average increases initial porosity, which then allows more filtrate to be processed. Figures 4.8c and 4.8d plot the mean throughput scores that correct for porosity changes, for filters of low and high porosity, respectively. We find that the mean throughput scores are also increasing functions of β; however,

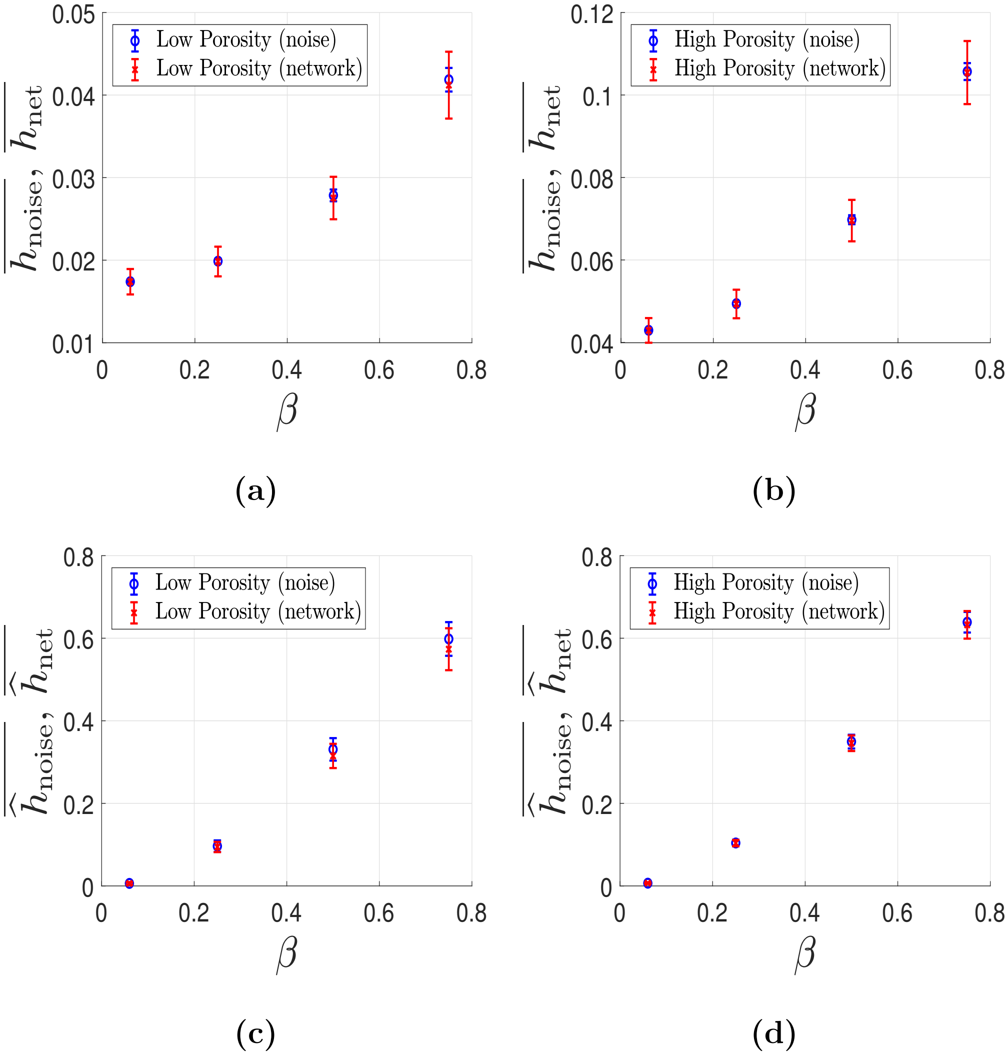

(a) **(b)**

(c) **(d)**

Figure 4.8 Mean throughput $\overline{h_{\text{noise}}}$, $\overline{h_{\text{net}}}$ (a,b) and mean throughput scores $\overline{\widehat{h}_{\text{noise}}}$, $\overline{\widehat{h}_{\text{net}}}$ (c,d) versus noise amplitude β under noise and network realizations. Low porosity $\phi \approx 0.25$ (a,c) and high porosity $\phi \approx 0.6$ (b,d) cases are shown. Vertical error bars are standard deviations for each mean value. Note that the scores (c,d) show relative change, so that, *e.g.*, an increase from 0 to 0.6 on the vertical axes means a 60% increase.

this increase (which is still significant, around 60% for $\beta = 0.75$ for both low and high porosity networks per Figures 4.8c and 4.8d) is due purely to the pore size variations. This implies that, for equal porosity networks, when the magnitude of the noise perturbation β is large enough, pore radius variations do lead to an appreciable change in total throughput. This further suggests that pore radius variations promote filtrate production, at least for the considered uniform pore size distribution.

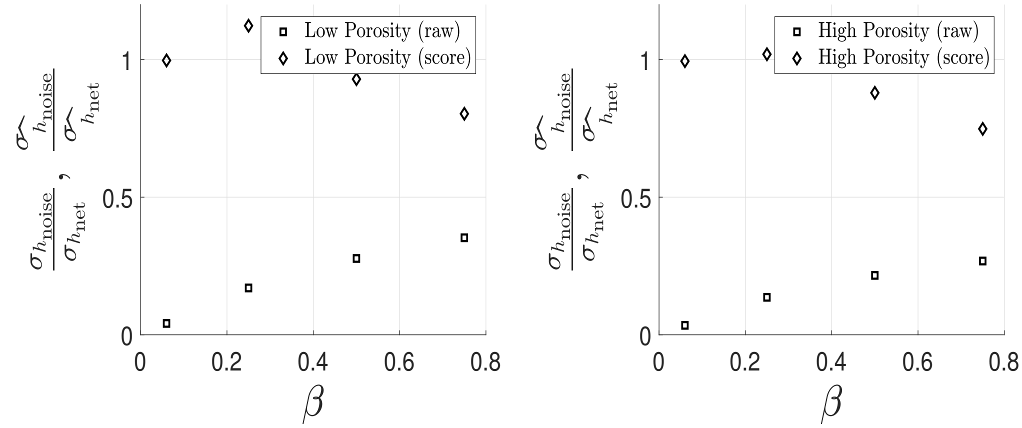

(a) **(b)**

Figure 4.9 Ratio of standard deviations of raw throughput (black squares) and throughput scores (black diamonds) for (a) Low porosity (corresp. Figures 4.8a and 4.8c) and (b) high porosity (corresp. Figures 4.8b and 4.8d).

We now study the variability of throughput and throughput scores induced by pore radius variations, represented by the error bars (standard deviation of each statistic) for all cases shown in Figure 4.8. To facilitate this comparison, we plot in Figure 4.9 the ratio of the standard deviations of the mean quantities under noise and network realisations (referred to simply as the s.d. ratio below) from Figure 4.8, for raw throughputs and their scores. A value of the s.d. ratio near 1 implies that the compared quantities have similar standard deviations, whereas a value near 0 says that variation induced by network realisations dominates that from noise. In both low and high porosity regimes (Figures 4.9a and 4.9b, respectively), we observe that the s.d. ratios for the raw throughput (black squares) are all below 0.5 for any value of noise amplitude β, thus the throughput variability from network realisations dominates that from noise. However, the s.d. ratios of the throughput scores (black diamonds) are close to 1 in both porosity regimes, for all β values considered. This finding shows that, when considering the total throughput metric, network porosity accounts for the differences between network and noise variability.

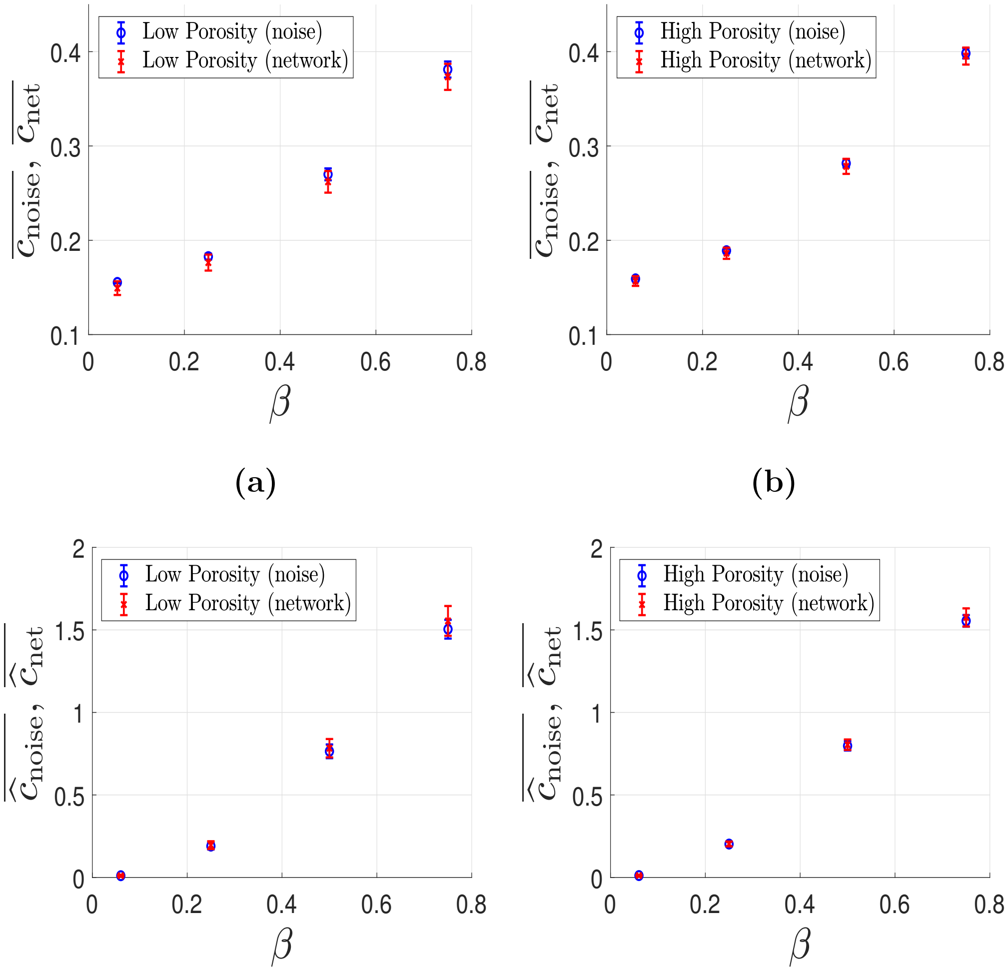

(a)

(b)

(c)

(d)

Figure 4.10 Mean concentration and concentration score.
Same setup as in Figure 4.8.

Figures 4.10a and 4.10b show mean concentrations $\overline{c_{\text{noise}}}$ and $\overline{c_{\text{net}}}$ of particles in the filtrate as a function of noise amplitude β for low and high porosity regimes. We observe that the mean raw concentrations in both cases are increasing functions of β. We attribute this increase largely to the increase of porosity with β, as evident in Equation (4.7), allowing more particles to pass through unfiltered and thus worsening foulant control. In contrast, Figures 4.10c and 4.10d plot the mean concentration scores $\overline{\widehat{c}_{\text{noise}}}$ and $\overline{\widehat{c}_{\text{net}}}$ (see Equations (4.8) and (4.9)), which correct for porosity changes: the increase with β seen here is a direct consequence of the pore size variations. For example, for $\beta = 0.75$, the perturbed networks show more than 150% increase in concentration when compared with porosity-corrected unperturbed counterparts. This implies that pore radius variations influence foulant concentration in the filtrate significantly for sufficiently large noise amplitude β, and in fact are detrimental for foulant control.

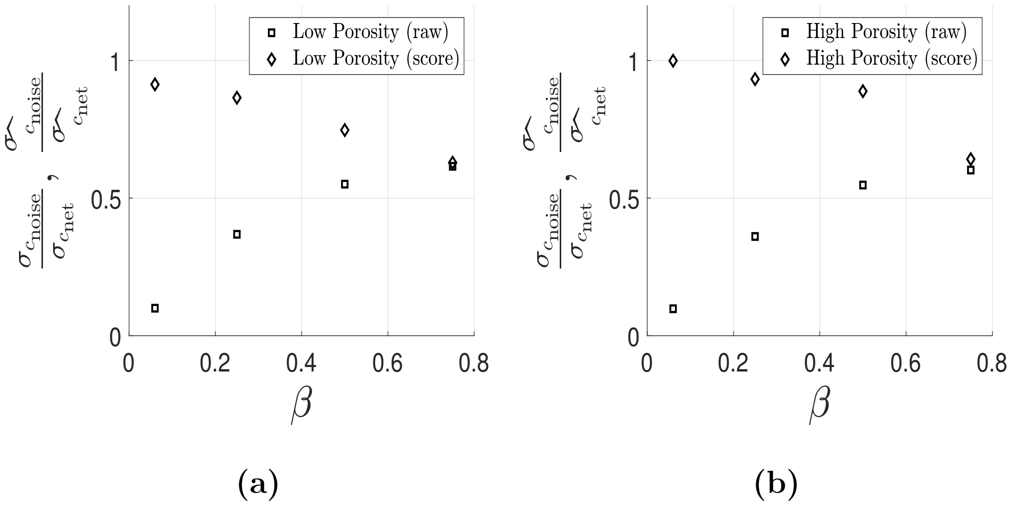

Figure 4.11 Same setup as Figure 4.9 for raw concentration and concentration scores. (a) Low porosity (corresp. Figures 4.10a and 4.10c) and (b) high porosity (corresp. Figures 4.10b and 4.10d).

Now, we discuss the observed variability of the raw mean concentration and concentration scores induced by pore size variations. Similar to the study of throughput variability, Figure 4.11 plots the ratios of standard deviations of the mean concentrations (raw values and scores) under noise and network realisations, found in Figure 4.10. The observed trends are similar to Figures 4.9a and 4.9b: before correcting for induced porosity changes, network variability dominates noise variability for all porosities and noise amplitudes tested, exemplified by the s.d. ratios for the raw concentrations (black squares). However, this dominance is weaker for particle concentration than for throughput: in Figure 4.11, the s.d. ratios for the raw concentrations are larger than those for the raw throughputs in Figure 4.9. This means that concentration, as a performance metric, experiences larger variations when pore radii are perturbed than does throughput. We further note that the s.d. ratio of concentration scores (black diamonds) is close to 1 for small β (underscoring the importance of porosity), but decreases as β increases. In other words, porosity changes due to network variations are solely responsible for concentration variability at small noise amplitudes, but not at high amplitudes.

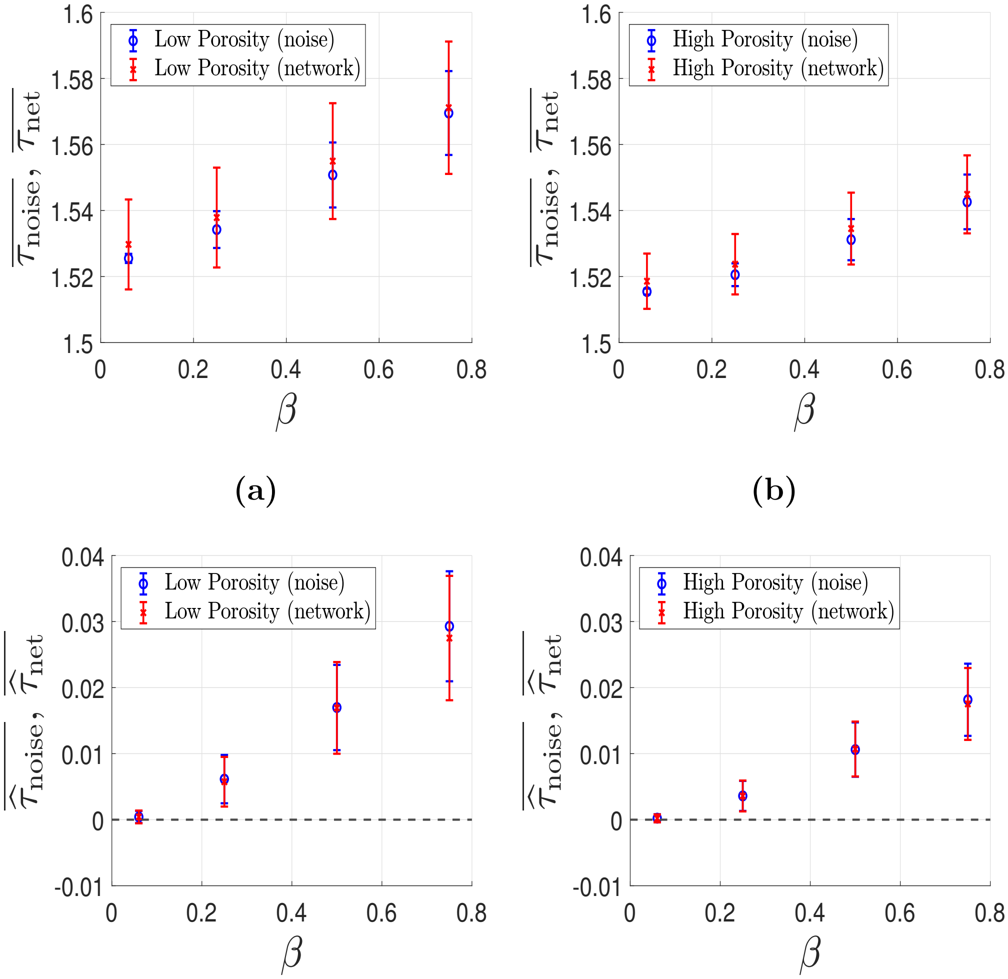

(a) (b)

(c) (d)

Figure 4.12 Mean tortuosity and tortuosity score. Same setup as in Figure 4.8.

As noted earlier, tortuosity (the average dimensionless path length of a fluid element as it passes through the pore network; see definition in Appendix C.4) is an important quantity determining membrane filter performance [48]. Figure 4.12 shows mean tortuosities $\overline{\tau_{\text{noise}}}$ and $\overline{\tau_{\text{net}}}$, and mean tortuosity scores $\overline{\widehat{\tau}_{\text{noise}}}$ and $\overline{\widehat{\tau}_{\text{net}}}$ as noise amplitude varies. We find that in both porosity regimes, network variability (red error bars) still dominates noise variability (blue error bars) if we do not correct for induced porosity variations. The dominance is less strong for higher noise amplitudes, however, where the error bar sizes become similar, indicating that sufficiently high noise amplitude induces similar variability in network tortuosity to that due to the network generation protocol. Figures 4.12c and 4.12d show the means of the tortuosity scores $\widehat{\tau}_{\text{noise}}$ and $\widehat{\tau}_{\text{net}}$; we observe that after correcting for porosity changes, noise and network variability are now very similar for all noise amplitudes considered, in both porosity regimes. This implies that, when porosity variations are accounted for, the effects of noise and network variability on tortuosity are comparable.

Furthermore, we observe that the mean tortuosity and tortuosity scores in Figure 4.12 are increasing functions of noise amplitude β in all cases, but the changes are modest compared to those in throughput seen in Figure 4.8 (see a further discussion in Appendix C.4 on how β affects τ). Overall, tortuosity variations do not exceed 4% for all parameters considered (note the vertical scales of Figures 4.12c and 4.12d). Based on this observation, we infer the relative influence of throughput and tortuosity scores on concentration scores. On the one hand, filters with larger throughput scores tend to allow more foulants to pass through and thus produce *higher* foulant concentrations in the filtrate. On the other hand, filters with larger tortuosity lead to *lower* concentrations [48]. Hence, as β increases, the increased mean throughput and tortuosity scores have opposite effects on mean concentration scores. The fact that we observe still an increased concentration score as β increases (per Figures 4.10c and 4.10d) implies that the effect of increasing throughput dominates that from increasing tortuosity. In other words, although pore size variations do increase pore network tortuosity (favorable for foulant control), this effect is apparently insufficient to lead to improved foulant removal when balanced against the tendency of the increased throughput to transport a greater proportion of foulant particles through the filter.

Before closing, we note in passing some perhaps unexpected features of the results. First, comparing Figures 4.12c and 4.12d, we observe that filters with higher porosity show a smaller increase in tortuosity with β. Second, we note that, according to Figures 4.12c and 4.12d for the smallest value of β used, some networks may have *smaller* tortuosity than their unperturbed counterparts, as shown by the first error bar crossing the zero line.

4.6 Ending Remarks

In this chapter, we have devised and implemented a network model for adsorptive fouling of a membrane filter whose pore structure is formed by randomly generating junctions and pores. Within this network representation, we have modelled pore size variations as random initial conditions (uniform multiplicative noise for the pore radii). We have studied these two sources of randomness – the random network generation protocol and pore radius variations – by comparing their effects on two key membrane filter performance metrics: total throughput and accumulated concentration of adsorptive foulants in the filtrate.

We report three principal findings. First, we find that the initial porosity of the pore network is a critical feature of the filter, and a strong determinant of performance. Secondly, we observe that the influence of pore radius variations on membrane performance becomes prominent when the noise amplitude is large. Lastly, we conclude that pore size (radius) variations are favorable for maximizing filtrate production, but unfavorable for foulant control.

To arrive at these conclusions, we first compare membrane network performances directly by varying noise amplitude. Then, to rule out the effect from variations in porosity, we formulate the corresponding porosity-corrected networks and study the relative change in performance metrics via a well-defined score.

We note that the reported findings were obtained by assuming a uniform distribution of pore radius variations, and furthermore we have not considered large-particle sieving. Considering sieving in addition to adsorptive fouling and exploring the influence of other pore size distributions will be a focus of future work.

CHAPTER 5

ON PORE-SIZE GRADED MEMBRANE NETWORKS

5.1 Overview

Pore-size gradients are often used in the design of membrane filters to increase filter lifetime and ensure fuller use of the initial membrane void volume. In this chapter, we model pore-size gradients in the setting of a membrane filter with an internal network of interconnected pores, and study the influence on membrane performance measures such as total filtrate throughput and accumulated contaminant concentration at the membrane downstream pore outlets. Within the limitations of our modeling assumptions, we find that there is an optimal pore-radius gradient that maximizes filter efficiency independent of maximal pore length (an input parameter that influences membrane geometry), and that membrane pore networks with longer characteristic pore length perform better.

5.2 Introduction

Membrane filtration is an industrial process that uses porous material to separate contaminants from feed solutions. It is crucial to commercial applications such as waste water treatment [75], radioactive sludge removal [25], beer clarification [78] and membrane bioreactors [35], among many others. Filtration is also relevant to many daily household uses including water purification [11], air filters [142, 134, 120, 80], and grease filters [137]. To design an ideal filter, one aims to tailor the geometric features of the filter (specifically, the pores' size, shape and connectivity) so that impurities are removed efficiently, while producing a required amount of filtrate up to a certain standard of purity.

Membrane filtration employs a wide variety of pressure-driven separation methods, distinguished by the scales of pore sizes at which they operate. For example, microfiltration is effective in sieving solids and bacteria; ultrafiltration is often employed in virus and toxin removal; nanofiltration is a popular final step for water treatment that removes major monovalent ions such as chloride and sodium; and reverse osmosis separates multivalent ions that escape from the previous methods by applying mechanical pressure to overcome osmotic pressure [131]. A wide range of materials may be used in membrane manufacture, but membrane materials in common use are roughly divided into two categories: polymeric and ceramic [42]. Membrane filters are also manufactured with many different spatial configurations of membrane materials (leading to differently-structured pores) such as node-fibril [105], flat-sheet [114] and multitube [84], either mimicking natural filters found in plants and animal organs or resulting from careful design considerations.

In addition to these intrinsic features, membrane filter design using a combination of materials and pore layouts has profound implications for performance, and is the main focus of this chapter. A well-designed membrane filter not only maintains particle retention capability but also provides sufficient output (filtrate) to serve the immediate needs of the application. Common membrane designs incorporate structural variations at the microscale (connectivity of interior pores, pore branching, etc.) as well as the macroscale; *e.g.*, pleated filters (also known as spiral-wound modules [12]) and multilayered membrane filters [93]. This last class of membranes has garnered particular attention from industrialists and practitioners for their versatility in applications. In multilayered membrane filters, single-layer membrane filters, each with a different characteristic pore size, may be stacked on top of each other to form a composite membrane with a distribution of pore sizes in its depth (in addition to any intra-layer pore size variations, which are assumed to be less important; but see Gu *et al.* [49] for more discussion of this feature). Common practice is to place the layers with larger pores upstream, allowing more fluid to pass through and providing more surface area to capture particles; and layers with smaller pores downstream to capture any particles that may escape from upstream layers.

We emphasize that the notions of porosity gradient and pore-size gradient are inherently different, though they are sometimes related; and the terms are often used interchangeably in various contexts within current literature. To illustrate, consider first a simple membrane structure where the membrane upstream and downstream surfaces are connected by single continuous pores (a "track-etched" type structure [6]). If such pores have circular cross-section (but with depth-varying radius) and a straight axis perpendicular to the membrane, then if one identifies local pore radius with pore size, a direct relation may be made between pore size gradient and porosity gradient: a pore size (radius) gradient does induce a porosity gradient (or vice versa). However, for a more general network of pores, one can easily design a network that has decreasing pore size in the depth but no porosity gradient, by appropriately increasing the number density of pores with depth. With this distinction between porosity and pore-size gradient in mind, we briefly review current relevant literature that considers either gradient, noting the key findings and motivating the work of the current chapter.

Many experimental studies have shown that improved performance can be achieved with **porosity-graded** multilayered membrane filters. In terms of membrane performance, the ability of porosity-graded ceramic filters to delay internal fouling when compared to common homogeneous ceramic filters has been discussed [90]; and the improved throughput production and foulant removal capability of a photocatalytic membrane with hierarchical porosity was also investigated [41]. Progress has also been made on the manufacturing side. Improved tunability of the physical membrane characteristics in porosity-graded membrane filter assembly has been demonstrated by Amin *et al.* [3]; a novel fabrication strategy of porosity-graded porous foams via 3D printing has been discussed by Cappaso *et* *al.* [20]; and recent advances in additive manufacturing techniques for porous materials with controllable structure have been reviewed by Guddati *et al.* [51]. On the other hand, much attention has also been given to manufacturing **pore-size-graded** filters with desired characteristics, such as the work of Dong *et al.* [36] on fabricating air filters represented as pore-size-graded networks (mimicking bryophyte leafs), and of Harley *et al.*, who present a novel strategy to build porous tubular scaffolds with prescribed pore-size gradient [52]. Kosiol *et al.* use gold nanoparticles as a probe to estimate the pore-size gradient in commercial and non-commercial parvovirus retentive membranes, as these gradient values were found to correlate strongly with virus retention [73]. The advantages of pore-size-graded filters in applications such as tissue engineering [34, 85, 118] and fuel cells [92] have also been discussed.

Several theoretical groups have also contributed to the breadth of the study on multilayered membrane filters with porosity gradients via mathematical modeling and numerical studies; for example studying filter performance optimization as a function of pore-size gradient within a simply-structured membrane [97, 46, 122, 112]; carrying out numerical simulation and analysis of performance of simple multilayered filter structures [39], and investigating geometric and topological properties of membrane networks [48]. There is also significant work on techniques to probe the microstructure of membrane filters, including imaging techniques used to recover network representations of membranes structures in 3D [14, 123] that further motivate and inform our modeling work using pore networks.

This chapter focuses on the modeling of **pore-size-graded** filters with no porosity gradient. We specifically exclude porosity variations so that the impact of pore-size gradient alone can be elucidated; and also because the membrane porosity has been shown to influence membrane network performance rather strongly, to the extent that no benefit would be anticipated by having porosity decrease in the membrane depth (see [48, 49], for example). Our goals are to model a membrane filter with a pore-size gradient and then to probe and explain the influence of this gradient on membrane performance metrics such as total filtrate throughput and particle retention (only adsorptive particle fouling is considered in this chapter). For the first goal, we model the membrane filter as a network of circularly-cylindrical pores. We introduce the pore-size gradient by dividing the membrane into bands of equal thickness (within each of which pore radius is constant), and designating a linearly decreasing sequence of radius values for pores from upstream to downstream bands. We generate membrane pore networks with such a banded structure following a random network generation procedure, adapted from that employed by Gu *et al.* [48]. We further impose that the porosity of each band, an influential geometric feature of membrane pore networks, is approximately equal across all bands, so that we reveal the sole influence of pore size (radius) gradient on membrane filter performance. In addition to studying pore size gradient variations, we also consider variations in maximal pore length, a model input parameter that controls the geometric structure of the pore network.

The chapter is outlined as follows: in Section 5.3, we describe the details of the mathematical model, first introducing how the banded pore networks are constructed with specified pore-size gradient in Section 5.3.1 and then presenting the governing equations for fluid flow and foulant particle transport in Section 5.3.2; in Section 5.4 we define the performance metrics we use to compare our membrane pore networks; in Section 5.5, we provide the appropriate physical scales of the problem and then summarize the model in nondimensional form; in Section 5.6, we present and explain our observations; and in Section 5.7, we conclude our findings.

5.3 Mathematical Modeling

In this section, we introduce a mathematical model that captures the multilayered membrane structure using a pore network representation. We first describe the general network generation protocol and how this creates pore junctions and cylindrical pores, and define our computational domain. After introducing our notions of pore-size gradient, band radius and band porosity, we provide a detailed algorithm that explains how we generate radius-graded banded networks under specific physical constraints. Lastly, we present the governing equations for fluid flow, foulant particle transport and pore radius evolution, and their solution techniques when they are posed on a network.

5.3.1 Pore Size-Graded Networks

We model a representative unit of a membrane filter as a block of porous material that occupies a cube with side length W (see [48] for a similar setup) and contains a network of pores. Each pore is assumed to be circularly cylindrical and thus fully characterized by its length and radius. We use the terms "pore size" and "pore radius" interchangeably from hereon. The unit consists of a membrane top surface with pore inlets, interior pore junctions (vertices of the network), pores (edges of the network), and a bottom membrane surface with pore outlets. The membrane unit is generated as follows: interior junctions are points represented by Euclidean coordinates, uniformly randomly placed in a rectangular box with height $2W$ and square cross section of side length W. Pores are constructed as slender circular cylinders, with axis along straight lines that connect the junctions according to a periodic connection metric (see Appendix D.1). More specifically, we connect junctions (possibly through the four vertical parallel walls) when they lie within a distance of $A_{\max}$ and at least $A_{\min}$ away from each other. These two parameters are referred to as the maximal and minimal pore lengths, respectively. Inlets and outlets are the intersection points between the pores thus generated and two horizontal planes at heights $Z = 0.5W$ and $Z = 1.5W$, respectively (thus Z is the coordinate perpendicular to the membrane surfaces). The space created between these planes forms our computational domain – a cube with

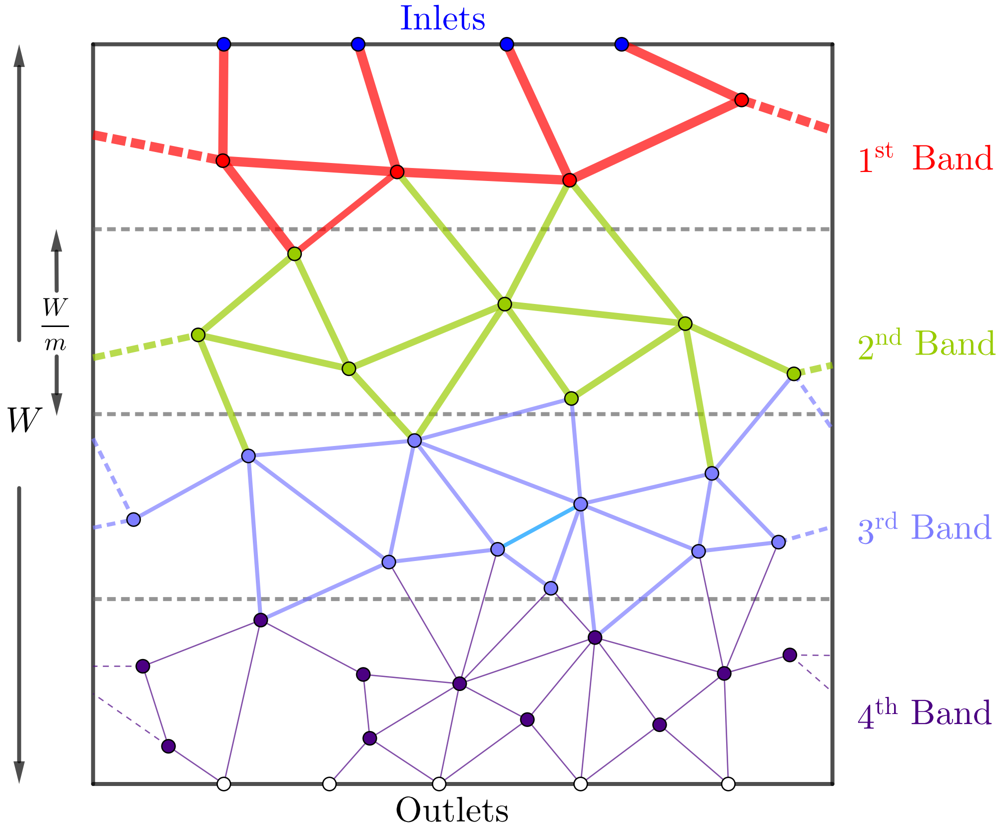

Figure 5.1 Schematic of a 3D banded network represented in 2D. Colored junctions and pores correspond to each band as follows: red 1st band; green 2nd band; light blue 3rd band and indigo 4th band. Blue dots are inlets. White dots are outlets. Dashed lines are pores created by the periodic boundary conditions (see Equation (D.3) in Appendix D.1).

side length W (referred to as **the domain** in the following), while the parts exterior to this cube are discarded.

In the following sections, we first introduce the notion of pore size (radius) gradients, as studied in this chapter, and define band porosity. In addition, in order to tune membrane porosity (a readily measurable quantity in practice), we devise a rule to determine the number of pore junctions to be placed (randomly) in the domain to complete the banded network generation protocol.

Bands and Radius Gradient

We introduce a pore radius gradient by first dividing the domain in the Z-direction (the coordinate direction perpendicular to the membrane upstream and downstream surfaces) into m bands, each of thickness W/m. See a 2D representation of a 3D schematic in Figure 5.1. Let V_k and E_k be the set of junctions and pores in the k^{th} band (numbered from the upstream surface; see the detailed definitions in Equations (D.4) and (D.6) in Appendix D.1). Each pore in E_k is assigned an initial radius

$$R_k = R_m + (m-k)sW, \quad 1 \leq k \leq m, \tag{5.1}$$

where s is the radius gradient and R_m is the radius of pores in the bottom band. This consideration assumes that the initial pore radius in each band is a constant. We say that a pore belongs to the k^{th} band when the largest proportion of its total length lies strictly inside the k^{th} band, and we then assign R_k as its radius (see the different thicknesses and color coding of pores across the bands in the schematic of Figure 5.1). We refer to R_k as the k^{th} **band radius** from hereon. We also call networks with $s = 0$ **uniform networks** and those with nonzero s values **graded networks**.

In this chapter, to reduce the number of degrees of freedom and to make our comparisons of different membranes as "fair" as possible, we impose the constraint that the average radius across all bands is equal to some value R_0, for any R_m and s values. More precisely, for each graded network, we find a range of (R_m, s) pairs corresponding to an average pore radius R_0 across the bands, and compare the performance of these networks versus their uniform counterparts with radius R_0. The average radius R_0 across the m bands satisfies

$$(\textit{Constraint 1a}) \qquad R_0 = \frac{1}{m}\sum_{k=1}^{m} R_k = R_m + \frac{sW}{2}\left(m-1\right). \tag{5.2}$$

Thus, once R_0 is prescribed, we can choose s and then uniquely determine R_m.

We here point out an important fact: to generate a banded network, in addition to declaring band radii using Equation (5.1), we must also specify an initial number of randomly placed junctions in each band. This in general leads to different band porosities (void volume in the band divided by volume of the containing slab, discussed in detail later). As the goal of our work is to isolate the influence of pore size (radius) gradients, we enforce that each band has the same porosity. To achieve this, we devise a guess-and-correct procedure detailed in the following sections.

Band and Membrane Porosity

Before we introduce the banded network generation procedures, we clarify the crucial definition of band porosity. The **band porosity** of the k^{th} band of a graded network with m bands is given by

$$\Phi_k = \frac{\frac{\pi}{2}\sum_{e_{ij}\in E} R_{ij}^2 L_{k,ij}}{W^3/m}, \tag{5.3}$$

where e_{ij} is the pore connecting junctions i and j with radius R_{ij}, and $L_{k,ij}$ measures the length of e_{ij} that lies within the k^{th} band (by which definition $L_{k,ij} = 0$ if e_{ij} has no component within layer k; see Appendix D.1 for a detailed definition of $L_{k,ij}$ and its distinction with edge length A_{ij}). The sum in Equation (5.3) is over all pores since $L_{k,ij}$ includes the contributions from pores that cross multiple bands. The numerator is the void volume of the k^{th} band (volume of empty space), while the denominator is the volume of the rectangular slab with a square cross section of side length W and height W/m. The **membrane porosity** is given by

$$\Phi = \frac{1}{m}\sum_{k=1}^{m} \Phi_k, \tag{5.4}$$

that is, the average band porosity across the bands. This definition is equivalent to the sum of total void volume divided by the volume of the cube with side length W.

In general, the band porosities and overall membrane porosity are functions of time, since pore radii evolve due to foulant particle deposition and adsorption; Equations (5.3) and (5.4) hold pointwise in time. In the following Section 5.3.1, however, we are concerned only with describing the initial membrane structure, hence we adopt a simpler notation by dropping the time dependence as we work only with **initial** porosities.

Constant Radius in Each Band

Here we present the methodology of generating radius-graded membrane networks. In this section only, for notational simplicity, Φ_k and Φ correspond to the **initial** porosity in the k^{th} band and **initial** membrane porosity. We divide the domain into m bands of equal thickness in the direction perpendicular to the membrane top surface, as motivated in Section 5.3.1. We assign a typical initial porosity value Φ for the membrane structure we consider, *e.g.*, $\Phi = 0.6$ that approximates commercial filters. The principal aim of this section is to estimate the number of points (pore junctions) needed in each band to generate networks that satisfy prescribed constraints, including Equation (5.2) and more to be detailed below.

To isolate the effect of pore radius gradients on membrane performance, we enforce that every band has approximately the same initial porosity (we cannot insist that band porosities be exactly equal due to the random nature of the network generation protocol). This (soft) constraint is given by

$$(\textit{Constraint 2a}) \qquad \Phi_n \approx \Phi_k, \quad n, k = 1, \ldots, m, \tag{5.5}$$

where the "≈" is to be made precise in the algorithm introduced below. Since the initial pore radius is constant within each band, Equation (5.3) simplifies to

$$\Phi_k := \frac{\frac{\pi}{2} R_k^2 \sum_{e_{ij} \in E} L_{k,ij}}{W^3/m}. \tag{5.6}$$

Using Equations (5.1) and (5.3), for arbitrary bands n and k, we have

$$\frac{W^3}{m}\Phi_n = \frac{\pi}{2} R_n^2 \sum_{e_{ij} \in E} L_{n,ij} \approx \frac{\pi}{2} R_k^2 \sum_{e_{ij} \in E} L_{k,ij} = \frac{W^3}{m}\Phi_k,$$

which implies

$$R_n^2 \sum_{e_{ij}\in E} L_{n,ij} \approx R_k^2 \sum_{e_{ij}\in E} L_{k,ij}. \tag{5.7}$$

We now relate N_k, the number of pore junctions randomly placed in the k^{th} band, to the sum in Equation (5.7) and use the result to provide an estimate for N_k, to generate pore networks that satisfy the constraints given in Equations (5.2) and (5.5). We use basic probabilistic arguments to deduce that $\sum_{e_{ij}\in E} L_{k,ij}$, total edge length in the k^{th} band, scales with $N_k\,(N_k-1)$ and other terms common to all other bands (so that they cancel from each side of Equation (5.7)). Details of this derivation are in Appendix D.2. Equation (5.7) then reduces to

$$R_n^2 N_n\,(N_n-1) \approx R_k^2 N_k\,(N_k-1)\,, \quad \forall n,k=1,\ldots,m, \quad n\neq k. \tag{5.8}$$

Since we consider only situations where pore size decreases in the membrane depth, a nonzero pore size gradient s implies that R_m, the radius in the m^{th} band, is the smallest (per Equation (5.1)). Thus, the m^{th} band requires more points than other bands to satisfy Equation (5.8), and motivates our initializing our algorithm with this band (more computationally efficient, since this choice minimizes the errors incurred in the sequential process outlined below). To estimate the N_k sequentially, we first prescribe s, the radius gradient. This fixes each band radius R_k via **Constraint 1**, Equation (5.2). We then make several guesses for N_m and stop when we find a value such that $\Phi_m \approx \Phi$. With N_m determined, we employ Equations (5.1) and (5.8) to obtain the relationship

$$R_m^2 N_m\,(N_m-1) \approx \left(R_m+(m-k)\,s\right)^2 N_k\,(N_k-1)\,, \tag{5.9}$$

which we solve to estimate the number of junctions, N_k, for all other bands.

The relationship Equation (5.9) is by no means exact, and can fail by some margin to guarantee equal porosity for each band when the gradient s becomes too large, but it provides a useful starting point. After estimating the N_k values as described, we compute the corresponding Φ_k and check their proximity to the prescribed value Φ. We correct Φ_k to Φ by adding or removing nodes randomly. This correction procedure starts with the m^{th} band and proceeds upstream. We iterate this procedure until the network achieves band porosities close to Φ within a prescribed relative tolerance $\epsilon = 0.005$. Variations in porosity as such are sufficiently small for the stability of our results on performance metrics (see [49] for details on the effect of porosity variations).

5.3.2 Governing Equations

In this section, we briefly describe the dimensional governing equations for flow of the feed solution and transport of foulant concentration in a single pore, then extend the description to a network of such pores using conservation laws at pore junctions. For more details of the derivation, we refer the reader to Gu *et al.* [48].

Fluid Flow

The feed is assumed to be a Newtonian fluid with viscosity μ, driven through a cylindrical pore with small aspect ratio via a pressure difference P_0. The flux Q_{ij} between junctions i and j is characterized by the Hagen-Poiseuille equation [103],

$$Q_{ij} = \mathbb{K}_{ij}\left(P_i - P_j\right), \quad e_{ij} \in E, \tag{5.10}$$

where $\mathbb{K}_{ij}$ is the conductance of the pore e_{ij}, given by

$$\mathbb{K}_{ij} = \begin{cases} \frac{\pi R_{ij}^4}{8\mu A_{ij}}, & e_{ij} \in E, \\ 0, & \text{otherwise}, \end{cases} \tag{5.11}$$

where R_{ij} and A_{ij} are the radius and length of e_{ij}. Enforcing conservation of flux at each junction leads to a system of equations for the pressure at each interior junction, subject to the boundary conditions

$$P_i = \begin{cases} P_0, & i \in V_{\text{top}}, \\ 0, & i \in V_{\text{bot}}, \end{cases} \tag{5.12}$$

where V_{top} and V_{bot} are the set of membrane pore inlets and outlets, respectively (see Equation (D.1) for their definitions in detail). Once the pressures are known, we use Equation (5.10) to find the flux in each individual pore. The scales for these equations are defined in Section 5.5.

Foulant Transport

In this chapter, only adsorptive particle fouling is considered, in which foulant particles much smaller than the pore radius are transported by the flow and adhere to the pore wall due to a variety of chemical or physical effects that depend on the affinity between the particles and the membrane material. C_{ij}, the concentration of foulant particles in pore e_{ij}, satisfies the steady state advection equation,

$$Q_{ij} \frac{\partial C_{ij}}{\partial Y} = -\Lambda R_{ij} C_{ij}, \tag{5.13}$$

where Λ is an affinity parameter that describes the interaction between foulant particles and the membrane material; and Y is a local coordinate along the pore in the direction of flux Q_{ij}. Equation (5.13) is paired with a boundary condition

$$C_{ij}\left(0, T\right) = \begin{cases} C_0, & i \in V_{\text{top}}, \\ C_i\left(T\right), & \text{otherwise}, \end{cases} \tag{5.14}$$

where $C_i\left(T\right)$ is the (unknown) concentration at junction i, determined by enforcing conservation of foulant particle flux, *i.e.*, $Q_{ij} C_{ij}$, at each junction i (for all adjacent j).

Pore Radius Evolution

Once we obtain the foulant concentration at each junction, we model pore size evolution with a decay rate directly proportional to the concentration at the upstream inlet (for a stronger justification of this model choice see [48]). More precisely, R_{ij}, the radius of a pore e_{ij}, satisfies

$$\frac{dR_{ij}}{dT} = -\Lambda \alpha C_i, \quad \alpha = \frac{V_p}{2\pi}, \quad e_{ij} \in E, \tag{5.15}$$

where V_p is the effective volume of each foulant particle. This ODE is subject to the initial condition

$$R_{ij}(0) = R_k, \quad e_{ij} \in E_k, \quad k = 1, \ldots, m, \tag{5.16}$$

that is, we assign an initial pore radius R_k to each pore that lies in the k^{th} band.

5.4 Performance Metrics

In this section, we define the performance metrics used in this chapter to evaluate membrane filter performance.

1. Membrane Lifetime, T_{final}.
   (a) (Flux extinction) It is the earliest time at which there exists no feasible path for fluid transit from the membrane top surface to the bottom. This corresponds to the case when flux reaches zero.
   (b) (Flux threshold) It is the earliest time at which flux level reaches below a prescribed threshold.
2. Filtrate Throughput $H(T)$,

$$H(T) = \int_0^T Q_{\text{out}}(T')\, dT', \tag{5.17}$$

$$Q_{\text{out}}(T) = \sum_{v_j \in \mathcal{V}_{\text{out}}} \sum_{i: e_{ij} \in E} Q_{ij}(T), \tag{5.18}$$

where $Q_{\text{out}}(T)$ is the total flux exiting the filter and $\mathcal{V}_{\text{out}}$ is the set of pore outlets at the membrane bottom surface. In particular, we are interested in

$H_{\text{final}} := H\left(T_{\text{final}}\right)$, the total volume of filtrate processed by the filter over its lifetime.

3. Initial Flux $Q_{\text{out}}\left(T=0\right)$.

4. Accumulated Concentration of Foulant at Membrane Outlet $C_{\text{aco}}\left(T\right)$ (**ACO** in short),

$$C_{\text{aco}}\left(T\right) = \frac{\int_0^T C_{\text{out}}\left(T'\right) Q_{\text{out}}\left(T'\right) dT'}{\int_0^T Q_{\text{out}}\left(T'\right) dT'} = \frac{\int_0^T C_{\text{out}}\left(T'\right) Q_{\text{out}}\left(T'\right) dT'}{H\left(T\right)}, \tag{5.19}$$

where

$$C_{\text{out}}\left(T\right) = \frac{\sum\limits_{v_j \in \mathcal{V}_{\text{out}}} \sum\limits_{i: e_{ij} \in E} C_j\left(T\right) Q_{ij}\left(T\right)}{Q_{\text{out}}\left(T\right)} \tag{5.20}$$

is the instantaneous foulant concentration at the membrane outlet. Of particular interest is $C_{\text{final}} := C_{\text{aco}}\left(T_{\text{final}}\right)$, which provides a measure of the aggregate particle capture efficiency of the filter over its lifetime.

5. Following Griffiths *et al.* [47], we also investigate a combined score that captures the mass of particles retained in the filter,

$$\Xi = H_{\text{final}}\left(1 - C_{\text{final}}\right), \tag{5.21}$$

which captures the trade-off between throughput and concentration usually observed in filtration experiments, *i.e.*, filters producing a large throughput tend to have low impurity retention. We refer to Ξ as the **filter mass capacity** (or simply **capacity**) in the following discussions as it represents the mass of impurity that has been deposited in the membrane at the end of its lifetime.

6. Band porosity and membrane porosity as functions of time (per Equations (5.3) and (5.4), respectively),

$$\Phi_k\left(T\right) = \frac{\frac{\pi}{2}\sum_{e_{ij}\in E} R_{ij}^2\left(T\right) L_{k,ij}}{W^3/m}, \quad k = 1, \ldots, m, \tag{5.22a}$$

$$\Phi\left(T\right) = \frac{1}{m}\sum_{k=1}^{m} \Phi_k\left(T\right), \tag{5.22b}$$

and their changes from initial to final values, referred to as **band and membrane porosity usage**, respectively,

$$\Delta\Phi_k = \Phi_k\left(0\right) - \Phi_k\left(T_{\text{final}}\right), \quad k = 1, \ldots, m, \tag{5.23a}$$

$$\Delta\Phi = \Phi\left(0\right) - \Phi\left(T_{\text{final}}\right). \tag{5.23b}$$

Per Equation (5.5), $\Phi_k\left(0\right) \approx \Phi\left(0\right) \approx 0.6$ where $\approx$ is up to some tolerance ϵ.

We summarize the procedures described in Section 5.3.1 in Algorithm 5.1.

Algorithm 5.1 Filtration on Radii-Graded Networks.

1. Choose maximal pore length $A_{\max}$, average pore radius R_0 and porosity Φ.
2. Initialise radius gradient s. Find R_k as constrained by R_0 via Equation (5.2).
3. Generate N_G banded networks parametrized by $A_{\max}$ and R_k:
    (a) Guess N_m such that $\Phi_m \approx \Phi$.
    (b) Determine N_k for $k = 1, \ldots, m-1$ via Equation (5.9).
    (c) Generate networks using N_k random junctions in the k^{th} band according to the periodic connection metric defined in Equation (D.3).
    (d) Correct membrane porosity by adding or deleting junctions until it is within relative tolerance $\epsilon = 0.005$ to Φ. More precisely, we perform this procedure until $\left|1 - \frac{\Phi_{\text{corr}}}{\Phi}\right| < \epsilon$ where Φ_{corr} is the porosity during this iterative procedure.
4. Compute the performance metrics (defined in Section 5.4).
5. Go back to Item 2 by varying s.
6. Go back to Item 1 by varying $A_{\max}$.

5.5 Scales

We nondimensionalize the model presented in Section 5.3, key quantities introduced in Section 5.3.1 and the performance metrics defined in Section 5.4, with the following scales,

$$
\begin{gathered}
P = P_0 p, \qquad \left(A_{ij}, L_{k,ij}\right) = W\left(a_{ij}, l_{k,ij}\right), \\
\left(A_{\min}, A_{\max}\right) = W\left(a_{\min}, a_{\max}\right), \qquad \left(R_{ij}, R_0\right) = W\left(r_{ij}, r_0\right), \\
Q_{ij} = \frac{\pi W^3 P_0}{8\mu} q_{ij}, \qquad \mathbb{K}_{ij} = \frac{\pi W^3}{8\mu} \mathbb{k}_{ij}, \qquad \mathbb{k}_{ij} = \frac{r_{ij}^4}{a_{ij}}, \\
\left(C_{ij}, C_{\text{aco}}, C_{\text{int}}\right) = C_0\left(c_{ij}, c_{\text{aco}}, c_{\text{int}}\right), \qquad Z = Wz, \qquad \Lambda = \frac{\pi W P_0}{8\mu}\lambda, \qquad T = \frac{W}{\Lambda \alpha C_0} t.
\end{gathered}
\tag{5.24}
$$

Equation (5.1) for the initial pore radius in layer k, in dimensionless form now reads

$$
r_k = r_m + (m - k)\, s. \tag{5.25}
$$

Using the scales for pore radius R_{ij} and pore length $L_{k,ij}$ in the k^{th} band, band porosity now becomes

$$
\Phi_k(t) := \frac{\frac{\pi}{2} \sum_{e_{ij} \in E} r_{ij}^2(t)\, l_{k,ij}}{1/m}. \tag{5.26}
$$

The dimensionless performance metrics become

$$
h(t) = \frac{1}{\lambda} \int_0^t q_{\text{out}}(t')\, dt', \quad q_{\text{out}}(t) = \sum_{v_j \in V_{\text{bot}}} \sum_{v_i : (v_i, v_j) \in E} q_{ij}(t), \tag{5.27a}
$$

$$
c_{\text{aco}}(t) = \frac{\int_0^t c_{\text{out}}(t')\, q_{\text{out}}(t')\, dt'}{\int_0^t q_{\text{out}}(t')\, dt'}, \quad c_{\text{out}}(t) = \frac{\displaystyle\sum_{v_j \in V_{\text{bot}}} \sum_{v_i : (v_i, v_j) \in E} c_j(t)\, q_{ij}(t)}{q_{\text{out}}(t)}, \tag{5.27b}
$$

$$
\xi = h(t_{\text{final}})\, c_{\text{int}}(t_{\text{final}}). \tag{5.27c}
$$

Tables 5.1 and 5.2 summarize the key nondimensional parameters and quantities, their symbols/definitions and range of values.

5.6 Results and Discussions

In this section, we present results on the performance metrics of banded networks as the pore radius gradient s and maximal pore length $a_{\max}$ are varied. For every gradient

Table 5.1 Key Nondimensional Parameters

Parameter	Symbol	Values/Range
Maximum pore length	$a_{\max}$	$0.1, 0.15, 0.2$
Minimum pore length	$a_{\min}$	0.06
Radius in k^{th} band	r_k	$[2.5 \times 10^{-3}, 0.016]$
Uniform Radius	r_0	0.01
Radius gradient	s	$[0, 4 \times 10^{-3}]$
Total number of bands	m	4
Deposition coefficient	λ	5×10^{-7}
Initial membrane porosity	$\Phi(0)$	0.6
Initial band porosity	$\Phi_k(0)$	0.6
Relative error for porosity correction (see Algorithm 5.1)	ϵ	0.005

Table 5.2 Key Nondimensional Quantities

Quantity	Symbol	Formula/Range of Values
Pore Length	a_{ij}	$[a_{\min}, a_{\max}]$
Pore Radius	$r_{ij}(t)$	$[2.5 \times 10^{-3}, 0.016]$
Pore length in the k^{th} band	$l_{k,ij}$	see Appendix D.1
Porosity of the k^{th} band	$\Phi_k(t)$	$\frac{m\pi}{2} \sum_{e_{ij} \in E} r_{ij}^2(t)\, l_{k,ij}$
Membrane Porosity	$\Phi(t)$	$\frac{1}{m} \sum_{k=1}^{m} \Phi_k(t)$
Total Throughput	$h(t)$	$\frac{1}{\lambda} \int_0^t q_{\text{out}}(t')\, dt'$
ACO (see Equation (5.19) for nomenclature)	$c_{\text{aco}}(t)$	$\frac{\int_0^t c_{\text{out}}(t') q_{\text{out}}(t') dt'}{\lambda h(t)}$
Filter mass capacity (capacity)	ξ	$h(t_{\text{final}})\, c_{\text{int}}(t_{\text{final}})$

s, we generate 1000 networks independently using the banded network generation protocol described in Section 5.3.1 and collect the mean and standard deviation of each performance metric defined in Section 5.4. The system of ODEs Equation (5.15) is solved using a simple forward Euler method with a time step size of 2.5×10^{-4}. We investigate the trend of the mean performance metrics against gradient s and maximal pore length $a_{\max}$.

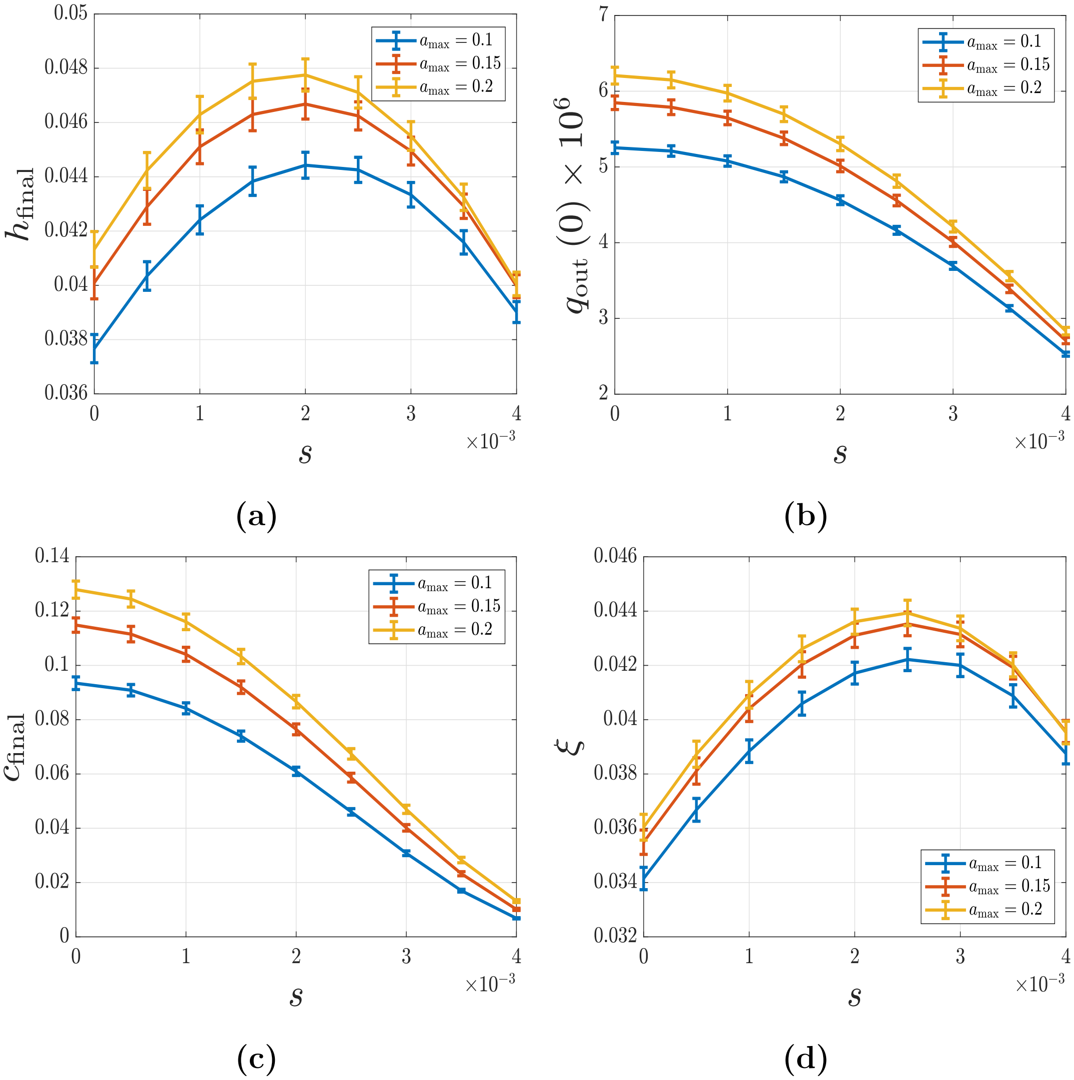

(a) **(b)**

(c) **(d)**

Figure 5.2 Performance metrics against radius gradient. (a) Total throughput; (b) initial flux; (c) accumulated foulant concentration; and (d) filter mass capacity.

In Figure 5.2, we present how performance metrics vary with pore-radius gradient s in banded networks with $m = 4$ bands, within each of which the initial pore radius is constant (specified by Equation (5.25)). Results are shown for three different values of the maximum pore length, $a_{\max}$. In Figure 5.2a, we show total filtrate throughput against pore radius gradient s. We observe that for each $a_{\max}$ value considered, we have a non-monotone trend with a clear maximum in total throughput at a radius gradient of $s = 2 \times 10^{-3}$ (apparently independent of $a_{\max}$, though the total filtrate throughput achieved in all cases is monotone increasing in $a_{\max}$). Figure 5.2b plots results for initial flux, showing it to be a monotone decreasing function in radius gradient s, and monotone increasing in maximal pore length $a_{\max}$. In Figure 5.2c, we plot final accumulated foulant concentration at membrane outlet against s. The trend is monotone decreasing in radius gradient for all $a_{\max}$ values considered (that is, highly graded networks provide better foulant control); and monotone increasing in $a_{\max}$. Figure 5.2d shows the filter mass capacity ξ (see Equation (5.21) and Equation (5.27c)), the (dimensionless) mass of particles retained inside the pore network throughout its lifetime, as a function of s. Here we see a non-monotone trend, with a clear optimal pore radius gradient, at about $s = 2.5 \times 10^{-3}$ (a little larger than that in observed in Figure 5.2a). In other words, for all $a_{\max}$ values considered, at the end of the filter lifetime, banded networks with this radius gradient value have captured the greatest mass of impurities. These results also show that the uniform networks have the worst filter mass capacity for each $a_{\max}$.

We first discuss the trends in radius gradient s observed in Figure 5.2. We rationalize the existence of a throughput-maximizing value for pore radius gradient by considering the extreme values of s. Our results show that, when compared to a uniform network ($s = 0$), banded networks with large radius gradient tend to have much lower flux due to the high-resistance small outlets in the bottom band; however, they have longer lifetime due to the large pore inlets upstream (we hypothesize that pores always close first at the upstream side of the membrane, a claim supported by an analytical result in Appendix D.3). Indeed, the flux trend with s is evident from

Figure 5.2b, which shows that non-graded networks have the largest initial flux for all $a_{\max}$ values considered. Pore size graded networks admit a trade-off between initial flux and filter lifetime as the gradient value varies, suggesting that an intermediate value of radius gradient should exist (and is found at $s = 2 \times 10^{-3}$) that maximizes total throughput. Furthermore, the monotone trend of concentration against radius gradient s observed in Figure 5.2c is also not unexpected. The smaller pores in the bottom band of strongly graded networks are much more effective at removing foulant particles.

We now comment on two interesting observations from Figure 5.2d – the maximum in filter mass capacity and the larger maximizing gradient value than that in Figure 5.2a. The latter is an artifact of the definition of filter mass capacity ξ – product of a concave total throughput with a clear local maximum (per Figure 5.2a) and a monotone increasing function $1 - c_{\text{aco}}$. In other words, a maximizing radius gradient for capacity must be larger than that for total throughput. Indeed, consider the following heuristic argument: suppose total throughput $h(s)$ (suppressing the "final" subscript) is maximized at a radius gradient $s = s_{h,\max}$, then the slope of filter mass capacity $\xi(s)$ at this value is

$$\begin{aligned}
\xi'(s_{h,\max}) &= \frac{d}{ds}\left(h(s)\, c_{\text{int}}(s)\right)|_{s=s_{h,\max}} \\
&= \cancelto{0}{h'(s_{h,\max})} c_{\text{int}}(s_{h,\max}) + h(s_{h,\max})\, c'_{\text{int}}(s_{h,\max}) \\
&= h(s_{h,\max})\, c'_{\text{int}}(s_{h,\max}) \\
&> 0.
\end{aligned}$$

Thus, filter mass capacity is increasing with s at the maximizing gradient value for total throughput. We return to this point later in Section 5.6.1.

We now briefly comment on the trend of the performance metrics as maximal pore length $a_{\max}$ varies in Figure 5.2. First, each metric varies monotonically with $a_{\max}$. More precisely, the larger the maximal pore length, the greater the total throughput (Figure 5.2a) and initial flux (Figure 5.2b); and the higher the accumulated foulant concentration (Figure 5.2c). With the prescribed membrane porosity level $\Phi = 0.6$, these observed trends appear consistent with the findings of Gu *et al.* [48], which exclusively focused on networks with uniform pore radius (gradient $s = 0$). Meanwhile, the reason for the higher foulant concentration from banded networks with larger $a_{\max}$ is that networks with longer pores tend to be less tortuous than those with shorter pores (smaller $a_{\max}$).[1]

5.6.1 Total Porosity Evolution

Though initially the porosity is approximately the same for each membrane, porosities decrease over time as fouling occurs. In this section, we present how overall membrane porosity evolves in time for each value of the maximal pore length. Our discussion focuses on the changes in membrane porosity and the final values achieved when filtration ceases, for each radius gradient value. We emphasize the difference $\Delta\Phi$ between the initial porosity $\Phi(0) = 0.6$ and the final porosity values, which we refer to as **porosity usage**, because it is proportional to the volume occupied by retained contaminants and thereby to the retained mass ξ (per Figure 5.2d) as well.

In each of Figures 5.3a–5.3c, we show, for each maximal pore length $a_{\max}$, the evolution of membrane porosity in time, for all radius gradients considered. Filter lifetime may be inferred from the various curves by noting the time at which they stop. To showcase the porosity usages of networks with each radius gradient, we condense them into Figure 5.3d by plotting the difference between initial and final porosity, $\Delta\Phi$. We notice that not only is $\Delta\Phi$ a non-monotone function of pore radius gradient s, but also the shape of the curves is very similar to those in Figure 5.2d (other than

---

[1] The membrane **tortuosity** is defined as the average (normalized) distance travelled by a fluid particle from membrane top surface to bottom. See [48] for its detailed definition and discussion of the negative exponential relationship between concentration and tortuosity.

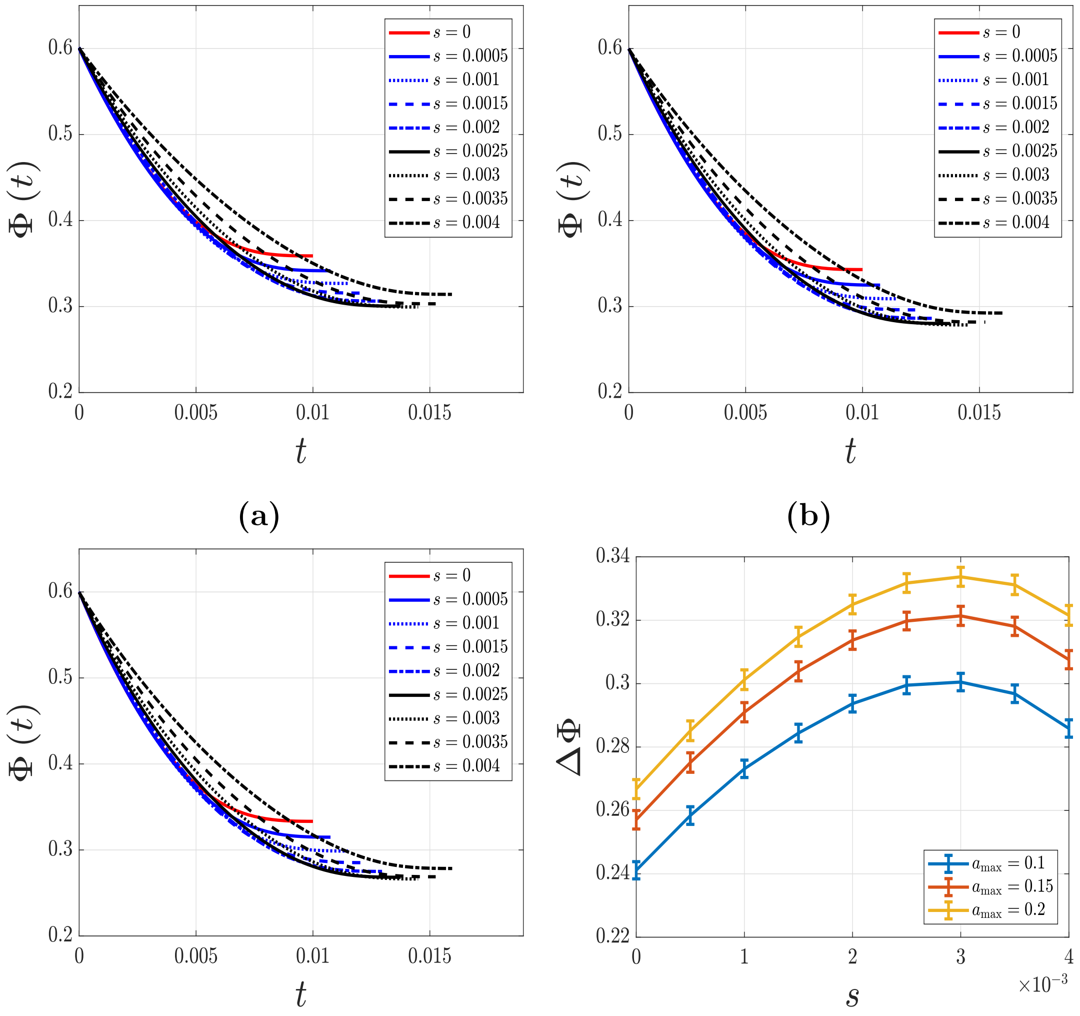

(a) **(b)**

(c) **(d)**

Figure 5.3 Total porosity evolution. (a) $a_{\max} = 0.1$; (b) $a_{\max} = 0.15$; (c) $a_{\max} = 0.2$. In (d), for each $a_{\max}$, membrane porosity usage (Equation (5.23b)) is plotted against radius gradient s. $\Phi(0) = 0.6$ is the initial porosity.

a small shift in the value of the maximizing radius gradient, from $s = 2.5 \times 10^{-3}$ to $s = 3 \times 10^{-3}$).

Now we check the maximum of capacity ξ in Figure 5.2d for consistency with the findings from Figure 5.3d, noting that (since we showed ξ must be increasing at a point to the left of the observed maximum) we only have to show that networks with the largest radius gradients $s = 4 \times 10^{-3}$ have less capacity than those with $s = 3.5 \times 10^{-3}$. From Figure 5.3d, we clearly see that networks with radius gradient

$s = 4 \times 10^{-3}$ incur less porosity change and thereby, have less capacity than networks with $s = 3.5 \times 10^{-3}$ for all time t (also true for all $a_{\max}$ values).

5.6.2 Band Porosity Evolution

While overall membrane porosity evolution shines light on the behaviour of pore-radius-graded networks, individual band porosity evolution helps us identify the depth of foulant penetration in the membrane, for each pore radius gradient value considered. In this section, we explore how band porosities change as the pore radius gradient s varies and aim to draw further insight from this evolution into indicators of good pore-size-graded filters. The following discussion again focuses on the quantitative changes of band porosities, and the final porosity values when filtration stops.

In Figure 5.4, we show the evolution of band porosities for the shortest maximal pore length considered ($a_{\max} = 0.1$), and for all radius gradient values s; the inset subfigure plots band porosity usage (the total change in band porosity, $\Delta\Phi_k$, see Equation (5.23a)) as a function of radius gradient s. In Figure 5.4a, the evolution of the 1st band porosity (the upstream band) shows that the larger the radius gradient, the larger the porosity decline (see inset subfigure). This is because the largest pore size gradient yields the largest 1st band pore radius and thereby the longest filter lifetime, allowing more particles to adsorb and thus using more empty space in the interior. We note in passing that though the lifetimes of the networks (evidenced by the times at which each porosity curve stops) are quite different, the final values of 1st band porosity for each gradient value are relatively close to each other (exemplified in the small range of vertical axis in the inset subfigure), which implies that the 1st band processes foulants similarly regardless of the pore radius gradient. In Figure 5.4b, we plot the evolution of the 2nd band porosity against time for each radius gradient value s. Here, the final porosity values are clearly separated according to their radius

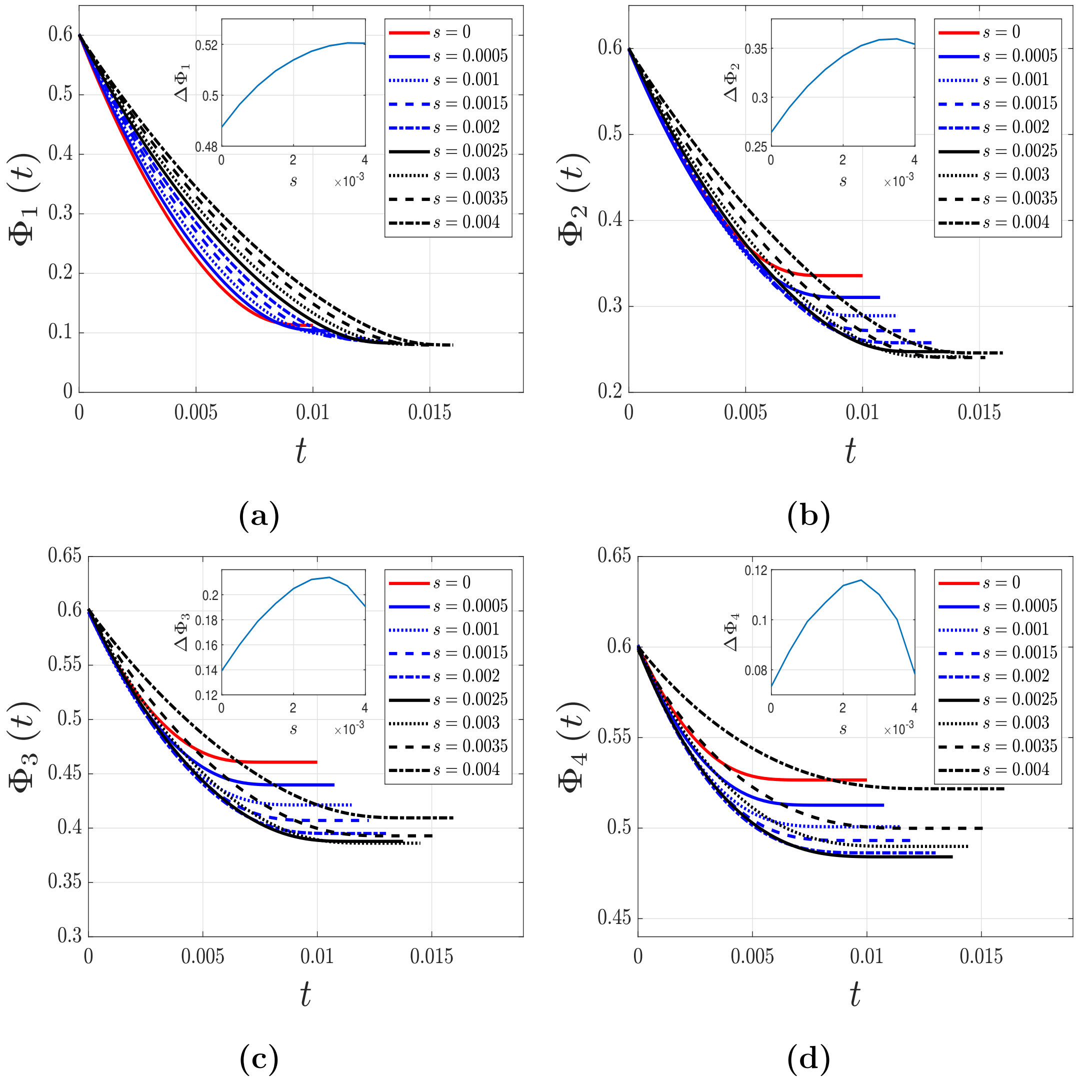

(a) (b)

(c) (d)

Figure 5.4 Band porosity evolution with $a_{\max} = 0.1$. (a) 1st band; (b) 2nd band; (c) 3rd band (d) 4th band. Each inset subfigure plots band porosity usage (the total change in band porosity over the filter lifetime) as a function of radius gradient s.

gradient values, in contrast to Figure 5.4a. In particular, the uniform networks (in red) clearly undergo the smallest porosity change over the filter lifetime, and thus retain the smallest mass of particles within this layer (consistent with Figure 5.2d). The porosity usage of this band increases with radius gradient s until $s = 3 \times 10^{-3}$ and $s = 3.5 \times 10^{-3}$, for which values the largest total change in band porosity is observed (see inset). In Figure 5.4c where we show 3rd band porosity evolution, the largest porosity change occurs in networks with a somewhat smaller gradient value

$s = 3 \times 10^{-3}$, with $s = 2.5 \times 10^{-3}$ having almost as large a change (but larger s-values showing smaller changes), implying that foulant particles penetrate deeper into membrane pore networks with these gradient values. Lastly, we see in Figure 5.4d that networks with radius gradient $s = 2.5 \times 10^{-3}$ (solid black) experience the largest change in 4th band porosity (corresponding to the maximum in the inset subfigure), suggesting that such networks allow the deepest penetration of foulants.

Meanwhile, membrane networks with $s = 0$ (uniform) and $s = 4 \times 10^{-3}$ (steepest gradient) each perform poorly in terms of mass capacity (Equation (5.27c)) in the 4th band as their 4th band porosity does not change as appreciably as that of networks with other radius gradient values. To explain this, in the case of uniform networks, their upstream pores close earlier than those in the graded counterparts (which have larger inlets due to the radius constraint via Equations (5.1) and (5.2)), thus prohibiting flow at an early stage by fouling upstream pores too quickly; in the case of $s = 4 \times 10^{-3}$ (the largest pore-size gradient used), the smaller downstream pores with their high resistance slow down the overall flow, causing the majority of fouling to also take place upstream.

In Figures 5.5 and 5.6, following Figure 5.4, we plot the band porosity evolution, for maximal pore lengths $a_{\max} = 0.15$ and $a_{\max} = 0.2$, respectively. We discover very similar correlations between the filter mass capacity and the fouling of downstream bands, to those just discussed for Figure 5.4 ($a_{\max} = 0.1$). The 1st band porosity change, $\Delta\Phi_1$, is always monotone increasing in the radius gradient, and uniform networks and those with the steepest gradient incur the least porosity usage in their 4th band. Altogether, we conclude that when taking total throughput, accumulated concentration of foulants and porosity usage all into account, membrane pore networks with radius gradient $s = 2.5 \times 10^{-3}$ make the most favourable filters. More importantly, this optimal value does not depend on $a_{\max}$.

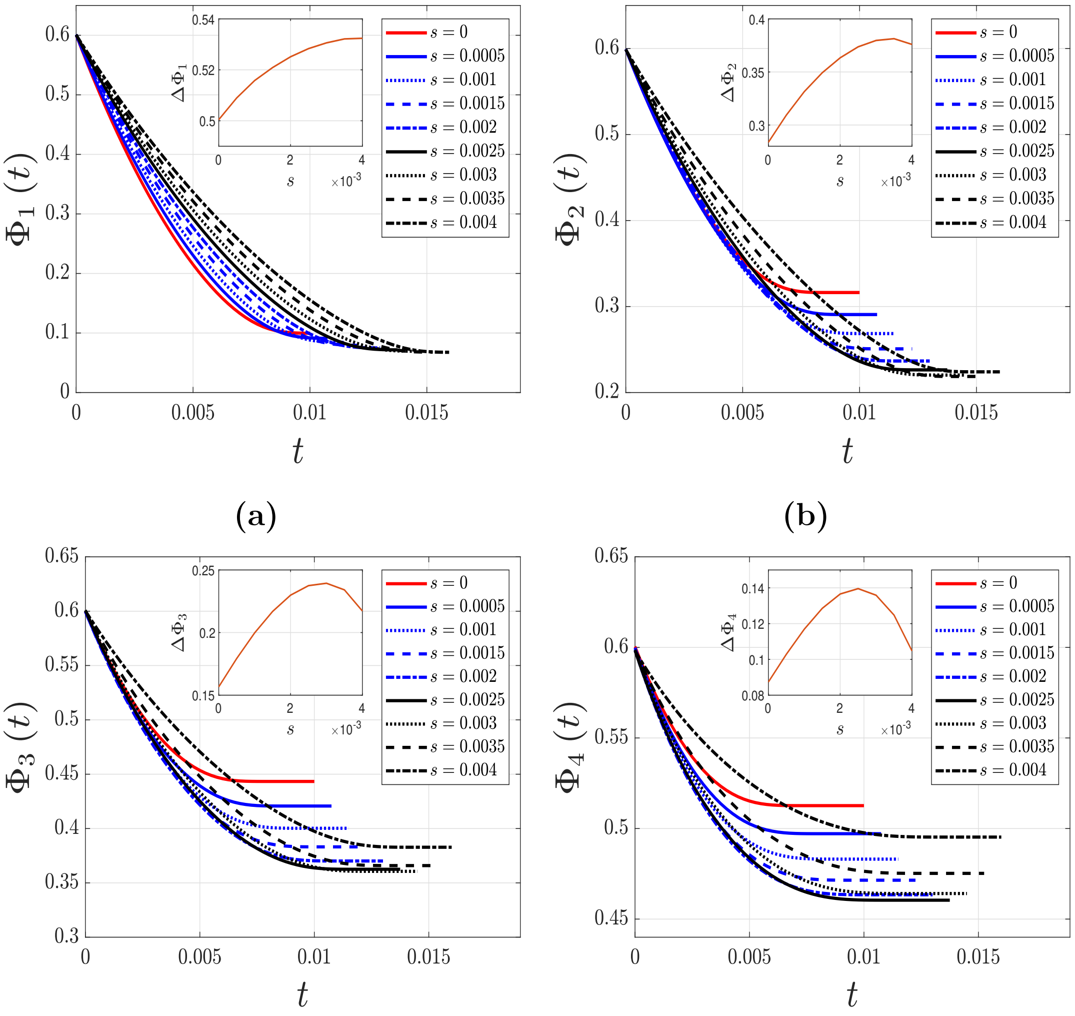

(a) **(b)**

(c) **(d)**

Figure 5.5 Same setup as Figure 5.4. $a_{\max} = 0.15$.

Through Figures 5.4–5.6, we observe that the maximizing radius gradients ($s = 2.5 \times 10^{-3}$) observed in Figure 5.2d all correspond to the largest amount of porosity usage $\Delta\Phi_4$ in the 4th bands. Though this correspondence may not be a definitive explanation for why $s = 2.5 \times 10^{-3}$ maximizes filter capacity, porosity usage in the 4th band may serve as a necessary indicator of a good filter.

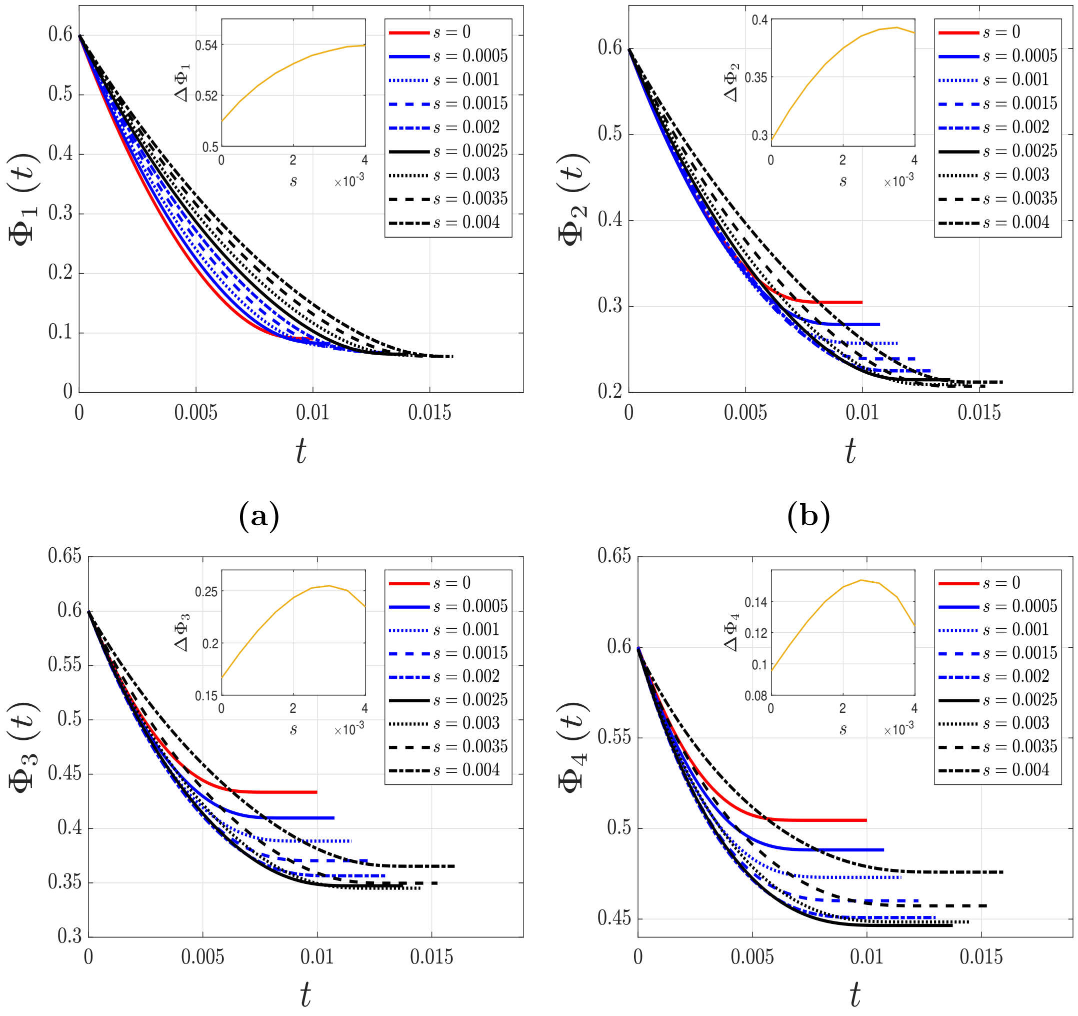

(a) (b)

(c) (d)

Figure 5.6 Same setup as Figure 5.4. $a_{\max} = 0.2$.

5.6.3 Performance Metrics with Flux Threshold

The results discussed so far are based on performance metrics evaluated at the end of the filter's lifetime, when there is no feasible flow path and flux through it falls to zero. In practice, when industrialists observe a low flux level in the filtration process, they tend to discard the fouled filters and replace with fresh ones. In this section, we mimic this procedure by imposing a minimal threshold for the flux level at which we halt the process and collect statistics of the performance metrics up to this critical time. The symbols for each performance metric F evaluated with an imposed flux threshold are labelled with a subscript, $F_{\text{threshold}}$.

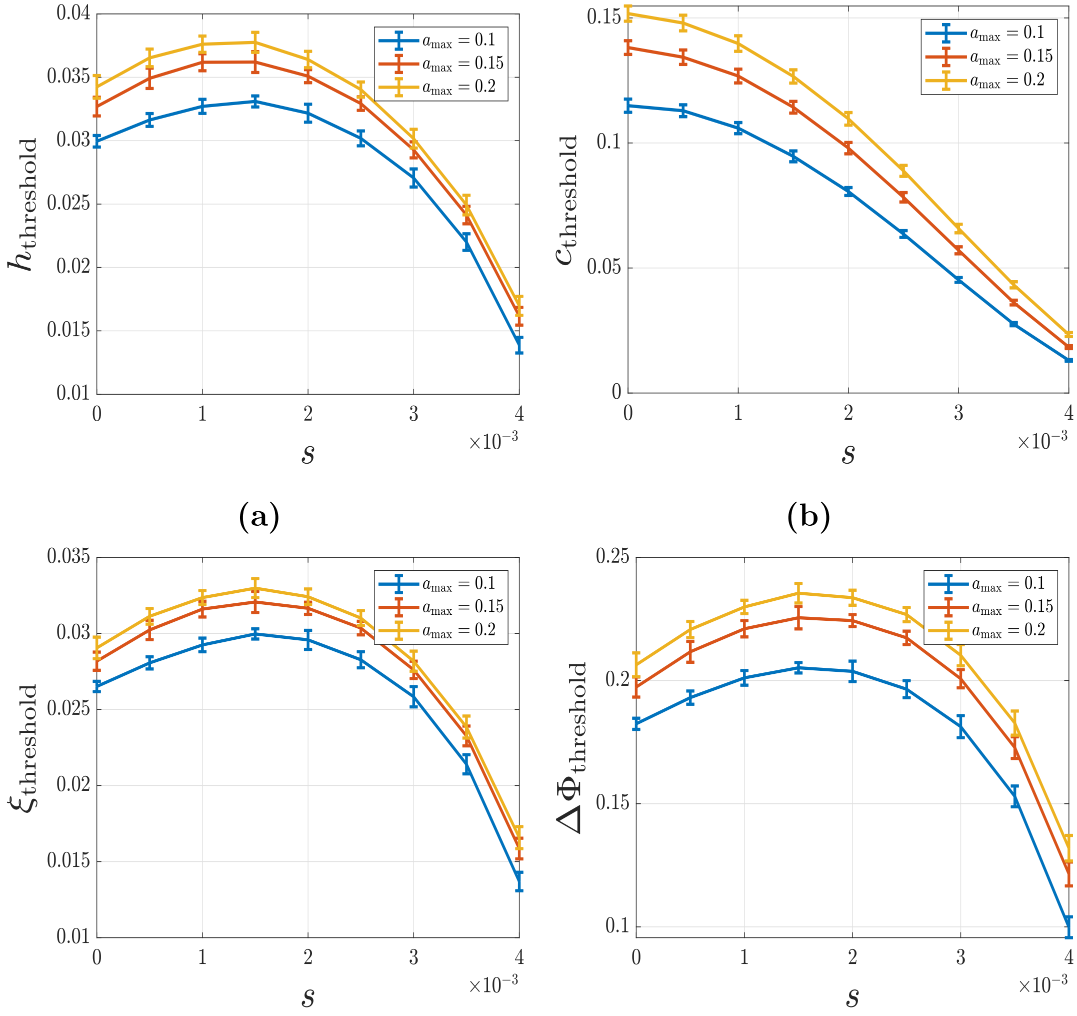

(a) (b)

(c) (d)

Figure 5.7 (a) Total throughput; (b) ACO; (c) filter mass capacity; and (d) porosity usage. Flux Threshold is 2×10^{-6}.

Figure 5.7 shows the performance metrics of radius-graded membrane networks where filtration is halted after the flux level drops below 2×10^{-6}, which is approximately 30% of the initial flux for uniform networks, and roughly 80% of that for the steepest-graded network with gradient value $s = 4 \times 10^{-3}$ (see the vertical scale of Figure 5.2b). From this observation alone, we anticipate that filters with smaller initial fluxes, namely, networks with large radius gradients, are more prone to halt filtration prematurely and are thereby disadvantageous under this filtration mode.

In Figure 5.7a, we plot total filtrate throughput against radius gradient for radius-graded networks that operate until they reach the imposed flux level. We again observe a maximizing radius gradient value, but note that its value at $s = 1.5 \times 10^{-3}$ is smaller than that in Figure 5.2a ($s = 2 \times 10^{-3}$), where networks operate until flux extinction. Thus, under the new threshold-based stopping criterion, filters with smaller radius gradient (and hence larger initial flux) are more favored in terms of throughput production. In fact, networks with $s \geq 3 \times 10^{-3}$ underperform more significantly than the uniform networks because their total filtering time is greatly shortened due to the imposed flux threshold. Figure 5.7b shows accumulated concentration of foulant against radius gradient. Here, we observe a monotone trend in both radius gradient s and in maximal pore length $a_{\max}$. These trends maintain qualitatively the same shape and order of magnitude as seen in Figure 5.2c, though we observe that here the concentration is pointwise (for every s) larger than that in Figure 5.2c. This is expected because filtration is stopped prematurely. In Figure 5.7c, we show the relationship between filter mass capacity and radius gradient under the flux threshold. We observe also a smaller maximizing radius gradient than in Figure 5.2d. This change is consistent with Figures 5.7a and 5.7b by the definition of capacity (Equation (5.27c)). Lastly, we present the membrane porosity usage against radius gradient in Figure 5.7d to correlate with Figure 5.7c. Indeed, the trends in both figures are very similar.

The results in Figure 5.7 imply that with the imposed lower threshold on fluid flux, membrane networks with a radius gradient of $s = 1.5 \times 10^{-3}$ should be preferred over others due to their combined score of filtrate production, particle retention capabilities, filter mass capacity and porosity usage. Once again, we note that this optimal value is independent of maximal pore lengths considered and thus is not influenced by membrane geometry. We would, however, anticipate that the optimal radius gradient will change (increase) if the imposed lower flux threshold is changed.

5.7 Ending Remarks

In conclusion, we have devised a general procedure to generate pore-size-graded banded membrane pore networks. We have studied the influence of the pore-size (radius) gradient s, and maximal pore length $a_{\max}$, on the performance metrics of these networks, under two setups of relevance to applications – filtration until flux extinction, or until a flux lower threshold is reached. We have also determined optimizing radius gradient values for some of the performance metrics considered (compiled in Table 5.3).

When filters run to extinction, we find that total filtrate throughput satisfies a non-monotone trend against pore radius gradient. More precisely, for the parameters we studied, membrane networks with a pore radius gradient value of $s = 2 \times 10^{-3}$ achieve maximal total filtrate throughput. However, accumulated foulant concentration at the membrane outlet is monotonically decreasing in s, suggesting that, for foulant control purposes only, one should prefer membrane networks with a radius gradient as large as possible. A metric that attempts to combine these two requirements is the mass capacity of the membrane, defined as the product of total throughput and accumulated foulant concentration in the membrane interior (per Equation (5.27c)). This quantity is also found to be non-monotone in s, with a pronounced maximum achieved at a pore-radius-gradient value of $s = 2.5 \times 10^{-3}$. This trend is affirmed by further investigation on band porosity evolution, where we observe a strong correlation between filter mass capacity and porosity usage in downstream bands of the membrane.

However, when we stop the filtration at a prescribed minimum flux level, we observe more universal behaviours in terms of performance metrics. For the chosen

Table 5.3 Optimal Radius Gradient Value for Each Performance Metric

Performance Metric (Section 5.4)	Metric Symbol	Optimal Radius Gradient
Until flux extinction		
Total throughput	h_{final}	2×10^{-3}
Initial flux	$q_{\text{out}}(0)$	0
Accumulated concentration of foulant at membrane outlet	c_{final}	0
Filter mass capacity	ξ	2.5×10^{-3}
Membrane porosity usage	$\Delta\Phi$	3×10^{-3}
Until flux threshold		
Total throughput	$h_{\text{threshold}}$	1.5×10^{-3}
Accumulated concentration of foulant at membrane outlet	$c_{\text{threshold}}$	0
Filter mass capacity	$\xi_{\text{threshold}}$	1.5×10^{-3}
Membrane porosity usage	$\Delta\Phi_{\text{threshold}}$	1.5×10^{-3}

model parameters, total filtrate throughput, filter capacity and porosity usage are all maximized at a radius gradient value of $s = 1.5 \times 10^{-3}$, while accumulated foulant concentration at membrane outlet remains a monotone decreasing function in radius gradient. The fact that we observe a smaller optimal radius gradient than that in the former filtration setup is mainly because of the advantage given to filters with large initial flux. Uniform networks benefit from this practice as we clearly see them rise up the ranks into the better performing filters. At the same time, graded networks with large radius gradients perform poorly because they tend to halt prematurely due to their small initial fluxes inflicted by the high-resistance downstream pores. We also anticipate that the optimal gradient value(s) for performance metrics considered in this chapter will depend on the flux threshold we impose (indeed, we expect that $s = 0$ may become the optimal value when the imposed flux threshold is small enough).

We also found that the observed trends in pore radius gradient persist for all values of the maximal pore length $a_{\max}$ considered. This suggests that our findings of how performance metrics depend on pore radius gradient are independent of variations in membrane interior microstructure (characterized by $a_{\max}$) and solely dependent on the variations in radius gradient.

For future work, we will include intra-layer pore size variations in radius graded banded networks. One analytical result based on the governing equations derived from our model of this chapter suggests that membrane networks with constant band radius achieve zero flux only when all inlets on membrane top surface have closed. In other words, filtration does not halt due to critical disconnections in the interior of the network but only when the radii of all inlets on the top surface have vanished. With intra-layer pore size variations, adsorptive behaviours at the global scale may become more complicated and more interesting than the constant band radius case. Additionally, other fouling mechanisms such as sieving may be introduced to provide a fuller view of the membrane filtration process. Furthermore, though we did not vary

λ (a band-independent parameter that captures particle-membrane affinity) in this study, we anticipate that variations in λ will only shift the results vertically without affecting the overall trend in radius gradient. An idea for future work would be to introduce band specific λ_k's, which represent multilayered membrane filters consisting of different materials.

CHAPTER 6

CONCLUSIONS AND FUTURE WORK

Here, we conclude the findings from previous Chapters and present some ongoing and future work. In Section 6.1, we highlight the essentials of the constructed mathematical models and summarize important messages from this dissertation. In Section 6.2, we present two open questions with some supporting preliminary details.

6.1 Conclusions

In Chapter 2, we explored the effect of intra-layer pore interconnectivity and pore size heterogeneity in multilayered membrane filters via three simple layered pore structures (representing basic building-blocks of a membrane): single-inlet non-connected branching pores; single-inlet connected pores; and two-inlet connected pores (see Figure 2.4). We found that for homogeneous models (membranes with the same initial pore radius in each layer), the relative performance of the structures is not strongly influenced by intra-layer connections. However, this observation did not persist in the heterogeneous case, when the pore size in each layer was perturbed by uniform noise. There, we discovered that the performance metrics of non-connected pore structures incur much wider variations as perturbation strength increases than the relatively robust connected models. As a result, intra-layer connectivity should be favored as part of the membrane design when the membrane has intrinsic or manufactured pore size variations.

In addition to the findings on the influence of intra-layer connectivity and pore size heterogeneity, we also observed some other curious phenomena. For instance, we saw that foulant concentration at the membrane outlet may increase over time because the rate of particle advection temporarily dominates that of particle deposition on the wall during pore constriction. Another example pertained to the effect of increasing the magnitude of the pore-size perturbations (the “noise strength”) on the average initial resistance of the three considered membrane pore structures. We found that the initial resistance of the single-inlet connected membrane does not always decrease as noise strength increases, but that of the two-inlet case does. This observation suggested that a two-inlet (or multi-inlet) connected membrane design is favorable.

In Chapter 3, we generalized the models of Chapter 2 to a network of connected pores. We first devised a random graph generation protocol designed to mimic real membrane pore networks. Pore junctions are connected when they lie within a certain maximal pore length, but outside a prescribed minimal distance. We then formulated the fluid flow, foulant advection and pore radius evolution first in each pore and then on the entire network using conservation principles. This system of equations was expressed as weighted graph operators acting on physical quantities such as pressure and foulant concentration at each pore junction. Meanwhile, these weighted graph operators fully characterized how the pores are connected. All simulations in this chapter assumed that the pores in the network have the same initial radius.

The main findings of Chapter 3 were two strong relationships between selected membrane geometric factors and performance metrics, nearly independent of model input parameters such as the maximal pore length (which we vary in our simulations). First, we found that membrane total throughput satisfies a power law against initial membrane porosity. This relation was particularly strong when initial porosity is larger than 0.5, a typical range for real commercial membrane filters. Second, we noted that the accumulated foulant concentration at the membrane outlet satisfies a negative exponential relationship against membrane tortuosity (the average normalized distance travelled by a fluid particle from membrane inlets on the top surface to outlets on the bottom surface). We also provided a primary recommendation for industrial practitioners: one should always favor membrane networks with shorter characteristic pore lengths, whether the industrial requirement is on minimal foulant concentration threshold or a fixed amount of filtration production.

In Chapter 4, we extended the general network model of Chapter 3 to include pore size (radius) variations as a model for manufacturing defects/inhomogeneities of the membrane pores. To model the pore size variations, we perturb each pore radius by a uniformly distributed noise with prescribed amplitude. We simulated the fluid flow, foulant advection and pore radius evolution on this network for a variety of noise distribution widths, and studied their influence on membrane performance metrics. We also compared this influence to the impact of network variations due to the random network generation procedure. Lastly, by noting that pore size variations inevitably change initial membrane porosity (an influential feature as noted in Chapter 3), we constructed porosity-corrected performance metrics, that is, a score involving the change in the chosen metric relative to that of an equivalent uniform pore-size network with equal porosity.

Our main finding was that the effect of pore size variations on membrane performance is eclipsed by that of network variations inherent to the random network generation protocols, unless the amplitude of the noise added to the pore sizes is overwhelmingly large. We further confirmed that initial membrane porosity is an important feature of the filter, by studying the trends of porosity-corrected performance metrics against noise amplitude. Lastly, we showed that having pore size variations appears to be a double-edged sword as regards membrane performance – it increases both total throughput (favorable) and accumulated foulant concentration in the filtrate (unfavorable) as the noise amplitude increases.

In Chapter 5, we studied fluid and foulant advection on pore size-graded networks and investigated how pore size gradient influences membrane performance metrics. We first constructed banded networks (large pores upstream, small pores downstream) that are natural extensions of the networks used in Chapters 3 and 4.

We reduced the size of the parameter space to study by enforcing two constraints: equal porosity in each band of the network; and fixed average pore radius across all bands, for any radius gradient considered. The goal was to quantify the effect of pore size gradient on performance metrics under two industrial standards – running the filtration until 1) zero flux or 2) a prescribed flux lower threshold.

Under the first standard, our results suggest that there is a radius gradient value that maximizes total throughput. Accumulated foulant concentration at membrane pore outlets appears to be a monotone decreasing function of radius gradient. Particle retention capability of the membrane (the total mass of impurity retained by the membrane over its lifetime) also appears to be optimized by a certain pore radius gradient (smaller than that which maximizes throughput). Within the limitations of our study, all findings were independent of maximal pore length, suggesting that the conclusions may be universal for the considered membrane pore structures.

Under the second standard where filtration is halted at some prescribed flux level, we found that the aforementioned trends from the first standard persisted, however, with optimal radius gradients shifting to smaller values. We believe this phenomenon is due to the flux-based cutoff adding much weight to the initial flux that such networks admit, a quantity that may be small for the more severely graded networks due to the relatively large initial resistance originating from their smaller downstream pores.

Through the main body of this dissertation, we have noticed the convenience and significance of the general pore network model. It lends to a systematic formulation of simple fluid dynamics on complicated geometries by capturing the network structure with conservation laws. We find this approach particularly promising as a general study of membrane filtration problems and look forward to applying it to other interesting dynamical problems posed on networks.

6.2 Future Work

In this section, we provide some basic setups for two future projects. In Section 6.2.1, we consider intra-layer pore radii variations in the banded networks introduced in Chapter 5 and explain the numerical procedures that generate radius-graded banded networks with prescribed physical and statistical constraints. In Section 6.2.2, we discuss membrane filtration in a network of pores with adsorption and sieving operating simultaneously. We investigate how the two fouling mechanisms interact and affect the performance of membrane networks in terms of total throughput and accumulated foulant concentration.

6.2.1 Non-constant Band Radius for Pore-size Graded Networks

In this section, we explain the necessary modifications to the procedure shown in Section 5.3.1 in order to incorporate pore size variations in each band. By this point, we already know the constant band radius R_k that follows Equation (5.1). We start by fixing a single network as generated in Section 5.3.1 with radius gradient s and initial band pore radii R_k. Our goal then is to determine the statistical parameters, namely, mean and standard deviation, of the pore radius distribution so that the *average* porosity is the same for each band (similar to Equation (5.5)).

We assume that $R_{k,ij}$, the radius in the k^{th} band for pore e_{ij}, follows some pore size distribution F_k (with nonnegative support). We denote the expectation operator, the mean and variance under this distribution by $\mathbb{E}[\cdot]$, μ_k and σ_k^2, respectively. The average band porosity satisfies

$$\mathbb{E}[\Phi_k] = \frac{\frac{\pi}{2}\mathbb{E}\left[R_{k,ij}^2\right]\sum_{e_{ij}\in E} L_{k,ij}}{W^3/m} = \frac{\frac{\pi}{2}\left(\mu_k^2+\sigma_k^2\right)\sum_{e_{ij}\in E} L_{k,ij}}{W^3/m}, \tag{6.1}$$

where we use the definition of the second moment of a probability distribution.

For each band, we have two unknown parameters μ_k and σ_k^2, for which we provide two constraints as follows. First, we set

$$\mu_k^2 + \sigma_k^2 = R_k^2, \tag{6.2}$$

where R_k is the constant band radius introduced in Equation (5.1) in Section 5.3.1. This ensures that the average band porosity $\mathbb{E}\left[\Phi_k\right] = \Phi_k^{\text{const}}$ (see Equation (5.6)), for $k = 1, \ldots, m$.

Second, we set

$$\mathrm{CV}_k := \frac{\sigma_k}{\mu_k} = \alpha, \quad k = 1, \ldots, m, \tag{6.3}$$

where CV_k is known as the Coefficient of Variation (CV in short) of the distribution F_k. Setting CV_k equal to some prescribed value α for every band ensures that the extent of pore radius variation relative to the mean radius is the same. We refer to α as the self-similarity constant and study the influence of its variations on membrane network properties and performance.

We observe that implementing Equations (6.2) and (6.3) yields a different gradient for the average band radius $\mathbb{E}\left[R_{k,ij}\right]$. Indeed, using both constraints, we have

$$\mu_k = \frac{R_k}{\sqrt{1+\alpha^2}} \tag{6.4}$$

which implies that the average band radius has a gradient of $\frac{s}{\sqrt{1+\alpha^2}}$. This makes sense because when $\alpha = 0$, we retrieve the constant band radius case.

Altogether, for a fixed network generated from Section 5.3.1 with gradient s, we now have devised a pore radius distribution F_k for the k^{th} band, with mean μ_k and variance σ_k^2 prescribed by Equations (6.2) and (6.3). We present an example distribution below.

Example 1. *If* F_k *is a log-normal distribution with parameter pair* $\left(\mu_{k,\mathrm{p}}, \sigma^2_{k,\mathrm{p}}\right)$*, determined by the desired mean pore size* μ_k *and variance* σ_k^2 *(and thus* $\overline{R_k^2}$ *is also known), then*

$$\mu_{k,\mathrm{p}} = \ln\left(\frac{\mu_k^2}{\sqrt{\mu_k^2+\sigma_k^2}}\right), \quad \sigma^2_{k,\mathrm{p}} = \ln\left(1+\frac{\sigma_k^2}{\mu_k^2}\right). \tag{6.5}$$

6.2.2 Sieving

The motivation for this section originates partly from experiments and numerical simulations conducted by Beuscher [13]. In that work, mono-sized spherical particles were sent through several layers of parallel circularly-cylindrical tubes with various radii. Each particle traverses through the layers until it encounters a tube with radius smaller than its own. This size exclusion mechanism, or *sieving*, eventually fouls the multilayered membrane filter.

In practice, the sieving process involves particles of size comparable to the pore sizes (simply, *sieving particles*, hereafter). The blockage time scale is also much shorter than that of adsorption. Sieving manifests in primarily two ways characterized by the extent of blockage – *complete blocking* and *incomplete blocking*. In the former case, sieving particles completely cover an inlet or clog a pore throat in the interior of the membrane, prohibiting local fluid flow henceforth. In the latter case, sieving particles partially cover the entrance of a pore throat and thus impede (but not completely prohibit) fluid flow by significantly narrowing the size of the entrance in a short amount of time (occurs much faster than adsorption). Feed solution still leaks through the partially blocked channel but at a considerably smaller volumetric flow rate. Due to the different natures of the sieving process in the two cases, we make a distinction between complete and incomplete blocking in our discussion.

Assumptions

We introduce some general assumptions about the sieving process and then provide the proper definitions to set up the numerical simulation. We will continue to use terminology defined for the graphical representation of a membrane network in Section 3.3.

Sieving particles in the feed solution are assumed to arrive at the membrane top surface following a Poisson process $N(T)$ with rate Γ, *i.e.,*

$$\text{Prob}\left(N\left(T\right)=k\right)=\frac{\left(\Gamma T\right)^{k}}{k!}e^{-\Gamma T},\quad k=0,1,2\ldots. \tag{6.6}$$

where $\text{Prob}\left(N\left(T\right)=k\right)$ is the probability of having k arrivals by time T. Particle sizes S_k (indexed by arrival) are independent and identically distributed (i.i.d.) with cumulative distribution function F, *i.e.,*

$$\text{Prob}\left(S_k<s\right)=F\left(s\right).$$

When the k-th particle of size S_k arrives at the entry of a particular edge (pore) e_{ij}, a size comparison is made: if the particle is strictly smaller than the radius of the edge R_{ij}, it will immediately pass through and arrive at the vertex j (pore junction). The subsequent direction of particle movement at the junction is governed by *preferential flow* (defined more precisely in the next subsection) — the larger the flux in an edge, the more likely the particle will take that route. A particle will continue to travel in this fashion through the membrane until either it enters an edge with radius smaller than (or equal to) its size and thereby blocks the pore; or it exits the membrane.

We also consider the following general assumptions that apply to any sieving process considered in this work.

Assumption 1. *We assume the following:*

1. *Blocking is irreversible, i.e., once an edge is blocked, it cannot be unblocked.*

2. *The size and the arrival of sieving particles are independent.*

Probabilistic Setup

We simulate blocking by first generating Poisson arrival times according to Equation (6.6). At each arrival time, a particle arrives at the top surface and chooses the entrance (any $v_i \in V_{\text{top}}$) with probability proportional to the flux outgoing v_i relative to the total flux from all $v_i \in V_{\text{top}}$. The sieving particle then goes through a series of size comparisons to the edge it attempts to go through. If the particle exits an edge, it will go to one of the neighboring downstream pores via the edge that connects them with probability determined by *preferential flow*, described more precisely below.

The general setup would be similar to that of Chapter 3. We first solve the discrete Laplace equation on the graph $G = (V, E)$ for pressure p with conductance as weights. Then we determine the flux matrix Q (also known as the in-degree flux weighted Laplacian) via Hagen-Poiseuille. Sieving particles perform a random walk following a transition matrix $\mathcal{P}$ obtained by normalizing the flux matrix by each row.

Definition 7. *(Preferential flow) Let $v_i \in V_{\text{top}} \cup V_{\text{int}}$. For $v_j \in \mathcal{N}(i)$ (neighbors of v_i), the probability of moving from v_i to v_j (via e_{ij}) is defined by*

$$\mathcal{P}_{ij}(T) := \text{Prob}\{v_i \to v_j\} = \begin{cases} \frac{\mathbf{Q}_{ij}(T)}{\sum_{v_j \in \mathcal{N}(i)} \mathbf{Q}_{ij}(T)}, & \forall v_i \in V \backslash V_{\text{bot}} \\ 0, & \text{otherwise} \end{cases}, \tag{6.7}$$

$$\pi_{0,i} = \begin{cases} \frac{\sum_{v_j \in \mathcal{N}(i)} \mathbf{Q}_{ij}}{\sum_{v_i \in V_{\text{top}}} \sum_{v_j \in \mathcal{N}(i)} \mathbf{Q}_{ij}}, & \forall v_i \in V_{\text{top}} \\ 0, & \text{otherwise} \end{cases} \tag{6.8}$$

where $\mathbf{Q}_{ij}(T)$ is the (local) flux that goes from vertices v_i and v_j through the edge e_{ij}, $\mathcal{N}(i)$ the set of neighbors adjacent to v_i, and π_0 the initial distribution of the position of sieving particle on the top surface of the membrane.

$\mathcal{P}$ is referred to as the normalized in-degree adjacency. Note that the neighbor set $\mathcal{N}(i)$ over which we sum the i-th row of $\mathbf{Q}$ works consistently with the definition of flux-weighted adjacency matrix $\mathbf{Q}$ as it contains only positive entries for flux to go from an upstream pore to a downstream one (while the reverse direction incurs zero flux). The initial distribution μ_0 of the random walker (representing the sieving particle) is the probability of entering the membrane at each vertex on the membrane surface. It is quantified by the proportion of outgoing flux at each vertex on the membrane surface relative to the total outgoing flux from all vertices on the membrane surface.

In light of Equation (6.7), we consider that sieving particles will more likely go to the downstream pore that has higher flux. One can view its motion as a random walker following the flow. More precisely, we say that a random walk (k-th arrived particle, k arbitrary) with position $Y_k \in V$ follows the one-step transition matrix $\mathcal{P}$ on V. By standard Markov chain terminology, $Y_k^{(n)}$ is the position of the random walk after n transitions that abides the n-step transition matrix $\mathcal{P}^n$, *i.e.,* n-th power of $\mathcal{P}$.

We say that under both adsorption and blocking, the conductance of the edge e_{ij} is given by

$$\mathbf{K}_{ij}\left(T\right) = \frac{\pi R_{ij}^4\left(T\right)}{8\mu A_{ij}} \mathbf{1}_{\{e_{ij} \text{ open}\}}\left(T\right), \tag{6.9a}$$

$$\overline{\mathbf{K}}_{ij}\left(T\right) := \mathbb{E}_{\text{Pois}}\left[\mathbf{K}_{ij}\left(T\right)\right] = \frac{\pi R_{ij}^4\left(T\right)}{8\mu A_{ij}} \alpha_{ij}\left(T\right), \tag{6.9b}$$

where $\alpha_{ij}\left(T\right)$ is the unconditional probability that the edge e_{ij} is open by time T (a cumulative probability). In other words, $\alpha_{ij}\left(T\right)$ describes the proportion of time that pore ij is open. We consider Equation (6.9a) as a simulation-based approach, while Equation (6.9b), the mean-field counterpart under the Poisson measure, is to describe the average effect of blocking on the conductance of the pore.

In the latter analytical approach, we are thus interested in calculating $\alpha_{ij}\left(T\right)$, which should contain factors involving arrival, transition on the graph and particle size distribution. Using standard theory of the Poisson process, we need to characterize the instantaneous probability of a blocking particle arriving at pore ij, labelled as $\beta_{ij}(T)$. Then, $\alpha_{ij}(T)$ is equivalent to the probability of observing zero arrival of blocking particles at this edge. More precisely,

$$\alpha_{ij}(T) = e^{-\Gamma \int_0^T \beta_{ij}(T')dT'}. \tag{6.10}$$

We will utilize the network structure by describing the relationship between the instantaneous blocking probability of β_{ij} and those of the upstream neighbors of the edge ij (by now we know the direction of flow via $\mathbf{Q}$). The key is to define a Markov chain operating on edges with a proper transition matrix. Each entry of the matrix depends on the state of all edges. This argument may be adapted from the mean-field theory of Markov chains such as [5, 58, 57, 129, 124] and dynamical systems on networks [101].

APPENDIX A

SUPPLEMENTARY MATERIAL FOR CHAPTER 2

In this appendix, we provide a brief numerical justification of the coarse-grained model introduced in Section 2.3 and the parameter value λ.

A.1 Norms for Accuracy and Sufficient Penetration

Consider the homogeneous model. Let $a_i(x,t)$ and $\hat{a}_i(x,t)$ be the radii in the i-th layer, found from the solutions of the continuum model and the coarse grained model, respectively (see Equations (2.8)–(2.10), and Equations (2.11)–(2.13)). We solve both models numerically using the same time step. We wish to ensure a sufficiently accurate coarse-grained approximation $\hat{a}_i$ to a_i, as well as identify parameter regimes that lead to particle penetration to some specified depth of the membrane. More precisely, we look for parameter pairs (m, λ) that satisfy the following conditions,

1. Accuracy:

   $$\left\| a_i(x,t) - \hat{a}_i(x,t) \right\|_{L^\infty(\mathbb{R}^+;L^2(\Omega_i))} < \delta_1,\ i = 1, 2, \dots, N < m,$$

   where

   $$\Omega_i = \left\{ x : \frac{i-1}{m} < x < \frac{i}{m} \right\}, \quad N = \lfloor \beta m \rfloor,\ 0 < \beta < 1;$$

   and

   $$\|f\|_{L^\infty(\mathbb{R}^+;L^2(\Omega_i))} = \sup_{t \geq 0} \left(\int_{\Omega_i} |f(x,t)|^2 \, dx \right)^{\frac{1}{2}}.$$

2. Sufficient penetration:

   $$\frac{\left\| a_N(x,0) - a_N(x,t_{\text{final}}) \right\|_{L^2(\Omega_N)}}{\left\| a_N(x,0) \right\|_{L^2(\Omega_N)}} > \delta_2.$$

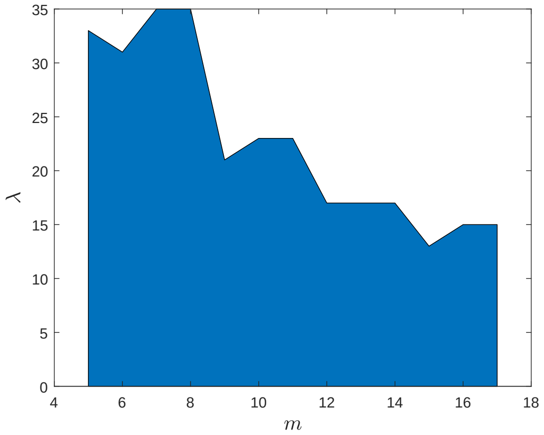

Figure A.1 Single-inlet model: region of parameters that are δ_1-accurate and allow sufficient δ_2 penetration. Parameter choice: $\delta_1 = 0.05$, $\delta_2 = 0.3$, $\beta = \frac{1}{3}$, $r_0 = 1$, $\phi_{\text{top}} = 0.4$.

For (i), we consider the L^2 error in space, which essentially records the volume of each pore. Once we find $\text{error}_i\,(t) := \|a_i\,(x,t) - \hat{a}_i\,(x,t)\|_{L^2(\Omega_i)}$, we compute its maximum (or L^∞ norm) over all time and compare it to our tolerance δ_1. We only check accuracy up to a certain layer depth, controlled by the parameter N.

For (ii), we measure the relative L^2 difference of the radius of a pore in the N-th layer, between times $t = 0$ and $t = t_{\text{final}}$. We desire that a sufficient amount of its volume is occupied by particles at the final time, with δ_2 as a minimum threshold. N is technically arbitrary but should be chosen with care. For example, if we desire roughly 30% of the membrane to be penetrated, we put $\beta = 0.3$. The floor function simply ensures that N is an integer.

We refer to Figure A.1 for a region of parameter pairs (m, λ) for the single-inlet model, with $\delta_1 = 5 \times 10^{-2}$, $\delta_2 = 0.3$ and $\beta = \frac{1}{3}$ while other membrane geometric parameters are held fixed.

A.2 Calculations and Proofs

Proof of Theorem 1

The two main non-dimensional equations associated with Theorem 1 are Equations (2.32) and (2.33), where $d_i = 1/m$. Note that Equation (2.33) can be viewed as a recurrence relation as follows:

$$c_i\left(t\right) = \left(\frac{1}{1+\frac{\lambda}{m a_i(t)\overline{u}_{\mathrm{p},i}(t)}}\right) c_{i-1}\left(t\right), \tag{A.1}$$

$$a_i'\left(t\right) = -c_{i-1}\left(t\right), \tag{A.2}$$

(where prime denotes d/dt) with initial and boundary conditions

$$c_0\left(t\right) = 1, \quad a_1\left(0\right) = a_0, \quad a_i\left(0\right) = a_0\kappa^{i-1},\ i = 1, \ldots, m.$$

Proof. Iterating Equation (A.1) m times on i, we obtain

$$c_m\left(t\right) = \prod_{j=1}^{m}\left(\frac{1}{1+\frac{\lambda}{m a_j(t)\overline{u}_{\mathrm{p},j}(t)}}\right),$$

where we used $c_0\left(t\right) = 1$ for all $t > 0$. Using Equation (2.32), we rewrite $c_m\left(t\right)$ as

$$c_m\left(t\right) = \prod_{j=1}^{m}\left(\frac{1}{1+\eta\nu_j a_j\left(t\right) r\left(t\right)}\right) =: \prod_{j=1}^{m} f_j\left(t\right), \tag{A.3}$$

where $\eta = \pi\lambda/(4m)$.

To derive a condition for the existence of a maximum, we first characterize the end time behaviour of $c_m\left(t\right)$. Using Equation (2.43), we see that

$$a_j\left(t\right) r\left(t\right) = \frac{a_j\left(t\right)}{\hat{r}_0}\sum_{i=1}^{m}\frac{d_i}{\nu_i a_i^4(t)} \to \infty, \text{ as } t \to t_{\text{final}},$$

which implies $c_m\left(t\right) \to 0$ as $t \to t_{\text{final}}$. Note that since $a_j\left(t\right) \in \mathcal{C}^1\left(0, t_{\text{final}}\right)$ for all j and all f_j are positive quantities without singularities, $c_m\left(t\right) \in \mathcal{C}^1\left(0, t_{\text{final}}\right)$. Hence by the mean value theorem, $c_m\left(t\right)$ will achieve a maximum whenever $c_m'\left(0\right) > 0$.

Taking a time derivative of $c_m(t)$ using the product rule of multiple functions, we have

$$c'_m(t) = \prod_{j=1}^{m} f_j(t) \sum_{j=1}^{m} \frac{f'_j(t)}{f_j(t)} \tag{A.4}$$

where we can find the derivative of f_j,

$$f'_j(t) = \frac{-\eta\nu_j \left(a'_j(t) r(t) + a_j(t) r'(t)\right)}{\left(1 + \eta\nu_j a_j(t) r(t)\right)^2} = -\eta\nu_j \left(r(t) a'_j(t) + a_j(t) r'(t)\right) f_j^2(t). \tag{A.5}$$

We combine Equation (A.2) with Equation (A.3) to obtain

$$a'_j(t) = -c_{j-1}(t) = -\prod_{i=1}^{j-1} f_i(t), \quad 2 \le j \le m, \tag{A.6}$$

$$a'_1(t) = -c_0(t) = -1 =: -f_0(t). \tag{A.7}$$

Inserting Equations (A.5)–(A.7) into Equation (A.4) and evaluating at $t = 0$, we have

$$c'_m(0) = -\eta \left(\prod_{j=1}^{m} f_j(0)\right) \left[\sum_{j=1}^{m} \nu_j f_j(0) \left(-r(0) \left(\prod_{i=0}^{j-1} f_i(0)\right) + a_j(0) r'(0)\right)\right],$$

whence we see that $c'_m(0) > 0$ is equivalent to

$$\sum_{j=1}^{m} \nu_j f_j(0) \left(-r(0) \left(\prod_{i=0}^{j-1} f_i(0)\right) + a_j(0) r'(0)\right) < 0, \tag{A.8}$$

as η and f_j are positive quantities.

Using Equation (2.43) to express $r(t)$, its time derivative, and the initial conditions for $a_i(0)$ in Equation (A.8),

$$r(t) = \frac{1}{m\hat{r}_0} \sum_{i=1}^{m} \frac{1}{\nu_i a_i^4(t)}, \quad r'(t) = -\frac{4}{m\hat{r}_0} \sum_{i=1}^{m} \frac{a'_i(t)}{\nu_i a_i^5(t)},$$

we arrive at the following equivalent condition to $c'_m(0) > 0$,

$$\left(\sum_{j=1}^{m} \nu_j \prod_{i=0}^{j} f_i(0)\right) \left(\sum_{j=1}^{m} \frac{1}{\nu_j \kappa^{4(j-1)}}\right) > 4 \left(\sum_{j=1}^{m} \frac{\prod_{i=0}^{j-1} f_i(0)}{\nu_j \kappa^{5(j-1)}}\right) \left(\sum_{j=1}^{m} \nu_j \kappa^{j-1} f_j(0)\right).$$

□

Analytical Formula for $\mathbb{E}\left[r_b\left(0\right)\right]$

Given the form of the initial resistance with random perturbations in Equation (2.50), we can explicitly compute

$$\mathbb{E}\left[r_b\left(0\right)\right] = \mathbb{E}\left[\frac{a_0^{-4}}{\hat{r}_0}\sum_{i=1}^{m} d_i\left(\sum_{j=1}^{\nu_i}\left(1+\epsilon_{ij}\right)^4\right)^{-1}\right] = \frac{a_0^{-4}}{\hat{r}_0}\sum_{i=1}^{m} d_i\mathbb{E}\left[\frac{1}{\sum_{j=1}^{\nu_i}\left(1+\epsilon_{ij}\right)^4}\right]$$

where the last step follows by linearity of expectations. We now compute the expectation in the summand with a fixed index i. First, since $\epsilon_{ij} \sim U\left(-b,b\right)$, it has cumulative distribution function $F_{\epsilon_{ij}}\left(x\right) = \frac{x+b}{2b}$. Therefore, if we define $Y_{ij} = \left(1+\epsilon_{ij}\right)^4$, then

$$F_{Y_{ij}}\left(y\right) = \mathbf{P}\left(\left(1+\epsilon_{ij}\right)^4 \le y\right) = \mathbf{P}\left(\epsilon_{ij} \le y^{\frac{1}{4}} - 1\right) = \frac{y^{\frac{1}{4}} - 1 + b}{2b}, \quad \left(1-b\right)^4 \le y \le \left(1+b\right)^4,$$

and thus the probability density of Y_{ij} is

$$f_{Y_{ij}}\left(y\right) = F'_{Y_{ij}}\left(y\right) = \frac{1}{8b}y^{-\frac{3}{4}}, \quad \left(1-b\right)^4 \le y \le \left(1+b\right)^4.$$

Employing the following integral statement,

$$\mathbb{E}\left[\frac{1}{X_1+\ldots+X_n}\right] = \mathbb{E}\left[\int_0^\infty e^{-t\left(X_1+\ldots+X_n\right)}dt\right],$$

where the expectation is taken with the density $f_{Y_{ij}}$, we have (via Fubini's theorem to justify the swapping of expectation and integration)

$$\mathbb{E}\left[\frac{1}{\sum_{j=1}^{\nu_i} Y_{ij}}\right] = \mathbb{E}\int_0^\infty e^{-t\sum_{j=1}^{\nu_i} Y_{ij}}dt = \int_0^\infty \mathbb{E}\left[e^{-t\sum_{j=1}^{\nu_i} Y_{ij}}\right]dt. \tag{A.9}$$

By the independent identically distributed assumption (of ϵ_{ij} and thus Y_{ij}), we rewrite the integrand as

$$\mathbb{E}\left[e^{-t\sum_{j=1}^{\nu_i} Y_{ij}}\right] = \left(\mathbb{E}e^{-tY_{i1}}\right)\ldots\left(\mathbb{E}e^{-tY_{i,\nu_i}}\right) = \left[\mathbb{E}e^{-tY}\right]^{\nu_i},$$

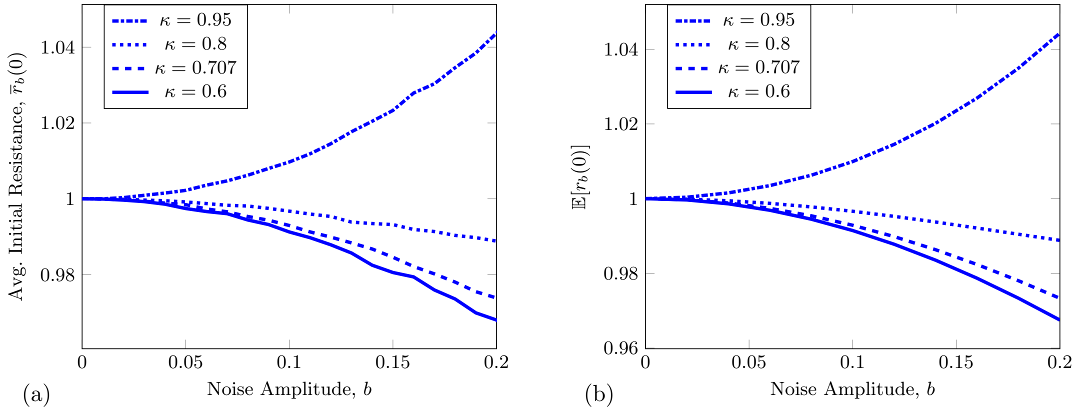

Figure A.2 Heterogeneous models: initial resistance for single-inlet model (a) Average $\bar{u}_b(0)$ over 10^5 simulations; (b) exact large number limit $\mathbb{E}[r_b(0)]$.

where we defined $Y \overset{d}{=} Y_{ij}$, which exists by the identical distribution assumption. We carry out the computation of the right hand side for Y and find

$$\begin{aligned}
\mathbb{E}\left[e^{-tY}\right] &= \frac{1}{8b}\int_{(1-b)^4}^{(1+b)^4} e^{-ty}y^{-\frac{3}{4}}dy \\
&\overset{z=ty}{=} \frac{1}{8b}\int_{t(1-b)^4}^{t(1+b)^4} e^{-z}\left(\frac{z}{t}\right)^{-\frac{3}{4}}\left(\frac{1}{t}\right)dz \\
&= \frac{1}{8bt^{\frac{1}{4}}}\left[\gamma\left(\frac{1}{4}, t\left(1+b\right)^4\right) - \gamma\left(\frac{1}{4}, t\left(1-b\right)^4\right)\right],
\end{aligned}$$

where $\gamma\left(s, x\right) = \int_0^x t^{s-1}e^{-t}dt$ is the lower incomplete gamma function. Altogether, we have

$$\mathbb{E}\left[r_b\left(0\right)\right] = \frac{a_0^{-4}}{\hat{r_0}}\sum_{i=1}^{m} d_i\kappa^{-4(i-1)}\int_0^{\infty}\left[\frac{1}{8bt^{\frac{1}{4}}}\left[\gamma\left(\frac{1}{4}, t\left(1+b\right)^4\right) - \gamma\left(\frac{1}{4}, t\left(1-b\right)^4\right)\right]\right]^{\nu_i} dt. \tag{A.10}$$

Figure A.2 shows the excellent agreement between the numerical and analytical results.

APPENDIX B

SUPPLEMENTARY MATERIAL FOR CHAPTER 3

In this appendix, we first provide justification for the pore radius evolution model shown in Equation (3.26), then define tortuosity and derive its formula using a probabilistic argument, and lastly set up a worked example that illustrates Algorithm 3.1.

B.1 Justification for the Pore Radius Evolution Model

In this section, we justify the form of the pore radius evolution equation Equation (3.26) using the (exact) solution for the foulant concentration model, Equation (3.18), to relate the rate of change of particle volume accretion inside a single pore to pore radius shrinkage. In the following derivation, we drop the indices ij for notational simplicity and assume that the radius R is spatially constant at each time T (though the arguments can be adapted to the variable radius case with a suitable bound on $\partial R/\partial Y$).

Let V_p be the particle volume. In a single pore (assumed circularly cylindrical), we consider an infinitesimally thin circular disk at distance Y from the pore inlet, with thickness dY. The particle flux difference across this disk is

$$\left(C\left(Y+dY,T\right)-C\left(Y,T\right)\right)\mathbf{Q}\left(T\right)\approx\frac{\partial C}{\partial Y}\left(Y,T\right)\mathbf{Q}\left(T\right)dY, \tag{B.1}$$

i.e., the number of particles per time deposited in the disk. The total particle volume adsorped in this pore is V_p times this quantity. We integrate Equation (B.1) over the length of the pore to obtain the total volume of deposited particles per time in the pore,

$$V_p\mathbf{Q}\left(T\right)\int_0^A\frac{\partial C}{\partial Y}\left(Y,T\right)dY=V_p\mathbf{Q}\left(T\right)\left[C\left(A,T\right)-C\left(0,T\right)\right] \tag{B.2a}$$

$$= V_p \mathbf{Q}(T) \boldsymbol{C}(T) \left(\exp\left(-\frac{\Lambda R(T) A}{\mathbf{Q}(T)} \right) - 1 \right) \tag{B.2b}$$

$$\approx -V_p \boldsymbol{C}(T) \Lambda R(T) A \tag{B.2c}$$

where we used the analytical expression Equation (3.18) for $C(Y,T)$ in the second equality. The final approximate Taylor expansion Equation (B.2c) is justified for sufficiently small values of the exponent, that is (using the scales in Section 3.4), provided

$$\mathbf{q}(t) \gg \lambda r_0 d, \tag{B.3}$$

where d is the largest pore length (see Equation (3.1)).

As foulant particle volume accumulates at the rate given in Equation (B.2c), pore volume $\mathrm{Vol}(T)$ also changes at this rate via

$$\frac{d\mathrm{Vol}(T)}{dT} = -V_p \boldsymbol{C}(T) \Lambda R(T) A. \tag{B.4}$$

At the same time, we relate the volume of the pore to its radius $\mathrm{Vol}(T) = \pi R^2(T) A$ and obtain

$$\frac{d\mathrm{Vol}(T)}{dT} = 2\pi R(T) \frac{dR}{dT} A. \tag{B.5}$$

Equating Equation (B.4) and Equation (B.5), we arrive at the form of Equation (3.26) with $\alpha = \frac{V_p}{2\pi}$.

B.2 Tortuosity

In this section, we define tortuosity of a graph representing a membrane filter pore network, and provide an explicit formula using the geometric and initial flow information from the network (found in Section 3.3). In all of our investigations, we restrict attention to the tortuosity of the initial pore network, with no regard for how it subsequently evolves under fouling, hence in the following discussion it should be understood that we consider properties of the network at time $t = 0$.

We define tortuosity as the average distance travelled by a fluid particle through the membrane via the network, relative to the thickness of membrane W. Now, given a path from any inlet to any outlet, we can associate it with its total initial flux, which we use as a weight for the path. This is equivalent to having the fluid particle perform a discrete random walk on the graph G directed by fluid flux at each junction. More precisely, the transition matrix $\mathbf{P}$ of this random walk is defined as follows. We omit the argument of $t = 0$ for notational simplicity.

We first enforce non-negativity of the flux matrix via the following modification. Consider $\mathbf{Q}_+$ and $\mathbf{Q}_-$, the positive and negative parts of $\mathbf{Q}$ respectively, such that $\mathbf{Q} = \mathbf{Q}_+ + \mathbf{Q}_-$. Owing to the skew-symmetry of $\mathbf{Q}$, we construct

$$\tilde{\mathbf{Q}} = \mathbf{Q}_+ - \mathbf{Q}_-^T, \tag{B.6}$$

which preserves the flow information (direction and magnitude) while enforcing non-negativity.

Definition 8. *(Transition Matrix) Given modified flux matrix $\tilde{\mathbf{Q}}$ in Equation (B.6), the transition matrix $\mathbf{P}$ is determined by rescaling $\tilde{\mathbf{Q}}$ by its row sum:*

$$\mathbf{P}_{ij} = \begin{cases} \dfrac{\tilde{\mathbf{Q}}_{ij}}{\displaystyle\sum_{v_j:(v_i,v_j)\in E} \tilde{\mathbf{Q}}_{ij}}, & (v_i, v_j) \in E, \quad v_i \in V_{\mathrm{top}} \cup V_{\mathrm{int}}, \\ 1, & v_i \in V_{\mathrm{bot}}, \quad j = i, \\ 0, & \textit{otherwise}. \end{cases} \tag{B.7}$$

For vertices in the bottom surface, fluid particles are absorbed, i.e. once they reach any $v \in V_{\mathrm{bot}}$, they stay there with probability one.

Let X_n be a random walk with transition $\mathbf{P}$, i.e. X_n is the vertex after the fluid particle has taken n steps on V. Let $\mathbb{P}$ be the induced probability measure. This random walk has a natural initial distribution (a column vector of length $|V|$),

$$\pi_{0i} = \mathbb{P}\left\{X_0 = v_i\right\} := \begin{cases} \dfrac{\displaystyle\sum_{v_j:(v_i,v_j)\in E} \tilde{\mathbf{Q}}_{ij}}{\displaystyle\sum_{v_i\in V_{\text{top}}} \sum_{v_j:(v_i,v_j)\in E} \tilde{\mathbf{Q}}_{ij}}, & v_i \in V_{\text{top}}, \\ 0, & \text{otherwise}, \end{cases} \tag{B.8}$$

namely, the probability of going to each inlet on the top surface is determined by the proportion of flux going through that inlet, relative to total flux.

Definition 9. *(Tortuosity) Let l_n be the total path length after the random walk has taken n steps. Tortuosity of the graph G is defined by $\mathbb{E}\left[\tau\right]$ where $\tau := \frac{l_m}{W}$ and m is the (deterministic) number of steps of the longest path from any inlet on the top surface to any outlet in the bottom surface.*

The integer m can be understood as a graph diameter where the notion of graph distance for m is encoded in the unweighted adjacency matrix $\mathbf{W}$ (entries are indicators of the existence of an edge). m is trivially bounded above by $|V_{\text{int}}| + 2$ (one step from V_{top} to V_{int} and V_{int} to V_{bot} respectively, and traverse all of V_{int} at worst), which we use here. Although this bound can be tightened by connectivity measures such as the smallest number of vertices that must be removed to disconnect a graph (see Coll *et al.* [27], for example), our algorithm (discussed after proving the formula Equation (B.9)) for $\mathbb{E}\left[\tau\right]$ does not incur significant computational cost from the size of m.

One may estimate this expected value by sending a large number of particles through the network and computing the average of path lengths. We here provide an explicit formula for $\mathbb{E}\left[\tau\right]$ that depends on the transition matrix $\mathbf{P}$ and a distance weight matrix $\mathbf{W}_E$, whose entries are

$$\mathbf{W}_{E,ij} = \begin{cases} \chi\left(v_i, v_j\right), & (v_i, v_j) \in E, \\ 0, & \text{otherwise}, \end{cases}$$

where $\chi(v_i, v_j)$ is the distance between vertices v_i and v_j via the metric χ defined in Equation (3.2). Using this formula directly obviates the use of large-number-of-particle simulations and thus reduces computational load significantly.

Proposition 2. *(Tortuosity formula)*

$$\mathbb{E}[\tau] = \frac{1}{W}\mathbb{E}[l_m] = \frac{\pi_0^{\mathrm{T}}}{W}\left(\sum_{n=1}^{m}\mathbf{P}^{n-1}\right)\operatorname{diag}(\mathbf{P}\mathbf{W}_E), \tag{B.9}$$

where $\operatorname{diag}(A)$ *is a column vector that lists the diagonal elements of a matrix* A.

Proof. We compute $\mathbb{E}[l_m]$. Denote the conditional probability and expectation

$$\mathbb{P}[\cdot \mid X_0 = i] = \mathbb{P}_i[\cdot], \quad \mathbb{E}[\cdot \mid X_0 = i] = \mathbb{E}_i[\cdot].$$

First, we observe by law of total expectation that

$$\mathbb{E}[l_m] = \sum_{i=1}^{|V|}\mathbb{E}[l_m \mid X_0 = i]\,\mathbb{P}\{X_0 = i\} = \sum_{i=1}^{|V|}\mathbb{E}_i[l_m]\,\pi_{0i} := \pi_0^{\mathrm{T}}\boldsymbol{U},$$

where π_0 is given by Equation (B.8) and $\boldsymbol{U} := (\mathbb{E}_i[l_m])_{v_i \in V}$. We now focus on an arbitrary element of $\boldsymbol{U}$. Noting that $\mathbb{E}_i[L_0] = 0$, and using linearity of expectation, law of total expectation, the Markov property of the random walk and symmetry of $\mathbf{W}_E$, we have

$$\begin{aligned}\mathbb{E}_i[l_m] &= \mathbb{E}_i\left[\sum_{n=1}^{m}(l_n - l_{n-1})\right] = \sum_{n=1}^{m}\mathbb{E}_i(l_n - l_{n-1}) \\ &= \sum_{n=1}^{m}\sum_{j\in V}\mathbb{E}_i(l_n - l_{n-1} \mid X_{n-1} = j)\,\mathbb{P}_i(X_{n-1} = j) \\ = \sum_{n=1}^{m}\sum_{j\in V}&\left(\sum_{k\in V}\mathbf{W}_{E,jk}\mathbf{P}_{jk}\right)\mathbf{P}_{ij}^{(n-1)} = \sum_{n=1}^{m}\sum_{j\in V}\mathbf{P}_{ij}^{(n-1)}(\mathbf{P}\mathbf{W}_E)_{jj}\end{aligned}$$

where $\mathbf{P}_{ij}^{(k)}$ is the k-th iterate of $\mathbf{P}$. Thus, in matrix form,

$$\boldsymbol{U} = \sum_{n=1}^{m} \sum_{j \in V} \begin{pmatrix} \mathbf{P}_{1j}^{(n-1)} \\ \cdot \\ \cdot \\ \cdot \\ \mathbf{P}_{|V|j}^{(n-1)} \end{pmatrix} \left(\mathbf{P}\mathbf{W}_E\right)_{jj} = \left(\sum_{n=1}^{m} \mathbf{P}^{n-1} \right) \operatorname{diag}\left(\mathbf{P}\mathbf{W}_E\right),$$

using the fact that $\mathbf{P}^{(n-1)} = \mathbf{P}^{n-1}$, completing the proof. □

In practice, to avoid taking large matrix powers when evaluating Equation (B.9), we have devised a fast algorithm in evaluating the geometric series $\sum_{n=1}^{m} \mathbf{P}^{n-1}$, by appealing to a geometric sum formula on matrices involving matrix inversions. We utilize the block upper triangular structure of $\mathbf{P}$ by block partitioning into components (known as a *divide and conquer*-type scheme) including the identity block in its southeast corner, to ease the computational load of inversions. Naive evaluation of the series is of complexity $O\left(m\left|V\right|^3\right)$ (cubic term from matrix multiplication and m additions) while our algorithm is $O\left(\left|V\right|^3\right)$.

We argue that the constant initial radius assumption on the pores deems τ a geometric parameter independent of fluid flow, even though its definition requires initial flow information and geometric information such as a distance weighted adjacency (see Equation (B.9)). In essence, we claim that τ does not vary too much until the filtration stopping criterion. Firstly, foulant concentration is monotonically decreasing along each edge, and thus the radii of all inlets, under the influence of foulant concentration in the feed solution (see Equation (3.29b)), go to zero earlier than all other downstream channels. Thus, adjacencies of the network do not change until the filter top surface is clogged. Secondly, though outflowing flux from an arbitrary junction changes over time as the filter fouls, the relative contribution from each outgoing edge does not vary greatly. Altogether, we expect that tortuosity does not depend heavily on the time of filtration but only on the initial geometry of the network. This feature makes tortuosity a universal parameter for foulant concentration.

Lastly, we note that a theoretical limit exists for tortuosity for both setups. As $N_{\text{total}} \to \infty$ (so that the membrane interior, top and bottom surface are uniformly densely packed with pore junctions), we can provide a simple lower bound for the limit in the following sense. Consider an arbitrary inlet-outlet pair. They will be connected by a path with vertical component 1. For the isolated setup, the horizontal component can be estimated as the average distance between two uniformly random points in 2D in a unit square, and is about 0.521 (length of YK in Figure B.1a). Together, these numbers provide a lower bound for the limiting tortuosity $\tau_{\min}$ of around $1.128 = \sqrt{1^2 + 0.521^2}$ for the isolated case. The argument for the periodic case is slightly more elaborate – while the vertical component of an average path is still 1, the horizontal component now is the average distance between two random points uniformly sampled from the squares $[0.5, 1.5]^2$ and $[0, 2]^2$, respectively (found to be 0.838 (length of YK in Figure B.1b)); thus an average path length is about 1.304. The difference arises because with the periodic metric, any inlet uniformly sampled from a unit square can potentially connect to outlets that are outside the unit square (bottom surface) but within 0.5 distance to the boundary (due to the constraint that search radius $d < 0.5$). These arguments provide some justification for the observations that the tortuosity in the periodic case may be larger than the isolated case. The numerical values given above are obtained by standard probabilistic calculations and numerical integration. We look forward to a more theoretical study of how tortuosity is affected by initial number of points, search radius and the underlying metric.

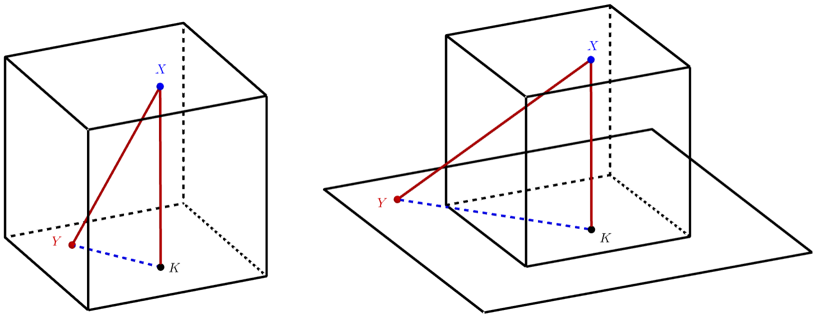

(a) **(b)**

Figure B.1 Tortuosity limit: (a) Isolated setup (unit cube); (b) periodic setup (unit cube and a square of side length 2 containing the bottom surface of the unit cube). X (blue) and Y (red) are uniformly sampled from the top and bottom membrane surface, respectively. K (black) in both figures is the projection of X onto the bottom surface; XK in both figures has length 1.

B.3 Worked Example

In this section, we provide an example of a simple network (see Figure B.2) to illustrate how the governing equations described in Sections 3.3.3–3.3.6 depend on the model parameters. The network is a reflected Y-shape, with two inlets and outlets of length 1/2 and one interior edge of length 1/3.

Each edge has conductance $\mathbf{k}_{ij}(t)$ per Equation (3.27). For this network, the conductance-weighted graph Laplacian, acting on the pressures at interior vertices, yields Equation (3.15) (the graph Laplace equation),

$$L_{\mathbf{k}}\boldsymbol{p}(t) = \begin{bmatrix} \mathbf{k}_{13}(t) + \mathbf{k}_{23}(t) + \mathbf{k}_{34}(t) & -\mathbf{k}_{34}(t) \\ -\mathbf{k}_{34}(t) & \mathbf{k}_{34}(t) + \mathbf{k}_{45}(t) + \mathbf{k}_{46}(t) \end{bmatrix} \begin{bmatrix} p_2(t) \\ p_3(t) \end{bmatrix}$$

$$= \begin{bmatrix} \mathbf{k}_{13}(t) + \mathbf{k}_{23}(t) \\ 0 \end{bmatrix} \tag{B.10}$$

where the final equality incorporates the boundary conditions Equation (3.28b). Then, the fluxes $\mathbf{q}_{ij}$ satisfy

$$\mathbf{q}_{13}(t) = \mathbf{k}_{13}(t)\left(1 - p_3(t)\right),$$

$$
\begin{aligned}
\mathbf{q}_{23}(t) &= \mathbf{k}_{23}(t)\left(1 - p_3(t)\right), \\
\mathbf{q}_{34}(t) &= \mathbf{k}_{34}(t)\left(p_3(t) - p_4(t)\right), \\
\mathbf{q}_{45}(t) &= \mathbf{k}_{45}(t)\, p_4(t), \\
\mathbf{q}_{46}(t) &= \mathbf{k}_{46}(t)\, p_4(t).
\end{aligned}
$$

To proceed, we then solve Equation (3.29a) (the advection graph Laplace equation) to find the foulant concentration at each vertex,

$$
\begin{aligned}
L_{\mathbf{q}}^{\text{in}}\boldsymbol{c} = \begin{bmatrix} \mathbf{q}_{13}+\mathbf{q}_{23} & 0 & 0 & 0 \\ -\mathbf{q}_{34}\mathbf{b}_{34} & \mathbf{q}_{34} & 0 & 0 \\ 0 & -\mathbf{q}_{45}\mathbf{b}_{45} & \mathbf{q}_{45} & 0 \\ 0 & -\mathbf{q}_{46}\mathbf{b}_{46} & & \mathbf{q}_{46} \end{bmatrix} \begin{bmatrix} c_3(t) \\ c_4(t) \\ c_5(t) \\ c_6(t) \end{bmatrix} &= \\
\left(\mathbf{q}\circ\mathbf{b}\right)^{\mathrm{T}}\boldsymbol{c}_0 = \begin{bmatrix} \mathbf{q}_{13}\mathbf{b}_{13} & \mathbf{q}_{23}\mathbf{b}_{23} \\ 0 & 0 \\ 0 & 0 \\ 0 & 0 \end{bmatrix} \begin{bmatrix} 1 \\ 1 \end{bmatrix} &= \begin{bmatrix} \mathbf{q}_{13}\mathbf{b}_{13}+\mathbf{q}_{23}\mathbf{b}_{23} \\ 0 \\ 0 \\ 0 \end{bmatrix} \qquad \text{(B.11)}
\end{aligned}
$$

where the 3rd equality uses the boundary condition Equation (3.29b).

After obtaining the concentrations $c_i(t)$ for each vertex, we evolve edge radius via Equation (3.30).

By appealing to the symmetry of this network, one may reduce the system for the dynamics of network evolution to a system of two non-autonomous nonlinear ordinary differential equations (ODEs), describing the radius evolution $r_{34}(t)$ and $r_{45}(t)$ (which by symmetry is equal to $r_{46}(t)$), with a closed solution for the linear shrinkage rate of $r_{13}(t) = r_{23}(t)$. Since our principal concern here is the end state of the network, we do not present or study this system here.

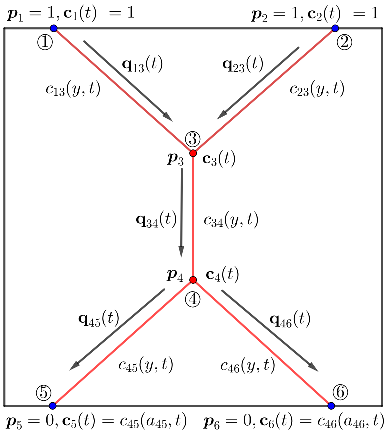

Figure B.2 2D schematic of a reflected-Y network with labelled physical quantities presented in Section 3.4.

APPENDIX C

SUPPLEMENTARY MATERIAL FOR CHAPTER 4

In this appendix, we provide a brief description of the network generation procedure, the associated graph operators, detailed definitions of performance metrics and tortuosity (also see its derivation in Appendix B.2), and lastly the porosity correction procedure.

C.1 Network Generation

We generate a membrane pore network via a variant of the Random Geometric network. To generate the set of pore junctions $\mathcal{V}$, we place N_{total} randomly distributed points (following a uniform distribution) in a rectangular box of height $2W$, with square cross-section of length W. We connect points that lie within a distance of $l_{\max}W$, but also at least δW apart, where δ is a control parameter (fixed throughout this work) such that when chosen large enough, it ensures validity of the Hagen-Poiseuille framework used to model fluid flow. These connections form a set of pores $\mathcal{E}$ and together with the junction set $\mathcal{V}$ we obtain an initial network $G = G\left(\mathcal{V}, \mathcal{E}\right)$. We say $(v_i, v_j) \in \mathcal{E}$ when two junctions $v_i, v_j \in \mathcal{V}$ form a pore.

We then cut through the rectangular box with two horizontal planes at heights $0.5W$ and $1.5W$, respectively. The intersections of these two planes and the set of pores $\mathcal{E}$ form the set of inlets $\mathcal{V}_{\text{in}}$ and outlets $\mathcal{V}_{\text{out}}$, respectively. Altogether, the above procedure forms the domain for fluid flow and fouling, described in Section 4.3.

C.2 The Graph Laplacian

We associate each network G with a (weighted) graph Laplacian, a generalization of the finite difference discretization of the classic Laplace operator $\nabla \cdot \nabla$. It is a square matrix whose off-diagonal terms indicate connection weights, and whose diagonal terms record the total weights of neighbors of each discretization point (junction). In our work, the most relevant weight is the conductance K_{ij} of each pore, given by

$$\mathbf{K}_{ij} = \frac{\pi R_{ij}^4}{8\mu L_{ij}}.$$

Then the **K**-weighted graph Laplacian is defined as

$$\mathbf{L}_K := \mathbf{D} - \mathbf{K}, \tag{C.1}$$

where

$$\mathbf{D}_{ij} = \begin{cases} \sum_{l=1}^{|\mathcal{V}|} \mathbf{K}_{il}, & j = i, \\ 0, & \text{otherwise}, \end{cases} \tag{C.2}$$

where $|\mathcal{V}|$ is the number of junctions.

While the above setup characterizes the flux inside an individual pore, we employ conservation of flux at each interior vertex v_i throughout the network,

$$0 = \sum_{v_j:(v_i,v_j)\in E} \mathbf{Q}_{ij}. \tag{C.3}$$

Combining Equations (3.3) and (C.3), we form a graph Laplace equation for the pressures P at each vertex, to which we add the specified pressure drop boundary conditions,

$$\mathbf{L}_K \boldsymbol{P}(v_i) = 0, \quad v_i \in \mathcal{V}_{\text{int}}, \tag{C.4}$$

$$\boldsymbol{P}(v) = P_0, \quad v \in \mathcal{V}_{\text{in}}, \tag{C.5}$$

$$\boldsymbol{P}(v) = 0, \quad v \in \mathcal{V}_{\text{out}}. \tag{C.6}$$

Once the pressures $\boldsymbol{P}(v_i)$ are found for all interior junctions $v_i \in \mathcal{V}_{\text{int}}$, we use Equation (3.3) to find flux $\mathbf{Q}_{ij}$ in each pore to form a flux matrix $\mathbf{Q}$ with i and j as row and column indices, respectively.

Using conservation of particle flux at each junction, we arrive at the following advection Laplace equation for foulant concentration $C_i\left(T\right)$ at each vertex $v_i \in \mathcal{V}_{\text{int}}$,

$$\mathbf{L}_{\mathbf{Q}}^{\text{in}} C = \left(\mathbf{Q} \circ \mathbf{B}\right)^{\mathrm{T}} C_0,\ \mathbf{B}_{ij} = \exp\left(\frac{-\Lambda R_{ij} L_{ij}}{Q_{ij}}\right), \tag{C.7}$$

$$C_0 = \left(C_{\text{top}}, \ldots, C_{\text{top}}, 0, \ldots, 0\right)^{\mathrm{T}}, \tag{C.8}$$

where $\mathbf{L}_{\mathbf{Q}}^{\text{in}} = \mathbf{D}_{\mathbf{Q}^{\mathrm{T}}} - \left(\mathbf{Q} \circ \mathbf{B}\right)^{\mathrm{T}}$ is the *advection Laplacian* with a sink $\mathbf{B}$ (also see Equation (3.23)), whose form arises from an analytical solution to Equation (3.17a). T and $\circ$ denote matrix transpose and the element-wise multiplication, respectively. See [48] for a detailed derivation of this linear system.

C.3 Performance Metrics

Volumetric throughput of a membrane filter over its operational lifetime is a commonly-used measure of overall efficiency. The volumetric throughput $H(T)$ through the filter is defined by

$$H\left(T\right) = \int_0^T Q_{\text{out}}\left(T'\right) dT', \tag{C.9}$$

$$Q_{\text{out}}\left(T\right) = \sum_{v_j \in \mathcal{V}_{\text{out}}} \sum_{v_i : (v_i, v_j) \in E} \mathbf{Q}_{ij}\left(T\right), \tag{C.10}$$

where $Q_{\text{out}}\left(T\right)$ is the total flux exiting the filter. With the scales chosen in Equation (2.29), throughput H has scale

$$H = \frac{W^3}{\alpha C_0} h. \tag{C.11}$$

In particular, we compute $h_{\text{final}} := h\left(t_{\text{final}}\right)$, the total volume of filtrate processed by the filter over its lifetime.

To connect with experiments and applications, we briefly discuss the order of magnitude of the dimensional throughput H in Equation (C.11). The parameter α is of the order of foulant (contaminant) particle volume while C_0 is the number of particles per fluid (solvent) volume. The product αC_0 then yields an estimate of the volume ratio of the (contaminant) solute and the (fluid) solvent. For example, the permissible exposure limit by OSHA (Occupational Safety and Health Administration) for 1-dioxane in contaminated water is at a concentration of about 100 mg/L [130]. The density of 1-dioxane is close to that of water, and thus this level of concentration translates to a volume ratio (αC_0) of 10^{-4}. With this estimate and the order of magnitude for dimensionless throughput H seen in Figure 4.3a (about 10^{-2}), H then is of the order of $10^2 W^3$ where W^3 represents the volume of a cubic unit of a membrane filter of side length W. This estimate suggests that this cubic unit will process filtrate volume of order 100 times its membrane material volume, given the parameters used in this work.

Another performance measure is the accumulated foulant concentration in the filtrate, which captures the aggregate particle capture efficiency of the filter. The accumulated foulant concentration is defined by

$$C_{\text{acm}}(T) = \frac{\int_0^T C_{\text{out}}(T')\, Q_{\text{out}}(T')\, dT'}{\int_0^T Q_{\text{out}}(T')\, dT'},$$

where

$$C_{\text{out}}(T) = \frac{\sum\limits_{v_j \in \mathcal{V}_{\text{out}}} \sum\limits_{v_i : (v_i, v_j) \in E} \mathbf{C}_j(T)\, \mathbf{Q}_{ij}(T)}{Q_{\text{out}}(T)}.$$

C_{acm} has scale $C_{\text{acm}} = C_{\text{top}} c_{\text{acm}}$. Of particular interest is $c_{\text{final}} := c_{\text{acm}}(t_{\text{final}})$, which provides a measure of the aggregate particle capture efficiency of the filter over its lifetime.

We further simplify the notations h_{final} and c_{final} to h and c in the main text as we consider only the end states of these performance measures in our analysis.

C.4 Tortuosity

Tortuosity τ of a membrane network is defined by the average distance travelled by a fluid particle from membrane top surface to bottom, relative to membrane thickness W. We here provide a formula via a probabilistic approach,

$$\tau = \frac{\pi_0^{\mathrm{T}}}{W} \left(\sum_{n=1}^{m} \mathbf{P}^{n-1} \right) \operatorname{diag}\left(\mathbf{P}\mathbf{W}_E \right), \tag{C.12}$$

where T means vector transpose and diag means the diagonal component of a matrix. Here we provide some intuition for each term. The initial distribution π_0 describes the probability of the fluid particle choosing an inlet on the membrane top surface. To calculate π_0, we compute the proportion of flux entering each inlet on the upstream surface relative to total flux. $\mathbf{P}$ within the sum describes the law of how a fluid particle traverses the network from one junction to its adjacent neighbors (known as *a step*); the upper limit m is the largest number of steps a particle takes to exit the membrane bottom surface, which can be found for each network. Lastly, $\operatorname{diag}\left(\mathbf{P}\mathbf{W}_E\right)$ describes the average distance travelled by the fluid particle in one step starting from each junction. We refer the reader to [48] for details of the derivation.

In our study, since we perturb each pore radius via Equation (2.48), tortuosity τ implicitly depends on the noise amplitude β through π_0 and $\mathbf{P}$ because they both involve the fluxes (affected by the pores' perturbed conductances).

C.5 Porosity Correction

In Item 3 (*porosity correction*) of the algorithm, we derive the expression of r_{pc} such that $\phi_{\mathrm{noise}} = \phi_{\mathrm{pc}}$. It relies on writing ϕ_{pc} in terms of ϕ_0 (see Item 1 and consider Equation (4.7) with $\beta = 0$), the porosity of the unperturbed network with initial radius r_0:

$$\phi_{\mathrm{noise}} = \phi_{\mathrm{pc}} = \frac{\pi}{2} r_{\mathrm{pc}}^2 \sum_{\mathrm{edge}} (\text{edge length})$$

$$
\begin{aligned}
&= \left(\frac{\pi}{2} r_0^2 \sum_{\text{edge}} (\text{edge length})\right) \left(\frac{r_{\text{pc}}}{r_0}\right)^2 \\
&= \phi_0 \left(\frac{r_{\text{pc}}}{r_0}\right)^2
\end{aligned}
$$

and thus $r_{\text{pc}} = r_0 \sqrt{\frac{\phi_{\text{noise}}}{\phi_0}}$.

APPENDIX D

SUPPLEMENTARY MATERIAL FOR CHAPTER 5

In this appendix, we first define pores and junctions in a specified band, and then provide the benchmark estimates for the number of junctions to be placed in each band of the porosity-graded networks introduced in Chapter 5. Lastly, we present several analytical results on the relationship between upstream and downstream pore closure time, which then leads to some insight on membrane network dynamics.

D.1 Junctions and Pores in a Band

In this appendix, we define the set of junctions (vertices) and pores (edges), and their respective band-specific counterparts. We use junctions and vertices, and pores and edges interchangeably.

In this work, we treat a junction and a pore as a point and a straight line respectively that lie in our dimensionless domain – the unit cube, even though the notion of a vertex and an edge is generally more abstract in terms of graph theory. Each junction v of the junction set V has a Euclidean coordinate $v = (v_x, v_y, v_z) \in [0,1]^3$, with z-direction positive pointing (down) from membrane top ($z = 0$) to bottom surface ($z = 1$). The coordinate of a junction depends on the random generation protocol outlined in Section 5.3.1. We further define the set of membrane pore inlets and outlets,

$$V_{\text{top}} = \{v \in V : v_z = 0\}, \tag{D.1a}$$

$$V_{\text{top}} = \{v \in V : v_z = 1\}. \tag{D.1b}$$

.

The set of edges E is formed by connecting the junctions via

$$E = \left\{e_{vw} \in V \times V : a_{\min} < \chi\left(v, w\right) < a_{\max}\right\}, \tag{D.2}$$

where $a_{\min}$ and $a_{\max}$ are the dimensionless minimal and maximal distance allowed between two junctions, respectively; $\chi\left(\cdot, \cdot\right)$ is a periodic metric, defined by

$$\chi\left(v, w\right) = \min_{\boldsymbol{z}} \left\|v - w\left(\boldsymbol{z}, 0\right) \mid \boldsymbol{z} = \left\{-1, 0, 1\right\}^2\right\|_2, \ a_{\max} \leq \frac{1}{m}. \tag{D.3}$$

that is, junctions close to the four sides parallel to the z-direction may be connected through the boundary. We require that $a_{\max}$ does not exceed the thickness of a band because otherwise edges may cross more than two bands and thus reduce or defeat the purpose of having a gradient of pore radii.

Next, we define precisely junctions and edges in a band. Denote the k^{th} band as the set of coordinates

$$V_k = \left\{v \in \left[0, 1\right]^3 \mid \frac{k-1}{m} \leq v_z < \frac{k}{m}\right\}. \tag{D.4}$$

We say a junction w lies in the k^{th} band if $w \in V_k$.

We treat each edge as a straight line in the unit cube,

$$e_{vw} = \left\{u \in \left[0, 1\right]^3 \mid u = \zeta v + \left(1 - \zeta\right) w, \quad 0 \leq \zeta \leq 1\right\}.$$

Let $L\left(e_{vw}\right)$ be the one-dimensional Lebesgue measure of e_{vw} such that $L\left(e_{vw}\right) = \chi\left(v, w\right)$. Define a band-specific length measure L_k such that

$$L_k\left(e_{vw}\right) = L\left(e_{vw} \cap V_k\right), \tag{D.5}$$

which computes the length of the edge strictly inside the k^{th} band (known in general as an intersection measure). We say that a pore belongs to the k-th band when the largest proportion of its length lies strictly inside the k-th band. More precisely, we define the set of the pores in the k^{th} band as

$$E_k = \left\{ e_{vw} \in E \mid L_k\left(e_{vw}\right) = \max_n L_n\left(e_{vw}\right) \right\}. \tag{D.6}$$

In this definition, we see that if $v, w \in V_k$, then $e_{vw} \cap V_k = e_{vw}$ while $e_{vw} \cap V_n = \emptyset$ for all n, which implies that the inequality is automatically satisfied.

The formula Equation (D.5) also facilitates the computation of Φ_k, the band porosity of the k^{th} band (Equation (5.3)), in the sense that we consider the lengths of edges that strictly lie in V_k; edges reaching two bands will contribute to the band porosities of the two bands separately. We simplify the notation as

$$L_{k,vw} := L_k\left(e_{vw}\right).$$

D.2 Number of Random Points in Each Band

With prescribed Φ and m, we provide an estimate of how many random points should be used in the k^{th} band, labelled N_k. We write total pore length as $\chi_{ij} := \chi\left(i, j\right)$ per Equation (D.3). More precisely, we use basic arguments to deduce that total edge length in the k^{th} band scales with N_k^2, i.e.

$$\sum_{e_{ij} \in E} L_{k,ij} \approx \sum_{e_{ij} \in E_k} \chi_{ij} = \overline{\chi}\left|E_k\right| = \overline{\chi}\frac{\overline{D}_k N_k}{2} = \tag{D.7}$$

$$= \frac{\overline{\chi}}{2}\left[\left(N_k - 1\right) p\left(A_{\min}, A_{\max}\right)\right] N_k = \frac{\overline{\chi}}{2} p\left(A_{\min}, A_{\max}\right) N_k\left(N_k - 1\right) \tag{D.8}$$

where $\overline{\chi}$, $\overline{D}_k$ and $p\left(A_{\min}, A_{\max}\right)$ are the average edge length, average number of neighbors in the k^{th} band and the probability of finding two random points being connected, respectively. The first approximation relies on the fact that the edges in the k^{th} band that cross boundaries do not have too much excess length outside the k^{th} band. The first equality is trivial. The second equality is because total number of edges in the k^{th} band is exactly equal to average number of neighbors times the number of junctions divided by 2 (to account for double counting). The third equality expresses the average number of neighbors $\overline{D}_k$ as the total number of neighbors a junction could have times the probability of obtaining a neighbor $p\left(A_{\min}, A_{\max}\right)$, which is independent of k and N_k. Assuming that we use a small $A_{\max}$, $\overline{\chi}$ does not depend too heavily on N_k and thus is approximately the same for all k. Since $\overline{\chi}$ is a sample mean with $|E_k|$ as the sample size, it can be approximated by the expected edge length (based on hypercube line-picking [135]) and therefore a constant independent of k.

D.3 Analytical Results on Pore Closure Time

In this section, we show that lifetime of a simplified network is governed by the radius of the top pore(s). More precisely, for such a simplified network, the radius of the inlets will always go to zero earlier than that downstream pores, **independent** of the initial upstream and downstream pore radii and model parameters. This result contributes to the claim that networks considered will also only clog at membrane inlet. This result also serves as a worked example for the general network solver (see also [48] for another example).

A membrane network stops functioning when there exists no more path connecting any inlet on the top surface to any outlet on the bottom surface. The critical event leading to filtration arrest is when the radius of a pore vanishes as the last straw that disconnects the main network into at least two disconnected subnetworks such that each subnetwork contains only a subset of the inlets or outlets but not both. We consider a simple setup (depicted in Figure D.1) which consists of an arbitrary pore junction connecting n_{up} upstream and n_{down} downstream pores.

The upstream and downstream pores all have a length of 1 unit (though they appear to have different lengths in Figure D.1, this choice of a common length does not affect our result). We solve the dimensionless governing equations (per scales presented in Section 5.5) for the unknown pressure $p_{\text{junc}}\left(t\right)$ and concentration $c_{\text{junc}}\left(t\right)$

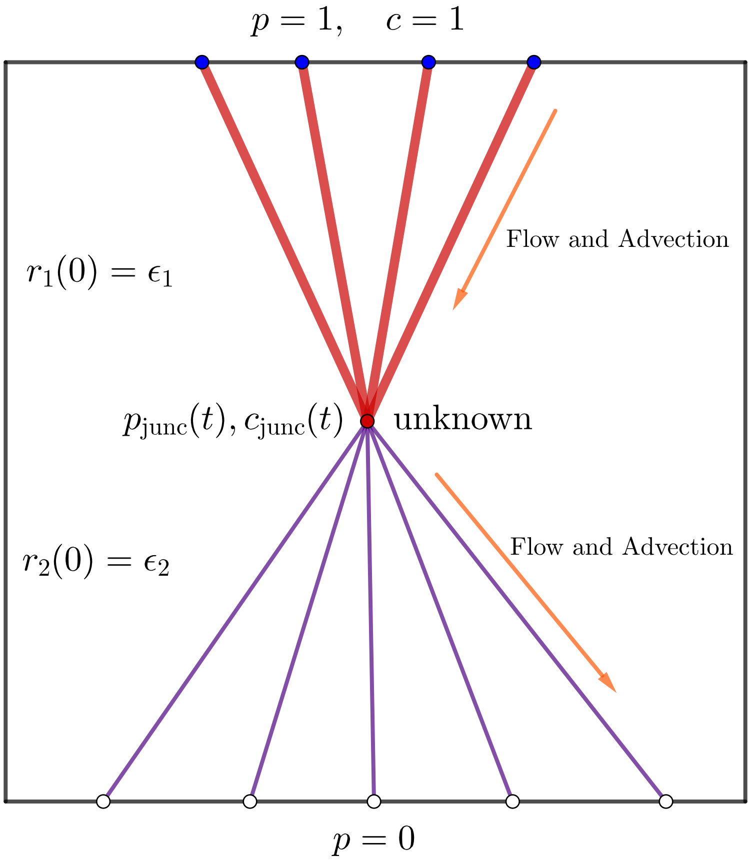

Figure D.1 Schematic of a simplified setup for Theorem 2. Colored junctions and pores correspond to each band as follows: red upstream pores and indigo downstream pores. Blue dots are inlets. The red dot is an interior junction. White dots are outlets. Here $n_{\text{up}} = 4$ and $n_{\text{down}} = 5$.

at the interior junction. Since the pore lengths are assumed the same, and the upstream (resp. downstream) pores obey the same boundary conditions for pressure and concentration, the radius and concentration evolution in these pores are therefore also the same. As a result, we simply monitor the evolution of quantities for one upstream and one downstream pore. Let $r_1(t)$ and $r_2(t)$ be the radius of each upstream and downstream pore, respectively.

Fluxes through each upstream and downstream pore, labelled $q_1(t)$ and $q_2(t)$ respectively, satisfy the dimensionless Hagen-Poiseuille equations,

$$\begin{aligned} q_1(t) &= \left(1 - p_{\text{junc}}(t)\right) r_1^4(t); \\ q_2(t) &= p_{\text{junc}}(t)\, r_2^4(t). \end{aligned}$$

where $p_{\text{junc}}(t)$ is the (unknown) pressure at the exit of the top pore. Conservation of flux yields

$$n_{\text{up}} q_1(t) = n_{\text{down}} q_2(t) \tag{D.9}$$

and therefore

$$p_{\text{junc}}(t) = \frac{n_{\text{up}} r_1^4(t)}{n_{\text{up}} r_1^4(t) + n_{\text{down}} r_2^4(t)} \implies q_1(t) = \frac{n_{\text{down}} r_1^4(t)\, r_2^4(t)}{n_{\text{up}} r_1^4(t) + n_{\text{down}} r_2^4(t)}. \tag{D.10}$$

Foulant concentration in the upstream pore, $c_1(y,t)$, satisfies the dimensionless advection equation,

$$q_1 \frac{\partial c_1}{\partial y} = -\lambda r_1 c_1, \quad c_1(0,t) = 1,$$

which has an analytical solution

$$c_1(y,t) = c_1(0,t) \exp\left(-\frac{\lambda y r_1(t)}{q_1(t)}\right) \overset{\textit{Equation (D.10)}}{=} \exp\left(-\lambda y \left[\frac{n_{\text{up}} r_1(t)}{n_{\text{down}} r_2^4(t)} + \frac{1}{r_1^3(t)}\right]\right).$$

The evolution of the pore radii satisfies

$$\frac{dr_1}{dt} = -1, \quad r_1(0) = \epsilon_1 \implies r_1(t) = \epsilon_1 - t;$$

$$\frac{dr_2}{dt} = -c_{\text{junc}}\left(t\right), \quad r_2\left(0\right) = \epsilon_2.$$

By conservation of particle flux at the junction, we have $n_{\text{down}} q_2\left(t\right) c_{\text{junc}}\left(t\right) = n_{\text{up}} q_1\left(t\right) c_1\left(1, t\right)$. Conservation of flux (per Equation (D.9)) reduces this to $c_{\text{junc}}\left(t\right) = c_1\left(1, t\right)$. Hence,

$$\frac{dr_2}{dt} = -c_1\left(1, t\right) = -\exp\left(-\lambda\left(\frac{n_{\text{up}}\left(\epsilon_1 - t\right)}{n_{\text{down}} r_2^4\left(t\right)} + \frac{1}{\left(\epsilon_1 - t\right)^3}\right)\right), \quad r_2\left(0\right) = \epsilon_2. \tag{D.11}$$

Theorem 2. *The solution* $r_2\left(t\right)$ *to Equation (D.11) satisfies* $r_2\left(t\right) > 0$ *for all* $t \in \mathcal{T} := \left[0, \epsilon_1\right]$, *for all* $\epsilon_1, \epsilon_2, \lambda > 0$ *and arbitrary positive integers* n_{up} *and* n_{down}.

Proof. We note first that $r_2\left(t\right) \geq 0$ for all $t \in \mathcal{T}$ since the initial condition is positive, i.e., $\epsilon_2 > 0$, the right hand side of Equation (D.11) is a nonpositive function, which goes to zero as $r_2 \to 0$, i.e., $\frac{dr_2}{dt} \to 0^-$ as $r_2 \to 0^+$. In other words, the radius of the downstream pore decreases to zero until it reaches zero and will not yield negative values. Therefore, to prove the claim that $r_2\left(t\right) > 0$ for all $t \in \mathcal{T}$, we suppose that there exists $t^* \in \mathcal{T}$ such that $r_2\left(t^*\right) = 0$ and arrive at a contradiction as follows.

We noted earlier that $r_2\left(t\right)$ is a monotone decreasing function, and in fact, is equal to 0 for all $t \geq t^*$. Now, when $r_2\left(t\right)$ is bounded away from 0, i.e., $t < t^*$, we divide both sides of Equation (D.11) by $r_2\left(t\right)$ and integrate to obtain

$$\log\left(r_2\left(t\right)\right) = \log\left(\epsilon_2\right) - I\left(t\right), \tag{D.12}$$

where

$$I\left(t\right) = \int_0^t \frac{1}{r_2\left(\tau\right)} \exp\left(-\lambda\left[\frac{n_{\text{up}}\left(\epsilon_1 - t\right)}{n_{\text{down}} r_2^4\left(\tau\right)} + \frac{1}{\left(\epsilon_1 - \tau\right)^3}\right]\right) d\tau. \tag{D.13}$$

Note that under the assumption that $r_2\left(t^*\right) = 0$, $I\left(t\right) \to -\infty$ as $t \nearrow t^*$. We now prove that $0 \leq \lim_{t \nearrow t^*} I\left(t\right) < \infty$ to arrive at our contradiction. Here, the lower bound is obvious since the integrand is nonnegative.

First, we note that (by simply removing a positive term from the argument of the exponential)

$$\lim_{t \nearrow t^*} I(t) \leq \lim_{t \nearrow t^*} \int_0^t \frac{1}{r_2(\tau)} \exp\left(-\frac{\kappa(\epsilon_1 - t)}{r_2^4(\tau)}\right) d\tau =: \lim_{t \nearrow t^*} \int_0^t f(\tau; \kappa, \epsilon_1)\, d\tau, \qquad \text{(D.14)}$$

where $\kappa = \frac{\lambda n_{\text{up}}}{n_{\text{down}}}$.

It would suffice to show that the integrand f is bounded on $[0, t]$ for $t \leq t^*$. We first note that when $r_2(\tau)$ is bounded away from 0, the integrand is continuous in r_2 (as an independent variable). We check the behaviour of the integrand in the limit as $t \to t^*$ or equivalently $r_2(t) \to 0^+$.

$$\begin{aligned}
\lim_{r_2(\tau) \to 0^+} \frac{1}{r_2(\tau)} \exp\left(-\kappa\left(\frac{\epsilon_1 - \tau}{r_2^4(\tau)}\right)\right) &\overset{u(\tau) = \frac{1}{r_2(\tau)}}{=} \lim_{u(\tau) \to \infty} \frac{u(\tau)}{\exp\left(\kappa(\epsilon_1 - \tau) u^4(\tau)\right)} \\
&\overset{\text{L'Hopital}}{=} \lim_{u(\tau) \to \infty} \frac{1}{4u^3(\tau) \exp\left(\kappa(\epsilon_1 - \tau) u^4(\tau)\right)} \\
&= 0.
\end{aligned}$$

Therefore, f is a continuous function on $[0, t^*]$ and achieves a maximum value $C_{\kappa,\epsilon_1} := \|f(t)\|_\infty < \infty$. We must then have

$$\lim_{t \nearrow t^*} I(t) \leq \lim_{t \nearrow t^*} \int_0^t f(\tau; \kappa, \epsilon_1)\, d\tau \leq t^* C_{\kappa,\epsilon_1} < \infty.$$

Thus, the right hand side of Equation (D.12) is finite, but the left hand side of it is not. We arrive at our contradiction. Therefore, there exists no $t^* \in \mathcal{T}$ such that $r_2(t^*) = 0$, which then proves the claim. □

However, the situation becomes far more complicated once pore size variation within each layer is involved. In fact, we show via examples that the radius of a downstream pore can go to zero before the upstream ones. Consider an inverted-Y shaped network with one upstream pore and two downstream pores, with initial radius ϵ_1, ϵ_2 and ϵ_3, respectively. Without loss of generality, we assume $\epsilon_2 > \epsilon_3$. Using a similar set of calculations to the case above using $n_{\text{up}} = 1$ and $n_{\text{down}} = 2$, we find that the outlet radii $r_2(t)$ and $r_3(t)$ satisfy the set of coupled ODEs,

$$\frac{dr_2}{dt} = \frac{dr_3}{dt} = -\exp\left(-\lambda\left(\frac{\epsilon_1 - t}{r_2^4(t) + r_3^4(t)} + \frac{1}{(\epsilon_1 - t)^3}\right)\right). \tag{D.15}$$

The difference between this setup and the one in Theorem 2 is that now the evolution of each downstream pore depend on each other because they have different initial conditions. Note that r_2 and r_3 simply differ by a constant $\epsilon_2 - \epsilon_3$. Thus, we can further deduce that

$$\frac{dr_3}{dt} = -\exp\left(-\lambda\left(\frac{\epsilon_1 - t}{(r_3(t) + \epsilon_2 - \epsilon_3)^4 + r_3^4(t)} + \frac{1}{(\epsilon_1 - t)^3}\right)\right) \tag{D.16}$$

From this, we observe that one can make $\epsilon_2 - \epsilon_3$ sufficiently large so that regardless of how small r_3 becomes, r_3 decreases at a nontrivial rate. This is a scenario different than the case in Equation (D.11). An explicit condition involving $\epsilon_1, \epsilon_2, \epsilon_3$ and λ may be derived.

We have tested using a numerical example with $\epsilon_1 = \epsilon_2 = 0.01$, $\epsilon_3 = 3 \times 10^{-3}$, $\lambda = 5 \times 10^{-7}$ (the same value used in Section 5.6) and have found that $r_3(t)$ goes to zero earlier than $r_1(t)$.

We conclude that the difference in initial conditions for pore radii does play a role in driving the dynamics of each pore. Downstream pore closure can be earlier than the upstream one. However, even if one downstream pore closes earlier, the local structure at the junction always reduces to the case where we have multiple upstream pores and one single downstream one, which is the setup used in Theorem 2 with n_{up} arbitrary and $n_{\text{down}} = 1$. In other words, the moment we encounter a lone downstream pore, then it will not close until all upstream pores have closed. With this heuristic argument (that can be chained upstream), we believe that a general membrane network with various initial conditions will only close on the top surface under adsorption. The introduction of sieving would contribute to instantaneous blocking of interior pores (see Section 6.2.2).

REFERENCES

[1] Ahn, Y., Park, S., Kim, G., Hwang, Y., Lee, C., Shin, H., and Lee, J. Development of high efficiency nanofilters made of nanofibers. *Curr. Appl. Phys. 6* (2006), 1030–1035. Nano Korea 2004 Symposium on NT Challenge.

[2] Ambashta, R. D., and Sillanpää, M. E. T. Membrane purification in radioactive waste management: a short review. *J. Membr. Sci. 396* (2012), 22–31.

[3] Amin, A., Merati, A. A., Bahrami, S. H., and Bagherzadeh, R. Effects of porosity gradient of multilayered electrospun nanofibre mats on air filtration efficiency. *J. Text. Inst. 108* (2017), 1563–1571.

[4] Aminabhavi, T. M., and Patil, V. B. Density, viscosity, refractive index, and speed of sound in binary mixtures of ethenylbenzene with n,n-dimethylacetamide, tetrahydrofuran, n,n-dimethylformamide, 1,4-dioxane, dimethyl sulfoxide, chloroform, bromoform, and 1-chloronaphthalene in the temperature interval (298.15-308.15) k. *J. Chem. Eng. Data 43* (1998), 497–503.

[5] Anderson, D. F., and Kurtz, T. *Stochastic Analysis of Biochemical Systems.* Berlin/Heidelberg, Germany: Springer, 2015.

[6] Apel, P. Track etching technique in membrane technology. *Radiat. Meas. 34* (2001), 559–566. Proceedings of the 20th International Conference on Nuclear Tracks in Solids.

[7] Auton, L., Pramanik, S., Dalwadi, M., MacMinn, C., and Griffiths, I. A homogenised model for flow, transport and sorption in a heterogeneous porous medium. *J. Fluid Mech. 932* (2021), A34.

[8] Bacchin, P., Derekx, Q., Veyret, D., Glucina, K., and Moulin, P. Clogging of microporous channels networks: role of connectivity and tortuosity. *Microfluid Nanofluidics 17* (2014), 85–96.

[9] Baker, M., and Taras, M. J. *The quest for pure water: The history of the twentieth century, volume 1 and 2.* Denver, Colorado: American Water Works Association, 1981.

[10] Barhate, R., and Ramakrishna, S. Nanofibrous filtering media: Filtration problems and solutions from tiny materials. *J. Membr. Sci. 296* (2007), 1–8.

[11] Barnaby, R., Liefeld, A., Jackson B., P., Hampton T., H., and Stanton B., A. Effectiveness of table top water pitcher filters to remove arsenic from drinking water. *Environ. Res. 158* (2017), 610–615.

[12] Basile, A., Gallucci, F., and Morrone, P. 6 - advanced carbon dioxide (co2) gas separation membrane development for power plants. In *Advanced Power Plant Materials, Design and Technology*, D. Roddy, Ed., Woodhead Publishing Series in Energy. Sawston, United Kingdom: Woodhead Publishing, 2010, pp. 143–186.

[13] Beuscher, U. Modeling sieving filtration using multiple layers of parallel pores. *Chem. Eng. Technol. 33* (2010), 1377–1381.

[14] Bijeljic, B., Andrew, M. G., Dong, H., Raeini, A. Q., Blunt, M. J., Mostaghimi, P., Alhashmi, Z., and iRock Technologies. Micro-ct images and networks. `https://www.imperial.ac.uk/earth-science/research/research-groups/pore-scale-modelling/micro-ct-images-and-networks/`, 2007. Accessed on 2021-11-30.

[15] Blunt, M. J., Bijeljic, B., Dong, H., Gharbi, O., Iglauer, S., Mostaghimi, P., Paluszny, A., and Pentland, C. Pore-scale imaging and modelling. *Adv. Water Resour. 51* (2013), 197–216.

[16] Bolton, G. R., Boesch, A. W., and Lazzara, M. J. The effect of flow rate on membrane capacity: development and application of adsorptive membrane fouling models. *J. Membr. Sci. 279* (2006), 625–634.

[17] Bolton, G. R., LaCasse, D., and Kuriyel, R. Combined models of membrane fouling: development and application to microfiltration and ultrafiltration of biological fluids. *J. Membr. Sci. 277* (2006), 75–84.

[18] Bonato, A., Lozier, M., Mitsche, D., Pérez-Giménez, X., and Prałat, P. The domination number of on-line social networks and random geometric graphs. In *Theory and Applications of Models of Computation. TAMC 2015. Lecture Notes in Computer Science* (2015), R. Jain, S. Jain, and F. Stephan, Eds., vol. 9076, Cham, Switzerland: Springer, pp. 150–163.

[19] Bowen, W. R., and Jenner, F. Theoretical descriptions of membrane filtration of colloids and fine particles: An assessment and review. *Adv. Colloid Interface Sci. 56* (1995), 141–200.

[20] Capasso, I., Liguori, B., and Verdolotti, L. Process strategy to fabricate a hierarchical porosity gradient in diatomite-based foams by 3d printing. *Sci. Rep. 10*, 612 (2020).

[21] Chang, C., and Chang, M. Preparation of multi-layer silicone/pvdf composite membranes for pervaporation of ethanol aqueous solutions. *J. Membr. Sci. 238* (2004), 117–122.

[22] Chang, S.-S., and Roper, M. Microvascular networks with uniform flow. *J. Theor. Biol. 462* (2019), 48–64.

[23] Chapman, A., and Mesbahi, M. Advection on graphs. In *Proc. 50th IEEE Conf. Decis. Control* (2011), pp. 1461–1466.

[24] Chew, J. W., Kilduff, J., and Belfort, G. The behavior of suspensions and macromolecular solutions in crossflow microfiltration: An update. *J. Membr. Sci. 601* (2020), 117865.

[25] Chiera, N. M., Bolisetty, S., Eichler, R., Mezzenga, R., and Steinegger, P. Removal of radioactive cesium from contaminated water by whey protein amyloids–carbon hybrid filters. *Royal Society of Chemistry Adv. 11* (2021), 32454–32458.

[26] Choi, S.-W., Zhang, Y., and Xia, Y. Three-dimensional scaffolds for tissue engineering: the importance of uniformity in pore size and structure. *Langmuir 26* (2010), 19001–6.

[27] Coll, V. E., Hook, J., Magnant, C., McCready, K. B., and Ryan, K. The proper diameter of a graph. *Discuss. Math. Graph Theory 40* (2020), 107 – 125.

[28] Collum, B. Process engineering. In *Nuclear Facilities*. Sawston, United Kingdom: Woodhead Publishing, 2017, ch. 6, pp. 139–183.

[29] Colombo, R. M., Guerra, G., Herty, M., and Schleper, V. Optimal control in networks of pipes and canals. *SIAM J. Control Optim 48* (2009), 2032–2050.

[30] Dall, J., and Christensen, M. Random geometric graphs. *Phys. Rev. E 66* (2002), 016121.

[31] Dalwadi, M. P., Griffiths, I. M., and Bruna, M. Understanding how porosity gradients can make a better filter using homogenization theory. *Proc. Royal Soc. A 471* (2015), 20150464.

[32] Daniel, R. C., Billing, J. M., Russell, R. L., Shimskey, R. W., Smith, H. D., and Peterson, R. A. Integrated pore blockage-cake filtration model for crossflow filtration. *Chem. Eng. Res. Des. 89* (2011), 1094–1103.

[33] Daniel, R. C., Schonewill, P. P., Shimskey, R. W., and Peterson, R. A. A brief review of filtration studies for waste treatment at the hanford site. Tech. Rep. PNNL-20023, Pacific Northwest National Laboratory, 2010.

[34] Di Luca, A., Ostrowska, B., Lorenzo-Moldero, I., Lepedda, A., Swieszkowski, W., Van Blitterswijk, C., and Moroni, L. Gradients in pore size enhance the osteogenic differentiation of human mesenchymal stromal cells in three-dimensional scaffolds. *Sci. Rep. 6*, 22898 (2016).

[35] Dizge, N., Koseoglu-Imer, D. Y., Karagunduz, A., and Keskinler, B. Effects of cationic polyelectrolyte on filterability and fouling reduction of submerged membrane bioreactor (mbr). *J. Membr. Sci. 377* (2011), 175–181.

[36] Dong, T., Hua, Y., Zhu, X., Huang, X., Chi, S., Liu, Y., Lou, C.-W., and Lin, J.-H. Highly efficient and sustainable pm filtration using piezo nanofibrous membrane with gradient shrinking porous network. *Sep. Purif. Technol. 289* (2022), 120753.

[37] Eren, T. The effects of random geometric graph structure and clustering on localizability of sensor networks. *Int. J. Distrib. Sens. Netw. 13* (2017).

[38] Ersahin, M. E., Ozgun, H., Dereli, R. K., Ozturk, I., Roest, K., and van Lier, J. B. A review on dynamic membrane filtration: Materials, applications and future perspectives. *Bioresour. Technol. 112* (2012), 196–206.

[39] Fong, D., Cummings, L., Chapman, S., and Sanaei, P. On the performance of multilayered membrane filters. *J. Eng. Math. 127* (2021), 1–25.

[40] Giglia, S., and Straeffer, G. Combined mechanism fouling model and method for optimization of series microfiltration performance. *J. Membr. Sci. 155* (1999), 261–275.

[41] Goei, R., Dong, Z., and Lim, T.-T. High-permeability pluronic-based tio2 hybrid photocatalytic membrane with hierarchical porosity: Fabrication, characterizations and performances. *Chem. Eng. J. 228* (2013), 1030–1039.

[42] Goswami, K. P., and Pugazhenthi, G. Credibility of polymeric and ceramic membrane filtration in the removal of bacteria and virus from water: A review. *J. Environ. Manage. 268* (2020), 110583.

[43] Grady, L. J. *Discrete Calculus: Applied Analysis on Graphs for Computational Science.* London, United Kingdom: Springer, 2010.

[44] Griffiths, I., and Stewart, P. A hybrid discrete–continuum model for modelling filtration. *J. Membr. Sci. 647* (2022), 120258.

[45] Griffiths, I. M., Kumar, A., and Stewart, P. S. A combined network model for membrane fouling. *J. Coll. Int. Sci. 432* (2014), 10–18.

[46] Griffiths, I. M., Kumar, A., and Stewart, P. S. Designing asymmetric multilayered membrane filters with improved performance. *J. Membr. Sci. 511* (2016), 108–118.

[47] Griffiths, I. M., Mitevski, I., Vujkovac, I., Illingworth, M. R., and Stewart, P. S. The role of tortuosity in filtration efficiency: A general network model for filtration. *J. Membr. Sci. 598* (2020), 117664.

[48] Gu, B., Kondic, L., and Cummings, L. A graphical representation of membrane filtration. *SIAM J. Appl. Math. 82* (2022), 950–975.

[49] Gu, B., Kondic, L., and Cummings, L. Network-based membrane filters: Influence of network and pore size variability on filtration performance. *J. Membr. Sci. 657* (2022), 120668.

[50] Gu, B., Renaud, D. R., Sanaei, P., Kondic, L., and Cummings, L. J. On the influence of pore connectivity on performance of membrane filters. *J. Fluid Mech. 902* (2020), A5.

[51] Guddati, S., Kiran, A. S. K., and Leavy, M. Recent advancements in additive manufacturing technologies for porous material applications. *Int. J. Adv. Manuf. Technol. 105* (2019), 193–215.

[52] Harley, B. A., Hastings, A. Z., Yannas, I. V., and Sannino, A. Fabricating tubular scaffolds with a radial pore size gradient by a spinning technique. *Biomaterials 27* (2006), 866–874.

[53] Hatano, Y., Das, A. K., and Mesbahi, M. Agreement in presence of noise: pseudogradients on random geometric networks. In *Proc. 44th IEEE Conf. Decis. Control* (2005), pp. 6382–6387.

[54] Herterich, J., Xu, Q., Field, R., Vella, D., and Griffiths, I. M. Optimizing the operation of a direct-flow filtration device. *J. Eng. Math. 104* (2017), 195–211.

[55] Ho, C.-C., and Zydney, A. L. Effect of membrane morphology on the initial rate of protein fouling during microfiltration. *J. Membr. Sci. 155* (1999), 261–275.

[56] Ho, C.-C., and Zydney, A. L. A combined pore blockage and cake filtration model for protein fouling during microfiltration. *J. Membr. Sci. 232* (2000), 389–399.

[57] Hoffmann, T., Porter, M. A., and Lambiotte, R. Generalized master equations for non-poisson dynamics on networks. *Phys. Rev. E 86* (2012), 046102.

[58] Hoffmann, T., Porter, M. A., and Lambiotte, R. *Random Walks on Stochastic Temporal Networks*. Berlin/Heidelberg, Germany: Springer, 2013, pp. 295–313.

[59] Huang, C., Yang, B., Chen, K., Chang, C., and Kao, C. Application of membrane technology on semiconductor wastewater reclamation: A pilot-scale study. *Desalination 278* (2011), 203–210.

[60] Hwang, K. J., Liao, C. Y., and Tung, K. L. Analysis of particle fouling during microfiltration by use of blocking models. *J. Membr. Sci. 287* (2007), 287–293.

[61] Iritani, E. A review on modeling of pore-blocking behaviors of membranes during pressurized membrane filtration. *Drying Tech. 31* (2013), 146–162.

[62] Ismail, A. F., and Goh, P. S. Microfiltration membrane. In *Encyclopedia of Polymeric Nanomaterials*, S. Kobayashi and K. Mällen, Eds. Berlin/Heidelberg, Germany: Springer, 2015.

[63] Jackson, N. B., Bakhshayeshi, M., Zydney, A. L., Mehta, A., van Reis, R., and Kuriyel, R. Internal virus polarization model for virus retention by the ultipor vf grade dv20 membrane. *Biotechnol. Prog. 30* (2014), 856–863.

[64] Jacod, J., and Protter, P. *Probability Essentials.* Berlin/Heidelberg, Germany: Springer, 2004.

[65] Jarvis, P., Carra, I., Jafari, M., and Judd, S. Ceramic vs polymeric membrane implementation for potable water treatment. *Water Res. 215* (2022), 118269.

[66] Jimenez-Martinez, J., and Negre, C. F. A. Eigenvector centrality for geometric and topological characterization of porous media. *Phys. Rev. E 96* (2017), 013310.

[67] Kanani, D. M., Fissell, W. H., Roy, S., Dubnisheva, A., and Fleischman, A.and Zydney, A. L. Permeability–selectivity analysis for ultrafiltration: effect of pore geometry. *J. Membr. Sci. 349* (2010), 405–410.

[68] Kiradjiev, K., Breward, C., and Griffiths, I. A model for the lifetime of a reactive filter. *J. Eng. Math. 133* (2022), 1–24.

[69] Kiradjiev, K., Breward, C., Griffiths, I., and Schwendeman, D. A homogenised model for a reactive filter. *SIAM J. Appl. Math. 81* (2021), 591–619.

[70] Kondic, L. Capstone Laboratory, Newark, New Jersey, New Jersey Institute of Technology. `http://cfsm.njit.edu/capstone`, 2018.

[71] Kory, J., Krupp, A. U., Please, C. P., and Griffiths, I. M. The effect of compressibility on the behaviour of filter media. *IMA J. Appl. Math. 85* (2020), 564–583.

[72] Kory, J., Krupp, A. U., Please, C. P., and Griffiths, I. M. Optimising dead-end cake filtration using poroelasticity theory. *Modelling 2* (2021), 18–42.

[73] Kosiol, P., Müller, M. T., Schneider, B., Hansmann, B., Thom, V., and Ulbricht, M. Determination of pore size gradients of virus filtration membranes using gold nanoparticles and their relation to fouling with protein containing feed streams. *J. Membr. Sci. 548* (2018), 598–608.

[74] Krupp, A., Griffiths, I., and Please, C. Stochastic modelling of membrane filtration. *Proc. R. Soc. A. 473* (2017), 20160948.

[75] Kuchenrither, R. D., Stone, L., and Haug, R. T. Omni-processor landscaping project. Tech. rep., Denver, Colorado, Water Environment Research Foundation, 2012.

[76] Li, W. *Fouling Models for Optimizing Asymmetry of Microfiltration Membranes.* PhD thesis, Cincinnati, Ohio, University of Cincinnati, 2009.

[77] Lin, Y., and Burggraaf, A. Experimental studies on pore size change of porous ceramic membranes after modification. *J. Membr. Sci. 79* (1993), 65–82.

[78] Lipnizki, F. Beer clarification. In *Encyclopedia of Membranes*, E. Drioli and L. Giorno, Eds. Berlin/Heidelberg, Germany: Springer, 2015, pp. 1–2.

[79] LIQTECH. Ceramic membrane knowledge. `https://liqtech.com/ceramic-membranes-dpf/silicon-carbide-ceramic-membrane/why-use-ceramic-membranes/`, 2020. Accessed on 2022-06-25.

[80] Liu, G., Xiao, M., Zhang, X., Gal, C., Chen, X., Liu, L., Pan, S., Wu, J., Tang, L., and Clements-Croome, D. A review of air filtration technologies for sustainable and healthy building ventilation. *Sustain. Cities Soc. 32* (2017), 375–396.

[81] Liu, Y., Gao, J., Ge, Y., Yu, S., Liu, M., and Gao, C. A combined interfacial polymerization and in-situ sol-gel strategy to construct composite nanofiltration membrane with improved pore size distribution and anti-protein-fouling property. *J. Membr. Sci. 623* (2021), 119097.

[82] Loh, S., Beuscher, U., Poddar, T., Porter, A., Wingard, J., Husson, S., and Wickramasinghe, S. Interplay among membrane properties, protein properties and operating conditions on protein fouling during normal-flow microfiltration. *J. Membr. Sci. 332* (2009), 93–103.

[83] Luckins, E., Breward, C., Griffiths, I. M., and Wilmott, Z. Homogenisation problems in reactive decontamination. *Eur. J. Appl. Math. 31* (2019), 782–805.

[84] Ma, R., Castro-Dominguez, B., Dixon, A. G., and Ma, Y. H. Scalability of multitube membrane modules for hydrogen separation: Technical considerations, issues and solutions. *J. Membr. Sci. 564* (2018), 887–896.

[85] Mannella, G., Conoscenti, G., Carfì Pavia, F., La Carrubba, V., and Brucato, V. Preparation of polymeric foams with a pore size gradient via thermally induced phase separation (tips). *Mater. Lett. 160* (2015), 31–33.

[86] Mehta, A., and Zydney, A. L. Permeability and selectivity analysis for ultrafiltration membranes. *J. Membr. Sci. 249* (2005), 245–249.

[87] Mehta, A., and Zydney, A. L. Effect of membrane charge on flow and protein transport during ultrafiltration. *Biotechnol. Progr. 22* (2006), 484–492.

[88] Meng, F., Chae, S.-R., Drews, A., Kraume, M., Shin, H. S., and Yang, F. Recent advances in membrane bioreactors: Membrane fouling and membrane material. *Water Res. 43* (2009), 1489–1512.

[89] Mochizuki, S., and Zydney, A. L. Theoretical analysis of pore size distribution effects on membrane transport. *J. Membr. Sci. 82* (1993), 211–217.

[90] Ng, T. C. A., Lyu, Z., Gu, Q., Zhang, L., Poh, W. J., Zhang, Z., Wang, J., and Ng, H. Y. Effect of gradient profile in ceramic membranes on filtration characteristics: Implications for membrane development. *J. Membr. Sci. 595* (2020), 117576.

[91] O'Dea, R., Crofts, J. J., and Kaiser, M. Spreading dynamics on spatially constrained complex brain networks. *J. R. Soc. Interface 10* (2013), 20130016.

[92] Oh, H., Park, J., Min, K., Lee, E., and Jyoung, J.-Y. Effects of pore size gradient in the substrate of a gas diffusion layer on the performance of a proton exchange membrane fuel cell. *Appl. Energy 149* (2015), 186–193.

[93] Onur, A., Ng, A., Batchelor, W., and Garnier, G. Multi-layer filters: Adsorption and filtration mechanisms for improved separation. *Front. Chem. 6* (2018), 417.

[94] Ostwal, M., Lu, X., Beuscher, U., and Pellegrino, J. Effect of microporous membrane properties and operating conditions on particle retention: Measurements and model studies. *Sep. Sci. Technol. 51*, 6 (2016), 1007–1021.

[95] Patanaik, A., Anandjiwala, R., and Boguslavsky, L. Development of high efficiency particulate absorbing filter materials. *J. Appl. Polym. Sci. 114* (2009), 275–280.

[96] Penrose, M. *Random geometric graphs.* Oxford, United Kingdom: Oxford University Press, 2003.

[97] Pereira, V., Dalwadi, M., and Griffiths, I. M. The role of caking in optimizing the performance of a concertinaed ceramic filtration membrane. *Phys. Rev. Fluids 6* (2021), 104301.

[98] Polyakov, S. V., Maksimov, E. D., and Polyakov, V. S. One-dimensional micro filtration model. *Theor. Found. Chem. Eng. 29* (1995), 329–332.

[99] Polyakov, Y. S. Depth filtration approach to the theory of standard blocking: Prediction of membrane permeation rate and selectivity. *J. Membr. Sci. 322* (2008), 81–90.

[100] Polyakov, Y. S., and Zydney, A. L. Ultrafiltration membrane performance: effects of pore blockage/constriction. *J. Membr. Sci. 434* (2013), 106–120.

[101] Porter, M., and Gleeson, J. *Dynamical Systems on Networks.* Cham, Switzerland: Springer, 2016.

[102] Printsypar, G., Bruna, M., and Griffiths, I. M. The influence of porous media microstructure on filtration. *J. Fluid Mech. 861* (2019), 484–516.

[103] Probstein, R. F. *Physicochemical Hydrodynamics.* Hoboken, New Jersey, USA: Wiley-Interscience, 1994.

[104] Pujar, N. S., and Zydney, A. L. Charge regulation and electrostatic interactions for a spherical particle in a cylindrical pore. *J. Coll. Int. Sci. 192* (1997), 338–349.

[105] Ranjbarzadeh-Dibazar, A., Barzin, J., and Shokrollahi, P. Microstructure crystalline domains disorder critically controls formation of nano-porous/long fibrillar morphology of eptfe membranes. *Polymer 121* (2017), 75–87.

[106] Reis, P., and Carvalho, M. Pore-scale analysis of condensate blockage mitigation by wettability alteration. *Energy J. 13* (2020), 4673.

[107] Roy, S. Innovative use of membrane technology in mitigation of ghg emission and energy generation. *Procedia Environ. Sci. 35* (2016), 474–482.

[108] Roy, S., Sinha, S., and Hansen, A. Role of pore-size distribution on effective rheology of two-phase flow in porous media. *Front. water 3*, 709833 (2021).

[109] Saksena, S., and Zydney, A. Pore size distribution effects on electrokinetic phenomena in semipermeable membranes. *J. Membr. Sci. 105* (1995), 203–215.

[110] Sanaei, P., and Cummings, L. J. Flow and fouling in membrane filters: effects of membrane morphology. *J. Fluid Mech. 818* (2017), 744–771.

[111] Sanaei, P., and Cummings, L. J. Membrane filtration with complex branching pore morphology. *Phys. Rev. Fluids 3* (2018), 094305.

[112] Sanaei, P., and Cummings, L. J. Membrane filtration with multiple fouling mechanisms. *Phys. Rev. Fluids 4* (2019), 124301.

[113] Sanaei, P., Richardson, G. W., Witelski, T., and Cummings, L. J. Flow and fouling in a pleated membrane filter. *J. Fluid Mech. 795* (2016), 36–59.

[114] Sano, T., Koga, Y., Ito, H., Duc, L. V., Hama, T., and Kawagoshi, Y. Effects of structural vulnerability of flat-sheet membranes on fouling development in continuous submerged membrane bioreactors. *Bioresour. Technol. 304* (2020), 123015.

[115] Siddiqui, M. U., Arif, A. F., and Bashmal, S. Permeability-selectivity analysis of microfiltration and ultrafiltration membranes: Effect of pore size and shape distribution and membrane stretching. *Membranes 6* (2016), 40.

[116] Singh, R. Dead-end filtration. In *Membrane Technology and Engineering for Water Purification*, C. O. F. Geraghty and N. Carter, Eds. Oxford, United Kingdom: Butterworth-Heinemann, 2014.

[117] Skilhagen, S. E., Dugstad, J. E., and Aaberg, R. J. Osmotic power–power production based on the osmotic pressure difference between waters with varying salt gradients. *Desalination 220* (2008), 476–482.

[118] Sobral, J. M., Caridade, S. G., Sousa, R. A., Mano, J. F., and Reis, R. L. Three-dimensional plotted scaffolds with controlled pore size gradients: Effect of scaffold geometry on mechanical performance and cell seeding efficiency. *Acta Biomater. 7* (2011), 1009–1018.

[119] Souza, V. C., and Quadri, M. G. N. Organic-inorganic hybrid membranes in separation processes: a 10-year review. *Braz. J. Chem. Eng. 30* (2013), 683–700.

[120] Sublett, J. L. Effectiveness of air filters and air cleaners in allergic respiratory diseases: A review of the recent literature. *Curr. Allergy Asthma Rep. 11* (2011), 395.

[121] Sun, W., Chen, T., Chen, C., and Li, J. A study on membrane morphology by digital image processing. *J. Membr. Sci. 305* (2007), 93–102.

[122] Sun, Y., Sanaei, P., Kondic, L., and Cummings, L. J. Modeling and design optimization for pleated membrane filters. *Phys. Rev. Fluids 5* (2020), 044306.

[123] Sundaramoorthi, G., Hadwiger, M., Romdhane, M. B., Behzad, A. R., Madhavan, R., and Nunes, S. P. 3d membrane imaging and porosity visualization. *Ind. Eng. Chem. Res. 55* (2016), 3689–3695.

[124] Talebi, M., Groote, J. F., and Linnartz, J.-P. M. G. The mean drift: Tailoring the mean field theory of markov processes for real-world applications. In *Analytical and Stochastic Modelling Techniques and Applications* (2017), N. Thomas and M. Forshaw, Eds., Cham, Switzerland: Springer, pp. 196–211.

[125] Tan, X., and Rodrigue, D. A review on porous polymeric membrane preparation. part i: Production techniques with polysulfone and poly (vinylidene fluoride). *Polymers 11* (2019), 1160.

[126] Tao, H. Spongelike structure. In *Encyclopedia of Membranes*, D. Enrico and G. Lidietta, Eds. Berlin/Heidelberg, Germany: Springer, 2016, pp. 1814–1815.

[127] Taylor, N., Ma, W., Kristopeit, A., Wang, S., and Zydney, A. L. Retention characteristics of sterile filters – effect of pore size and structure. *J. Membr. Sci. 635* (2021), 119436.

[128] Thiedmann, R., Manke, I., Lehnert, W., and Schmidt, V. Random geometric graphs for modelling the pore space of fibre-based materials. *J. Mater. Sci. 46* (2011), 7745–7759.

[129] Torrejon, D., and Emelianenko, M. Generalized master equations for random walks with time-dependent jump sizes. *SIAM Journal on Applied Mathematics 78* (2018), 1330–1349.

[130] United States Environmental Protection Agency. Technical fact sheet – 1,4-dioxane, Washington, D.C. `https://www.epa.gov/fedfac/technical-fact-sheet-14-dioxane`, 2017. Accessed on 2022-02-01.

[131] Van der Bruggen, B. Chapter 2 - microfiltration, ultrafiltration, nanofiltration, reverse osmosis, and forward osmosis. In *Fundamental Modelling of Membrane Systems*, P. Luis, Ed. Amsterdam, Netherlands: Elsevier, 2018, pp. 25–70.

[132] van der Schaft, A., Rao, S., and Jayawardhana, B. On the mathematical structure of balanced chemical reaction networks governed by mass action kinetics. *SIAM J. Appl. Math. 73* (2013), 953–973.

[133] Van der Sman, R. G. M., Vollebregt, H. M., Mepschen, A., and Noordman, T. R. Review of hypotheses for fouling during beer clarification using membranes. *J. Membr. Sci. 396* (2012), 22–31.

[134] Vijayan, V. K., Paramesh, H., Salvi, S. S., and Dalal, A. A. K. Enhancing indoor air quality –the air filter advantage. *Lung India 32* (2015), 473–479.

[135] Weisstein, E. W. Hypercube line picking From MathWorld–A Wolfram Web Resource. `https://mathworld.wolfram.com/HypercubeLinePicking.html`. Accessed on 2022-06-24.

[136] Wilson, C. *The invisible world: early modern philosophy and the invention of the microscope.* Princeton, New Jersey: Princeton University Press, 1995.

[137] Wong, N. H., Law, P. L., and Lai, S. H. Field tests on a grease trap effluent filter. *Int. J. Environ. Sci. Technol. 4* (2007), 345–350.

[138] Xie, Z., Ouyang, Z., and Li, J. A geometric graph model for coauthorship networks. *J Informetr. 10* (2016), 299–311.

[139] Xu, K., Wei, W., Chen, Y., Tian, H., Xu, S., and Cai, J. A pore network approach to study throat size effect on the permeability of reconstructed porous media. *Water 14* (2022), 77.

[140] Yan, J., Dong, K., Zhang, Y., Wang, X., Yu, A. A. A. J., and Ding, B. Multifunctional flexible membranes from sponge-like porous carbon nanofibers with high conductivity. *Nat. Commun. 10* (2019), 5584.

[141] Yang, S. Y., Park, J., Yoon, J., Ree, M., Jang, S. K., and Kim, J. K. Virus filtration membranes prepared from nanoporous block copolymers with good dimensional stability under high pressures and excellent solvent resistance. *Adv. Funct. Mater. 18* (2008), 1371–1377.

[142] Yu, C. H., Yiin, L.-M., (Tina) Fan, Z.-H., and Rhoads, G. G. Evaluation of hepa vacuum cleaning and dry steam cleaning in reducing levels of polycyclic aromatic hydrocarbons and house dust mite allergens in carpets. *J. Environ. Monit. 11* (2009), 205–211.

[143] Zahid, M., Rashid, A., Akram, S., Rehan, Z. A., and Razzaq, W. A comprehensive review on polymeric nano-composite membranes for water treatment. *J. Membr. Sci. Technol. 8* (2018), 179.

[144] Zeman, L. J., and Zydney, A. L. *Microfiltration and ultrafiltration: principles and applications.* New York, USA: Marcel Dekker, 1996.

[145] Zhang, W., Lim, C. C., Korniss, G., and Szymanski, B. K. Opinion dynamics and influencing on random geometric graphs. *Sci. Rep. 4*, 5568 (2014).

[146] Zsigmondy, R., Spear, E., and Norton, J. *The Chemistry of Colloids.* Hoboken, New Jersey, USA: Wiley, 1917.

[147] Zydney, A. L. High performance ultrafiltration membranes: pore geometry and charge effects. In *Inorganic Polymeric and Composite Membranes*, S. T. Oyama and S. M. Stagg-Williams, Eds., Membrane Science and Technology. Amsterdam, Netherlands: Elsevier, 2011, pp. 333 – 352.

[148] Zydney, A. L., Aimar, P., Meireles, M., Pimbley, J. M., and Belfort, G. Use of the log-normal probability density function to analyze membrane pore size distributions: functional forms and discrepancies. *J. Membr. Sci. 91* (1994), 293–298.